Plasmonics-enabled semiconductor photodetectors

Evgeniy Panchenko

ORCID: 0000-0002-9570-4443

A thesis presented for the degree of
Doctor of Philosophy

Submitted in total fulfilment of the requirements
of the degree of Doctor of Philosophy

July 20, 2017

School of Physics
The University of Melbourne
Australia

Abstract

The ever increasing demand for high-speed data processing requires faster operation of computer processors and peripherals. Despite the continual improvement in semiconductor technology processes which, in turn, leads to corresponding increases in logic gate switching frequency, the speed of the modern central processing units remains relatively constant. This speed limitation is primarily determined by metallic interconnects in the integrated circuits. Numerous enhancements have been introduced to conventional CMOS technology in order to decrease the resistance and capacitance of the interconnects. Even though these changes have markedly improved the characteristics of interconnects, further developments of this technology are extremely challenging and cost-ineffective. Therefore, as the current technology is rapidly reaching its limits, a new approach is required to overcome the existing issues and build high-speed digital devices.

Recent advances in the understanding of surface plasmon polaritons open up an opportunity to overcome this limitation and greatly increase the operating speed of future digital integrated circuits. Despite the exceptional properties of surface plasmons this task is challenging as it requires the optical components to be compatible with current planar technology. The main aim of this work is to progress research into the development of a technology which will permit overcoming current issues limiting increases in processor operation speed such as the RC parameters of metallic interconnects. In this thesis comprehensive analytical and numerical studies of a plasmonic input port, waveguide and modulator will be presented. Excitation of surface plasmons as well as their propagation along the waveguide will be experimentally demonstrated. It will be shown that waveguide-coupled metal-semiconductor-metal photodetectors enable an in-plane detection of the surface plasmons - an important property required for successful integration into modern semiconductor technology. The design presented here, therefore, could underpin a new class of optoelectronic devices that enable the integration of surface plasmons as signal carriers

in future high-speed optoelectronic processors.

The potential applications of surface plasmons are not limited to high-speed interconnects. The utilisation of the phenomenon of localised surface plasmons establishes an opportunity to create 2D materials with a tailored electromagnetic response. The second aim of this work, therefore, is to develop a technology which can improve the existing properties or add functionality to conventional photodetectors. This thesis focuses on a demonstration of planar polarisation-sensitive detectors and colour camera pixels. Plasmonic metasurfaces can be used to tailor the sensitivity of photodetectors to potentially arbitrary states of polarisation or wavelength of the incident beam. In this thesis a novel design for a polarisation-sensitive differential photodetector is presented. It will be experimentally demonstrated that such a photodetector exhibits a high robustness to intensity fluctuations which is a highly desirable property for telecommunication applications as well as being able to discriminate between different polarisation states. Furthermore, it is shown that plasmonic metasurfaces can also be used as integrated colour filters in camera pixels, permitting a fully planar design and eliminating the cross-talk issue associated with conventional pixels.

Declaration

This is to certify that:

(i) the thesis comprises only my original work towards the degree of the Doctor of Philosophy except where indicated in the Preface;

(ii) due acknowledgement has been made in the text to all other material used;

(iii) the thesis is fewer than the maximum word limit in length, exclusive of tables, maps, bibliographies and appendices

Signed _____ Date _____

Preface

This thesis was submitted as a requirement for the degree of Doctor of Philosophy (PhD) in the School of Physics, Faculty of Science at The University of Melbourne. The research activities behind this thesis were performed under the supervision of Prof. Ann Roberts and Dr. Timothy Denis James.

This thesis contains unpublished original work by the author except where acknowledgements and references are made to previous work. Jasper Cadusch contributed equally to designing (layout and nanoantennas, FEM simulations), fabricating (RIE, e-beam evaporation and EBL) and characterising (polarisation response) the differential photodetectors discussed in Section 8.1. The rest of the measurements (designing and performing SPCM measurements, electrical characterisation) were made independently by the author of this thesis. Jasper Cadusch must be also recognised for his assistance during the fabrication (e-beam evaporation, RIE) of the waveguide-coupled MSM photodetectors (see Chapter 5) and plasmonic pixel (see Chapter 8). Dr Laurens Henry Willems van Beveren assisted in obtaining Hall measurements of ITO films (see Section 6.3.1). Dr Ori Avayu from Tel Aviv University performed NSOM measurements of plasmonic waveguides (see Chapter 4) and Mr Stephen Gregory (School of Physics) bonded some of the fabricated samples.

All the samples throughout this thesis were fabricated at the Melbourne Centre for Nanofabrication (MCN). Dr Timothy James, Dr Matteo Altissimo and Dr Fatima Eftekhari all gave expert advice regarding advanced fabrication techniques during various process development stages.

Experimental advice in regard to sample characterisation was provided by Dr Timothy James, Dr Daniel Gomez and Prof Ann Roberts.

Some of the figures used in this thesis have been taken from other works. In

these instances the appropriate source has been cited at the end of the figure caption to acknowledge the source. Over the course of this work several publications and presentation were based on the work presented herein. They are listed below for reference.

The PhD candidature of the author was supported with scholarships from The University of Melbourne as Melbourne International Fee Remission Scholarships (MIFRS), Melbourne International Research Scholarships (MIRS), The N.D. Goldsworthy Scholarship for Physics and projects costs provided by ARC Discovery Project grants.

List of publications

Publication arising from PhD thesis

Evgeniy Panchenko, Jasper J Cadusch, Timothy D James, and Ann Roberts. 'Plasmonic metasurface-enabled differential photodetectors for broadband optical polarization characterization.' *ACS Photonics*, 3(10):1833–1839, 2016.

Evgeniy Panchenko, Timothy D James, and Ann Roberts. 'Modified stripe waveguide design for plasmonic input port structures.' *Journal of Nanophotonics*, 10(1):016019–016019, 2016.

Evgeniy Panchenko, Jasper J. Cadusch, Timothy D. James, and Ann Roberts. 'Plasmonics-enabled metal-semiconductor-metal photodiodes for high-speed interconnects and polarization sensitive detectors.' *In Proc. of SPIE Vol*, vol. 10106, pp. 1010619-1. 2017.

Evgeniy Panchenko, Timothy D James, and Ann Roberts. 'Waveguide coupled MSM photodiode for surface plasmon polariton detection.' *In 2014 Conference on Optoelectronic and Microelectronic Materials & Devices.*, pp. 242-243. IEEE, 2014.

Evgeniy Panchenko, Jasper J. Cadusch, Timothy D James, Daniel Gomez, and Ann Roberts. 'Planar surface plasmon detection technique for high speed interconnects in integrated circuits.' *In Preparation.*

Evgeniy Panchenko, Jasper J. Cadusch, Timothy D James, Daniel Gomez, and Ann Roberts. 'Plasmonic metasurface-enabled hyperspectral camera pixel.' *In Preparation.*

Other publications

Cadusch, Jasper J., **Evgeniy Panchenko**, Nicholas Kirkwood, Timothy D. James, Brant C. Gibson, Kevin J. Webb, Paul Mulvaney, and Ann Roberts. 'Emission enhancement and polarization of semiconductor quantum dots with nanoimprinted plasmonic cavities: towards scalable fabrication of plasmon-exciton displays.' *Nanoscale*, 7(33): 13816-13821, 2015.

Timothy D James, **Evgeniy Panchenko**, Nguyen T. L., Paul Mulvaney, Timothy J. Davis, and Ann Roberts. 'Polarisation to colour transformation via nano-antenna enhanced quantum dot emission.' *In 2014 Conference on Optoelectronic and Microelectronic Materials & Devices.*, pp. 246-247. IEEE, 2014.

LH Willems van Beveren, **Evgeniy Panchenko**, Nik Anachi, Lachlan Hyde, Dan Smith, Timothy D James, Ann Roberts, and JC McCallum. 'Indium tin oxide film characterization using the classical hall effect.' *In 2014 Conference on Optoelectronic and Microelectronic Materials & Devices*, pages 144–145. IEEE, 2014.

Acknowledgments

I would like to thank Prof Ann Roberts, who has been my supervisor from day-one, for accepting me as a PhD student, incredible support and guidance throughout. I also extend my deep gratitude to my co-supervisor Dr Timothy D. James for providing excellent support and advice and motivating me to complete this thesis. I am very appreciative for having Prof David N. Jamieson as the member and A/Prof Jeffrey McCallum as the chair of my advisory committee and for their discussions and suggestions, which have greatly improved the quality of my work.

I would also like to acknowledge the other senior members of the School of Physics for always being available for discussions and providing valuable advice, namely Prof Kenneth Crozier, Prof Robert E. Scholten, Dr David A. Simpson, Mr Stephen Gregory and Dr Brett Johnson. I would like to thank A/Prof Jeffrey McCallum, Dr Brett Johnson and Michael Stuiber for providing some of the electrical measuring tools for experiments. I want to thank Tal Ellenbogen for welcoming me in his laboratory in Tel Aviv. The PhD experience was made much more bearable thanks to fellow students, Stuart K. Earl, Michael H. Stuiber, Zhi Qin Teo, Amir Djalalian-Assl, and Kelvin Xu. Special thanks also to Jasper J. Cadusch for the collaborative work, indispensable conversations and having a fun time instead of writing my thesis. This thesis would not have been possible without all the support from my family over the years, and is dedicated to them; Mum, Dad, Wife, my uncle and his family.

I would also like to acknowledge the support of the University of Melbourne and the Australian Government through the Melbourne International Research Scholarship. In addition, I would like to acknowledge specifically the School of Physics for providing The N.D. Goldsworthy Scholarship for Physics, which has enabled this thesis to be completed in a timely manner. I would also like to acknowledge the Australian Research Council for its contribution to the funding of this research and the Laby Foundation for providing me a travel scholarship to attend an international

conference and Tel Aviv University.

"In theory, there is no difference
between theory and practice...
In practice - there is."

Walter J. Savitch

Contents

Abstract **i**

Preface **iv**

List of publications **vi**

Acknowledgments **viii**

1 Introduction **1**

1.1 Photonics vs Plasmonics 3

1.2 Logic gates with plasmonic interconnects 5

1.2.1 Plasmonic logic gate proposal 8

1.3 Plasmonic-enhanced photodetectors with advanced properties 10

1.4 Thesis goals 19

1.4.1 Thesis goals summary 20

1.4.2 Thesis structure 21

2 Theoretical background and literature review **22**

2.1 Surface plasmon theory 23
2.1.1 The IMI interface 28
2.1.2 The MIM interface 28
2.1.3 Drude – Sommerfeld model 29
2.2 Surface plasmon polariton excitation 31
2.2.1 Prism coupling 32
2.2.2 Grating coupling 33
2.2.3 Near-field excitation 34
2.2.4 Summary 35
2.3 Surface plasmon detection 36
2.3.1 Near-field imaging 36
2.3.2 Far-field imaging 38
2.3.3 Conversion techniques 41
2.3.4 Summary 42
2.4 Plasmonic waveguides 43
2.4.1 Band gap waveguides 43
2.4.2 Stripe weveguides 45
2.4.3 Slot waveguides 47
2.4.4 Summary 48
2.5 Semiconductor plasmonics 48
2.5.1 Linear effects 48

2.5.2 Non-linear effects . . . 52

2.5.3 Summary . . . 58

2.6 Conclusion . . . 58

3 Modelling and fabrication techniques 59

3.1 Numerical simulations . . . 59

3.1.1 Finite element method . . . 60

3.2 Fabrication . . . 64

3.2.1 Electron-beam lithography . . . 64

3.2.2 Electron-beam evaporation . . . 68

3.2.3 Reactive ion etching . . . 69

3.2.4 Hydrofluoric acid wet etching . . . 70

3.2.5 Annealing and thermal oxide growth . . . 71

3.3 Characterisation . . . 71

3.3.1 Scanning electron microscopy . . . 71

3.3.2 Electrical characterisation . . . 72

3.3.3 Near-field scanning optical microscopy . . . 73

3.3.4 Scanning photocurrent microscopy . . . 74

3.4 Conclusion . . . 75

4 Design of input port for plasmonic integrated circuits 77

4.1 Introduction . . . 77

4.2 Design and simulations 78
4.3 Waveguide improvement techniques 84
4.3.1 Reduction of the mode confinement 85
4.3.2 Waveguide expansion 89
4.4 Application of microwave theory to plasmonic waveguides 91
4.4.1 Characteristic impedance definition and matching techniques . 92
4.5 Fabrication 97
4.6 Experimental results 97
4.7 Conclusion 100

5 Planar surface plasmon detection 102

5.1 Introduction 102
5.2 Surface plasmon detection 102
5.2.1 Electron-hole pair generation 103
5.2.2 Hot-electron generation 104
5.3 Metal-semiconductor-metal photodetectors 105
5.4 Fabrication 109
5.5 Experimental results 110
5.6 Conclusion 114

6 Progress towards a surface plasmon modulator 115

6.1 Design and theory of operation 115

6.1.1 Metal-oxide-semiconductor capacitor structure 116

6.2 Waveguide-embedded plasmon modulator 118

6.3 ITO film fabrication and characterisation 125

6.3.1 Hall-effect measurements 125

6.3.2 CV measurements 128

6.4 Summary 130

7 Plasmonic interconnects summary **132**

8 Plasmon-enhanced photodetectors **135**

8.1 Plasmonic metasurface-enabled differential photodetector 135

8.1.1 Introduction 135

8.1.2 Design and theory of operation 136

8.1.3 Fabrication 143

8.1.4 Experimental results 144

8.1.5 Summary 150

8.2 Plasmonic camera pixel 151

8.2.1 Introduction 151

8.2.2 Design and theory of operation 151

8.2.3 Fabrication 159

8.2.4 Experimental results 164

8.2.5 Summary 172

9 Plasmonic-enhanced photodetectors summary **174**

10 Thesis summary and future work **176**

10.1 Thesis outcomes 176

10.2 Future work 177

10.2.1 Logic gates with plasmonic interconnects 177

10.2.2 Plasmonic-enhanced photodetectors 179

10.3 Summary 180

Bibliography **180**

Appendix A **202**

List of Figures

1.1 Graph showing the evolution of processor speed with time. The speed 'saturation' is observed at ∼3-3.5 GHz. Taken from [4]. 1

1.2 Equivalent electric circuit of the interconnect between logic gates can be represented by an RLC-filter. The parameters are dependent on the length dx of the wire. 2

1.3 Photonic ring resonators **(a)** [14] and waveguide with an introduced defect **(b)** [15][1]. Both structures have dimensions of tens or hundreds of micrometers. 3

1.4 Basic operation steps **(a)** which must be performed by plasmonic logic gates to create a fully functional integrated circuit. Schematic diagrams of conventional logic gate **(b)** and logic gate with plasmonic interconnects **(c)**. 6

1.5 Surface plasmon detection using MSM photodetectors **(a)**, PIN photodiodes **(b)** and bipolar phototransistors **(c)**. 6

1.6 Schematic representation of plasmonic modulator connected to the output of the logic gate. 7

1.7 Schematic representation of plasmonic 'NOT' logic gate. 9

1.8 Schematic representation **(a)** and false-coloured SEM image of physical implementation attempt **(b)** of the plasmonic waveguide-coupled MSM photodetector with embedded modulator. 9

1.9 The principles of polarisation-encodded signal transmitting systems. . 11

1.10 The beam intensity fluctuations in polarisation-encodded signal transmitting systems may cause misinterpretations of the signal despite the persisting state of polarisation. 13

1.11 Schematic representation of system utilising single-ended signalling. Noise which affects the transmission line will appear at the output of the receiver. 14

1.12 Schematic representation of system utilising differential signalling. In this regime noise affects both channels of the transmission line. Since the noise is in-phase on both complementary inputs of the receiver it will be subtracted from the signal and will not appear at the output. 14

1.13 Schematic representation of two spiral MSM photodetectors with rectangular **(left)** and chiral **(right)** nanoantennas. 15

1.14 Schematic representation of a common digital camera sensor **(d)** design. The incoming light passes a microlens array **(a)** and is then filtered by a mosaic colour filter **(b)**. The resulting beam is detected by photosensitive array of pixels **(c)**. Taken from [75]. 16

1.15 Schematic representation of a RGB colour pixel crossection. Rays reaching microlenses at large angles can illuminate a neighbour detector resulting in pixel crosstalk. 17

1.16 SEM image of a differential spiral photodetector **(a)** and plasmonic colour camera pixel **(b)**. Plasmonic metasurfaces are used to make photodetectors sensitive to the polarisation or wavelength of the light respectively. 18

2.1 Schematic representation of electron density at the surface interface and accompanying electric field. 22

2.2 Schematic representation of a multilayer interfaces supporting the surface plasmon polaritons propagation. 25

2.3 Even **(a)** and odd **(b)** coupled modes propagating along the IMI interface. Gray (ϵ_1) and blue (ϵ_2) colours represent metal and dielectric respectively. 28

2.4 Even **(a)** and odd **(b)** coupled modes propagating along the MIM interface. Gray (ϵ_2) and blue (ϵ_1) colours represent metal and dielectric respectively. 29

2.5 Graphs showing the values of real **(left)** and imaginary **(right)** parts of dielectric permittivity for gold, obtained from the Drude model (solid black line) and experimental data (red dots) from [89]. Taken from [26][2]. 31

2.6 Dispersion relations for SPP on silver film and light lines in air and silica. Photon in silica has larger momentum than the SPP on Ag-Air interface. 32

2.7 Prism coupling to SPP using Kretschmann **(a)** and Otto **(b)** configuration. 33

2.8 Excitation of SPP using grating coupling. The difference in wavevectors is compensated by an amount related to the grating period. . . . 34

2.9 Near-field excitation of surface plasmons using a metal-coated optical fibre with small aperture. 35

2.10 Common techniques used for detecting surface plasmons. 36

2.11 Excitation and detection of surface plasmons on the surface of nanowire. **(a)** Excitation scheme. **(b)** Microscope image of a nanowire. **(c)** Near-field image obtained by SNOM. **(d)** Cross-cut along the chain dotted line. Taken from [103][3]. 37

2.12 Imaging of SPP using quantum dots. **(i)** Optical image of Ag nanowire. **(ii)** The QD emission under large-area laser illumination. **(iii-vi)** The QD emission with different polarisation angle of excitation laser. Taken from [29][4]. 39

2.13 Schematic representation of surface plasmon excitation by nanoslit and its scattering by grating structure into far-field. Taken from [105][5]. 40

2.14 Schematic representation of an SPP semiconductor detector. Taken from [18][6]. 41

2.15 Topographic **(a)** and near-filed **(b,c)** images of plasmonic Bragg mirror obtained by SNOM. Propagation of the SPP excited using 1550 nm **(b)** and 1600 nm **(c)** wavelengths respectively. Propagation direction is from right to left. Taken from [23]. 44

2.16 Topographic **(a)** and near-field **(b)** images of an SPP waveguide in a Bragg mirror. Taken from [23]. 44

2.17 Schematic representation of 45° bent plasmonic waveguide **(a)** and FEM simulation **(b)** propagating wave. Taken from [111][7]. 45

2.18 Symmetric **(a)** and asymmetric **(b)** stripe waveguide configurations. . 46

2.19 Normalised E_y field component distribution for different stripe thicknesses. Taken from [16][8]. 46

2.20 Symmetric **(a)** and asymmetric **(b)** slot waveguide structures. 47

2.21 Possible approaches for surface plasmon modulation. 49

2.22 Simple plasmonic waveguide network **(a)** with two inputs I1, I2 and single output O. Plot **(b)** shows the dependence of the output scattering intensity from the phase shift between inputs (black line) or when only a single input (either I1 or I2) is used (green line). Scattering (i,iii) and QD emission (ii,iv) images of the structure with different phase shifts between inputs. Taken from [29][9]. 50

2.23 Examples of plasmonic waveguide networks capable of realising basic logic functions. Taken from [29][9]. 50

2.24 Schematic representation of cascaded logic elements **(a)** and fluorescent image of designed waveguide network **(b)**. I1 and I2, O and C are inputs, output and control signal of the circuit respectively. Taken from [117][10]. 51

2.25 Schematic representation of MIM waveguide **(a)** and magnetic field mapping inside the resonator in 'ON' and 'OFF' states **(b)** respectively. Taken from [20][11]. 52

2.26 Dependence between the modulation depth and change of real **(a)** and imaginary **(b)** parts of refractive index respectively. Different lines correspond to various lengths between the modulator cavities. Taken from [20][12]. 53

2.27 Schematic representation of an all-optical modulator **(a)** and transmission spectra through it **(b)**. Taken from [22]. 55

2.28 Signal transmission spectra through the modulator **(a)** in 'ON' and 'OFF' states. Distribution of magnetic field **(b,c)** inside the device. Taken from [22]. 55

2.29 SEM image of the nanoantenna array on VO_2 substrate **(a)** and normalised reflection spectra of the metasurface in cold and hot states **(b)**. Taken from [121]. 56

2.30 Schematic representation of modulator based on thermo-optical phenomenon **(a)** and its cross section **(b)**. Taken from [122]. 57

3.1 Locally modified mesh in FDTD **(a)** and FEM **(b)** models. FEM model is less memory-demanding as the mesh is modified only within a certain region. Taken from [129]. 62

3.2 Simulation models of the plasmonic camera pixel (see Section 8.2 for more details). Figures **(a)** and **(b)** show the models with coarse and fine meshes respectively. The corresponding simulation results **(c)** and **(d)** are significantly different at certain points. The insufficient meshing can, therefore, lead to not only inaccurate but also incorrect results. 63

3.3 A schematic diagram of the electron-beam lithography tool. Taken from [131][13]. 65

3.4 The SEM images of the grating structures exposed with the same base dose of 900 µC/cm^2 without **(a)** and with **(b)** PEC correction. The middle of the first structure is overexposed due to the charge accumulation effect. 66

3.5 A common fabrication process involving the EBL lithography. 67

3.6 The marker pattern for multilayer exposure design in Klayout **(a)** and implemented on the sample **(b)**. 68

3.7 Schematic diagram of the electron-beam evaporator. Taken from [135]. 69

3.8 Schematic diagram of the reactive ion etching tool. Taken from [136]. 70

3.9 SEM image of the gold stripe. The resolution allows to see the grains on the gold surface. 72

3.10 Schematic representation of an NSOM system operating in collection mode. Taken from [139]. 73

3.11 Schematic representation of NSOM operating regimes: **(a)** reflection mode, **(b)** transmission mode, **(c)** collection mode. 74

3.12 Normalised photocurrent maps of the differential photodetector (see Section 8.1.4 for details). 75

4.1 Schematic representation of plasmonic input port coupled with a stripe waveguide. Incident p-polarized light with momentum k_0 excites an SPP (with momentum k_{SPP}) which is focused into waveguide. 79

4.2 Dispersion curves for silver **(a)** and gold **(c)** slabs with different cladding dielectrics and associated with them SPP propagation lengths **(b)**,**(d)**. Magenta and red dashed lines represent light-in-air and light-in-silica wave vectors respectively. 80

4.3 Normalised electric field distribution on the top of the waveguide in case of shallow **(a)** and through **(b)** grating designs. The insets depict the schematic representation of the structures. 83

4.4 Normalised electric field distribution on two plasmonic ports with 5 µm **(a)** and 300 nm **(b)** wide waveguides. Narrow waveguide exhibits a larger attenuation of surface plasmons. 84

4.5 Normalized electric field profile **(a)** and distribution along x **(b)** and y **(c)** coordinates of rectangular shape waveguide. Green curve represents the waveguide outline. 85

4.6 Schematic representation of plasmonic input port with hybrid-shape waveguide. Incident p-polarized light with momentum k_0 excites an SPP (with momentum k_{SPP}) which is focused into waveguide. 86

4.7 The crossection of a modified stripe waveguide. The top surface is curved with the radius of 200 nm to decrease attenuation. 86

4.8 The normalised electric field profile of the modified stripe waveguide with circle radius of 150 nm **(a)** and 300 nm **(b)** respectively. 87

4.9 The evolution of the real (blue) and imaginary (green) parts of the effective mode index. The waveguide mode index approaches that of a rectangular waveguide as the radius of curvature is increased ($n_{rec} = 1.55 - 0.041i$). 87

4.10 The normalized electric field distribution **(a)** on the top surfaces of the rectangular (green) and modified stripe (blue) waveguides. Graphs **(b)** and **(c)** show the distribution of a z-component of electric field on the rectangular and modified stripe waveguides respectively. 88

4.11 Possible fabrication techniques of hybrid-shape waveguide. 89

4.12 The evolution of the real (blue) and imaginary (green) parts of the effective mode index as a function of the waveguide width. The expansion of the waveguide allows to reduce the loss by the factor of 2.5. 90

4.13 Fundamental **(a)** and second order **(b)** modes supported by 550 nm wide waveguide. The higher order mode has much greater imaginary part of the effective mode index n_{eff} and, therefore, experience higher attenuation. 90

4.14 Schematic representation of a MIM plasmonic waveguide with field lines between the metallic parts. Electric (green) and magnetic (magenta) integration paths are used for V and I determination respectively. 94

4.15 The distribution of electric **(a)** and magnetic **(b)** field lines around symmetric stripe waveguide. 94

4.16 Poynting vector distribution along the cross section of the stripe waveguide. Curved black line shows the integration area where $P_z > max(P_z)/e^2$. 96

4.17 The dependence of the dielectric loaded waveguide characteristic impedance from the width. 96

4.18 SEM images of 500 nm wide aluminium **(a)** and 2.5 µm wide gold **(b)** waveguides respectively. The scale bar for image **(a)** is 3 µm and 5 µm for **(b)**. 98

4.19 Optical images of 0.5 and 1.5 µm waveguides made of aluminium **(a,b)** and gold **(c,d)**. 98

4.20 The AFM scans **(a,c)** and surface plasmon maps **(b,d)** of the 0.5 and 1.5 µm wide gold waveguides respectively. 99

4.21 The AFM scan **(a)** and surface plasmon map **(b)** of the 5 µm wide aluminium waveguide. 100

5.1 Schematic representation of a waveguide-coupled MSM photodetector with excitation grating. 106

5.2 A band diagram of biased MSM photodetector **(a)** describing two possible mechanisms of photocurrent generation. $q\Phi_B$ is a height of the Schottky barrier, E_v, E_c and E_F are valence, conduction and Fermi energy levels respectively. Schematic representation of MSM photodetector coupled with waveguide **(b)** and equivalent electric circuit of the detector **(c)**. The surface plasmon outcoupling mechanism on MSM photodetector **(d)**. 107

5.3 Normalised electric field map of the photodetector active region (under grating). 108

5.4 Simulated power flow into the substrate as a function of grating period and duty cycle. A higher power flow indicates a more efficient surface plasmon outcoupling into the substrate. 109

5.5 Scanning electron microscope images of the entire structure **(a)** and close-up of the MSM photodetector grating **(b)**. 110

5.6 Measured I-V curve of the MSM photodetector **(a)**. Dependence of the normalized scattering intensity from MSM fingers from polarization of the excitation beam **(b)**. 111

5.7 Bright-field image of a waveguide-coupled MSM photodetector **(a)**. Scattering from the fingers (circled) of 2.5 µm wide waveguide-coupled MSM photodetector for s (TE) **(b)** and p (TM) **(c)** polarization of the excitation beam respectively. 112

5.8 Difference of scanning photocurrent maps of a waveguide-coupled MSM photodetector obtained under TM (0°) and TE (90°) polarised 635 nm laser beam. 113

5.9 Photocurrect as a function of polarisation angle **(a-d)** for different waveguide lengths. Root mean square values of signals at each waveguide length (crosses) and normalised plasmon intensity (dotted line) are shown on **(e)**. 114

6.1 Schematic representation of a waveguide-embedded plasmonic ITO modulator **(a)**, its cross-section **(b)** and SEM image **(c)** of an implementation attempt (modulator section is artificially coloured in purple). 116

6.2 Normalised electric field map of the fundamental mode supported by the modulator in "OFF" **(a)** and "ON" **(c)** states respectively. Graphs **(b)**,**(d)** show the electric field distribution across the vertical cut-line through the middle of the waveguide. 117

6.3 The dependence between the wavelength and the real **(a,b)** and imaginary **(c,d)** parts of the ITO permittivity and refractive index respectively. The colours represent different carrier concentrations. 119

6.4 The schematic representation and initial parameters for the ITO plasmonic modulator model. One-dimensional case is considered. 122

6.5 The potential distribution across the active area of the ITO modulator. 123

6.6 A charge carrier concentration profile of the ITO layer in the plasmonic modulator. 123

6.7 The real and imaginary parts of the dielectric permittivity **(a)** and refractive index **(b)** of the ITO layer in "ON" (green) and "OFF" (blue) states respectively. 124

6.8 Photo of the ITO samples with Al foil as a shadow mask before the Cr contacts deposition. 126

6.9 Schematic representation of a setup for the Hall Effect measurement of the ITO film. 126

6.10 Hall resistance as a function of the applied magnetic field. Both samples showed a linear dependence from the magnetic field, although the sputtered ITO film has larger resistance compare to the e-beam evaporated. 128

6.11 A schematic representation of the MOS capacitor structures **(a)** used for SiO_2 insulation properties determination and a photo **(b)** of the fabricated sample under 2.5x magnification. 129

6.12 CV characteristics of 3 measured MOS capacitors. The breakdown occurs at -0.4 V and +0.25 V and remains stable among the samples. 130

8.1 FEM calculated normalized distribution of charge density on the nanoantenna surface. Figures **(a)** and **(b)** show the cases when the electric field of the incident wave is perpendicular and parallel to the long axis of the nanorod respectively. Figures **(c)** and **(d)** show distribution of surface charge density on chiral nanoantennas illuminated with right and left circularly polarised light respectively. 137

8.2 FEM calculated normalized absorption spectra for normally incident orthogonal polarisations for linear **(a)** and chiral **(b)** Al nanoantennas. The spectra consist of several distinct resonances. 138

8.3 Schematic representation showing both channels of photodetectors integrated with nanorods to sense either linear (left) or circular (right) polarisation states **(a)**. Active areas of channels (A and B) are formed between common and signal contacts. A band diagram under bias and a circuit diagram of each photodetector are shown on **(b)**. E_v, E_c and E_F are valence, conduction and Fermi energy levels respectively. Experimental setup used to obtain wavelength-dependent differential photocurrent measurements **(c)**. 139

8.4 FEM calculated potential distribution on the surface **(a)** and inside **(b)** the silicon substrate of the differential photodetector under 1 V bias. Since there is no potential gradient between the signal leads (red) carriers generated within this region will not contribute to the output signal. 140

8.5 Scanning electron microscope image of the spiral photodetector **(a)**. Nanoantennas are absent between two signal contacts. The active regions with square **(b)**, rectangular **(c)** and chiral **(d)** nanoantennas respectively. The scale bar for image **(a)** is 10 µm and 1 µm for images **(b)**,**(c)**,**(d)**. 141

8.6 The detector shown in **(a)** is equipped with linear nanoantennas arranged to detect the polarization state of cyclindrical vectros beams (radial and azimuthal basis states). The design implemented in **(b)** consists of orthogonal linear gold nanoantenna of various lengths. It is designed to extend the operating wavelength range of the linear polarization detector from the visible into the near infrared region. . . 142

8.7 An IV characteristic showing the differential photodetector's channel in darkness and under illumination **(a)**. Generated photocurrent as a function of an incident power **(b)**. 145

8.8 Normalised photocurrent maps of a single channel of linear-polarisation sensitive photodetector for different polarisation angles of the incident beam. The photocurrent generated by this channel increases with progression of the polarisation angle. 145

8.9 Normalised photocurrent maps of a photodetector with rectangular nanoantennas obtained with orthogonal polarisation states of the light. The nanoantennas of channel A (Ch A) and B (Ch B) are oriented along x and y axis of the graph respectively. The maximum photocurrent appears when the incident electric field is perpendicular to the long axis of the nanoantenna. 146

8.10 Normalised photocurrent affected by a signal power fluctuation from both channels of photodetectors with rectangular **(a)**, square **(b)** and chiral **(c)** sets of nanoantennas. As can be seen, differential photocurrent of each photodetector **(d)**,**(e)**,**(f)** is not affected by this type of noise. Figure **(g)**,**(i)** and **(j)** show the amplitude of the differential signal at each orthogonal state of polarisation. The rotation of HWP and QWP are relative to the fast axis of the polariser. 147

8.11 Differential signals at different wavelengths for photodetectors with rectangular **(a)**, square **(b)** and chiral **(c)** nanoantennas (the solid lines are polynomial fits of experimental data to guide the eye). The side graphs show root mean square values of photocurrent and reflect a differential responsivity at each wavelength. 148

8.12 Measured signal to noise ratios for the linear **(a)** and circular **(b)** photodetectors. The line is a polynomial fit to guide the eye. The measured SNR is a function of both the antenna reflectivity and the Si MSM photodetector responsivity. 149

8.13 Two main colour schemes used to create a full gamut: RGB **(a)** and CMY **(d)**. Each main colour in the model is represented via bandpass **(b)** or rejection **(e)** filters. The colour filter used in digital camera consists of either RGGB **(c)** or CMYY **(f)** patterns depending on which colour model is used. 152

8.14 Schematic representation of a simple perfect absorber structure. . . . 153

8.15 Schematic representation of two sets of plasmonic filters used in plasmonic camera pixel design. A filter composed of circular **(left)** and rectangular **(right)** nanoantena sets will show null or high polarisation responsivity respectively. 154

8.16 **(a)** Plot of the simulated normalised absorption of plasmonic nanoantenna for different lengths. **(b)**, **(c)** and **(d)** are absorption spectra in visible region for nanoantenna with 60, 100 and 180 nm respectively. These nanoantenna are used to create blue, green and red filters. . . . 155

8.17 **(a)** Plot of the simulated absorption in back mirror of the plasmonic pixel for different lengths of the nanorod. **(b)**, **(c)** and **(d)** are absorption spectra in infrared region for nanoantenna with 150, 205 and 230 nm respectively. These nanoantenna are used to create 1130, 1350 and 1530 nm bandpass filters. 156

8.18 Schematic diagrams of plasmonic camera pixels based on MSM **(a)** and Schottky **(b)** photodetectors. The equivalent electric circuit of the each pixel is represented by 4 **(c)** or 3 **(d)** doides with common cathodes. 157

8.19 Plasmonic camera pixel designs utilising MSM **(a)**,**(b)** and Schottky **(c)** configurations respectively. The insets on each figure show the entire pixel design. 158

8.20 Plasmonic colour pixel fabrication steps. 159

8.21 SEM images of nanoantenna metasurfaces after RIE step. **(a)** and **(b)** show the plasmonic filters for MSM and Schottky photodetector designs respectively. The filters consist of either nanorods **(c)** or nanodiscs **(d)**. 160

8.22 SEM image **(a)** of plasmonic nanorod metasurface obtained at 30° angle. Figure **(b)** shows the measured height of supporting nanopillars. 161

8.23 SEM image of the entire plasmonic colour pixel structure utilising Schottky configuration. 162

8.24 SEM images of different regions of the plasmonic colour pixel: **(a)** contact with one of the photodetectors, **(b)** metallisation around the pixel (the inset shows a schematic representation of the etching profile), **(c)** centre of the pixel and **(d)** plasmonic colour filter. 163

8.25 Image of plasmonic camera pixels taken under illumination with s- and p-polarised light. Top and bottom rows show pixels utilising Schottky and MSM designs respectively. Both configurations show strong polarisation response. 165

8.26 Normalised simulated absorption in nanoantenna and measured reflection spectra from blue **(a)**, green **(b)** and red **(c)** channels of plasmonic colour pixel. 166

8.27 Normalised reflection spectra from plasmonic pixel colour filters utilising the MSM **(a)** and Schottky **(b)** configurations respectively. Figures **(c)** and **(d)** show the reflection gamut of these pixels. 167

8.28 Image of a functional plasmonic colour pixel utilising MSM configuration. The labels show the assignations of each aluminium contact. . 168

8.29 IV characteristics of each colour channel of the plasmonic pixel utilising MSM **(a)** and Schottky **(b)** configurations respectively (with no illumination). 169

8.30 IV characteristics of each colour channel of the plasmonic camera pixel utilising the MSM configuration under illumination. Figures **(a)**,**(b)** and **(c)** show the illumination spectra. The IV curves obtained under these spectra are shown in **(d)**,**(e)** and **(f)** respectively. As can be seen the lower photocurrent is generated by detector with a filter designated for particular part of the spectrum. 169

8.31 Scanning photocurrent microscopy maps of central area of plasmonic pixels with the MSM **(a)** and Schottky **(b)** configurations respectively. 171

10.1 Concept design of a 'NAND' logic gate with plasmonic interconnects. 178

10.2 Schematic representation of differential photodetector capable of full determination of the Stokes parameters of an incident field. 179

A1 Electronic schematic of transimpedance amplifier specially designed for differential photodetector. The inset demonstrates the printed circuit board of the amplifier. 203

A2 Interface of the LabView program developed for the SPCM setup. . . 204

1. Introduction

The ever-increasing demand for high-speed data processing requires faster operation of computer processors (CPU) and peripherals. This becomes extremely important when performing sequential tasks that cannot be parallelised across multiple computational nodes (e.g cryptography and non-linear simulations). Despite the gradual improvement in semiconductor technology processes [1] (such as the decrease in transistor gate dimensions) which, in turn, should lead to a corresponding increase in the frequency of logic gate switching, the speed of modern CPUs remains relatively constant (see Fig.1.1). Since the switching speed of discrete transistors can be very high [2, 3] the constraint, therefore, lies outside the logic gates.

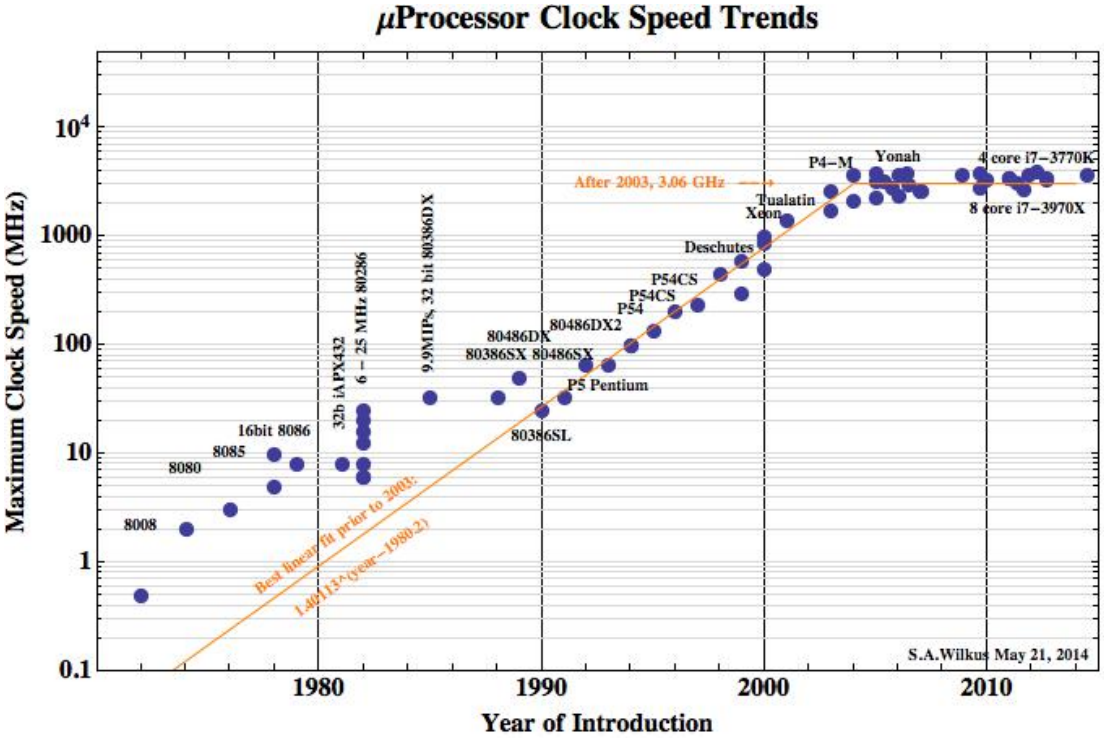

Figure 1.1: Graph showing the evolution of processor speed with time. The speed 'saturation' is observed at ∼3-3.5 GHz. Taken from [4].

This speed limitation is primarily determined by metallic interconnects in the integrated circuits [5]. The underlying phenomenon is a signal propagation delay - a physical limit of the propagation velocity of the electrical signal in the chip. A typical interconnect between logic gates must be considered to appreciate the physical processes behind this phenomenon. An example of typical section of transmission line is shown in Fig.1.2. A metallic strip sits on an insulating layer above a ground plane. The characteristics of this transmission line are dependent on the length dx of this wire which has a total inductance Ldx, capacitance Cdx and resistance Rdx. The equivalent electric circuit of such an interconnect is shown in Figure 1.2. The serial and parallel resistors represent the loss in the metal and the insulating properties of the SiO_2 layer. The inductor and capacitor represent the reactive loss associated with the alternating current transmission through the wire. Since the inductance of the wire and the leakage current through the insulating layer of silica are negligibly small, the equivalent circuit can be further simplified to an RC filter [6]. The bandwidth and, in its turn, the speed of the interconnect is reduced by the time required to charge the capacitor. This RC constant, therefore, defines the speed limit of the microelectronic circuit regardless of the speed of each individual logic gate.

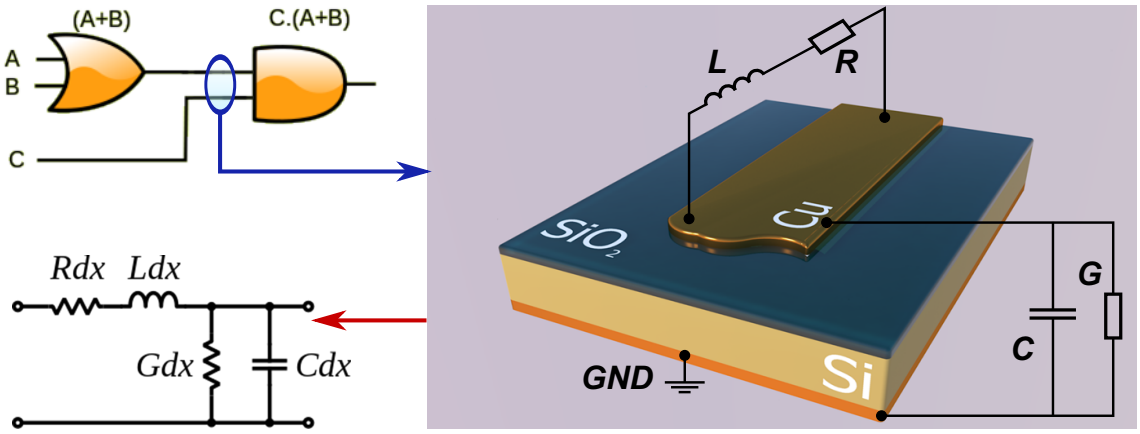

Figure 1.2: Equivalent electric circuit of the interconnect between logic gates can be represented by an RLC-filter. The parameters are dependent on the length dx of the wire.

Numerous enhancements have been introduced to conventional CMOS technology such as substitution of Al interconnects with Cu [7, 8] and utilization of low-k dielectrics [9] for interlayer insulation in order to decrease the resistance and capacitance of the interconnects. Even though these changes have markedly improved the characteristics of interconnects, further developments of this technology are extremely challenging and cost-ineffective. Therefore, as the current technology is

rapidly reaching its limits a new approach is required to overcome the existing issues and build high-speed digital devices.

1.1 Photonics vs Plasmonics

The idea of using light as the fundamental basis for computing is not new [10, 11]. Photons, have physical characteristics that are fundamentally different from electrons. The wave nature of light leads to numerous advantages of optical technologies for the transmission, recording, processing and storage of information. The performance of optical logic elements can greatly exceed that of existing electronic devices in terms of speed as well as noise immunity [12, 13]. This technology allows the creation of not only optical components for high-speed data transmission via fiber optic, but also all-optical processors that perform high-speed computing with no intermediate signal conversion from optical to electrical.

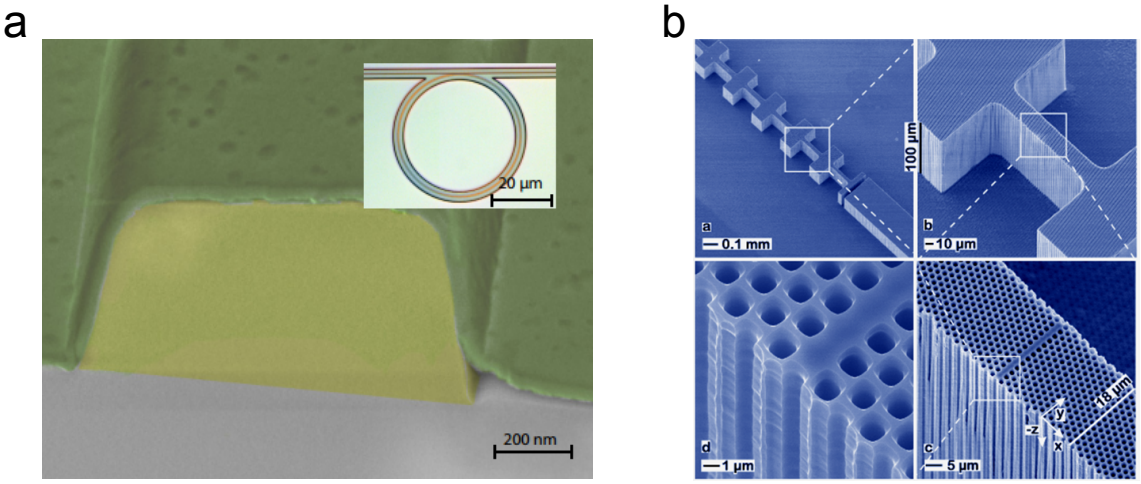

Figure 1.3: Photonic ring resonators **(a)** [14] and waveguide with an introduced defect **(b)** [15][1]. Both structures have dimensions of tens or hundreds of micrometers.

Recent research in silicon photonics has demonstrated the potential for using light as a signal carrier, not only for long-distance communications, but also for on-chip interconnects. Various optical elements such as waveguides [16, 17, 18, 19], modulators [20, 21, 22] and filters [22, 23] have been successfully integrated into microelectronic circuits.

[1]Mller, F., A. Birner, U. Gsele, V. Lehmann, S. Ottow, and nH Fll. "Structuring of macroporous silicon for applications as photonic crystals." Journal of Porous Materials 7, no. 1-3 (2000): 201-204. With permission of Springer

Nevertheless, despite the advantages possessed by devices based on the principals of photonics, they also have substantial drawbacks. The most significant is the fact that photonic devices are much larger in size (see Fig.1.3) compared with classical electronic devices. This is due to the wave nature of light itself, namely, the effect of diffraction [24] and significantly limits the extent to which such photonic logic elements can be integrated into complex chips such as microcontrollers or processors. A more serious drawback is the poor electric field confinement provided by photonic waveguides and, as a consequence, the weak interaction between the light and the waveguide media. This, again, results in large dimensions of active photonic elements such as modulators [25] required to achieve a sufficient level of modulation depth. Therefore, due to this significant mismatch between the dimensions of electronic and photonic elements, true integration is still unattainable.

A more promising technology, in terms of very-large-scale integration (VLSI), is the emerging field of plasmonics. It utilizes surface plasmons which are oscillations of the electron gas at the interface between metal and dielectric (the surface plasmon phenomenon is described in detail in Chapter 2). The ability of surface plasmons to circumvent the diffraction limit [26] as well as to provide strong field confinement [18] opens up significant opportunities for using them to guide signals between logic gates in modern integrated circuits where small dimensions are highly desirable. Moreover, a much higher sensitivity of surface plasmons to the properties of surrounding media (compared to purely photonic elements) permits the design of submicron active components. Passive devices such as wave plates [27], filters [28] and logic gates [29] as well as active elements such as tunable antennas [30, 31] and detectors [18, 19] utilizing plasmonic phenomena have been demonstrated. The aforementioned devices exhibit subwavelength confinement of light accompanied by strong electric field enhancement.

The combination of nanoscale dimensions and strong field confinement, relative to classic photonic elements, make utilisation of surface plasmons in integrated circuits of great interest. The field of plasmonics, therefore, possesses significant potential to overcome existing limitations and ultimately integrate well with existing microelectronics technology to produce promising photonic components.

1.2 Logic gates with plasmonic interconnects

As mentioned previously, the speed of modern digital electronic circuits is limited not by the speed of their discrete components, such as transistors or logic gates, but by the interconnects between them. It should also be noted that such an issue appears mostly for long-range interconnects [5] (for example data and address buses) as the resistance and capacitance of the wires increase proportionally with length. Short wires connecting transistors or even nearby logic gates usually do not limit the bandwidth since their RC characteristic is still negligibly small. Long interconnects are usually used to link the functional blocks of the processor such as cache memory, arithmetic and logic units and registers. It is, therefore, attractive to substitute this 'bottleneck' with high-speed optical buses leaving the internal structure of logic gates unchanged. This will provide better compatibility with existing CMOS technology and make the final products cheaper, which is essential from a commercial point-of-view. The inevitable losses associated with plasmonic waveguides can be overcome by using a gain medium [32] or repeaters along the interconnects.

Exhibiting the key property of diffraction-unlimited wave confinement, plasmonic waveguides can become a technology that will combine the advantages of optical communications and existing nanoscale CMOS components. The key requirement for hybrid optoelectronic digital integrated circuits is the utilisation of surface plasmons with the same frequency. This is essential for designing full-optical logic gates which are capable of controlling the propagation of one surface plasmon by means of another. Such a property will permit cascading the logic gates and create sophisticated circuits such as multiplexers or adders. Since the length of the waveguides can vary greatly (depending on the distance between the source and destination), it can lead to a phase shift at the inputs of a logic gate. These elements, therefore, must be insensitive to the phase of the plasmon wave.

Similar to existing electronic logic elements, plasmonic gates must perform four (see Fig.1.4a) basic operations. These operations include guiding, sensing, amplification and modulation and are essential for circuit functioning. Prior to being guided, surface plasmons must be excited and tapered into the waveguide using a plasmonic input port. A detailed investigation of an example of such a structure is presented in Chapter 4.

Schematic diagrams of a conventional logic gate and a logic gate with plasmonic

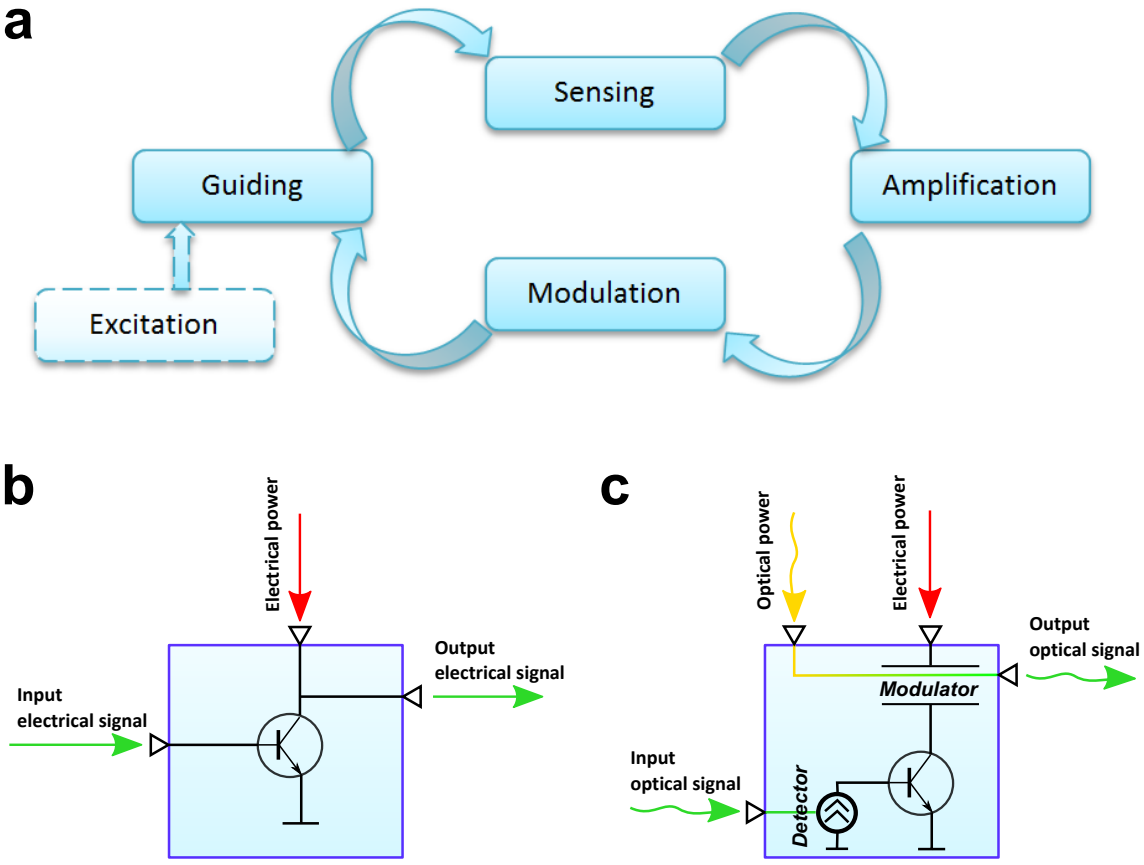

Figure 1.4: Basic operation steps **(a)** which must be performed by plasmonic logic gates to create a fully functional integrated circuit. Schematic diagrams of conventional logic gate **(b)** and logic gate with plasmonic interconnects **(c)**.

interconnects are shown in Figure 1.4b and Figure 1.4c respectively. In the case of the plasmonic gate the internal electric circuit remains unchanged but the input and output stages are modified to operate with optical signals. The input of the logic gate is connected to a photodetector which performs the conversion of the input plasmonic signal into an electric current. This current, in turn, is used to trigger the logic gate. The output of the circuit is loaded with a modulator which is used to modulate the propagation of another surface plasmon.

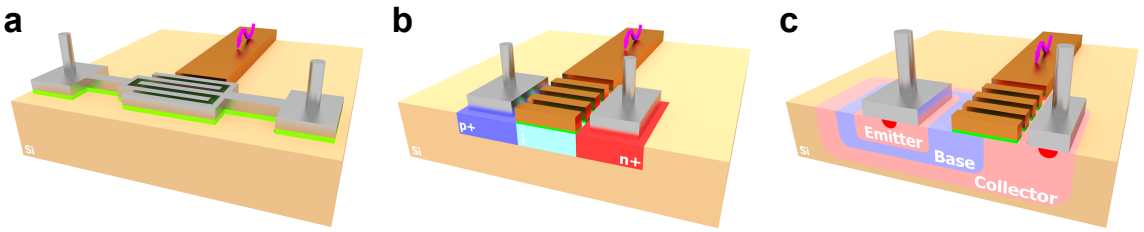

Figure 1.5: Surface plasmon detection using MSM photodetectors **(a)**, PIN photodiodes **(b)** and bipolar phototransistors **(c)**.

The propagating plasmon can be guided to a certain destination and then converted into an electric signal using photodetectors. Surface plasmon sensing can be performed by the same kind of photodetectors used to detect photons. Depending on the requirements the task can be carried out by metal-semiconductor-metal photodetectors (high speed; see Fig.1.5a), PIN photodiodes (high responsivity; see Fig.1.5b) or even bipolar or MOS transistor structures (see Fig.1.5c). The noticeable feature of the latter is an ability to detect and amplify the signals simultaneously. Although this design has some drawbacks, its utilisation may be preferential in high-density integrated circuits design. Numerical and experimental studies of plasmonic photodetectors are presented in Chapters 5 and 8.

A post-sensing signal amplification step is uncommon in classic electronic logic gates but is critical for plasmonic circuits. A signal fanout (connecting a single output to multiple inputs) in electronic logic gates does not significantly affect the output voltage. Therefore, the levels of logic "0" and "1" remain constant. Splitting of the plasmonic signal to n different inputs, on the other hand, will proportionally decrease the intensity at each input n-times. The signal, thus, must be amplified to compensate for this intensity reduction. A simple transistor or differential amplifiers [33] could be implemented on the chip and used to amplify the input signal to address this issue.

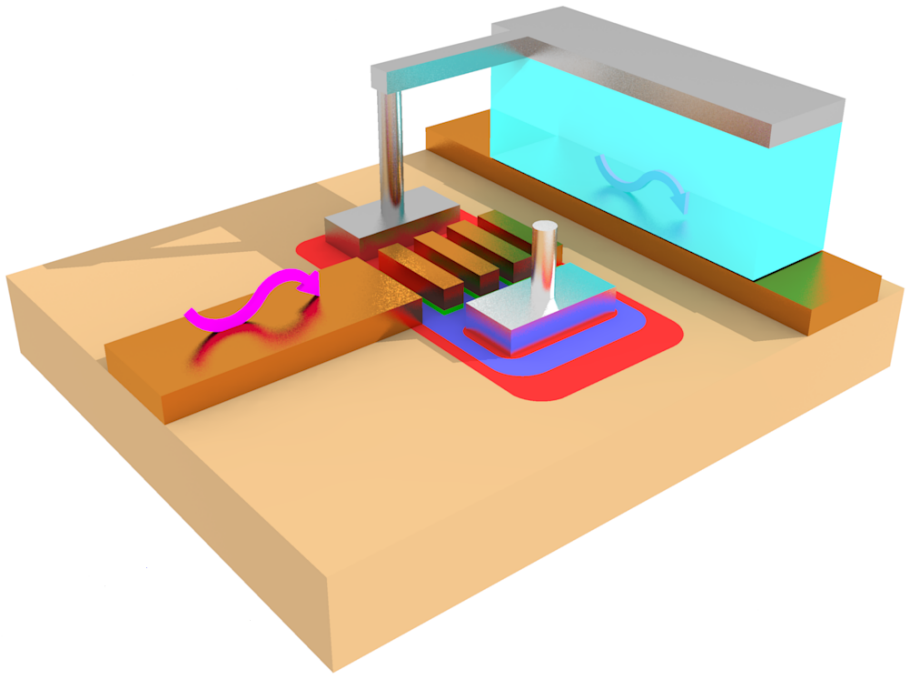

Figure 1.6: Schematic representation of plasmonic modulator connected to the output of the logic gate.

Finally, the circuit must be capable of dynamically modulating the state of its output to fulfil the plasmonic logic gate functionality. This can be achieved by utilising modulators - devices which permit the modulation of the propagation of an optical wave changing either the refractive index (real part) or the absorption coefficient (imaginary part) of the material [34]. An ability to change both the real and imaginary part of the refractive index of semiconductor to modulate the propagation of surface plasmons has recently been demonstrated in [20, 21, 22]. A high sensitivity of surface plasmons to the properties of surrounding media enables modulators with submicron dimensions. Metal-insulator-metal waveguides can be used to further enhance the electric field confinement inside the active area of the modulator (see Fig.1.6) which can be used, in turn, to achieve a better modulation depth. A comprehensive study of MIM waveguide based modulators is presented in Chapter 6.

1.2.1 Plasmonic logic gate proposal

A potential design for a simple plasmonic logic gate, implemented on the silicon substrate, is shown in Figure 1.7. Two plasmonic input ports are used to couple a freely propagating optical wave into surface plasmons which are then coupled into waveguides. These waveguides are used to direct propagating plasmons between input and output components of the logic gate. The surface plasmon used to trigger the logic gate input can be called 'controlling' while the surface plasmon propagating through the modulator can be called 'controlled' respectively.

The controlling plasmon decays in the active region of the photodetector creating photocurrent which is then amplified and used to trigger the circuit. Depending on the logic gate type one or multiple inputs can be used. The output of the gate is loaded with a plasmonic modulator. In the 'OFF' state, when no potential is applied to the modulator, the controlled surface plasmon can propagate through the modulator with little attenuation. On the other hand, when the modulator is in the 'ON' state, the controlled plasmon encounters a lossy medium within the modulator and, therefore, is strongly attenuated. Using another photodetector the controlled surface plasmon can be converted into an electrical signal for compatibility with existing interfaces.

The proposed design permits the cascading of logic gates - the connection of one logic gate output to the input of another. The schematic layout shown in

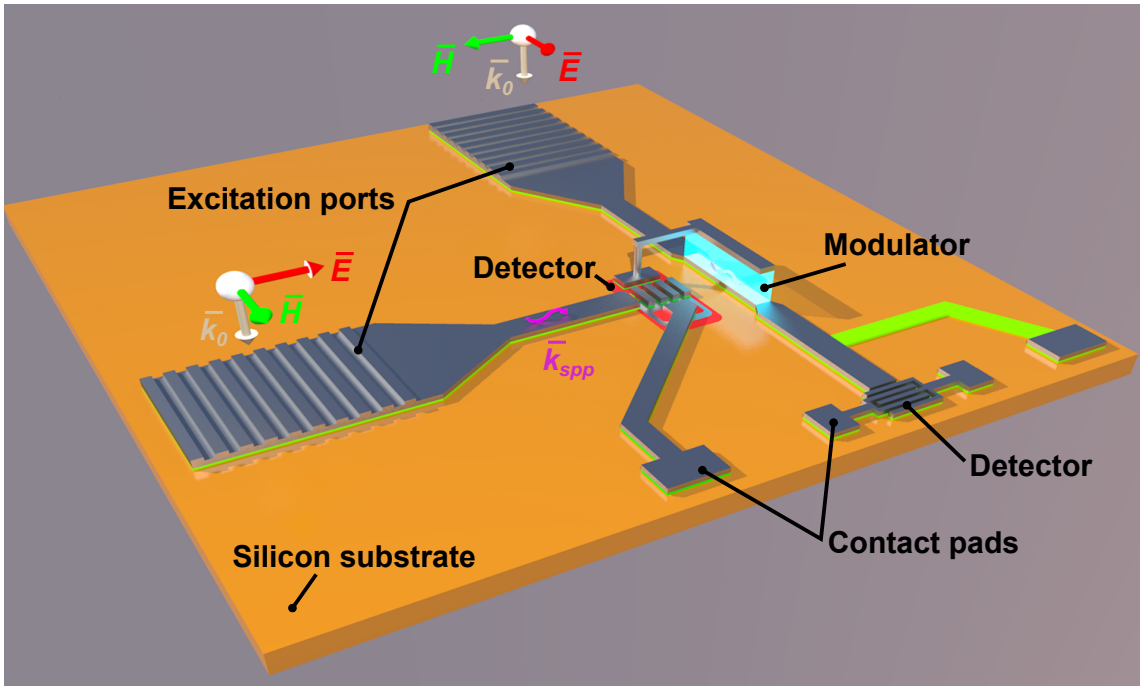

Figure 1.7: Schematic representation of plasmonic 'NOT' logic gate.

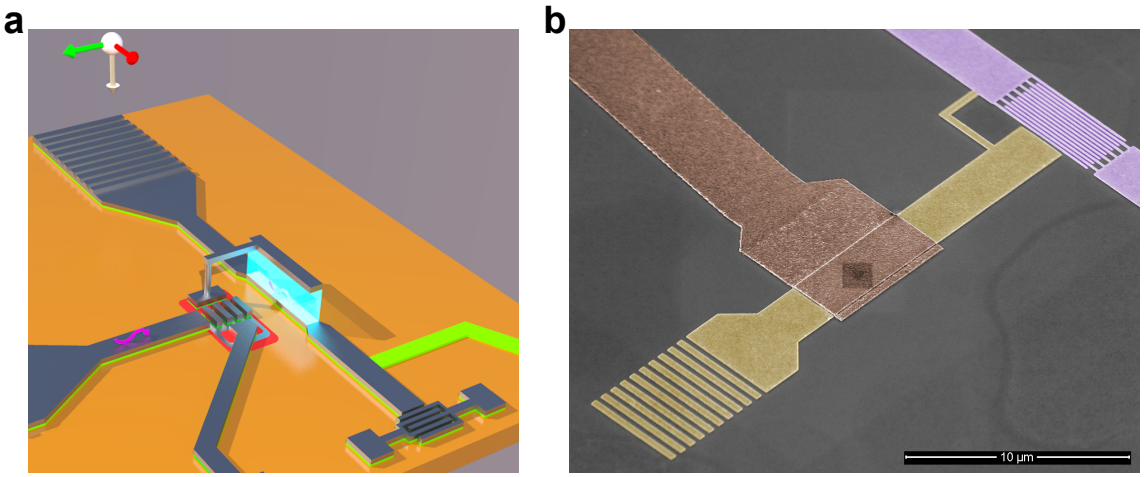

Figure 1.8: Schematic representation **(a)** and false-coloured SEM image of physical implementation attempt **(b)** of the plasmonic waveguide-coupled MSM photodetector with embedded modulator.

Figure 1.7 acts as a 'NOT' logic gate and can be modified to implement other functions. Ultimately, the realisation of a 'NAND' or 'NOR' logic gate will enable functional completeness [35] so any boolean function can be implemented using them in combination. Such a design, therefore, can be used to create fully functional electro-plasmonic digital integrated circuits.

1.3 Plasmonic-enhanced photodetectors with advanced properties

Possible applications of surface plasmons extend far beyond their use in digital integrated circuits. It has been recently demonstrated that plasmonic metasurfaces - two-dimensional arrays of plasmonic nanoantennas, can be used to build various optical devices such as flat lenses [36], polarisation elements [28] or colour filters [37]. These metasurfaces provide an ability to tailor their electromagnetic properties by changing the geometry of their building blocks. Combining a planar design [36, 38] and CMOS compatibility [39], plasmonic metasurfaces open up an opportunity for low-cost, large-scale production desirable for commercial devices. These plasmonic metasurfaces, therefore, can be introduced into conventional photodetectors improving existing properties or even enabling novel functionality.

Plasmonic metasurfaces can be used to produce a significant improvement in the performance of polarisation sensitive photodetectors. Currently, this sensitivity is mostly enabled by additional optical components such as waveplates and polarisers which are incorporated into an optical system. Since these optical components usually have macroscopic dimensions, the total photodetector assembly becomes bulky. Another issue is associated with exotic polarisations of the light such as azimuthally or radially polarised beams. Systems used to sense these usually require sophisticated optical components that further increase the price and size. Plasmonic metasurfaces, on the other hand, have already been shown to have a sensitivity to various polarisations of the light while retaining nanoscale dimensions [40, 41]. Therefore, the incorporation of these metasurfaces into conventional photodetectors can be beneficial in terms of overcoming the issues described above. Such plasmonic-enhanced photodetectors could play a central role in the fields of optical telecommunications or scientific equipment.

Ever-increasing data volumes are placing increasing demands on long-distance high-speed data transmission interfaces. Wavelength-division multiplexing (WDM) technology permitted increasing the transmission rate by splitting a data stream into multiple channels with different carrier frequencies. Such systems have been demonstrated to achieve a 112 Tb/s bit rate over a seven-core optical fibre [42, 43]. To transmit information, the afore-mentioned systems represent the digital bits (logic “0” and “1”) as different intensities of light. To further increase the transmission rate and security [44, 45] the polarisation of a beam can be used to

code data instead of, or in addition to, its intensity or phase.

Polarisation is a fundamental property of electromagnetic radiation that can be used to probe biological [46] and physical [47] systems, as a channel for data transport and storage and as basis states in quantum computing [48]. Polarised light microscopy can elucidate information about orientation order within cells below the diffraction limit [49] or strain and variations in crystal geometry in materials. The use of different polarisation states can be used to increase the capacity of optical data storage systems [50, 51] and the potential for using polarisation to increase the bit rate and data security of optical telecommunication systems [52, 44, 45] is well-known. Conventional detectors, however, are sensitive to only the intensity of an electromagnetic wave and additional optical elements such as waveplates, polarizers and liquid crystal devices are required in the beam path to determine the state of polarisation of the field. Such components are bulky and can compromise the speed and cost of optical systems limiting their utility.

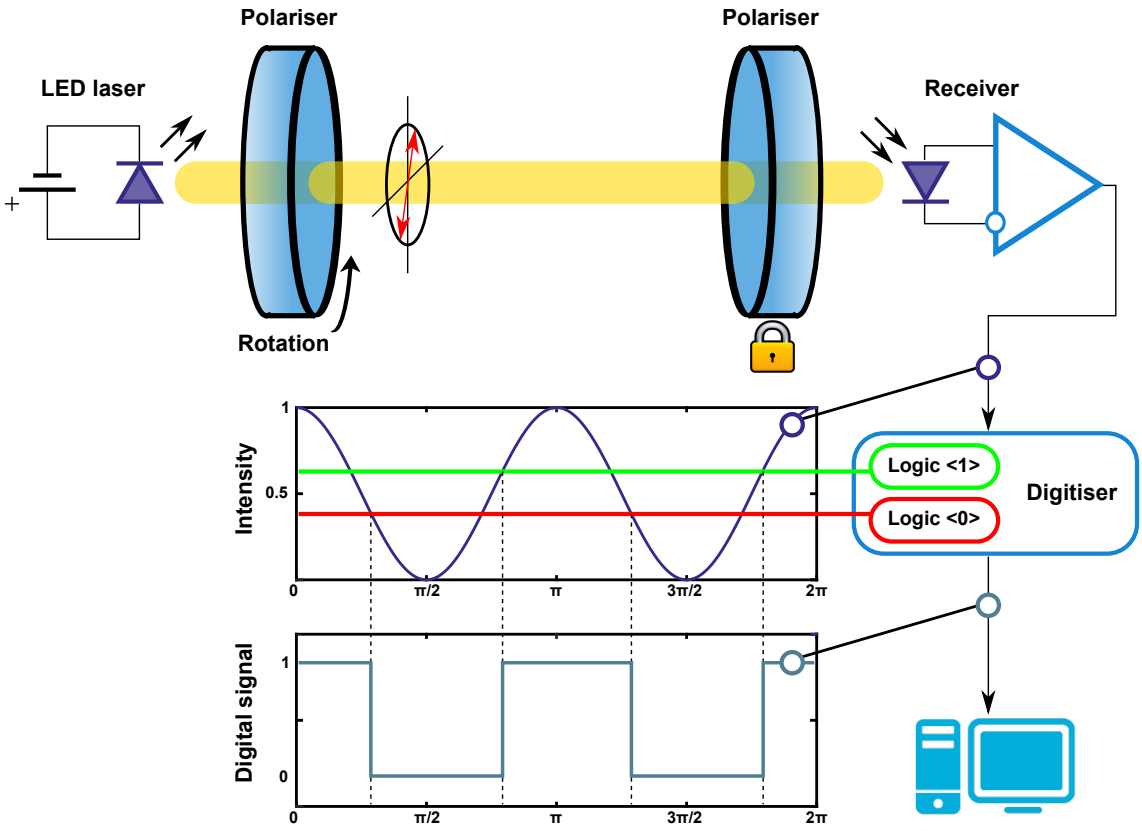

Figure 1.9: The principles of polarisation-encodded signal transmitting systems.

In response, there has been a significant investment of effort into the miniaturization of optical elements including lenses [53, 54], waveplates [38, 55] and polarisation filters [56] using plasmonics relying on the excitation of propagating or

standing waves on the boundary between a dielectric and a metallic particle or surface. This effort has largely centred on passive optical devices due to the relative ease of fabrication and characterization compared to active optical devices. Polarisation sensitive photodiodes found in the literature tend to respond directly to only one polarisation state and have a null or suppressed response to the other. The device demonstrated in [57], for example, generates a measurable photocurrent for only one of the circular polarisation basis states.

Figure 1.9 shows a schematic representation of a polarisation-encoded signal transmitting system. A simple addition of polarisation optics to the receiver and transmitter permits polarisation sensitivity of the system. Assuming the receiver optics is constant, the output signal is dependent on the angle between two polarisers and is proportional to $\cos^2(\theta)$, where θ is the rotation angle of the polariser on the transmitting side. Setting the limits to the initial signal intensity I_0 at the input to be recognised as logic "0" and "1" (usually 0...1/3 and 2/3...1 for CMOS logic respectively) the signal can be digitised. The digital data, therefore, can be encoded by altering the polarisation state on the transmitter's side and transferred to the receiver using a polarisation-maintaining optical fibre or free space. Nonetheless, despite all positive aspects, these systems are less robust to noise [58] and require special techniques to reduce its influence.

Although optical systems are insensitive to electromagnetic noise they still suffer from several factors which decrease the signal-to-noise ratio [59]. Figure 1.10 shows the prime source of noise in such kind of systems. Even though the polarisation of the light is used to encode the signal, the output is referenced to the zero and maximum intensity I_0 of the transmitter. This type of system is called single-ended (see Fig.1.11). The noise which might affect the signal while it is propagating over the transmission line will appear at the input of the receiver. Since the second input is connected to the ground (referenced to zero intensity), the receiver will amplify the noise together with the actual signal. Thus, the output signal in this type of systems is represented by an amplified superposition of transmitted data and noise. Additional post-processing is required to localize and eliminate noise from the output.

Therefore, any sudden change of the intensity due to damage to the optical fibre, thermal fluctuations or unstable coupling can be misinterpreted as logic "0" despite the constant state of polarisation. Such signal intensity fluctuations require a continuous adjustment of logic "0" and "1" intensity levels [60] which, in turn, leads

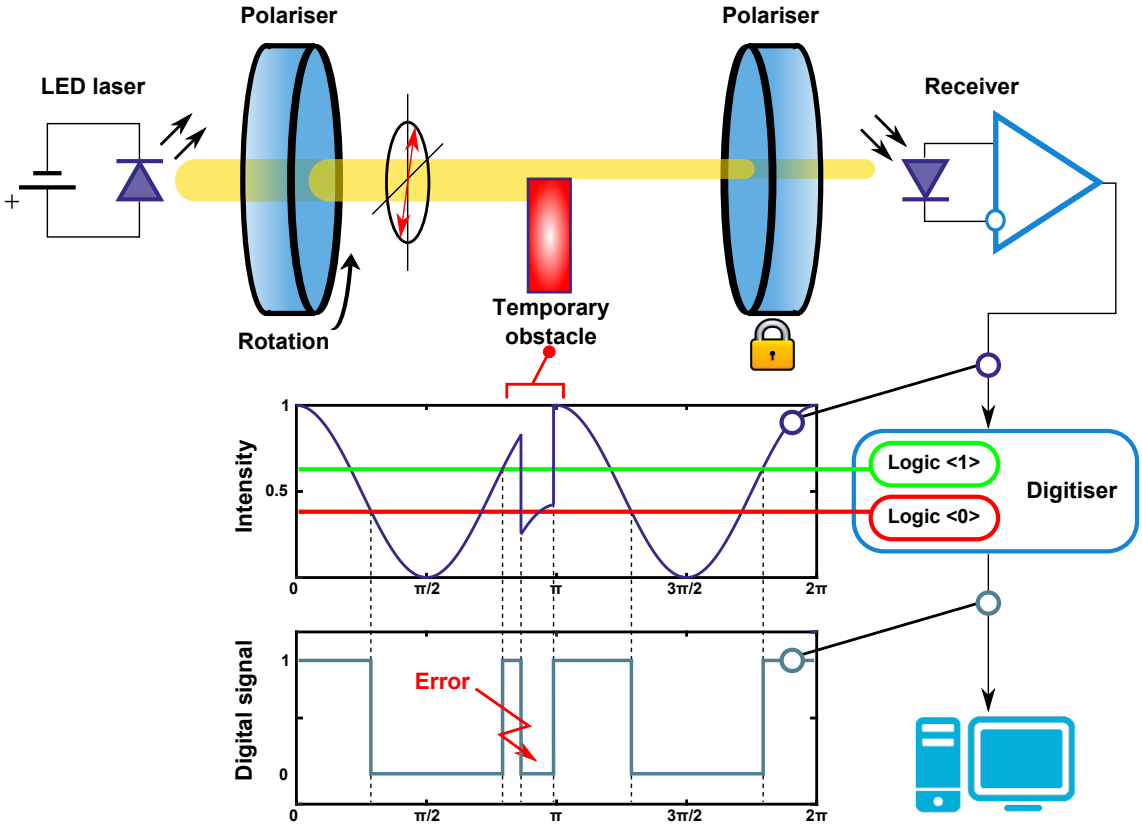

Figure 1.10: The beam intensity fluctuations in polarisation-encodded signal transmitting systems may cause misinterpretations of the signal despite the persisting state of polarisation.

to a rise in system complexity, lower reliability and cost inefficiency. In addition, the high channel compression (modest systems can use up to 0.2 nm [61] channel separation) makes the system highly sensitive to each channel's spectral characteristics [62]. For systems with high channel density the wavelength distribution of neighbouring channels can overlap [63], introducing cross-talk. Finally, due to filter thermal drift [64] the central wavelength of each channel alters its position which, again, can contact to cross-talk.

Differential detection approaches are often used to improve the robustness of a system to noise. This type of transmission is called differential (or balanced) signalling (see Fig.1.12). The technique involves using two complementary signals and creating a differential response in the detector rather than relying on their independent outputs. The noise will affect both the complementary signals and will appear at the inputs of the receiver in-phase. Since the circuit amplifies only the difference between its inputs, the noise will be automatically subtracted from the output signal. Such interfaces exhibit much better noise resistance compared with

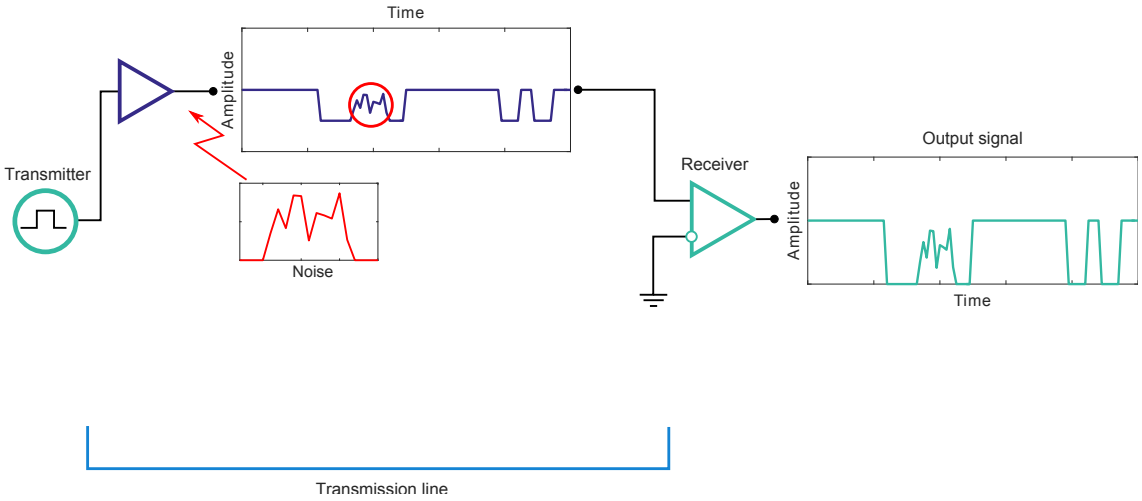

Figure 1.11: Schematic representation of system utilising single-ended signalling. Noise which affects the transmission line will appear at the output of the receiver.

those that are single-ended [65] and are widely used in electronics [66, 67] where a high bit rate is required. In optical systems such interfaces can significantly reduce, or even eliminate, the influence of intensity and thermal fluctuations of a signal. Differential (or balanced [68]) photodetectors are widely used in differential phase-shift keying (DPSK) optical systems [69] as well as for small-signal measurements in scientific experiments. In these systems the phase of a data signal is referenced to that of the control which can be transfered via a different channel or be represented by the phase-delayed initial signal.

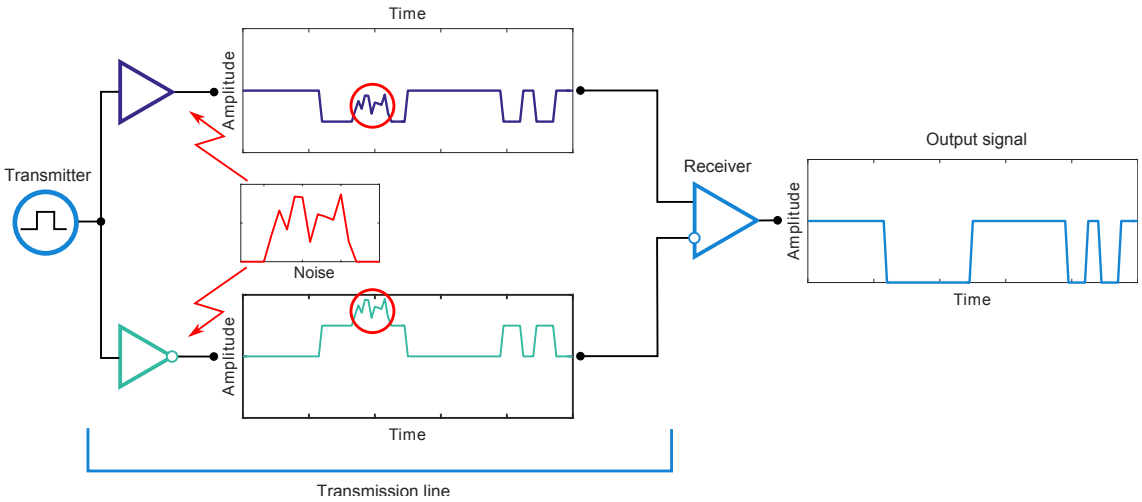

Figure 1.12: Schematic representation of system utilising differential signalling. In this regime noise affects both channels of the transmission line. Since the noise is in-phase on both complementary inputs of the receiver it will be subtracted from the signal and will not appear at the output.

A similar technique can be used to reduce the effect of noise in polarisation-

sensitive detectors. The principle of operation of such optical transmission systems is similar to their electrical analogues. To eliminate the influence of the absolute light intensity, two complementary detectors with enhanced sensitivities to each of the orthogonal polarisation states are required to analyse the signal. The differential amplifier is then used to subtract the photocurrents from these detectors and amplify the difference. In this case the detection mechanism is referenced to the relative difference in sensitivities of each of the complementary photodetectors to one of the orthogonal polarisation states. Traditionally this is performed using polarisation optics such as a liquid crystal device or wave plates. Usually these devices are bulky and/or exhibit relatively slow speed characteristics. For modern electronic applications, however, minimising the device footprint is critical. Therefore, the utilisation of plasmonic metasurfaces (see Fig.1.13) will be highly beneficial as this can provide a nanoscale alternative to conventional optical elements and promote the design of high-speed, noise-robust photodetectors for future telecommunication systems.

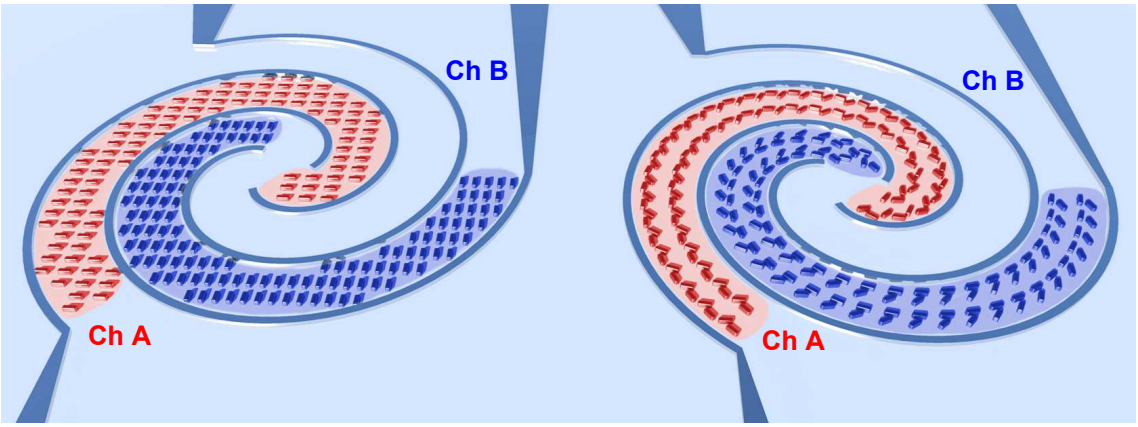

Figure 1.13: Schematic representation of two spiral MSM photodetectors with rectangular **(left)** and chiral **(right)** nanoantennas.

Surface plasmons can also be used to improve the colour selectivity of modern digital cameras. Since its invention [70] the digital camera has become an integral part of many modern devices. It possesses advantages over film cameras such as having fewer mechanical parts, no requirement for film or its development and the ability to digitally process images 'on-the-fly'. The first digital cameras were bulky and provided low resolution, but the technology has developed to the point where even smartphones possess cameras with millions of pixels. The utilization of digital cameras is not limited to the consumer segment but also includes scientific (for example spectrometers [71], streak cameras [72]) and biomedical applications where sensors with high resolution, speed and sensitivity are important. Such cameras

might also have an extended wavelength sensitivity into ultraviolet, near-IR and deep infrared spectra [73, 74].

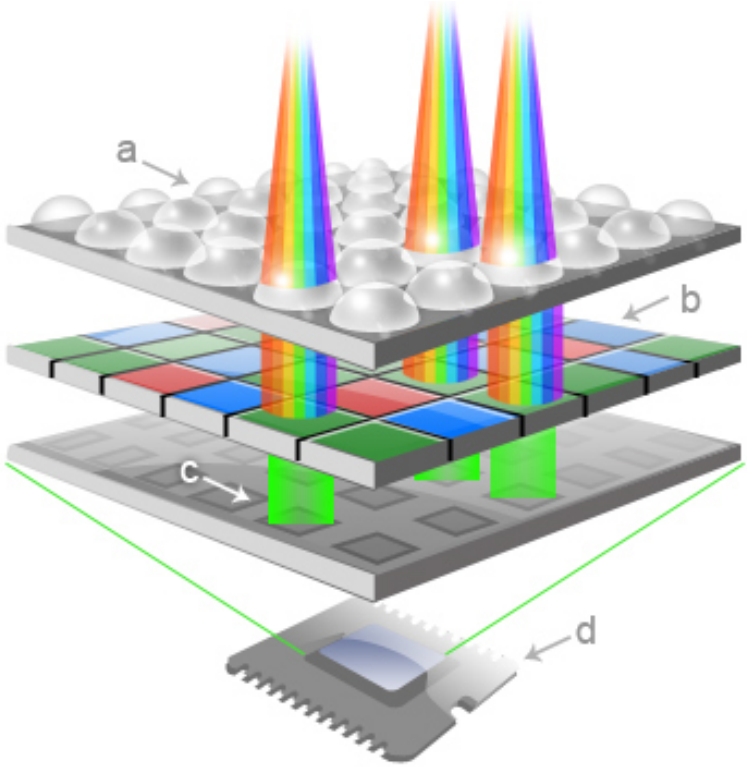

Figure 1.14: Schematic representation of a common digital camera sensor **(d)** design. The incoming light passes a microlens array **(a)** and is then filtered by a mosaic colour filter **(b)**. The resulting beam is detected by photosensitive array of pixels **(c)**. Taken from [75].

The pixel is an elementary unit of the digital camera. It has two primary characteristics - size and spectral sensitivity, defining the maximum resolution and application field of the camera. The pixel size imposes a fundamental limit on the amount of information that can be recorded on a sensor with a certain size. The resolution of the sensor, therefore, can be increased by increasing the overall area of the sensor or reducing the single pixel size. Both methods have the same goal - increasing number of the pixels on the sensor. Since compact, high-resolution sensors are of greatest interest for portable devices such as mobile phones and digital cameras, significant effort has been investigated in improving the image quality provided by small-area sensors [76, 77]. Although there has been remarkable success [78] in recent years, reducing the pixel size still faces challenges in implementation and requires improvements in current technology to meet the demand for ultra-compact cameras.

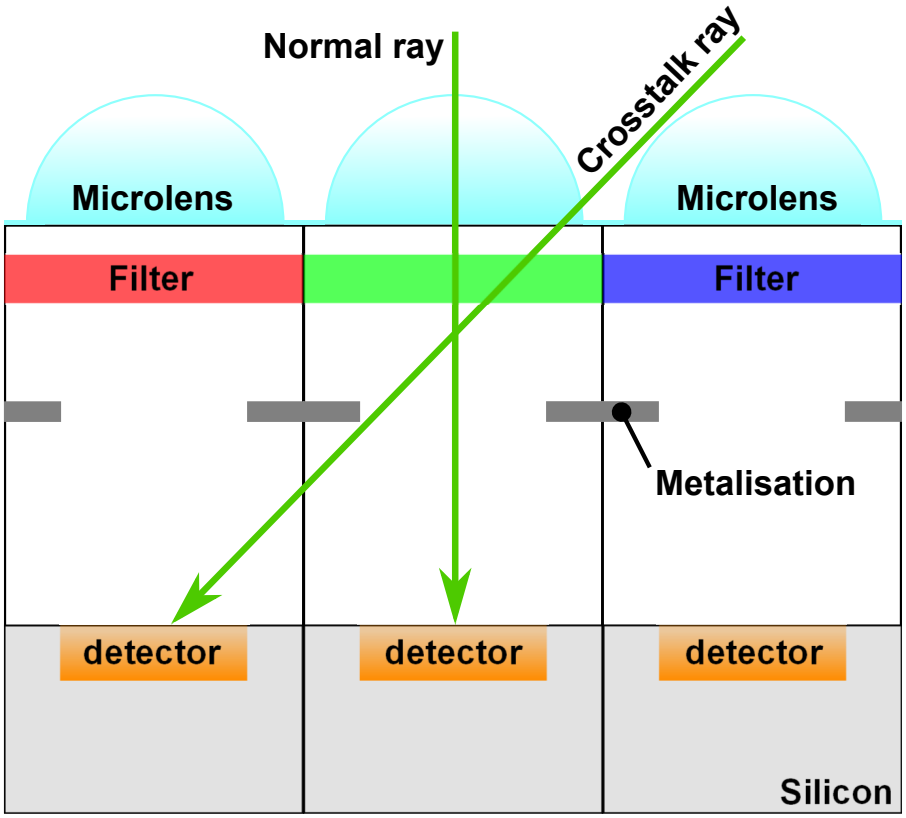

Figure 1.15: Schematic representation of a RGB colour pixel crossection. Rays reaching microlenses at large angles can illuminate a neighbour detector resulting in pixel crosstalk.

To understand these difficulties, brief overview of modern digital camera technology must be provided. The operation principal of the majority of commercially available camera sensors is based on the design shown in Figure 1.14. The incoming light is focused onto the pixel area by a microlens array (see Fig.1.14a). Focusing is necessary to decrease interpixel cross-talk [79]. The light then goes through a mosaic filter (see Fig.1.14b) with some colour pattern (such as Bayer or X-Trans filter). These filters are used to capture colour information since the sensor has no wavelength specificity. Finally, the filtered light is incident on an array of photodetectors (see Fig.1.14c). The most commonly used arrays are charge-coupled devices (CCDs) and active-pixel sensors (APSs, sometimes called CMOS). Each cell represents a single pixel and is dedicated to detecting a certain part of the visible spectrum in one region of the image. The actual image resolution, therefore, is smaller than the resolution of the matrix. In addition, an infrared filter (not shown in Figure 1.14) is usually included in from of the microlenses to decrease noise.

Figure 1.15 shows a schematic representation of cross-sections through three

pixels each responsible for detection of either red, green or blue. The first issue with a decrease of the pixel size is associated with the phenomenon of diffraction. When pixel dimensions become comparable to the wavelength, the diffraction effects become significant and microlenses are insufficient to focus light [80] on the detector. Also, since filters and microlenses are fabricated in different lithography steps [56] the alignment of these layers become challenging. The second issue is associated with colour filters. Usually these filters are made of dyes or pigments and transmit a particular wavelength spectrum while the remainder is absorbed [81]. For sufficient absorption, the thickness of a filter must be of the order of several hundreds of nanometers. Thicker filters provide better bandpass characteristics. At the same time, when the sensor is illuminated at some angle a certain part of the beam can affect a neighbouring detector leading to so-called 'pixel cross-talk' [56, 82]. The degree of neighbour exposure is directly proportional to the thickness of the filter. This can, in turn, blur the image and decrease the colour resolution. The effect increases when the pixel dimensions decrease as more and more light will affect the surrounding photodetectors. There is a trade-off, therefore, between the quality of the filter and pixel cross-talk which applies a lower bound on pixel dimensions.

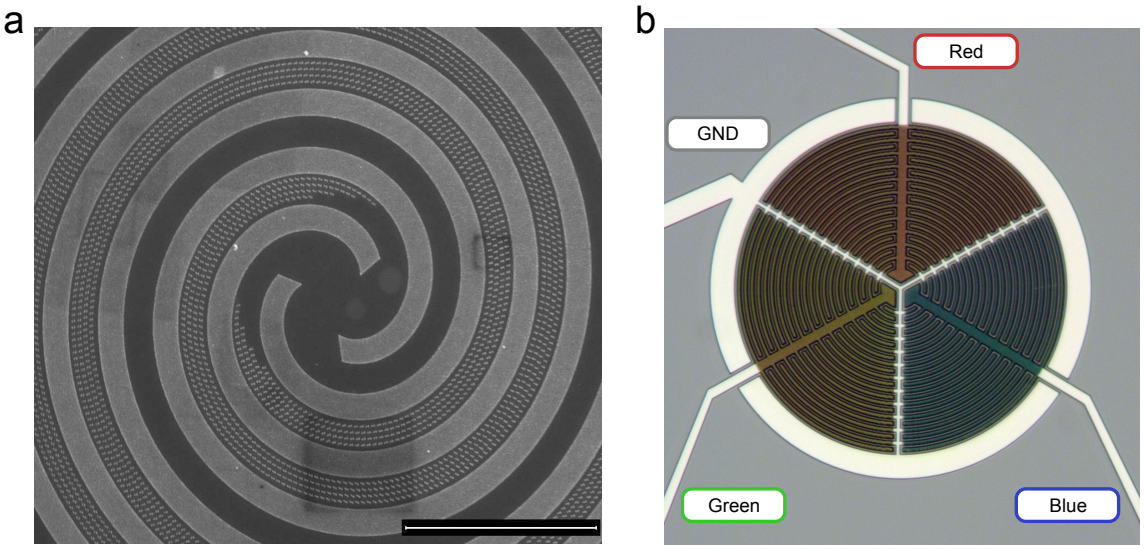

Figure 1.16: SEM image of a differential spiral photodetector **(a)** and plasmonic colour camera pixel **(b)**. Plasmonic metasurfaces are used to make photodetectors sensitive to the polarisation or wavelength of the light respectively.

In contrast, filters based on localized surface plasmons exhibit better characteristics as the pixel size decreases to micron or even submicron dimensions [83]. The simplest design will require only one metalisation layer with a thickness below 100 nm and, therefore, does not require complicated fabrication. Furthermore, plasmonic filters can add an additional flexibility to the filter design and enable

polarisation sensitivity (see Section 8.1). It has also been shown that utilisation of a Schottky barrier between nanoantennas and a substrate can extend the sensitivity of a detector to the near-IR [84] and beyond [85].

A numerical investigation and experimental demonstration of photodetectors with incorporated plasmonic metasurfaces are presented in Chapter 8. Tailored nanoantennas, together with an innovative MSM detector configuration (see Fig.1.16a), enabled intensity fluctuation insensitive photodetectors capable of distinguishing linearly and circularly polarised beams. It has also been demonstrated that plasmonic metasurfaces can be used in camera pixels (see Fig.1.16b) to create planar colour filters. These filters are embedded into the pixel channels and fabricated in the same technological step and so are easier to fabricate. Furthermore, they do not suffer from cross-talk problems [56, 82] that limit the size of conventional colour pixels.

1.4 Thesis goals

The main aim of this work is to progress on development of plasmonic components which will permit overcoming the current issues limiting the future increase in processor operation speed such as the RC parameters of metallic interconnects. The substitution of metallic interconnects with optical plasmonic waveguides presents many challenges. Unlike the conventional wires used in microelectonics technology, plasmonic waveguides cannot have an arbitrary shape and, therefore, must be carefully designed to operate at a particular wavelength. Prior to being guided, a mechanism to excite surface plasmons must be introduced to couple freely propagating electromagnetic (EM) radiation into waveguide structures. Moreover, the wave nature of plasmonic signals requires the development of detection and modulation mechanisms in order to exhibit plasmonic logic gate functionality. In this thesis comprehensive analytical and numerical studies of a plasmonic input port, waveguide and modulator will be presented. Coupling a propagating EM wave into the surface plasmon as well as its propagation along the waveguide will be experimentally demonstrated. It will be shown that waveguide-coupled metal-semiconductor-metal photodetectors enable in-plane detection of the surface plasmons - an important property required for successful integration into modern semiconductor technology.

The second aim of this work is to develop a technology which can improve existing properties or add functionality to conventional photodetectors. This thesis

focuses on applications to the development of polarisation-sensitive detectors and colour camera pixels. Utilisation of plasmonic metasurfaces can be used to tailor the sensitivity of photodetectors to an almost arbitrary state of polarisation or wavelength of the incident beam. There are significant challenges associated with integrating these metasurfaces into the photodetectors. Ultimately, the integration must be performed during the fabrication process, in the same technological steps. In this thesis a novel design for a polarisation-sensitive differential photodetector is presented. It will be experimentally demonstrated that such a photodetector exhibits a high robustness to intensity fluctuations which is a highly desirable property for telecommunication applications. Furthermore, it will be shown that plasmonic metasurfaces can also be used as colour filters in camera pixels, permitting a fully planar design and eliminating the cross-talk issue associated with conventional pixels.

1.4.1 Thesis goals summary

In summary, to progress the development of the goals discussed above of creating logic gates with plasmonic interconnects and novel plasmonics-enabled photodetectors and camera pixels, the specific outcomes of this thesis were the:

- Development of a plasmonic input port design that facilitates coupling of far-field radiation into surface plasmons and further tapering into the waveguide.
- Development of a planar metal-semiconductor-metal photodetector design capable of detecting surface plasmons in-plane.
- Development of a fabrication method that is capable of producing waveguide-coupled metal-semiconductor-metal photodetectors in the same technological step.
- Characterisation of indium-tin-oxide and evaporated silica films properties, necessary for understanding the breakdown mechanism and progress plasmonic modulator fabrication.
- Development of a novel plasmon-enabled differential photodetector design which permits a noise-robust discrimination of the incident beam polarisation states.
- Development of a planar camera pixel design with plasmonic colour filters that doesn't suffer from the pixel cross-talk effect.

1.4.2 Thesis structure

Chapter 2 contains a detailed analysis of surface plasmon phenomena as well as a review of the literature discussing existing methods for surface plasmon excitation, guiding, detection and modulation. In Chapter 3, the details of all fabrication techniques for producing plasmonic nanoantennas, waveguides and Schottky photodetectors are examined, along with methods for numerical analysis of plasmon devices. A detailed analytical, numerical and experimental investigation of the plasmonic input port and waveguides is presented in Chapter 4. Numerical and experimental studies of the in-plane surface plasmon detection technique using metal-semiconductor-metal photodetectors are presented in Chapter 5. Chapter 6 is concerned with analytical and numerical studies of metal-insulator-metal waveguide-based plasmonic modulator, along with a thorough characterisation of e-beam evaporated indium-tin-oxide and silica films. A numerical investigation and experimental demonstration of novel photodetector designs with incorporated plasmonic metasurfaces, enabling the polarisation and colour sensitivities, are presented in Chapter 8. Future work and applications for the research presented in the thesis are discussed in the concluding Chapter 10.

2. Theoretical background and literature review

Surface plasmons are coherent oscillations of the electron gas at the interface between a metal and dielectric. The electron oscillations are always accompanied by electromagnetic fields (see Fig.2.1) induced inside both metal and dielectric. Surface plasmons can be divided into two categories. If surface plasmon propagates along a planar dielectric-metal interface it is called a surface plasmon polariton (SPP). On the other hand, if it exists as a standing wave on the closed interface of a nanoparticle it is called localised surface plasmon (LSP).

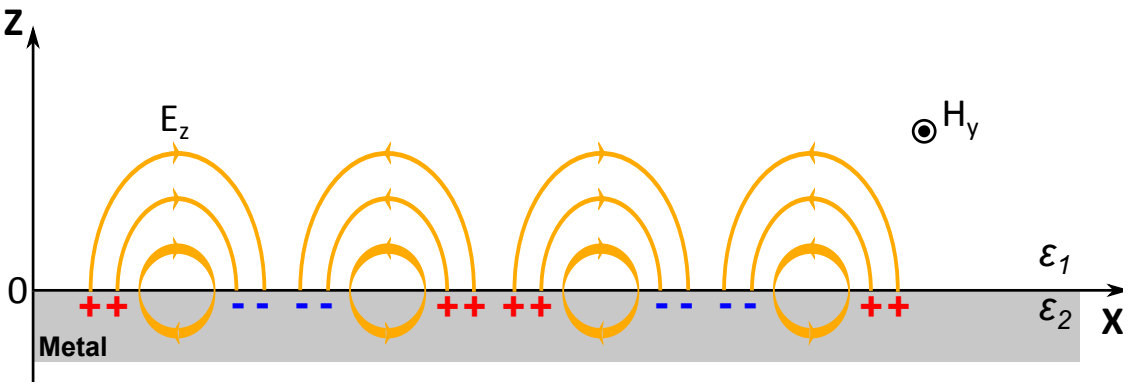

Figure 2.1: Schematic representation of electron density at the surface interface and accompanying electric field.

Surface plasmons exhibit a number of remarkable properties such as high sensitivity to the properties of propagating medium and strong field confinement [26]. As in the case with photonic waveguides, plasmonic circuits do not have an RC limitation and could have a bandwidth of several THz.

Surface plasmons can only exist at the interfaces where dielectric permittivity changes its sign ($\epsilon_1 > 0, \epsilon_2 < 0$, see Fig.2.1) such as dielectric-metal or dielectric-

highly doped semiconductor (for low energy photons). The wavelength of surface plasmon polariton is always smaller than the wavelength of freely propagating light and can be calculated using the following expression [26]:

$$\lambda_{SPP} = \sqrt{\frac{\epsilon_1 + \epsilon_2}{\epsilon_1 \cdot \epsilon_2}} \cdot \lambda_0, \tag{2.1}$$

where λ_0 is a wavelength of incident light, ϵ_1 and ϵ_2 are the permittivities of the dielectric and metal respectively. The field of plasmonics opens up great possibilities for creation of nanoscale active plasmonic devices suitable for integration with modern CMOS integrated circuits.

2.1 Surface plasmon theory

The properties of an SPP can be fully described by Maxwells equations. This permits the analytic prediction of the behaviour of nanoscale metallic structures in an electromagnetic field. In this chapter electromagnetic properties of metals at optical frequencies are discussed and the wave equations describing the propagation of surface plasmons on different interfaces will be derived. Maxwells equations for macroscopic electromagnetic fields are a set of four partial differential equations in following form (in SI units):

$$\nabla \cdot \vec{D} = \rho_{ext} \tag{2.2a}$$

$$\nabla \cdot \vec{B} = 0 \tag{2.2b}$$

$$\nabla \times \vec{E} = -\frac{\partial \vec{B}}{\partial t} \tag{2.2c}$$

$$\nabla \times \vec{H} = J_{ext} + \frac{\partial \vec{D}}{\partial t}, \tag{2.2d}$$

where $\vec{D}$ is the displacement field, $\vec{H}$ is the magnetising field, $\vec{E}$ is the electric field, $\vec{B}$ is the magnetic field, ρ_{ext} and J_{ext} are external charge and current densities respectively.

For isotropic and linear materials the relationships between $\vec{E}$, $\vec{D}$, $\vec{B}$ and $\vec{H}$ can

be found by using the following equations:

$$\vec{D} = \epsilon_0 \epsilon \vec{E} = \epsilon_0 \vec{E} + \vec{P} \tag{2.3a}$$

$$\vec{B} = \mu_0 \mu \vec{H}, \tag{2.3b}$$

where ϵ_0 and ϵ are the vacuum and relative permittivities of the material respectively, $\vec{P}$ is the polarisation density and μ_0 and μ are the vacuum and relative permeabilities respectively (here we assume $\mu = 1$).

Assuming that the external stimuli are absent (external charge and current are equal to zero) it is possible to combine both curl equations (Eq.2.2c) and (Eq.2.2d) to obtain the Helmholtz equation:

$$\nabla \times \nabla \times \vec{E} = -\mu_0 \frac{\partial^2 \vec{D}}{\partial t^2} \tag{2.4a}$$

$$\nabla^2 \vec{E} - \frac{\epsilon}{c^2} \frac{\partial^2 \vec{E}}{\partial t^2} = 0, \tag{2.4b}$$

where the triple product expansion is used to simplify the left hand side of (Eq.2.4a) and $c = \frac{1}{\sqrt{\mu_0 \epsilon_0}}$ is the speed of light.

Taking into account the harmonic nature of electric field $\vec{E}(\vec{r}, t) = \vec{E}(\vec{r}) e^{i\omega t}$, the equation (Eq.2.4b) can be rewritten in frequency domain as the Helmholtz equation:

$$\nabla^2 \vec{E} + k^2 \vec{E} = 0, \tag{2.5}$$

where $k = n\frac{\omega}{c}$ is a wavenumber and $n = \sqrt{\epsilon}$ is the complex refractive index.

Consider two semi-infinite blocks of material with permittivities ϵ_1 and ϵ_2. The boundary lies in the $x - y$ plane at $z = 0$. The discontinuous dielectric function in this problem depends only on z and, thus, $\epsilon = \epsilon(z)$. Taking all this into account it is possible to write the propagating wave as $\vec{E}(x, y, z) = \vec{E}(z) e^{i\beta x}$. Here $\beta = k_x$ is the complex propagation constant of the wave in medium. Substitution of this

expression into (Eq.2.5) gives the wave equation for the surface plasmon polariton:

$$\frac{\partial^2 \vec{E}(z)}{\partial z^2} + (k^2 - \beta^2)\vec{E} = 0. \tag{2.6}$$

The similar equation exists for the magnetic field $\vec{H}$ [26]:

$$\frac{\partial^2 \vec{H}(z)}{\partial z^2} + (k^2 - \beta^2)\vec{H} = 0. \tag{2.7}$$

The equation (Eq.2.6) has two sets of solutions with each representing a different type of the wave. The first set is for the wave which has E_x, E_z and H_y components and all other components are equal to zero. This wave is called a transverse magnetic (TM) or p mode. Similarly, the other wave has H_x, H_z and E_y as non-zero components. Such a wave is called a transverse electric (TE) or s mode.

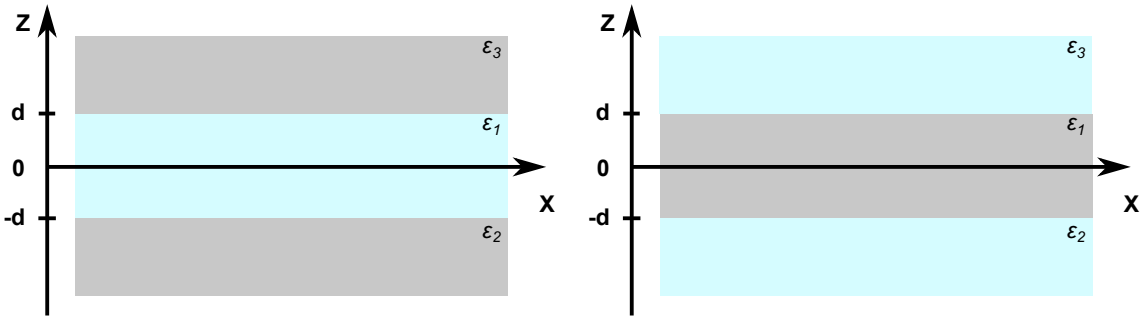

Figure 2.2: Schematic representation of a multilayer interfaces supporting the surface plasmon polaritons propagation.

Surface plasmon waves can be guided by many types of interface including the simplest dielectric-metal interface presented in Figure 2.1 as well as more those in complex three-layer structures so called insulator-metal-insulator (IMI) and metal-insulator-metal (MIM) interfaces [26, 86]. The symmetric and asymmetric variations of IMI and MIM interfaces are of high interest for hybrid electro-plasmonic integrated circuits and, therefore, will be discussed in this work.

A general schematic representation of such an interface is shown in Figure 2.2. Here the material with permittivity ϵ_1 is sandwiched between materials with permittivities ϵ_2 and ϵ_3 respectively. Surface plasmon polaritons propagate along the x-axis.

Solving the wave equation (Eq.2.6) for this system yields the solution for the field components of a fundamental TM mode for each material:

$$\left.\begin{aligned} H_y &= Ae^{i\beta x}e^{-k_3 z} \\ E_x &= iA\frac{1}{\omega\epsilon_0\epsilon_3}k_3 e^{i\beta x}e^{-k_3 z} \\ E_z &= -A\frac{\beta}{\omega\epsilon_0\epsilon_3}e^{i\beta x}e^{-k_3 z} \end{aligned}\right\} \qquad z > d \tag{2.8}$$

$$\left.\begin{aligned} H_y &= Ce^{i\beta x}e^{k_1 z} + De^{i\beta x}e^{-k_1 z} \\ E_x &= -iC\frac{1}{\omega\epsilon_0\epsilon_1}k_1 e^{i\beta x}e^{k_1 z} + iD\frac{1}{\omega\epsilon_0\epsilon_1}k_1 e^{i\beta x}e^{-k_1 z} \\ E_z &= C\frac{\beta}{\omega\epsilon_0\epsilon_1}e^{i\beta x}e^{k_1 z} + D\frac{\beta}{\omega\epsilon_0\epsilon_1}e^{i\beta x}e^{-k_1 z} \end{aligned}\right\} \qquad -d < z < d \tag{2.9}$$

$$\left.\begin{aligned} H_y &= Be^{i\beta x}e^{-k_2 z} \\ E_x &= -iB\frac{1}{\omega\epsilon_0\epsilon_2}k_2 e^{i\beta x}e^{-k_2 z} \\ E_z &= -B\frac{\beta}{\omega\epsilon_0\epsilon_2}e^{i\beta x}e^{-k_2 z} \end{aligned}\right\} \qquad z < -d. \tag{2.10}$$

Together with the boundary conditions at $z = d$ and $z = -d$, representing the continuity of H_y and E_x fields, and momentum matching in all region equations (Eq.2.8)-(Eq.2.10) give dispersion relation for a three-layer system with complex dielectric constants in each region:

$$e^{-4k_1 d} = \frac{\left(\frac{k_1}{\epsilon_1} + \frac{k_2}{\epsilon_2}\right)}{\left(\frac{k_1}{\epsilon_1} - \frac{k_2}{\epsilon_2}\right)}\frac{\left(\frac{k_1}{\epsilon_1} + \frac{k_3}{\epsilon_3}\right)}{\left(\frac{k_1}{\epsilon_1} - \frac{k_3}{\epsilon_3}\right)}. \tag{2.11}$$

In general, each dielectric permittivity is arbitrary and (Eq.2.11) is a common solution for such multilayer systems. In special cases when top and bottom materials have the same dielectric permittivity ($\epsilon_2 = \epsilon_3$) and, thus, the same wavenumbers ($k_2 = k_3$), the relation (Eq.2.11) separates into two equations:

$$\tanh k_1 d = -\frac{k_2 \epsilon_1}{k_1 \epsilon_2} \tag{2.12a}$$

$$\tanh k_1 d = -\frac{k_1 \epsilon_2}{k_2 \epsilon_1} \tag{2.12b}$$

Equations (Eq.2.12a) and (Eq.2.12b) represent the odd and even TM modes respectively. The cases of IMI and MIM interfaces for both of these modes will be considered further.

For TE modes the components of electric and magnetic fields can be calculated using following expressions:

$$\left.\begin{aligned} E_y &= A e^{i\beta x} e^{-k_3 z} \\ H_x &= -iA \frac{1}{\omega \mu_0} k_3 e^{i\beta x} e^{-k_3 z} \\ H_z &= A \frac{\beta}{\omega \mu_0} e^{i\beta x} e^{-k_3 z} \end{aligned}\right\} \quad z > d \tag{2.13}$$

$$\left.\begin{aligned} E_y &= B e^{i\beta x} e^{k_2 z} \\ H_x &= iB \frac{1}{\omega \mu_0} k_2 e^{i\beta x} e^{k_2 z} \\ H_z &= B \frac{\beta}{\omega \mu_0} e^{i\beta x} e^{k_2 z} \end{aligned}\right\} \quad z < -d. \tag{2.14}$$

Continuity of $\vec{E}_y$ and $\vec{H}_x$ at the interface [26] implies the condition:

$$B(k_2 + k_3) = 0. \tag{2.15}$$

Since both Re(k_2) and Re(k_3) must be grater than 0, this condition is fulfilled only if B = 0 which implies that also A = 0. Therefore, there is no surface modes exist for TE polarisation. Surface plasmons exist only for TM polarisation.

2.1.1 The IMI interface

In the case of an IMI (see Fig.2.3) interface, a metal core is placed between dielectric cladding. To ensure coupling between surface plasmons on the upper and lower interfaces, the thickness of the core must be sufficiently small - for example comparable to or smaller than the decay length of the interface mode [26].

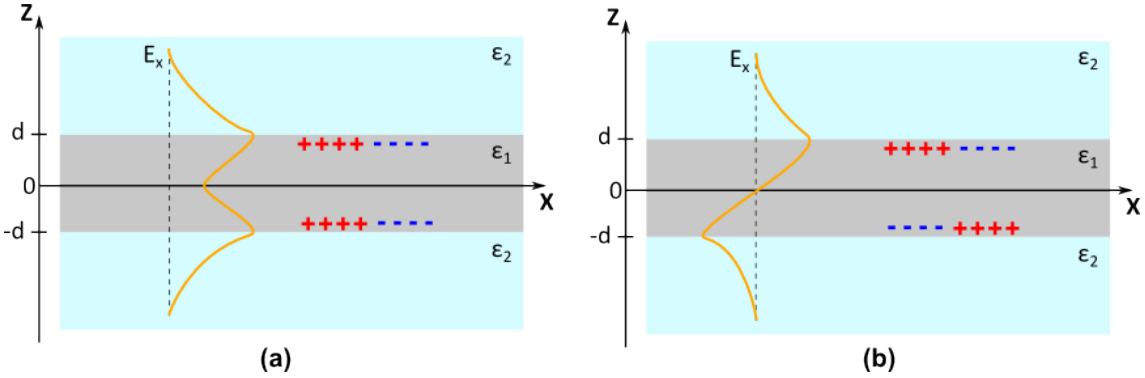

Figure 2.3: Even **(a)** and odd **(b)** coupled modes propagating along the IMI interface. Gray (ϵ_1) and blue (ϵ_2) colours represent metal and dielectric respectively.

Both symmetric and antisymmetric TM modes can be supported by this interface. Unlike symmetric modes, the propagation length of the antisymmetric modes increases with decreasing core thickness. Such modes are called long-range surface plasmon polaritons [26, 16]. It should be mentioned that these modes exist only for symmetric structures when the permittivities of the top and bottom dielectrics are the same. For asymmetric configurations the attenuation of these modes increases because of the phase mismatch. For example, a significantly larger permittivity of the bottom dielectric will result in the top plasmon mode leaking into the substrate. Such a mode is called a leaky mode and experiences strong attenuation [16].

2.1.2 The MIM interface

The case of a MIM interface (see Fig.2.4) is a compliment of the IMI configuration and consists of a dielectric core sandwiched between two metal slabs. Similarly to the previous interface, this configuration can support both symmetric and antisymmetric modes [26].

A fundamental antisymmetric TM mode does not have a cut-off thickness when

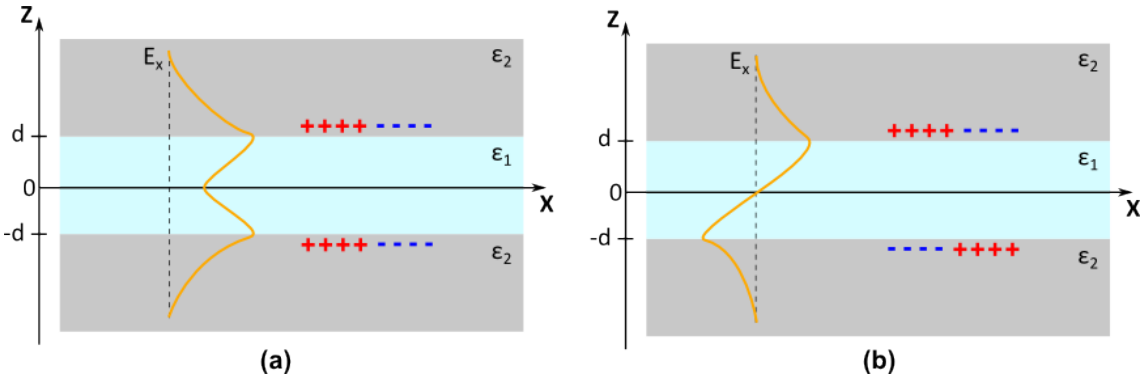

Figure 2.4: Even **(a)** and odd **(b)** coupled modes propagating along the MIM interface. Gray (ϵ_2) and blue (ϵ_1) colours represent metal and dielectric respectively.

the dielectric core thickness decreases [87]. This opens up the opportunity of achieving a very high field confinement even at low frequencies, for example in the case of infrared light. Additionally, the small penetration of electric field into the metal at these frequencies results in large propagation lengths. Various modifications of such a configuration have been previously studied theoretically [86] and experimentally [17].

2.1.3 Drude – Sommerfeld model

While the dependence of the relative permittivity of material and the wavelength of the light for most transparent dielectrics can be found using the Sellmeier equation [88], the dispersion relation for metals and heavily doped semiconductors requires a more complex approach. The Drude-Sommerfeld free electron model is usually used to determine such a relation. This model assumes that electrons in metal behave as a nearly-free electron gas, forming an electron plasma inside the metal. The potential of the crystal lattice (effective electron mass is used instead) and electron-electron interactions are neglected.

Combining all the assumptions discussed above, it is then possible to derive a differential equation, which describes the displacement from equilibrium, $\vec{r}$, of an electron in response to an applied alternating electric field stimulus:

$$m_e \frac{\partial^2 \vec{r}}{\partial t^2} + m_e \gamma \frac{\partial \vec{r}}{\partial t} = -eE_0 e^{-i\omega t}, \tag{2.16}$$

where m_e is an effective electron mass, e is an electron charge, E_0 is an amplitude of applied electric field and γ is a damping frequency of the electron gas. Equation (Eq.2.16) is also called Drude-Sommerfeld model for the free electron gas.

The solution of (Eq.2.16) is $\vec{r}(t) = r_0 e^{-i\omega t}$. Also a polarisation density with n electrons is equal to $\vec{P} = -ne\vec{r}(t)$ [26]. Combination of these two equations with (Eq.2.3a) gives an expression for a electric displacement:

$$\vec{D} = \epsilon_0 \left(1 - \frac{\omega_p^2}{\omega^2 + i\gamma\omega}\right) \vec{E}, \tag{2.17}$$

where ω_p is the plasma frequency given by:

$$\omega_p = \sqrt{\frac{ne^2}{\epsilon_0 m_e}}. \tag{2.18}$$

The dielectric permittivity of the free electron gas, therefore, is given by:

$$\epsilon_m(\omega) = 1 - \frac{\omega_p^2}{\omega^2 + i\gamma\omega}. \tag{2.19}$$

The equation (Eq.2.19) describes the relative permittivity of an ideal free electron gas. In the case of real metals and, especially, semiconductors the ionic background of the crystal structure must also be taken into account. In this case the polarisation caused by the free electrons can be described as $\vec{P}_\infty = \epsilon_0(\epsilon_\infty - 1)\vec{E}$ and (Eq.2.19) can be rewritten as:

$$\epsilon_m(\omega) = \epsilon_\infty - \frac{\omega_p^2}{\omega^2 + i\gamma\omega} \tag{2.20}$$

Although the Drude-Sommerfeld model can reasonably accurately describe the permittivity in infrared and red light spectra, it is not applicable at higher frequencies. The inaccuracies result from the fact that high-energy photons can excite lower band electrons into the conduction band [86]. For noble metals like Au or Ag the interband transition occurs in the visible part of spectrum. Therefore, experimental data (for example from [89]) for metal permittivities must be used to accurately

calculate surface plasmon resonances at high frequencies. In addition to that, the properties of metals also depend on the size of a structure and deposition methods [26].

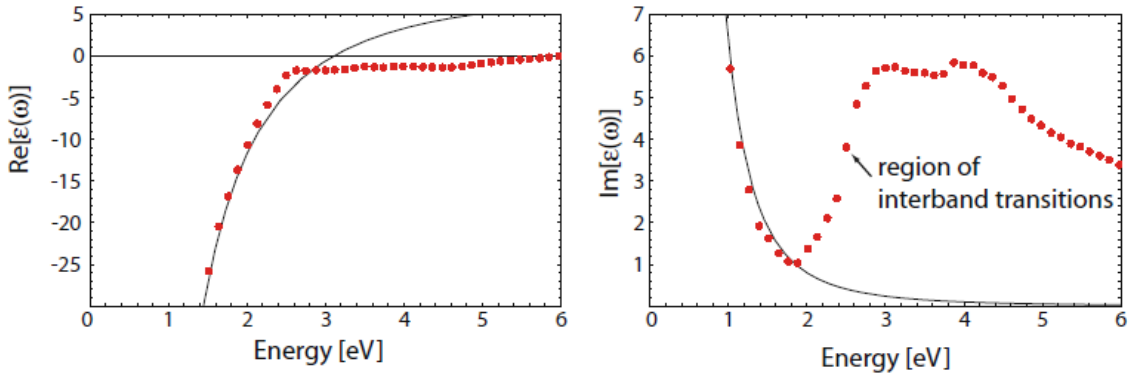

Figure 2.5: Graphs showing the values of real **(left)** and imaginary **(right)** parts of dielectric permittivity for gold, obtained from the Drude model (solid black line) and experimental data (red dots) from [89]. Taken from [26][1].

As can be seen from Figure 2.5 the Drude model fits the experimental data for gold up to 2 eV (the model describes dielectric permittivity $\epsilon(\omega)$ of gold). For higher energies the model strongly deviates from the experimental data due to the interband transition. Nevertheless, the Drude model can give a satisfactory approximation of the dielectric permittivity of semiconductors [90].

2.2 Surface plasmon polariton excitation

Surface plasmons polaritons can be excited by either injecting electrons into the metallic structure [91, 92] or using photons [93]. Optical excitation is preferred as it is more flexible and does not require specialised equipment [94]. Therefore, SPP excitation by electrons is outside the scope of this work.

For optical excitation of SPP it is required that a photon has the same energy and momentum as the SPPs. Since freely propagating photons will always have a lower momentum due to the difference in dispersion relations [26], the excitation of surface plasmon polaritons by direct illumination of the metal surface is impossible. Therefore, special techniques must be utilised in order to match the wave vectors. Some of these techniques will be discussed in this section.

[1]Maier, Stefan Alexander, "Plasmonics: Fundamentals and Applications", p.14, Springer 2007. With permission of Springer Nature.

2.2.1 Prism coupling

As mentioned before, a freely propagating photon will always have a lower momentum than a surface plasmon. At the same time, a photon with a certain frequency propagates in a more optically dense medium its momentum is larger. Figure 2.6 shows dispersion relations for surface plasmons at a silver-air interface (blue) and two light lines: light-in-air (dashed purple) and light-in-SiO_2 (dashed red). As can be seen, the photon in silica has a larger momentum than the surface plasmon at the silver-air interface ($k_{SiO_2} = k_{SPP} + \Delta k$). This opens up an opportunity to excite surface plasmons using a silica prism.

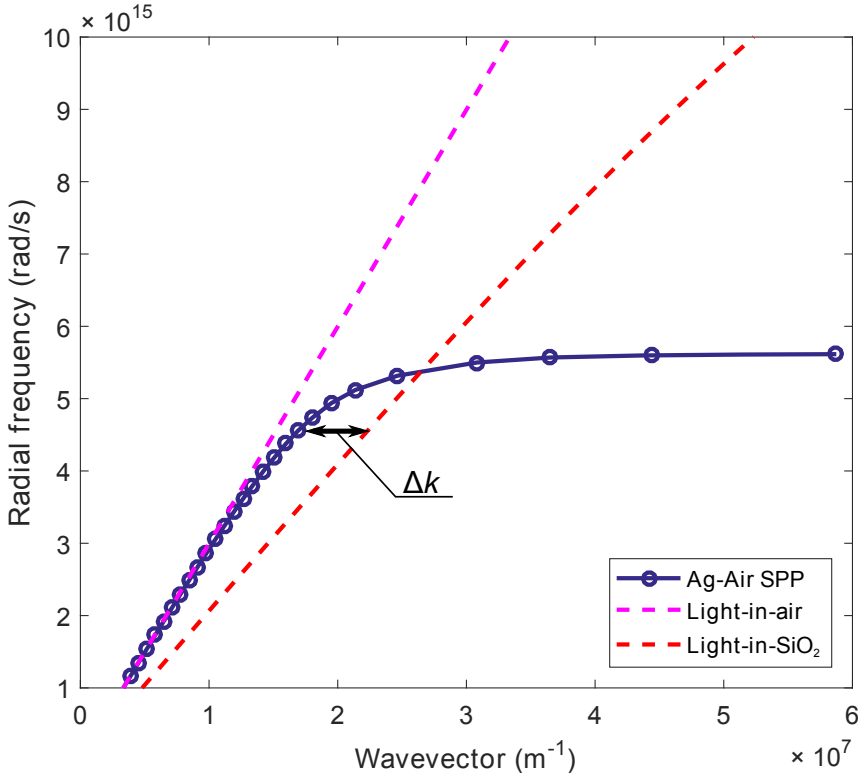

Figure 2.6: Dispersion relations for SPP on silver film and light lines in air and silica. Photon in silica has larger momentum than the SPP on Ag-Air interface.

In the prism coupling scheme the wavevector of the surface plasmon is calculated using the following formula:

$$k_{SPP} = k_0 \sqrt{\epsilon_1} \sin\theta, \tag{2.21}$$

where k_0 is the wavevector of the light in vacuum, ϵ_1 is the dielectric permittivity of the prism material and θ is the angle of illumination. For certain values of ϵ_1 and

θ it is possible to match the wavelectors and excite SPPs on the interface between metal and air. Different configurations can be used (see Fig.2.7) to excite the SPP using this technique.

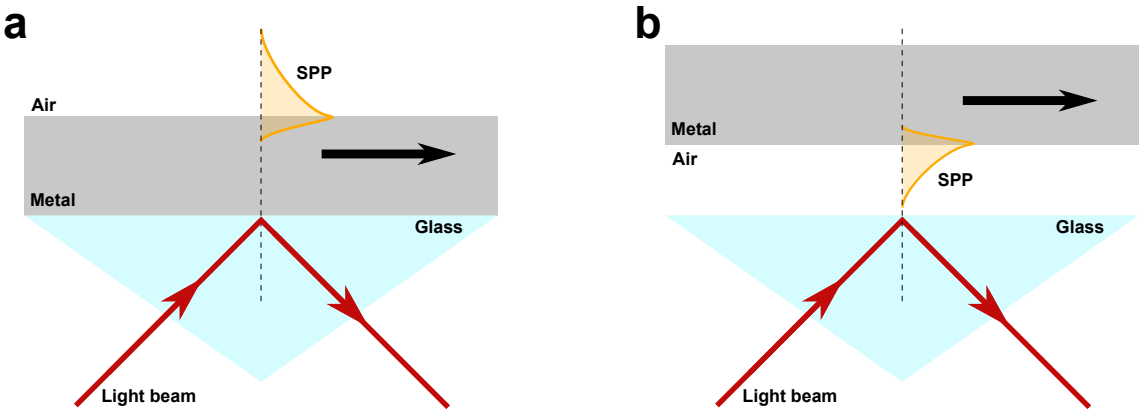

Figure 2.7: Prism coupling to SPP using Kretschmann **(a)** and Otto **(b)** configuration.

In the Kretschmann configuration (see Fig.2.7a) a thin metal film is deposited directly on the top surface of a prism. The light beam enters the prism at an angle greater than the angle of total internal reflection and photons tunnel through the metal layer [26] and excite surface plasmons on the metal-air interface. For the Otto configuration (see Fig.2.7b), the prism is placed very close to the metal surface. Total reflection from the prism-air interface excites SPPs via photon tunneling. In both configurations, the excitation of surface plasmon could be confirmed by registering a decrease in the reflected beam intensity.

The Kretschmann configuration is widely used for biosensing applications [95] and in lab-on-a-chip sensors, based on surface plasmon resonance (SPR) [96]. The Otto configuration, in turn, is commonly used to test the quality of the sample surface when direct contact with the surface cannot be achieved [97].

2.2.2 Grating coupling

A grating on a metal surface can also be used to excite SPPs (see Fig.2.8). In this case, the difference between the projection of the incident light wavevector onto the surface and the SPP propagation constant is compensated by an amount related to the grating period [26].

The value of the surface plasmon wavevector in this case can be calculated using

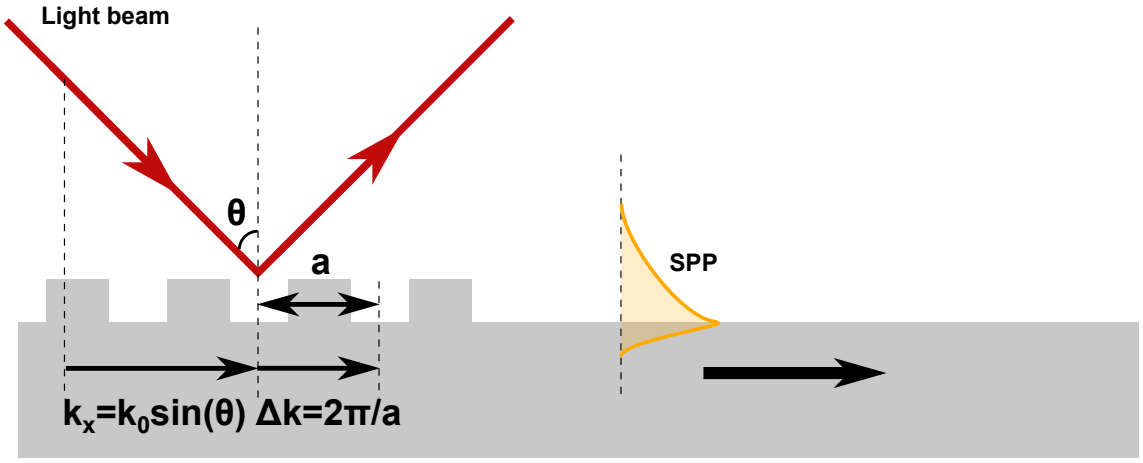

Figure 2.8: Excitation of SPP using grating coupling. The difference in wavevectors is compensated by an amount related to the grating period.

the following formula:

$$k_{SPP} = k_0 \sin\theta \pm m\frac{2\pi}{a}, \tag{2.22}$$

where a is the grating period and $m = (1, 2, 3, 4\ldots)$ is an integer representing the diffraction order. This technique can also be used in reverse mode, enabling the coupling of surface plasmons back into the far-field.

The advantage of this method is that it is possible to define the wavevector of the surface plasmons by only the grating period. This opens up an opportunity to use convenient normal incidence illumination for SPP excitation. It should also be mentioned that expression (Eq.2.22) is strictly valid only in the case of shallow gratings. Deep gratings can introduce significant changes into the dispersion relation which become evident in grooves of depth of the order of 20 nm [26].

2.2.3 Near-field excitation

The above-mentioned methods are applicable for far-field excitation of surface plasmons. Such techniques enable the excitation of SPPs over a macroscopic area with dimensions of several wavelengths or larger. Near-field techniques [98, 99] must be utilised in order to locally excite surface plasmons at particular locations on the surface. A metal-coated optical fibre with aperture much smaller than the wavelength ($a \ll \lambda$) can be used for this purposes (see Fig.2.9).

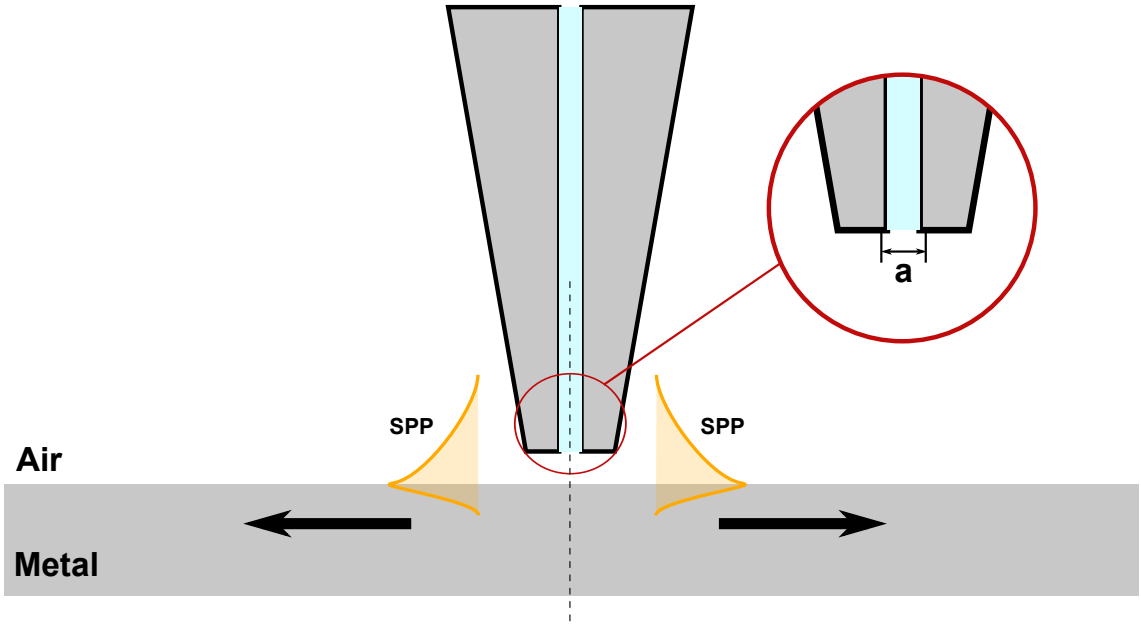

Figure 2.9: Near-field excitation of surface plasmons using a metal-coated optical fibre with small aperture.

Because of the small aperture of a fibre, the light radiated will have a wavevector components comparable to that of the SPP. The fibre must be brought very close to the surface so the photons can tunnel into the metal film and, therefore, excite surface plasmons. This technique is often used to test plasmonic structures such as waveguides [100] or nanowires [101], as it permits local excitation of surface plasmons in desired locations. This method is also suitable for excitation of localised surface plasmons [102] and their subsequent spectroscopy.

2.2.4 Summary

Various methods for exciting surface plasmon polariton have been presented in this sections. Grating couplers can be used to build future hybrid optoelectronic circuits as they are easy to implement, require no additional laboratory equipment and have relatively small dimensions compared to other techniques.

2.3 Surface plasmon detection

Detection of surface plasmons is an essential consideration for building logic gates with plasmonic interconnects. There are several techniques which can be used to detect propagating surface plasmons (see Fig.2.10). Generally, these techniques can be divided into three groups: either utilising near- or far- fields and by conversion of the SPP energy into an electric current.

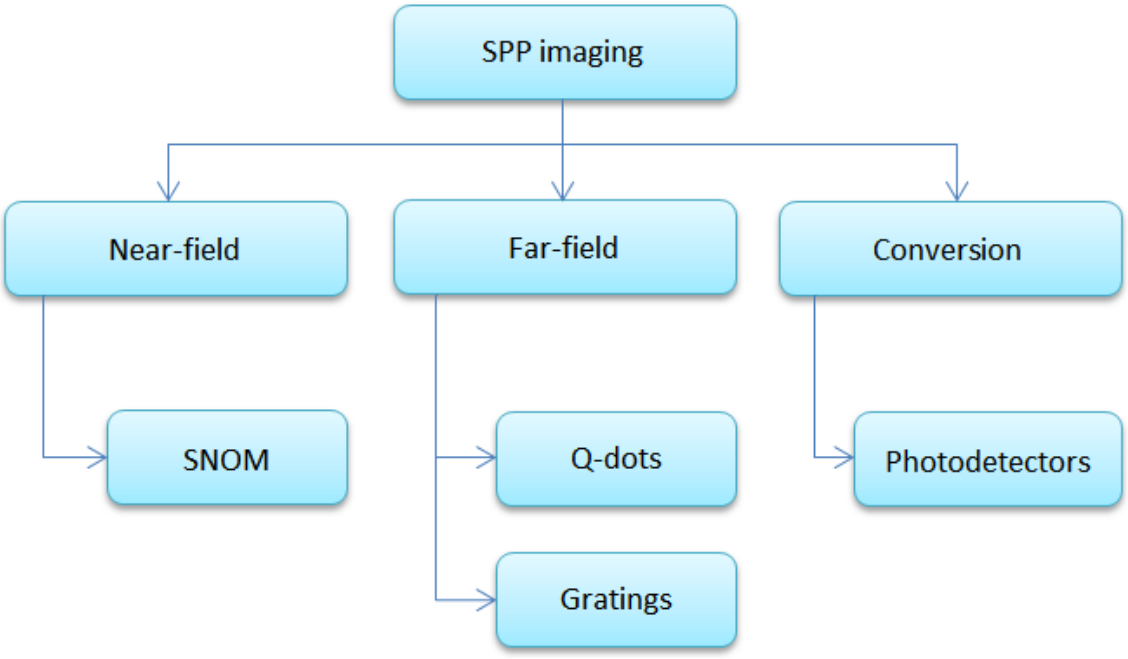

Figure 2.10: Common techniques used for detecting surface plasmons.

Some of these methods may be inapplicable in certain cases. Moreover, some exhibit better resolution while others can be more easily implemented. Therefore, each of these methods possess its own advantages and can be used depending on the particular application. A detailed review of each method will be presented in this section.

2.3.1 Near-field imaging

Scanning near-field optical microscopes (SNOM) can be used to map surface propagating plasmons. This method is based on coupling of the evanescent field above a surface into the tapered optical fibre [26]. The optical fibre is placed very close to the surface under investigation. The distance between the metal film and the

fibre should not exceed the evanescent decay length - from tens to hundreds of nanometers, depending on the used frequency and metal film. Specialised feedback techniques are used to control the vertical position of the tip (similar to a scanning tunneling microscope).

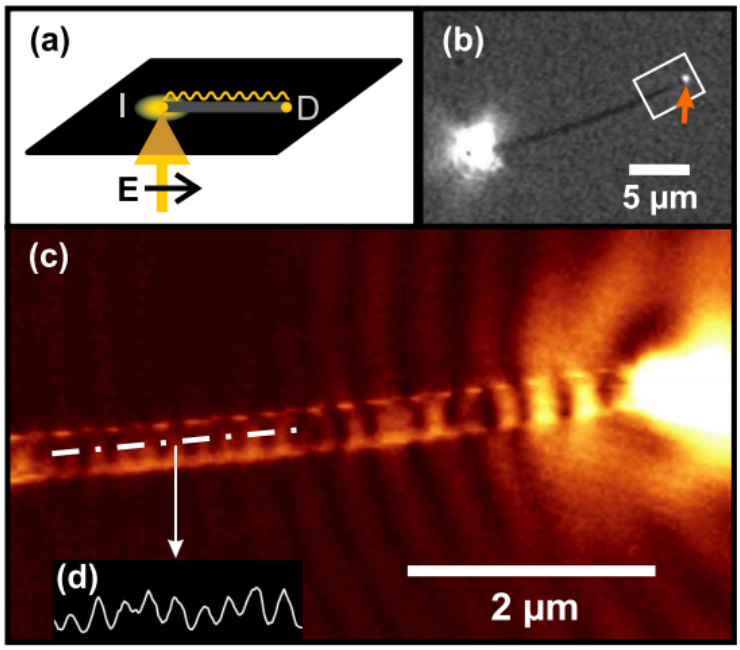

Figure 2.11: Excitation and detection of surface plasmons on the surface of nanowire. **(a)** Excitation scheme. **(b)** Microscope image of a nanowire. **(c)** Near-field image obtained by SNOM. **(d)** Cross-cut along the chain dotted line. Taken from [103][2].

SNOM provides the most accurate investigation of SPP electric field distribution in both longitudinal and lateral directions. A number of SPP parameters can be studied using this technique such as mode profile, propagation length and field confinement. Also it is possible to not only detect SPPs but also to locally excite them (see Section 2.2.3). These facts make the near-field detection method an indispensable tool when accurate investigation of SPP propagation is required. Furthermore, SNOM provides an ability to map the electric field around the waveguide which can be useful when studying evanescent field coupling or parasitic interactions between waveguides.

An example of near-field detection method utilisation has been demonstrated in [103]. A focused laser beam polarised along the wire excites an SPP at one of

[2]Reprinted figure with permission from [Ditlbacher, Harald, Andreas Hohenau, Dieter Wagner, Uwe Kreibig, Michael Rogers, Ferdinand Hofer, Franz R. Aussenegg, and Joachim R. Krenn. "Silver nanowires as surface plasmon resonators." Physical Review Letters 95, no. 25 (2005): 257403. Copyright 2017 by the American Physical Society

the ends (see Fig.2.11a). The electric field distribution along the wire was mapped using SNOM (see Fig.2.11c). As can be seen, the electric field is modulated due to reflection of the SPP from the distal end of the wire. SNOM provides nanoscale resolution well below the diffraction limit (see Fig.2.11b and Fig.2.11c).

Nevertheless, the SNOM technique has several drawbacks. First of all, scanning takes a significant amount of time. This method is also appropriate only for studying SPPs at a metal-air interface. Utilisation of this method for waveguides coated with a thick layer of dielectric (dielectric-loaded waveguides [104] for example) is difficult, due to the extremely weak evanescent field outside the dielectric. The most significant drawback in terms of miniaturisation is the fact that this method is not scalable as it requires specialised scientific equipment. It is also suitable only for small scanning areas (of the order of 100 µm) as the travelling distance of the tip is limited by the piezo-stage.

2.3.2 Far-field imaging

Another approach involves far-field imaging to map surface plasmon propagation. This technique may involve utilisation of a scattering grating or quantum dots (QD). The main purpose of those is to couple surface plasmons back into the far-field. In this case a simple microscope with high magnification objective can be used to detect the presence of SPPs.

Quantum dots

The utilisation of QDs to map surface plasmon propagation has been demonstrated in [29]. Quantum dots were placed into the evanescent field of the SPPs. Some power is absorbed by the QDs and re-radiated into far-field. The brightness of these emitters is proportional to strength of electric field.

The nanowires were firstly coated with a 30-50 nm layer of Al_2O_3 as a spacer to minimise the influence of the quantum dots on the SPP. They were then uniformly

[3]Reprinted with permission from Wei, Hong, Zhipeng Li, Xiaorui Tian, Zhuoxian Wang, Fengzi Cong, Ning Liu, Shunping Zhang, Peter Nordlander, Naomi J. Halas, and Hongxing Xu. "Quantum dot-based local field imaging reveals plasmon-based interferometric logic in silver nanowire networks." Nano Letters 11, no. 2 (2010): 471-475. Copyright 2017 American Chemical Society.

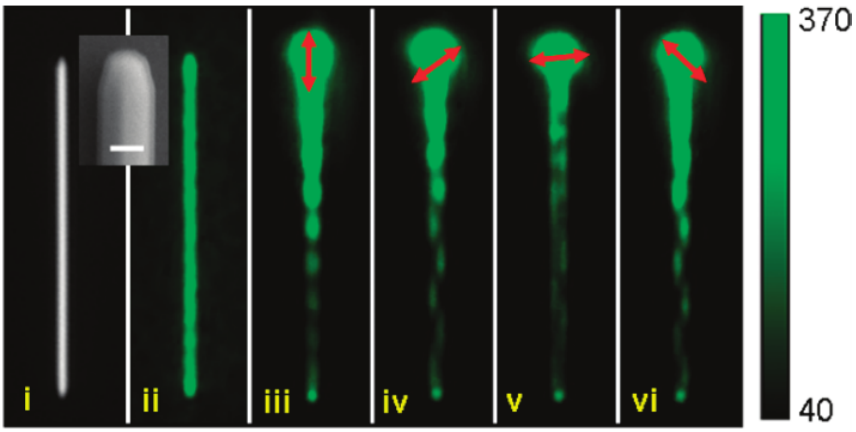

Figure 2.12: Imaging of SPP using quantum dots. **(i)** Optical image of Ag nanowire. **(ii)** The QD emission under large-area laser illumination. **(iii-vi)** The QD emission with different polarisation angle of excitation laser. Taken from [29][3].

spin-coated with CdSe@ZnS quantum dots. Then each nanowire was illuminated with a He-Ne laser (632.8 nm) at one of its ends. The peak of QD emission spectrum was at 655 nm. The electric field distribution of the excited SPP was mapped by collecting of emission from the QDs with microscope objective through the 633 nm long-pass filter. Figure 2.12 shows examples of the obtained images.

A distinct advantage of this method is that it is possible to use different wavelengths for excitation and detection. Depending on the size and type of the quantum dots the emitted electromagnetic wave can have different frequency that the excitation. This makes detection much easier as the excitation light can be filtered. However, since optical microscope is used to detect surface plasmons, the maximum resolution is limited by diffraction.

Scattering grating

Another way to couple SPPs to far-field radiation is to use a corrugated surface [26]. When SPP reaches the scattering grating it is reduced its momentum by Δk and can be radiated into the far-field. The value of Δk is determined by the grating period. The same phenomenon is used for grating coupling to excite the surface plasmons (see Section 2.2.2).

[4]Reprinted with permission from Sorger, Volker J., Rupert F. Oulton, Jie Yao, Guy Bartal, and Xiang Zhang. "Plasmonic fabry-prot nanocavity." Nano Letters 9, no. 10 (2009): 3489-3493. Copyright 2017 American Chemical Society.

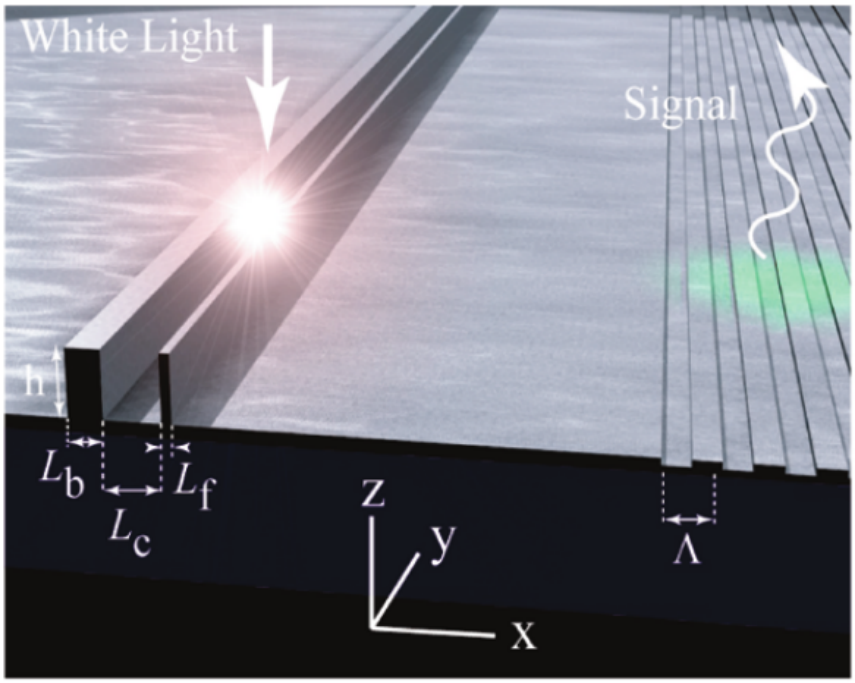

Figure 2.13: Schematic representation of surface plasmon excitation by nanoslit and its scattering by grating structure into far-field. Taken from [105][4].

An example of the use of a grating structure for surface plasmon outcoupling was presented in [105]. A grating was milled in a silver film using focused ion beam (FIB). White light from a xenon lamp was focused into the slit (see Fig.2.13) to excite SPPs. One of the slit borders had a transmission of 2% permitting part of the SPP energy to leave the slit and propagate towards the grating structure. When the SPP reaches the grating it was coupled into the far-field and then collected by a spectrometer objective.

A significant advantage of this method is its simplicity. The corrugations can be created during the lithography process with no additional steps. Moreover, it can be used even if a protective dielectric layer is deposited on the scattering grating.

This technique, nevertheless, has a number of drawbacks. Firstly, this method provides no information about the field distribution or the propagation distance of the SPP. It permits the SPP detection only at a particular point of the waveguide and the method is destructive as almost all power in the SPP radiated into the far-field and the SPP will propagate no further.

2.3.3 Conversion techniques

The energy of an SPP can be directly converted into a voltage or current. Such a conversion can be performed using common optoelectronic devices such as photodiodes or phototransistors [106, 18]. Similarly to photons, surface plasmons can decay in the semiconductor, generating electron-hole pairs [18] or hot-electrons [84]. The amplitude of the voltage or current in this case is proportional to the energy of the SPP and the flux.

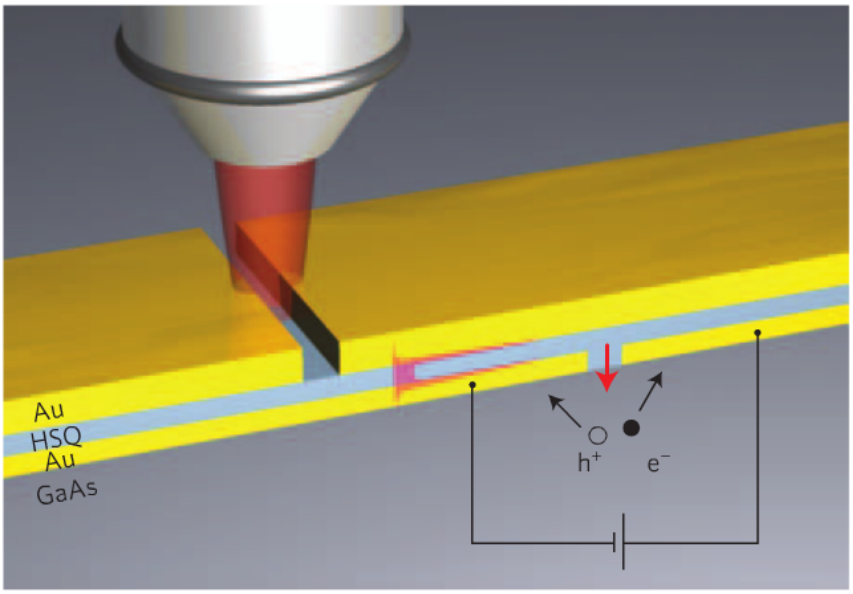

Figure 2.14: Schematic representation of an SPP semiconductor detector. Taken from [18][5].

The flexibility of this technique opens up the possibility of detecting SPPs using various types of photodetectors. An example of SPP detection using a GaAs metal-semiconductor-metal (MSM) photodetector was demonstrated in [18]. The SPP was excited in a metal-insulator-metal waveguide by focusing a laser beam on a slit in the top metal stripe (see Fig.2.14). The bottom stripe had another slit allowing the SPP to decay into the semiconductor substrate. Two metal stripes separated by the lower slit were used as photodetector contacts. The authors reported that this structure demonstrated an extremely fast response time of 0.3-2.5 ps. The method,however, provides no information about the field distribution and is not suitable for SPP mapping. It is also associated with high losses as plasmon decay is required for photoconversion.

[5]Reprinted by permission from Macmillan Publishers Ltd: Nature Photonics, advance online publication, 19 April 2009 — doi:10.1038/nphoton.2009.47

2.3.4 Summary

The following table provides a brief summary of the methods discussed in this section:

Table 2.1: Surface plasmon detection methods summary.

Method	Spatial resolution	Applications	Disadvantages
SNOM	High	Presence of SPP, mode profile, field distribution along the waveguide in both transverse and longitudinal planes	Requires direct access to the metal surface and bulky laboratory equipment
Quantum dots	Depends on microscope resolution, diffraction limited	Presence of SPP, field distribution and strength	Resolution is fundamentally limited by diffraction, requires additional technological steps to introduce quantum dots onto waveguide
Gratings	Low	Presence of SPP, field strength	High losses, reradiated wavelength coincides with excitation one
Optoelectronic conversion	Medium	Presence of the SPP, field strength	High losses, requires semiconductor materials

Of the methods discussed above, grating outcoupling and semiconductor detection are of particular interest for designing logic gates with plasmonic interconnects as they can be embedded into the integrated circuit. This, in turn, opens up an opportunity to create hybrid optoelectronic digital devices.

2.4 Plasmonic waveguides

The application of surface plasmons excited on broad interfaces is limited and rarely extends from SPR biosensing and surface quality measurements. The utilisation of SPPs in digital integrated circuits requires separation of different signals and each signal must be guided to its destinations without interacting with neighbours. Similarly to photonics or microwave technology, plasmonic waveguides can be used to separate and guide the signals. Some of the waveguide configurations will be discussed in this section.

2.4.1 Band gap waveguides

To control SPPs along a metal-dielectric interface it is essential to create conditions allowing its propagation in only a certain direction [26]. The SPP propagation in other directions is, therefore, restricted. These lateral barriers can be implemented by using Bragg mirrors - arrays of periodic defects such as holes or pillars [107]. These mirrors are widely used to obtain band gaps at microwave [108] and optical [109, 110] wavelengths.

Bragg mirrors are very sensitive to the wavelength of propagating SPPs. Therefore, the band gap exists only for an SPP with a certain frequency. Utilisation of Bragg mirrors to control the propagation of surface plasmons has been demonstrated in [111] where Bragg mirror was formed by gold particles (see Fig.2.15a) arranged in a triangular lattice deposited on 40 nm thick gold substrate. The resulting structure has a band gap at free-space wavelengths around $\lambda = 1500$ nm. As can be seen from Figure 2.15b, the SPPs with a wavelength of $\lambda = 1550$ nm can propagate without experiencing high attenuation, while SPPs with a wavelength of $\lambda = 1600$ nm (see Fig.2.15c) are strongly attenuated.

Such structures have great potential for designing surface plasmon waveguides. Waveguides in such a structure can be implemented by introducing a local defect which will break the Bragg reflection and, therefore, permit SPP propagation inside this defect. An example of a linear defect in a Bragg mirror capable of guiding surface plasmons was demonstrated in [23] and shown in Figure 2.16a.

The bending angle is 30°. Surface plasmons with a wavelength of $\lambda = 1515$ nm

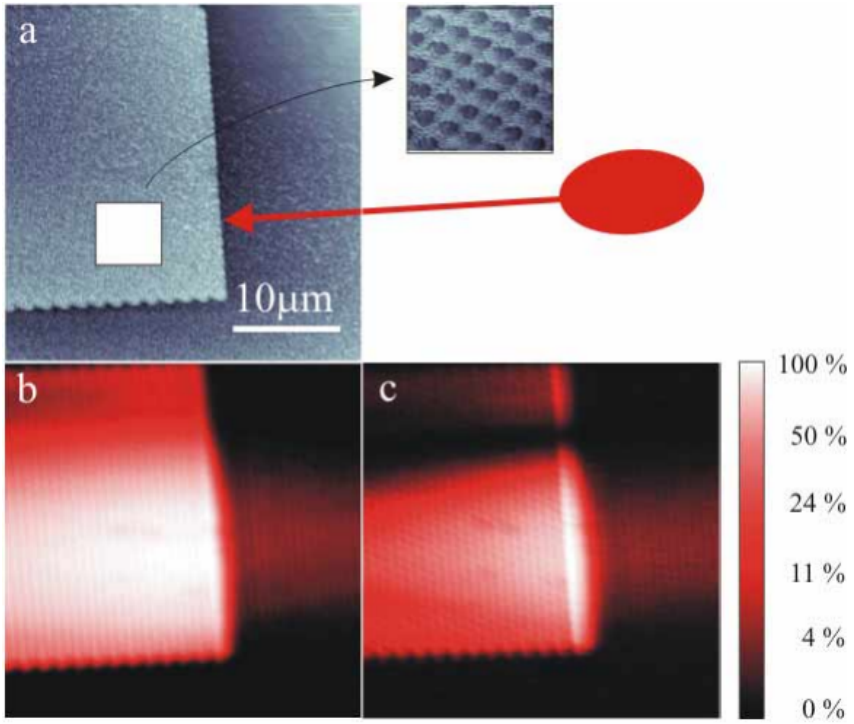

Figure 2.15: Topographic **(a)** and near-filed **(b,c)** images of plasmonic Bragg mirror obtained by SNOM. Propagation of the SPP excited using 1550 nm **(b)** and 1600 nm **(c)** wavelengths respectively. Propagation direction is from right to left. Taken from [23].

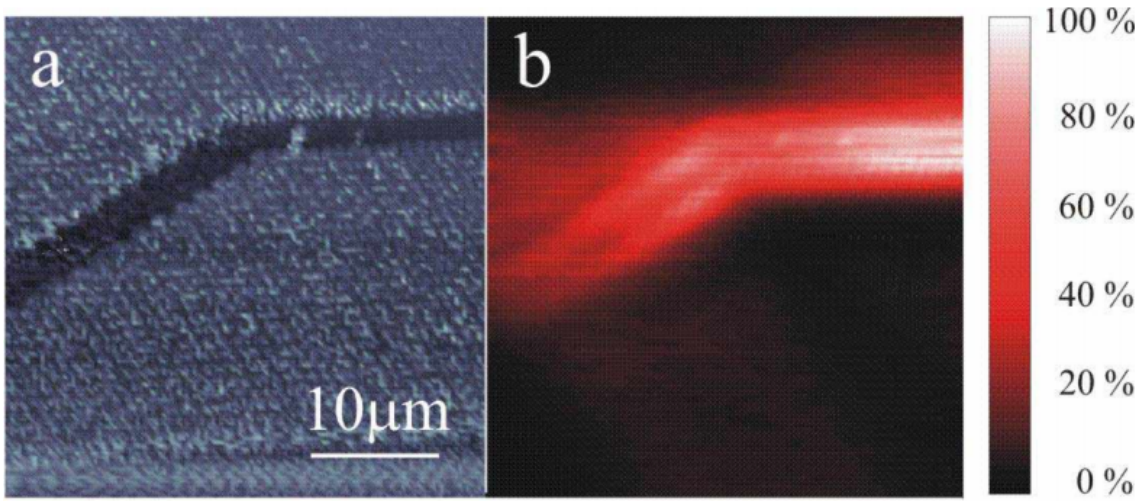

Figure 2.16: Topographic **(a)** and near-field **(b)** images of an SPP waveguide in a Bragg mirror. Taken from [23].

are excited at the right side of the structure and propagate in the direction of the waveguide. As can be seen from Figure 2.16b, strong leakage into the surrounding lattice is observed after the turn. This happens because the band gap is dependent on the SPP momentum and, therefore, exists only for a certain propagation direc-

tion. As a result, SPPs travelling in other directions do not have the same level of confinement.

The structure of the Bragg crystal lattice must be changed along the SPP propagation direction in order to overcome this issue. An investigation of such a crystal structure was carried out in [111].

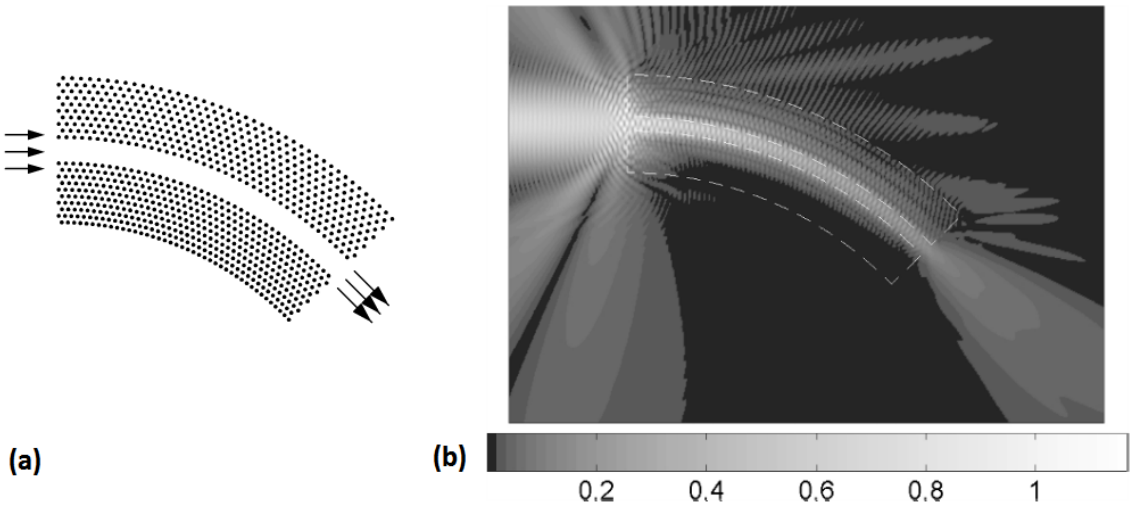

Figure 2.17: Schematic representation of 45° bent plasmonic waveguide **(a)** and FEM simulation **(b)** propagating wave. Taken from [111][6].

The structure shown in Figure 2.17a has been obtained by the gradual rotation of crystal lattice along the linear defect through 45°. As a result, the Bragg mirror has a constant band gap throughout the defect. FEM simulation showed that SPP can propagate along such a waveguide with smaller loss (due to the suppressed leakage) than through the configuration shown in Figure 2.16.

2.4.2 Stripe weveguides

An SPP stripe waveguide is a variation of IMI structure (see Section 2.1.1) where the width w of the stripe is finite. Usually it is a rectangular metal stripe with a thickness t ($t < w$) embedded into homogeneous (symmetric waveguide) or inhomogeneous (asymmetric waveguide) dielectric medium (see Fig.2.18). Such a structure is very easy to fabricate using equipment utilised in modern CMOS technology which makes these structures interesting for plasmonic integrated circuits manufacturing.

[6]Sndergaard, Thomas, and Sergey I. Bozhevolnyi. "Surface plasmon polariton guiding in photonic bandgap structures." In Surface Plasmon Nanophotonics, pp. 73-86. Springer Netherlands, 2007. With permission of Springer.

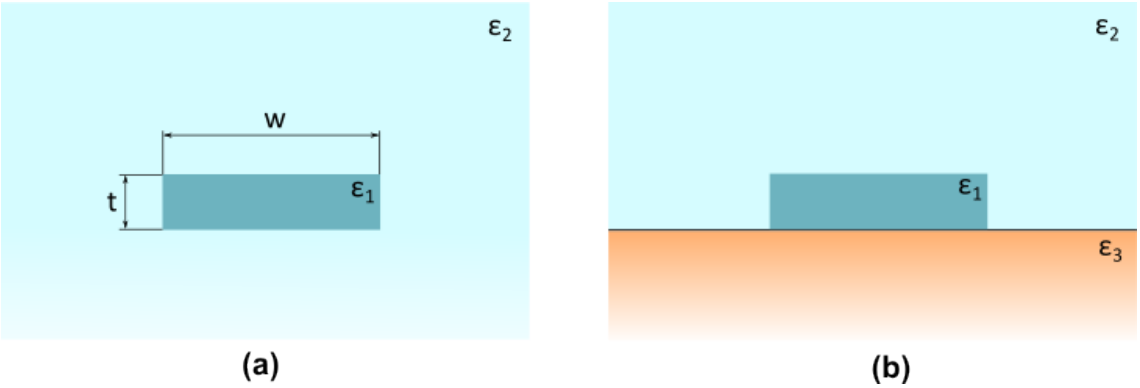

Figure 2.18: Symmetric **(a)** and asymmetric **(b)** stripe waveguide configurations.

A comprehensive numerical investigation of these waveguides was performed in [16]. As was mentioned in Section 2.1.1, stripe waveguides can support both symmetric and antisymmetric modes. Because of the finite width of the stripe, the supported modes are not purely TM, but rather hybrid and, therefore, include both TM and TE components. Also, in contrast with an infinitely wide IMI interface, the mode analysis cannot be performed analytically and requires a numerical approach. The mode profile can greatly vary, depending on the difference in permittivities of the surrounding dielectrics. In the case when the sub- and superstrate have significantly different permittivities, a long range SPP mode cannot propagate through such an interface due to the phase mismatch between the top and bottom surface plasmons [16].

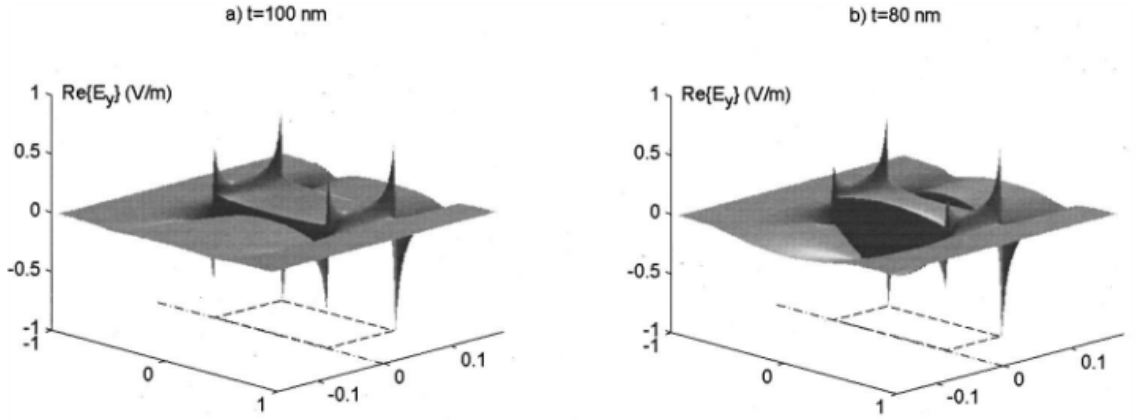

Figure 2.19: Normalised E_y field component distribution for different stripe thicknesses. Taken from [16][7].

Despite the simplicity of the structure and its compatibility with existing mi-

[7]Reprinted figure with permission from Berini, Pierre. "Plasmon-polariton waves guided by thin lossy metal films of finite width: Bound modes of symmetric structures." Physical Review B 61, no. 15 (2000): 10484. Copyright 2017 by the American Physical Society.

croelectronics technology, these waveguides have drawbacks associated with SPP propagation. Power in such waveguides is mostly guided [16] along the edges (see Fig.2.19). This can be an issue for applications where uniform power distribution along the cross-section of a waveguide is required (for example waveguide splitters, passive filters and couplers). Additionally, for asymmetric stripe waveguides the fundamental mode shows a cutoff at some stripe width due to the leakage into the substrate [112].

2.4.3 Slot waveguides

An SPP slot waveguide is a case of a MIM configuration when the thickness t of a slit is finite. The dielectric core is embedded between the two metal slabs (see Fig.2.20). Coupling between top and bottom surface plasmons occurs through the dielectric and, therefore, can be much stronger than in case of IMI structure. The field confinement in slot waveguides can also be much stronger. The fundamental mode of symmetric waveguide configuration (see Fig.2.20a) does not have a cutoff wavelength as the width decreases and exists even when the width is nearly zero [87]. This opens up an opportunity for scaling down the dimensions of waveguides and active plasmonic elements into hundreds or even tens of nanometers.

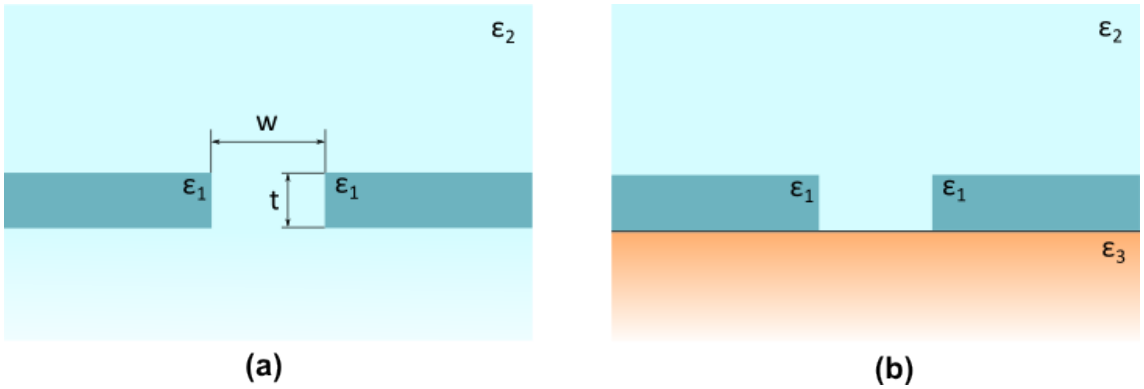

Figure 2.20: Symmetric **(a)** and asymmetric **(b)** slot waveguide structures.

Unlike stripe waveguide, this structure can support not only TM but also quasi-TEM modes [112]. Slot waveguides can also exhibit relatively low losses at near-infrared frequencies [113] which permits an application of microwave theory to plasmonic waveguides [114, 115]. To calculate properties of designed structures analytically. An example of microwave theory applied to the design of a passive plasmonic circuit was demonstrated in [116].

Another noticeable feature of slot waveguides is that they can be easily transformed into plasmonic modulators. High field intensity in the slit enhances interactions between plasmons and dielectric core medium. The attenuation of propagating surface plasmons can be modulated by bias application to metallic slabs of the waveguide and this approach was demonstrated in [21]. A surface plasmon modulator based on the slot waveguide structure will be discussed in Chapter 6.

2.4.4 Summary

In this section three types of plasmonic waveguides have been discussed. Both stripe and slot waveguides can have small dimensions and are compatible with modern CMOS fabrication technology. Therefore, they are of a great interest for building future hybrid integrated circuits.

2.5 Semiconductor plasmonics

An ability to modulate propagation of surface plasmons is essential for building a functional logic gates. It was previously demonstrated that periodic structures can have band gaps for SPPs at a certain frequency. However, for plasmonic semiconductors a mechanism for modifying the position of the plasmonic band gap is needed.

The surface plasmon modulation mechanism can be implemented either using linear or non-linear effects (see Fig.2.21). The application of these effects will be discussed in this section.

2.5.1 Linear effects

The key phenomenon that underlies a linear modulation is interference between surface plasmons. It should be noted that by itself, this method does not involve any semiconductor properties but it permits the realisation of all basic logic elements. This method is based on the utilisation of multiple input plasmonic networks. It was previously demonstrated [29] that all boolean logic operations can be performed by

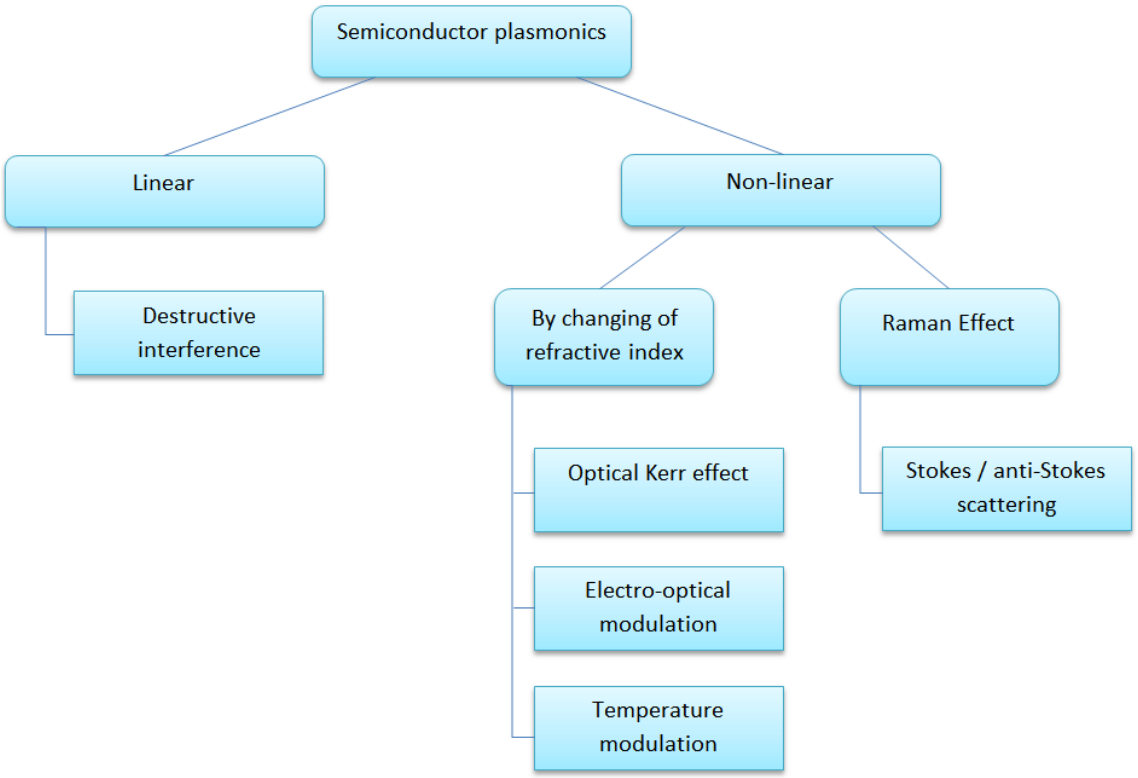

Figure 2.21: Possible approaches for surface plasmon modulation.

using various combinations of waveguides. Figure 2.22a shows an example of such a waveguide network. A short silver nanowire was attached to the long one, forming a y-junction. Such a network forms a simple interferometer. The 'inputs' I1 and I2 were used to excite surface plasmons. A scattering intensity was measured at the 'output' O and quantum dots were used to map the SPPs distribution along the waveguide network.

The dependence of scattering intensity at the output O on the phase shift between inputs is shown in Figure 2.22b. The green line shows the intensity at the output when only one of the inputs (either I1 or I2) is used. As can be seen, in this case the intensity at the output remains constant, as both inputs are equivalent. When both inputs I1 and I2 are in use, the interference of two surface plasmons will result in intensity fluctuation at the output O and the black line in Figure 2.22b shows the dependence of the output intensity on the phase shift between two input signals. Scattering and fluorescent images of the junction with a phase shift between inputs are presented in Figure 2.22c. With a zero phase shift (i,ii) the maximal scattering intensity is observed at the output (a bright spot in the yellow circle). If the phase difference is $\pi/2$ the scattered intensity at the output is minimal (iii,iv) as a result of destructive interference between two surface plasmons.

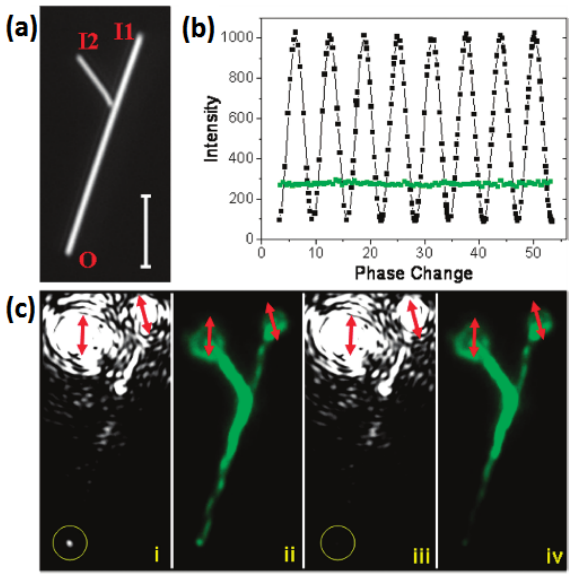

Figure 2.22: Simple plasmonic waveguide network **(a)** with two inputs I1, I2 and single output O. Plot **(b)** shows the dependence of the output scattering intensity from the phase shift between inputs (black line) or when only a single input (either I1 or I2) is used (green line). Scattering (i,iii) and QD emission (ii,iv) images of the structure with different phase shifts between inputs. Taken from [29][8].

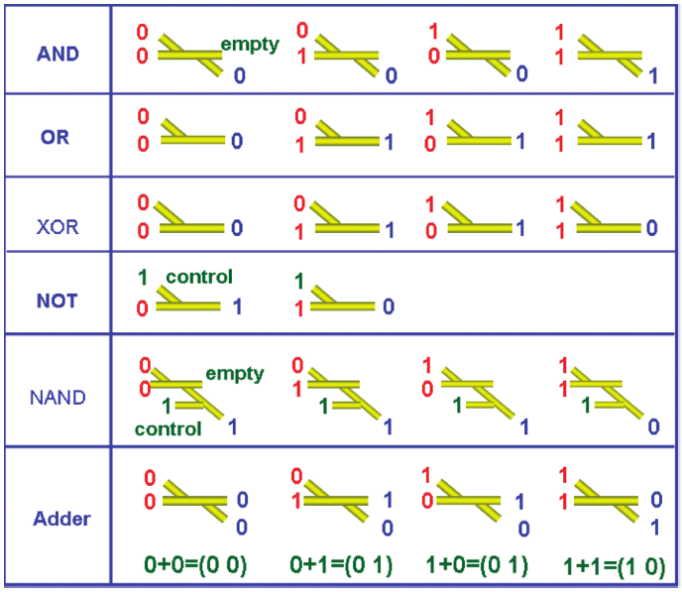

Figure 2.23: Examples of plasmonic waveguide networks capable of realising basic logic functions. Taken from [29][8].

The waveguides configurations shown implement 'OR' or 'XOR' logic operations,

[8]Reprinted with permission from Wei, Hong, Zhipeng Li, Xiaorui Tian, Zhuoxian Wang, Fengzi Cong, Ning Liu, Shunping Zhang, Peter Nordlander, Naomi J. Halas, and Hongxing Xu. "Quantum dot-based local field imaging reveals plasmon-based interferometric logic in silver nanowire networks." Nano Letters 11, no. 2 (2010): 471-475. Copyright 2017 American Chemical Society.

depending on the phase shift between inputs I1 and I2. Using various network designs it is possible to obtain all functional elements required to build complex logic circuits. Some possible implementations are shown in Figure 2.23. The control signals (green colour) are used in some network configurations and represent constant logic '0' or '1'.

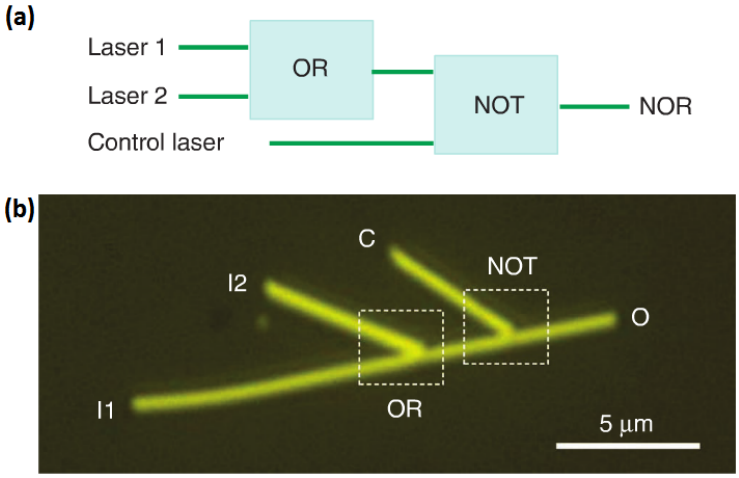

Figure 2.24: Schematic representation of cascaded logic elements **(a)** and fluorescent image of designed waveguide network **(b)**. I1 and I2, O and C are inputs, output and control signal of the circuit respectively. Taken from [117][9].

Another work [117] demonstrates an ability to cascade such logic gates. As an example, 'OR' and 'NOT' elements were connected in series, thereby, implementing a 'NOR' logic function (see Fig.2.24).

The remarkable advantage of such structures is their simplicity. All logic gates can be implemented using different numbers and lengths of interferometer arms. This approach, however, is inapplicable for complex logic circuits. The power at the output is dependent on the input phase which results in uncertainty in the implemented logic function due to the possible difference in the length of interconnects. Furthermore, the input signals are not amplified which makes fanout of the output impossible since it cannot be used as an input signal for another logic gate.

[9]Reprinted by permission from Macmillan Publishers Ltd: Nature Communications , advance online publication, 12 July 2011 — doi:10.1038/ncomms1388

2.5.2 Non-linear effects

As mentioned before, one of the main advantages of surface plasmons is their sensitivity to the properties of the interface along which they propagate. In contrast to photonic elements, even a small change in the dielectric permittivity of the surrounding dielectric leads to a substantial shift in plasmon resonance or a change in attenuation. It is possible, therefore, to design active plasmonic elements with dimensions much smaller than corresponding photonic devices. Different non-linear effects can be used to modulate the surface plasmon propagation will be discussed in this section.

Electro-optical modulation

Various research groups have demonstrated [20, 21] the possibility of electro-optical modulation of surface plasmons. One of designs utilises a Fabry-Perot resonator [20] which was embedded into a MIM waveguide (see Fig.2.25a). The operating wavelength of the resonator was designed to be $\lambda = 850$ nm.

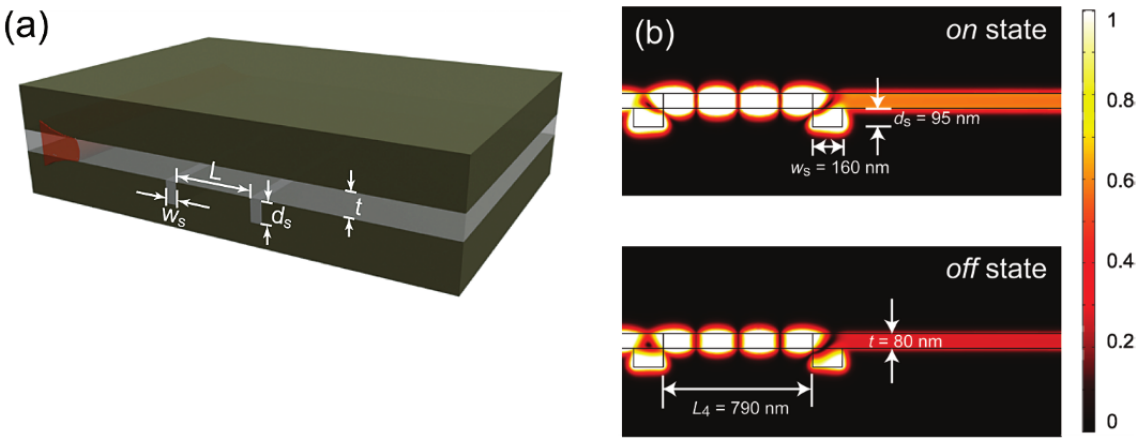

Figure 2.25: Schematic representation of MIM waveguide **(a)** and magnetic field mapping inside the resonator in 'ON' and 'OFF' states **(b)** respectively. Taken from [20][10].

Simulations showed that the modulation depth ($M = \frac{I_{ON}-I_{OFF}}{I_{ON}}$, where I_{ON} and I_{OFF} are power flows transmitted through the interferometer in 'ON' and 'OFF' states respectively) depends on both the real $\Delta n'$ and imaginary $\Delta n''$ parts of the

[10]Reprinted with permission from Cai, Wenshan, Justin S. White, and Mark L. Brongersma. "Compact, high-speed and power-efficient electrooptic plasmonic modulators." Nano Letters 9, no. 12 (2009): 4403-4411. Copyright 2017 American Chemical Society.

refractive index (see Fig.2.26). Changing the value of either of these has a different effect on the SPP propagation through the structure. Changing the real part of the refractive index (see Fig.2.26a) results in a shift in resonance frequency leading to a rapid decay of the SPP while an increase in the imaginary part (see Fig.2.26b) leads to reduction of the output power flow due to the increase in absorption inside the modulator. Thus, as can be seen from Figure 2.26 to achieve a modulation depth of 3 dB ($M = 0.5$) it is sufficient to obtain a change in either real or imaginary parts of refractive index of $\Delta n' = 0.008$ or $\Delta n'' = 0.004$ respectively.

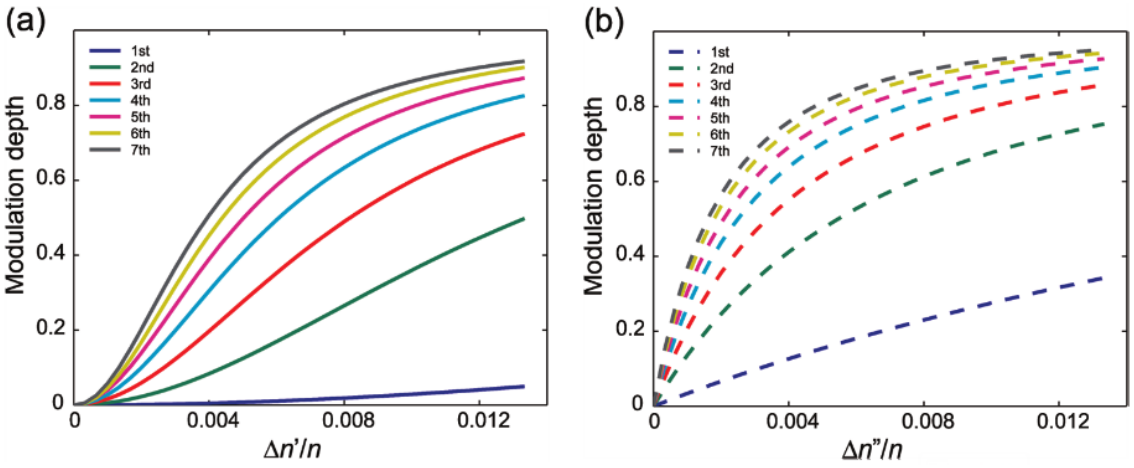

Figure 2.26: Dependence between the modulation depth and change of real **(a)** and imaginary **(b)** parts of refractive index respectively. Different lines correspond to various lengths between the modulator cavities. Taken from [20][11].

The spatial distributions of the magnetic field inside the resonator in the 'ON' and 'OFF' states are shown in Figure 2.25b. The power flow through the resonator was reduced by the factor of 2 (-3 dB). Authors propose to use the Franz-Keldysh effect - a change in optical absorption of semiconductors induced by applied electric field. Utilising this effect it is possible to achieve the necessary change $\Delta n''$ at an applied voltage of about 1 V. It was assumed that such an electro-optic modulator is capable of operating at frequencies of 100 GHz, with propagation losses of no more than 3 dB, modulation depth of 3 dB and power dissipation of 1 fJ/bit [20].

The main advantages and disadvantages of this SPP modulation approach in terms of designing of hybrid optoelectronic integrated circuits are:

\+ Compatibility with existing technology of integrated circuits

[11]Reprinted with permission from Cai, Wenshan, Justin S. White, and Mark L. Brongersma. "Compact, high-speed and power-efficient electrooptic plasmonic modulators." Nano Letters 9, no. 12 (2009): 4403-4411. Copyright 2017 American Chemical Society.

+ Large modulation depth with relatively small dimensions

+ Compactness

- Relatively high losses

These surface plasmon modulators are, therefore, of a great interest for building hybrid optoelectronic circuits.

Optical Kerr effect

The Kerr effect is a change in the refractive index of a material under the influence of an applied electric field [118]. This change is very fast [119] and is, therefore, of interest for high-speed integrated circuits. The change in refractive index can be calculated using the following expression:

$$\Delta n = \lambda K E^2, \tag{2.23}$$

where λ is a wavelength, E is an electric field and K is the Kerr constant, which depends on material. All materials exhibit this dependence, but some of them have significantly larger Kerr coefficient than others.

An all-optical modulator utilising the Kerr effect has been demonstrated in [22]. A schematic representation of this device is shown in Figure 2.27a. This device is again based on the MIM waveguide. The device has a resonator which is filled with material having a large Kerr constant and a two resonant stubs embedded into the waveguide.

This structure has two resonant frequencies at vacuum wavelengths of $\lambda_1 = 563$ nm and $\lambda_2 = 816$ nm respectively (see Fig.2.27b). The wavelength λ_1 was selected as the signal while the wavelength λ_2 was used to change the refractive index of the dielectric inside the resonator. When the refractive index is changed by $\Delta\epsilon = 0.05$ the transmission through the device at signal wavelength λ_1 increases from 0.03 to 0.5, therefore, permitting modulation. The resonant stubs are used to prevent pump light transmission through the modulator and the grooves form a bandstop filter for the wavelength λ_2 to reflects the pump light.

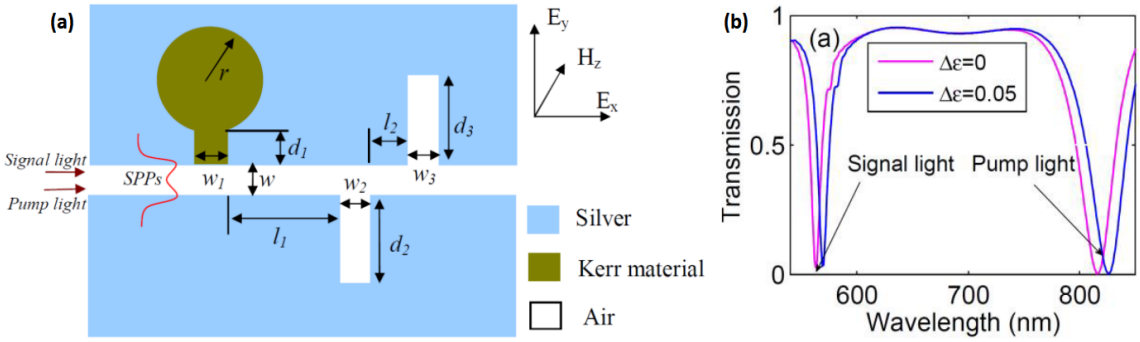

Figure 2.27: Schematic representation of an all-optical modulator **(a)** and transmission spectra through it **(b)**. Taken from [22].

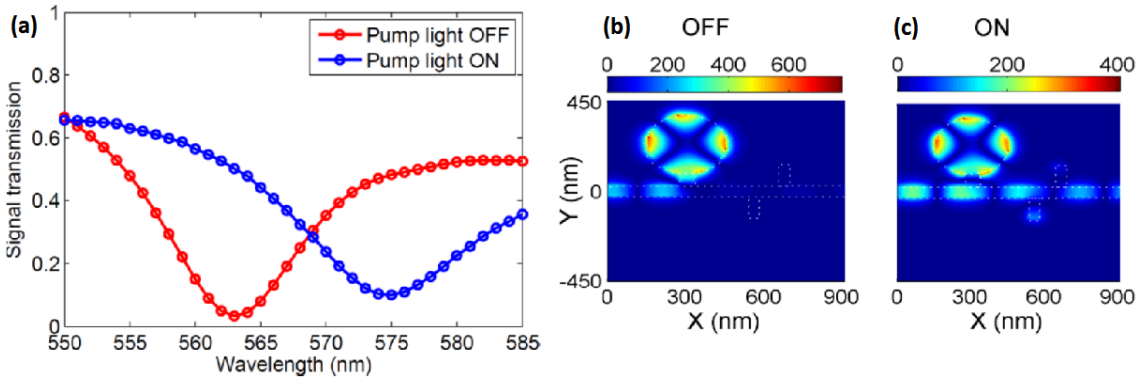

Figure 2.28: Signal transmission spectra through the modulator **(a)** in 'ON' and 'OFF' states. Distribution of magnetic field **(b,c)** inside the device. Taken from [22].

The spectral dependence of the signal transmission with the pump light 'ON' and 'OFF' is shown in Figure 2.28a. As can be seen, the presence of the pump causes the red shift of the transmission spectra which results in 50% reduction of transmission at 563 nm. The magnetic field distribution (at 563 nm wavelength) with the modulator in the 'ON' and 'OFF' states are shown in Figure 2.28b,c. Simulations [22] demonstrated that such a device will have a response time of around 100 fs for an intensity of the pump light of 650 MW/cm^2.

The main advantages and disadvantages of this SPP modulation approach in terms of designing of hybrid optoelectronic integrated circuits are presented below:

\+ Fast response

\+ Compactness

\- Weak non-linear interaction

- Requirement of high intensity of pump light
- Requirement of different wavelengths for signal and pump light
- Unable to cascade elements

Since the Kerr effect is relatively weak, a high intensity of the pump light is essential to achieve sufficient modulation depth which, in turn, leads to high heat dissipation that limits the utilisation of this approach in high-level integration integrated circuits.

Temperature modulation

Some materials exhibit a strong dependence of the refractive index on temperature. One prominent representative of such materials is vanadium dioxide (VO_2). At room temperature VO_2 forms monoclinic crystal lattice, but at temperature of $t > 68°C$ a phase transition occurs and the crystal structure switches to tetragonal. This phase transition is accompanied by significant change in the dielectric permittivity: for example the permittivity values at a wavelength of $\lambda = 1550$ nm for the monoclinic and tetragonal crystal structures are ϵ_1=9.7+2.9i and ϵ_2=-14.1+30.5i respectively [120].

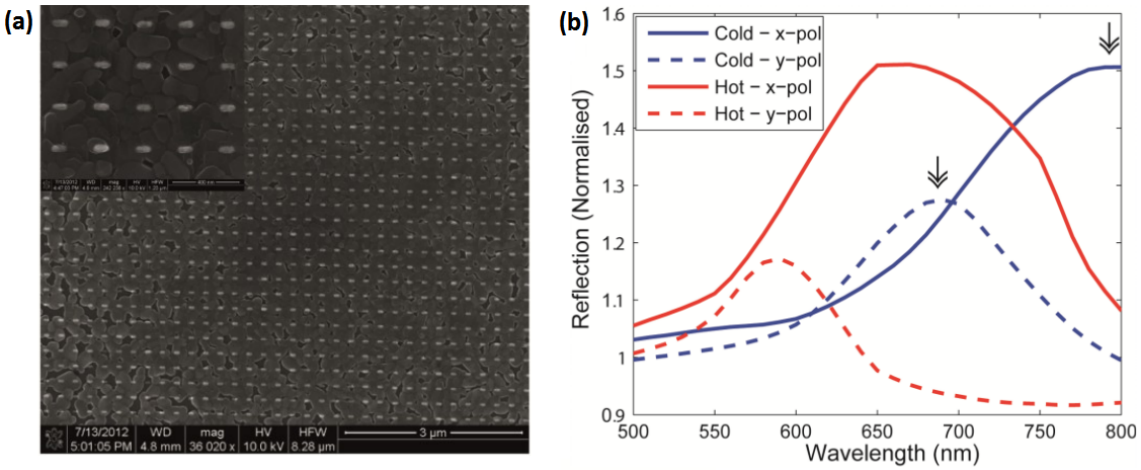

Figure 2.29: SEM image of the nanoantenna array on VO_2 substrate **(a)** and normalised reflection spectra of the metasurface in cold and hot states **(b)**. Taken from [121].

This property of vanadium dioxide can be used to create tunable plasmonic elements. An ability to adjust the resonant frequency of plasmonic metasurfaces was

demonstrated in [121]. An array of nanoantennas was fabricated on VO_2 substrate and normalised reflection spectra of the nanoantenna array at different temperatures are shown in Figures 2.29a,b respectively. As can be seen, the phase transition of vanadium dioxide blue-shifts the resonance of this metasurface.

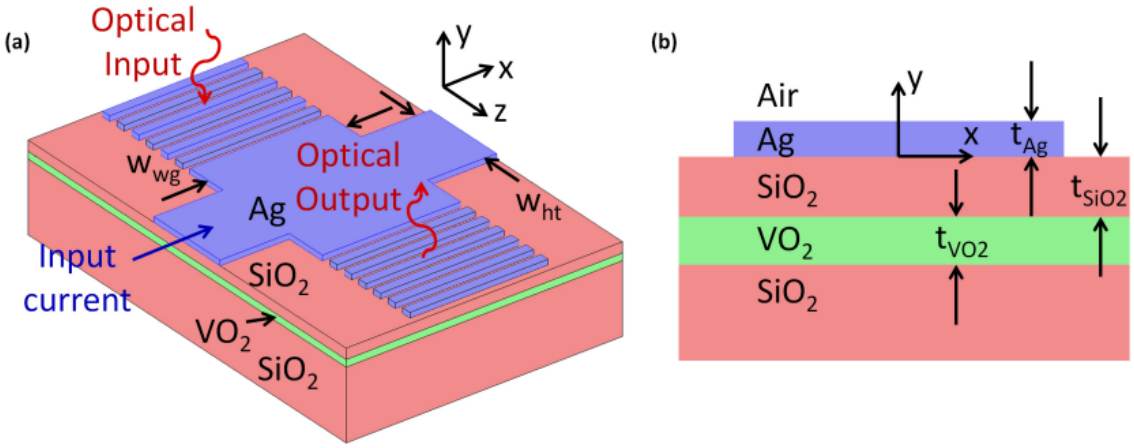

Figure 2.30: Schematic representation of modulator based on thermo-optical phenomenon **(a)** and its cross section **(b)**. Taken from [122].

The idea of using vanadium dioxide for plasmonic modulators has been proposed in [122]. A buried layer of VO_2 (see Fig.2.30b) is used to control the propagation of surface plasmons. Gratings are used to couple and decouple surface plasmons (see Fig.2.30a). In the 'OFF' state the plasmon propagates along the waveguide with low loss. When electric current is turned on, due to the local heating of vanadium dioxide layer its crystal structure changes, leading to a change in waveguide properties. The surface plasmon propagating along the waveguide in the 'ON' state will experience a strong attenuation.

The main advantages and disadvantages of this SPP modulation approach in terms of designing of hybrid optoelectronic integrated circuits are presented below:

+ Simplicity

- High power consumption

- High heat dissipation

- Low Speed (long relaxation time)

Although the transition time from cold to hot states can occur extremely fast (at order of 100 fs), the relaxation time can vary from 3 ns up to 1 ms depending on

various conditions [120]. Another issue is associated with the high heat dissipation of thermo-optic modulators making their integration in digital devices impractical.

2.5.3 Summary

Different approaches based on linear and non-linear phenomena has been discussed in this section. It was demonstrated that all these methods are capable of building functional plasmonic modulators. Some of the analysed structures can be successfully used as an interface between the electronic circuits and telecommunication technology. Among the modulation techniques discussed in this section, the absorption modulators based on the change of imaginary part of the refractive index phenomenon are of particular interest for building logic gates with plasmonic interconnects, as only they exhibit low power consumption and the small dimensions essential for VLSI technology.

2.6 Conclusion

In this chapter the theoretical background describing surface plasmon phenomena is presented as well as a comprehensive analysis of existing methods of excitation, guiding, detection and modulation. The potential of each technique to build a compact logic gate with plasmonic interconnects was evaluated. The analysis showed that excitation of surface plasmons using grating coupling in conjunction with stripe waveguides shows the best scalability and compatibility with existing fabrication methods. The optoelectronic conversion of SPP energy into voltage or current (utilisation of photodetectors) combines the advantages of well-developed CMOS technology and potential for plasmonic interconnects and is, therefore, chosen to be the main detection method investigated in this work. Finally, among all the modulation techniques presented in this chapter, absorption modulators better meet the miniaturisation requirement imposed by VLSI technology and, thus, are more likely to play a vital role in future hybrid optoelectronic circuits.

Modelling and fabrication techniques required to design and manufacture logic gates with plasmonic interconnects and photodetectors will be discussed in the next chapter.

3. Modelling and fabrication techniques

Fabrication of active electronic devices is a comprehensive multistage process involving the use of multiple tools and techniques. Because of the required nanoscale dimensions the incorporation of plasmonic elements into these devices makes the design and fabrication processes even more challenging. High precision simulation techniques and tools are necessary to successfully design and build the active optoelectronic devices presented in this thesis.

This chapter will outline the numerical methods utilised to simulate plasmonic structures as well as semiconductor devices. The discussion of these methods will then be followed by a description of the various fabrication tools and techniques used to undertake the research presented here. Finally, different characterisation methods used to conduct experiments and collect data will be described.

3.1 Numerical simulations

Numerical analysis is a method of solving the problems of mathematical analysis using numerical approximation. It is often utilised to solve complex problems where analytical approaches are inefficient or do not exist. This includes but not limited to: complex geometries, non-linear materials and electromagnetic potential of sophisticated systems. It permits finding of an approximate solution with a given accuracy [123]. The photonic devices investigated here have complex geometries and are composed of materials with non trivial optical properties. Hence, numerical methods are required to understand and predict their performance and design devices.

Numerical methods provide great opportunities to simulate the interaction of electromagnetic waves with metallic structures - a key aspect of surface plasmon phenomenon. This approach is widely used to simulate the response of plasmonic metasurfaces at different wavelengths [39, 37] and in polarisation states [28] as well as for plasmonic waveguide mode analysis [19]. Numerical methods also enable the simulation of non-linear plasmonic responses such as second harmonic generation [124].

The choice of numerical method depends on a particular problem, its dimension and complexity. The field of plasmonics is considered highly demanding in terms of computational time. The most popular numerical methods utilised to solve plasmonic-related problems are Finite Element Method (FEM) and Finite Difference Time-Domain (FDTD) [125]. The FDTD method covers a wide frequency range in a single simulation run and permits the simulation of non-linear material properties such as second harmonic generation [126, 127]. Nevertheless, this method is relatively inefficient for complex geometry simulations as it requires a very fine spatial discretisation in order resolve electromagnetic wavelengths in small geometrical features which results in undesirably long solution times. On the other hand, FEM permits a local increase in accuracy in certain areas. This is a highly desirable property when precision varies over the computational domain and permits meeting these accuracy requirements without a significant increase of computational time or required memory [125]. This method, therefore, is more applicable for simulation of complex geometries at a single wavelength when the optical properties of materials at this wavelength are known (for example the dielectric permittivity of metals [89]). FEM was chosen as the main simulation method for this work.

3.1.1 Finite element method

The finite element method (FEM) is computational technique used to obtain approximate solutions to a variety of boundary value problems. Simulation programs utilising this method can be used to model a wide range of complex problems including the interaction of light with plasmonic nanostructures, thermal flows in fluid cells and charge transport in solid state semiconductors. This method is used to divide the problem into simplified parts and solve partial differential equations (PDEs) as a set of algebraic expressions. These expressions can be solved in matrix form and, therefore, require less computational time.

The main method used to divide the boundary value problem into set of finite elements is called a discretisation strategy [128]. Each finite element, therefore, represents a small spatial domain where an approximation has been made. An illustration of a FEM discritisation can be made using a one-dimensional problem (the general problem can be solved by extrapolation of current method). Consider the one-dimensional (1D) differential equation:

$$\begin{cases} \frac{d^2}{dx^2}u(x) = f(x) & , x \in (0,1) \\ u(x)|_{x=0} = u(x)|_{x=1} = 0, \end{cases} \tag{3.1}$$

where $f(x)$ is given and $u(x)$ is an unknown functions. The first step involves reforming the original boundary value problem into its variational (weak) form. Then, if $u(x)$ is a solution for (Eq.3.1) then for any smooth function $v(x)$ that satisfies conditions $v(x)|_{x=0} = v(x)|_{x=1} = 0$ is true that:

$$\int_0^1 f(x)v(x)dx = \int_0^1 \frac{d^2}{dx^2}u(x)v(x)dx. \tag{3.2}$$

Using partial integration the expression (Eq.3.2) can be converted into:

$$\int_0^1 f(x)v(x)dx = -\int_0^1 \frac{d}{dx}u(x)\frac{d}{dx}v(x)dx. \tag{3.3}$$

It is then possible to discretise functions $u(x)$ and $f(x)$ into n mesh nodes. The desired functions can be represented as a sum of basis functions $v_i(x)$:

$$u(x) = \sum_{i=1}^{n} u_i v_i(x) \tag{3.4a}$$

$$f(x) = \sum_{i=1}^{n} f_i v_i(x). \tag{3.4b}$$

The equation (Eq.3.3) can then be rewritten:

$$\sum_{i=1}^{n} f_i \int_0^1 v_i v_j dx = -\sum_{i=1}^{n} u_i \int_0^1 \frac{d}{dx} v_j \frac{d}{dx} v_i dx \quad , j = 1, ..., n. \tag{3.5}$$

Denoting by $\vec{u}$ and $\vec{f}$ the column vectors $(u_1, ..., u_n)^t$ and $(f_1, ..., f_n)^t$ and defining $M = (M_{ij}) = \int_0^1 v_i v_j dx$ and $L = (L_{ij}) = \int_0^1 \frac{d}{dx} v_j \frac{d}{dx} v_i dx$, the expression (Eq.3.5) can be rewritten in matrix form:

$$M\vec{f} = -L\vec{u}. \tag{3.6}$$

Therefore, the problem has been reduced from second order partial differential equation to the algebraic problem that can be solved by inversion of matrix L [128].

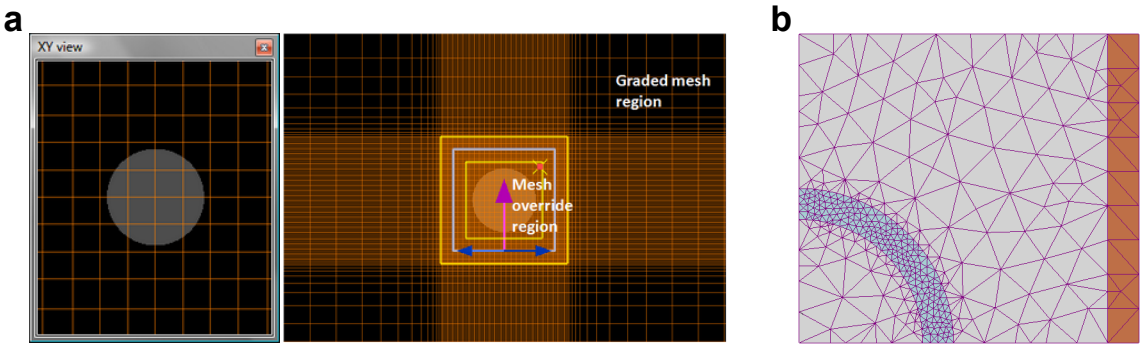

Figure 3.1: Locally modified mesh in FDTD **(a)** and FEM **(b)** models. FEM model is less memory-demanding as the mesh is modified only within a certain region. Taken from [129].

The fundamental element of the FEM is a mesh which is used to divide the region of interest into small parts. The size of the mesh defines the spatial precision of the simulation - the finer the mesh the better is the accuracy. An insufficient mesh size can lead to incorrect results (see Fig.3.2). On the other hand a fine mesh leads to a substantial increase in computational time and memory required. Unlike the finite-difference time-domain (FDTD) method the FEM provides an ability to locally modify the mesh size within a certain region (see Fig.3.1a,b) in the case of a complex geometry containing objects with different scale sizes. Therefore, the simulation accuracy may be increased in particular areas (for example in dense materials) while the mesh of the rest of the model remains reasonably dense. This enables a high simulation accuracy in a reasonable computational time.

COMSOL Multiphysics is a simulation software package implementing the FEM

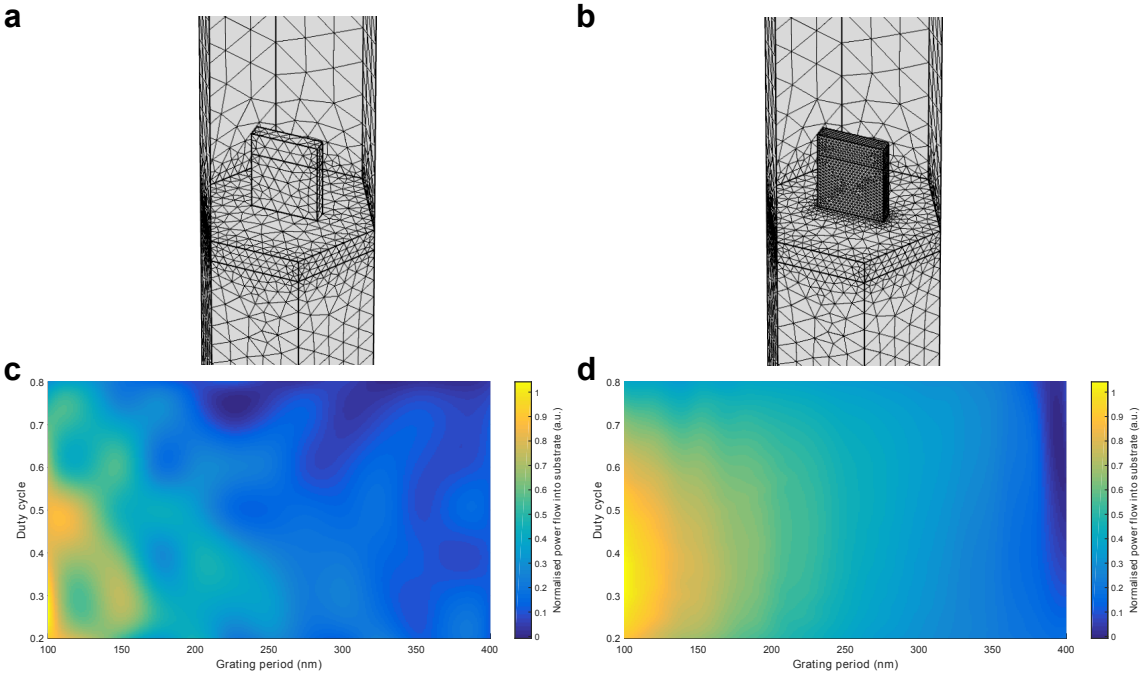

Figure 3.2: Simulation models of the plasmonic camera pixel (see Section 8.2 for more details). Figures **(a)** and **(b)** show the models with coarse and fine meshes respectively. The corresponding simulation results **(c)** and **(d)** are significantly different at certain points. The insufficient meshing can, therefore, lead to not only inaccurate but also incorrect results.

to solve various scientific and engineering problems. It provides a number of modules specialised for solving particular problems such as RF module, Wave Optics module, Semiconductor module and others. Throughout this project the COMSOL Multiphysics RF Module was used to simulate the interaction of light with nanoscale objects. The geometry is defined using a user-friendly graphical interface. The RF module solves the inhomogeneous Helmholtz equation:

$$\nabla \times (\mu_r^{-1} \nabla \times \vec{E}) - k_0^2 \epsilon_r \vec{E} = 0, \tag{3.7}$$

where ϵ_r and μ_r^{-1} are the relative permittivity and permeability tensors respectively, k_0 is the free space wave number and $\vec{E}$ is the electric field to be found. The FEM, therefore, requires the input of the permittivity and permeability of every material used in the simulation at every point in the region of interest. The optical constants of metals, such as Ag, Al and Au were taken from [89]. Although these values were obtained for bulk materials and, therefore, may deviate from the actual values for nanostructures, they permit a sufficiently accurate approximation for tasks concerned in this work.

Various boundary conditions can be used to properly define the model. Periodic boundary conditions (PBCs) are used on the lateral boundaries to simulate the response of plasmonic metasurfaces - infinitely wide arrays of nanoantenna. Here, there is a specific relationship between the fields on opposite boundaries. At normal incidence, for example, the fields on these boundaries must be equal. Scattering boundary conditions (SBCs) are used to simulate individual structures such as plasmonic waveguides or single nanoantenna. The SBCs are transparent for normal incident electromagnetic waves. For non-normal incident waves, however, some reflections may take place. Although for most properly designed models this effect is negligible, for higher accuracy the SBCs must be used together with perfectly matched layers (PMLs) to decrease reflections from model's boundaries.

Utilisation of numerical approach for solving of complex problems requires significant computational power. The demand grows rapidly as the accuracy of simulation increases. The simulations throughout this work were conducted on a computational cluster with 32 2.5 GHz Intel Xenon®E5-2650 CPUs and 256 GB of RAM.

3.2 Fabrication

3.2.1 Electron-beam lithography

Electron-beam lithography (EBL) is a method for defining predetermined patterns on an electron-sensitive film (a resist) coated substrate using a focused beam of electrons [130, 131]. A simplified schematic diagram of the tool is presented in Figure 3.3. This technique offers a much higher spatial resolution than conventional optical UV lithography [132]. The EBL resolution is not diffraction limited and is, therefore, suitable for creating structures with dimensions of several nanometers. As a direct write point-by-point method, however, exposure times can be considerable. The electron beam scans the exposing area in series while in a mask-based lithography (for example in conventional UV lithography) the exposition of the whole pattern takes place simultaneously. As a result, the EBL is best-suite to prototyping.

A Vistec EBPG 5000+ EBL tool at the Melbourne Centre for Nanofabrication (MCN) was used to expose the nanostructure patterns presented in this thesis. The tool operates at a 100 kV accelerating potential and permits a minimum spot size

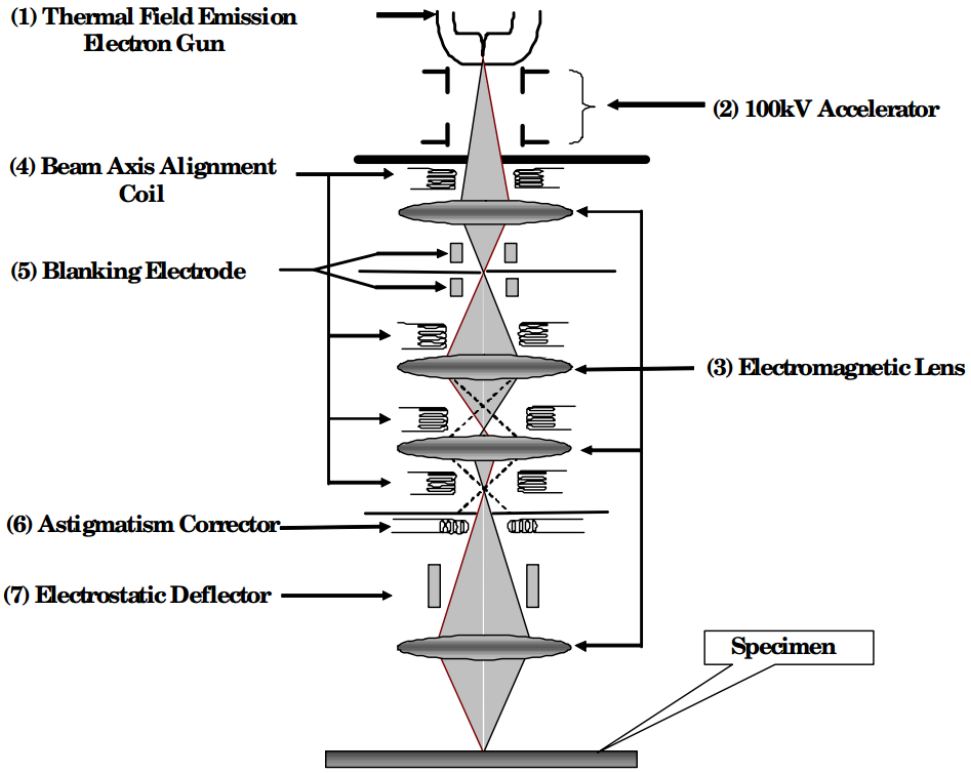

Figure 3.3: A schematic diagram of the electron-beam lithography tool. Taken from [131][1].

of 2 nm. The permitted beam current ranges from 50 pA up to 100 nA. A variety of apertures (from 200 µm to 400 µm) permits a balance between the beam spot size and the current used. The system is also equipped with a scattered electron detector and, therefore, provides the capacity to obtain SEM images of the sample before exposure which is essential in the multistep lithography used in the research undertaken here. The comprehensive control system permits automatic astigmatism and sample tilt correction.

The Beamer© software is used to convert the patterns created in GDSII file type compatible software (KLayout 0.24.8 was used) into the GPF file format recognised by the EBL tool. The software also provides tools for addressing pattern overlap, beam step size adjustment and controlling the distribution of main and sub-fields. In addition to this, the program incorporates algorithms which can noticeably decrease the exposure time by optimising the pattern writing order in the case of large arrays. It also provides an ability to perform a proximity error correction (PEC) of the patterns - method which permits taking into account the charge accumulation and optimise the exposure dose. This is extremely important for nanoantenna arrays as

well as for grating structures (see Fig.3.4).

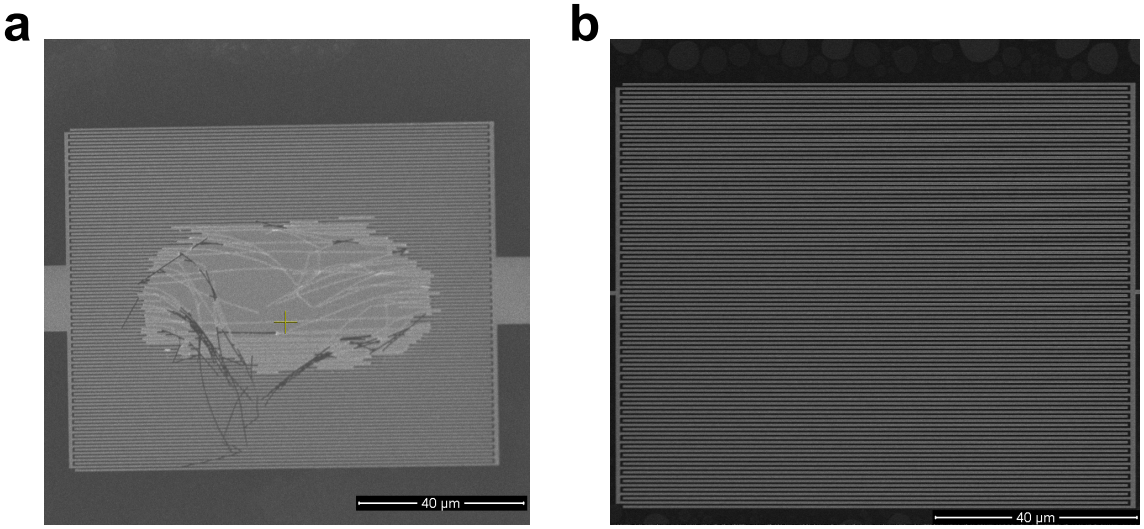

Figure 3.4: The SEM images of the grating structures exposed with the same base dose of 900 µC/cm^2 without **(a)** and with **(b)** PEC correction. The middle of the first structure is overexposed due to the charge accumulation effect.

Depending on the process used, both negative and positive tone resists may be used for EBL exposure. The positive resists are usually used for lift-off process. The prime positive resist used in this research is an A-type polymethyl methacrylate (PMMA) dissolved in anisole. A resolution down to 7 nm can be achieved with high voltage EBL exposure [133]. Another positive resist used in this project is a ZEP520A (α-Methylstyrene) [134]. It provides a higher resolution compared with PMMA and is more resistive to reactive ion etching. Despite its benefits, ZEP resist is much more expensive than the PMMA and, therefore, utilised only when high precision is required.

A typical lithography fabrication process is shown in Figure 3.5. The silicon wafer used is, firstly, cleaned with acetone and isopropanol (IPA) and then spin-coated with a layer of resist. The thickness of the resist is dependent on the desired structure thickness and is usually taken to be approximately 4 times thicker. The thickness is controlled by the rotation speed which can be varied from 100 to 5000 rpm. After the spin-coating process the resist is baked on a hot plate to evaporate the solvent. A typical fabrication process requires baking at 180°C for 5 min. For a high-resolution process or a process involving wet etching the spin-coated sample

[1]2010 Wu, Cen Shawn, ChiiDong Chen, and Yoshiyuki Makiuchi. Originally published in Wu, C. S., Chen, C., & Makiuchi, Y. (2010). High-energy electron beam lithography for nanoscale fabrication. INTECH Open Access Publisher under CC BY 3.0 license. Available from: DOI: 10.5772/8179

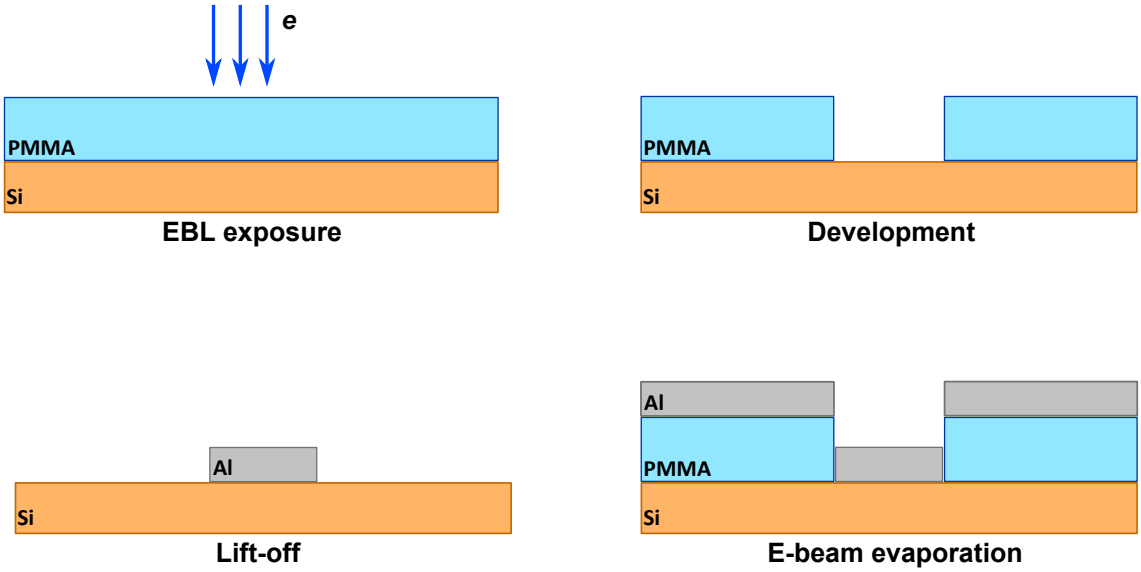

Figure 3.5: A common fabrication process involving the EBL lithography.

is, firstly, baked for 15 min at 100°C followed by another 10 min at 170°C. This improves solvent evaporation and prevents the sample from outgassing in vacuum. The exposed resist is then developed in a mixture of methyl isobutyl ketone (MIBK) and IPA in the ratio of 1:3. The development takes 1 min and is followed by rinsing the sample in fresh IPA. Metal is then deposited using the e-beam evaporation technique which will be discussed further. The final step is lift-off which is performed in 70°C acetone with moderate agitation. Depending on the metal and its thickness the lift off process can take a long time, but can be accelerated by placing the beaker containing the sample into an ultrasonic bath. Note that this step is incompatible with poorly adhering materials as it can damage the structures. The sample is then rinsed with IPA and deionised water and dried using a flow of nitrogen.

Multiple-step lithography

The fabrication of complex devices usually involves multiple lithography steps. This, in turn, requires a mechanism for realigning the coordinate systems between exposures. Similarly to optical lithography alignment markers are utilised for this purpose. The Vistec EBPG 5000+ EBL tool permits alignment to within ±10 nm which is well beyond the accuracy usually offered by optical lithography tools.

A typical alignment pattern consists of 3 metal squares with a side length of 20 µm (see Fig.3.6). A good contrast in the SEM image between the markers and the

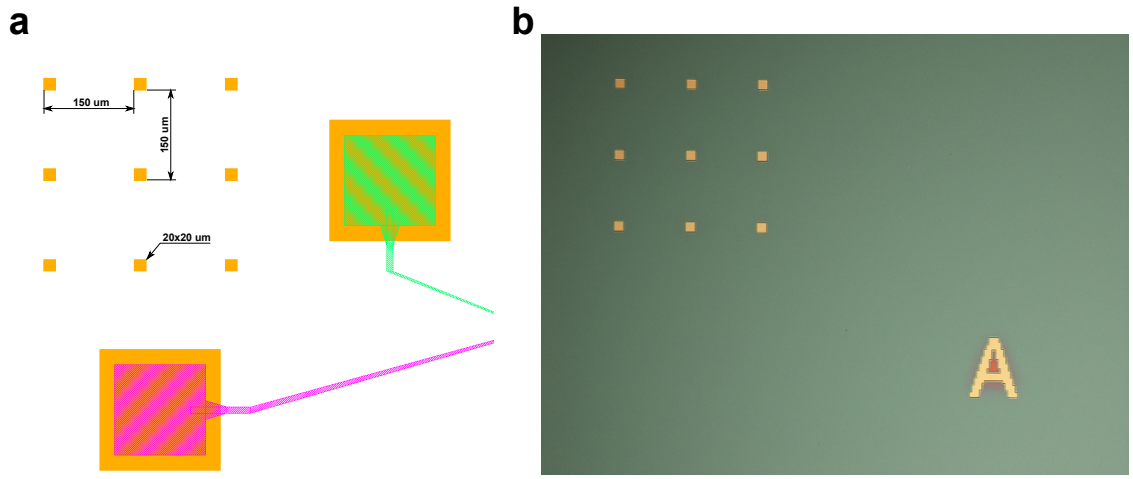

Figure 3.6: The marker pattern for multilayer exposure design in Klayout **(a)** and implemented on the sample **(b)**.

substrate is necessary for precise alignment. Therefore, the metal and its thickness will depend on the substrate material. In this project a 65 - 85 nm thick gold film is used for markers. A minimum distance of 150 µm between the markers is required to avoid misrecognition of neighbouring markers. The EBL tool performs a search algorithm to find the centre of the marker and uses it to align the coordinate system between exposures. The algorithm requires an approximate value of the absolute coordinates of the markers as a starting point for the search and these coordinates can be found using an optical microscope.

3.2.2 Electron-beam evaporation

The deposition of thin films of metals and dielectrics is required for all the devices investigated in this project. Electron beam physical vapor deposition or e-beam evaporation is a method of thin film deposition using an electron beam. When the beam hits the anode with a certain material in it (see Fig. 3.7) it causes its atoms to transform into the gas phase. These atoms then precipitate onto the target which is located above the anode. Films with thicknesses ranging from 0.5 nm and up to several micrometers can be deposited using this method.

The Intlvac NanoChrome II e-beam evaporator was used in this project to deposit thin films. The samples were placed above the crucible containing the evaporation material and the tool chamber is then pumped to a pressure of 7x10^{-6} Torr. The Melbourne Center for Nanofabrication provides a set of predefined evaporation pro-

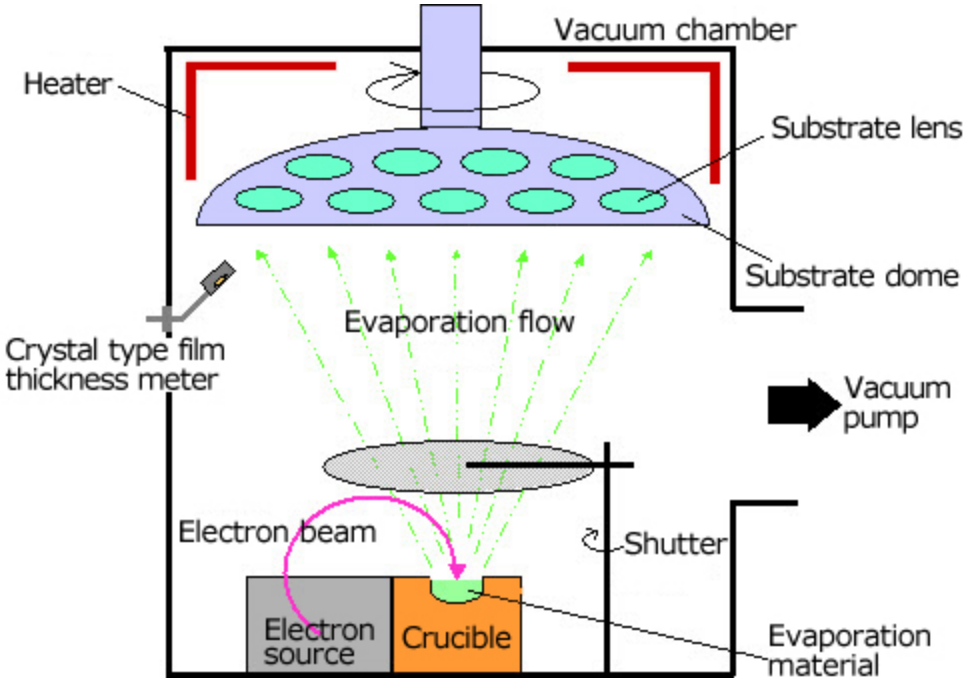

Figure 3.7: Schematic diagram of the electron-beam evaporator. Taken from [135].

files for various materials. The evaporation rate can be set by user and usually varies from 0.2 to 1.5 Å/s depending on the material. Is was empirically discovered that compound materials such as SiO_2 or ITO should be deposited at a low evaporation rate (0.2-0.5 Å/s) while metals can be evaporated at higher rates (0.6-1 Å/s). This produces good quality films with low roughness. After the evaporation the sample is allowed to cool for 5-10 min and the chamber is then vented to atmospheric pressure.

3.2.3 Reactive ion etching

Reactive ion etching (RIE) is a dry etching method that utilises a plasma (see Fig. 3.8) to remove material from certain areas of the sample. It permits a higher degree of anisotropy compared to wet etching techniques and, therefore, preferable for fabrication on the nano-scale. An Oxford Instruments PLASMALAB100 ICP380 tool was used throughout the project to etch silicon.

A combination of Ar and Cl_2 gases with flow speeds of 5 and 30 sccm, respectively, were used to etch the samples. The etching was performed at a pressure of 5 mTorr. The depth of the etching depends on time and usually takes from 10 s to 1 min. PMMA cannot be used as an etch mask, since the etch rate of the silicon should be higher than the etch rate of the mask. Therefore, gold and ZEP520A resist were

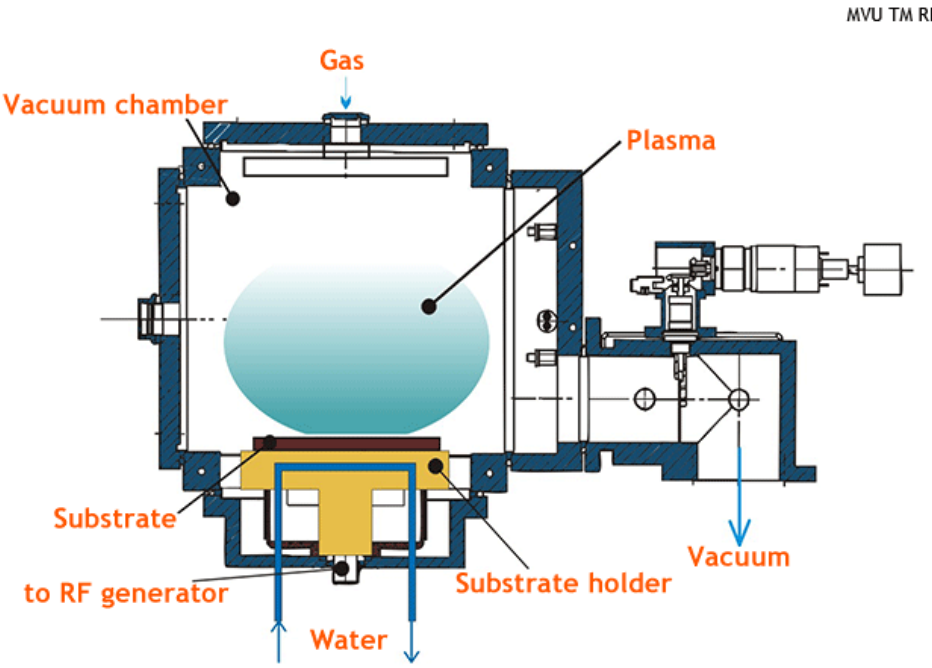

Figure 3.8: Schematic diagram of the reactive ion etching tool. Taken from [136].

used to pattern the wafer. The mask residues must be removed after the etching step prior to the next fabrication step.

3.2.4 Hydrofluoric acid wet etching

A native oxide layer always presents on the surface of silicon wafers. To form a high quality Schottky barrier this needs to be removed prior to metal deposition. This is usually performed using hydrofluoric acid (HF acid) which is very selective and the silicon etch rate for this chemical is negligible. This provides assurance that the semiconductor structures will not be affected during the etching step in contrast to RIE.

The etch rate of SiO_2 greatly depends on the solution temperature and the HF concentration. In this project HF acid concentrations from 1% to 4% were used giving etch rates from 5 to 25 nm/min at 24°C respectively. The samples were subsequently thoroughly rinsed with deionised water to remove any HF residue which may be left after etching.

3.2.5 Annealing and thermal oxide growth

A HiTech Furnace was used to thermally grow oxide films (SiO_2) on silicon wafers. The furnace can be used for both dry (up to 300 nm) and wet (from 300 nm and above) oxidations and during the process the furnace chamber heats up to 1100°C. The oxidation time is proportional to the film thickness and usually takes 2.5-4 hours. After oxidation the film thickness is confirmed using a Bruker Contour GT-I optical profilometer. The same furnace was used to anneal ITO films for 10 min at 450°C.

3.3 Characterisation

The devices were characterised during and after the fabrication to confirm their geometry and their optical and electronic properties. Various electrical and optical characterisation methods were used to perform the task.

3.3.1 Scanning electron microscopy

Scanning electron microscopy (SEM) is a technique which obtains images of the fabricated structures with dimensions well below the diffraction limit of optical microscopes [132]. An SEM produces image of the sample by scanning it with a focused beam of electrons. Since the electron wavelength is much smaller than that of visible light a resolution down to 0.4 nm [137] can be achieved. SEM microscopes can operate in various modes (backscattered electrons, secondary emitted electrons and etc.) depending on the type of information which is required from the sample. The most commonly used mode is secondary electron detection. In this mode the microscope counts the number of electrons emitted by the excited atoms and creates an image of the topography (see Fig.3.9) of the inspected sample.

A FEI NovaNanoSEM 430 tool was used throughout the project to inspect the samples after certain fabrication steps to confirm if they were successful. The samples were scanned in a deep vacuum using 3-5 kV accelerating voltages and 56-360 pA currents. The tool permits tilting the sample from 0° to 40° and arbitrary rotation to inspect the height of the fabricated structures. Higher currents should be

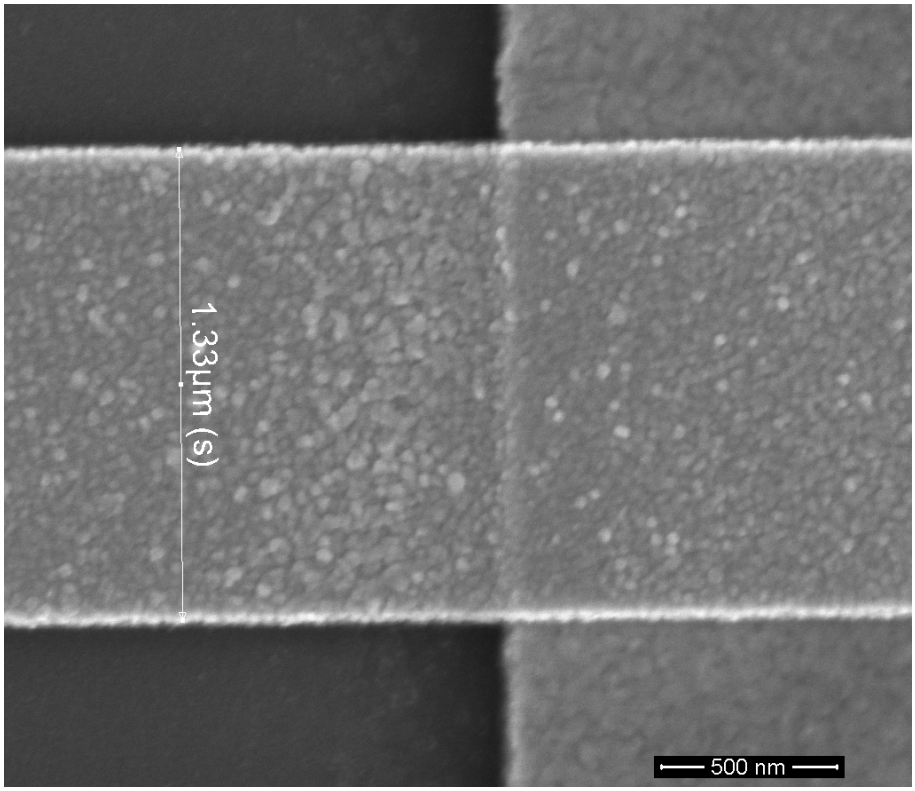

Figure 3.9: SEM image of the gold stripe. The resolution allows to see the grains on the gold surface.

used with care since they can damage the structures.

3.3.2 Electrical characterisation

The characteristics of Schottky photodetectors depend significantly on the fabrication process used. The contamination of the surface or the presence of a native oxide layer will affect their characteristics. In addition, the prototyping of devices involves the utilisation of non-optimised fabrication procedures which, in turn, results in the characteristic fluctuations and low yield. Therefore, each photodetector needs to be fully characterised prior to obtaining optical measurements so the results can be normalised. Samples were glued into a ceramic LCC20 package and bonded using a Kulicke & Soffa 4522D Wedge bonder with aluminium wire.

Bonded samples were characterised electrically to investigate the properties of the metal-semiconductor contacts. A Keithley 487 source meter was used obtain the current-voltage (IV) characteristics of each photodetector. The tool was software-controlled to perform a voltage sweep from -5 V to 5 V or from -1 V to 1 V for

Al-Si and Ti-Si Schottky barriers respectively. The current through the sample was measured using the same instrument and recorded on computer. A typical IV curve should show an MSM-like behaviour (see Fig.8.7) with minor deviations. It was found that Ti-Si Schottky detectors exhibit high dark currents and the height of the barriers is lower than Al-Si detectors. This is discussed further in Chapter 5;

3.3.3 Near-field scanning optical microscopy

Near-field scanning optical microscopy (NSOM) is an optical method that can be used to observe nanostructures with dimensions below the diffraction limit [138] at high resolution. This technique probes the evanescent field (see Fig.3.10) and potentially permits mapping of the electric field amplitude along the investigated structures. The distance between a sample and NSOM tip is usually of order of several nanometers. This distance is controlled by an active feedback mechanism similar to such in atomic force microscopes (AFM) which ensures that this distance remains constant. Near-field microscopy is a useful technique for the investigation of propagating plasmonic modes along waveguide networks.

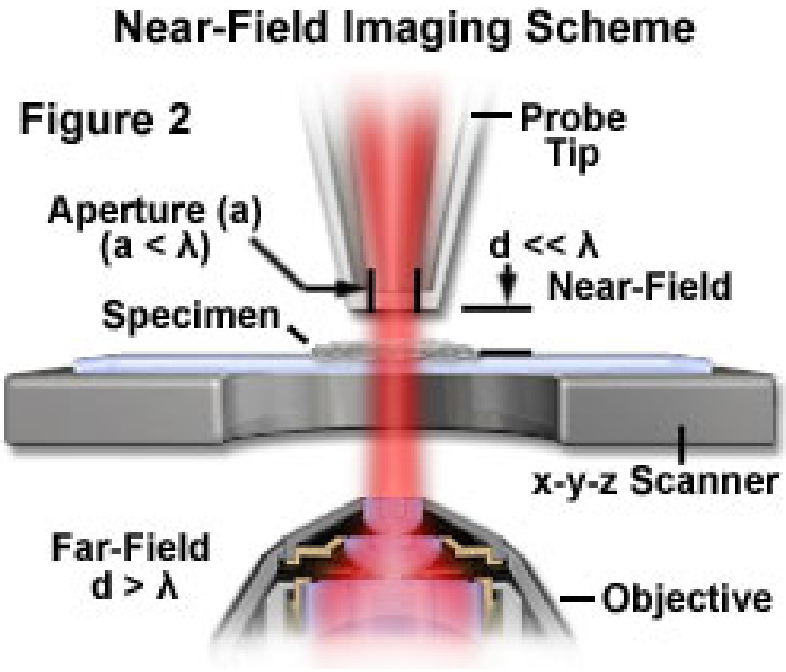

Figure 3.10: Schematic representation of an NSOM system operating in collection mode. Taken from [139].

NSOM is capable of operating in several modes. In so-called reflection mode, the NSOM tip is used to locally illuminate the sample and a microscope objective

is used to collect the reflected light (see Fig.3.11a). Transmission mode is used for transparent samples. Similarly to the reflection mode, the tip is used to illuminate the sample, but in this case microscope objective is used to collect the light transmitted through the sample (see Fig.3.11b). The NSOM tip can also be used in collection mode (see Fig.3.11c) when the sample is illuminated externally and the tip collects the photons. This mode of operation has been used to map the surface plasmon propagation along waveguides [140].

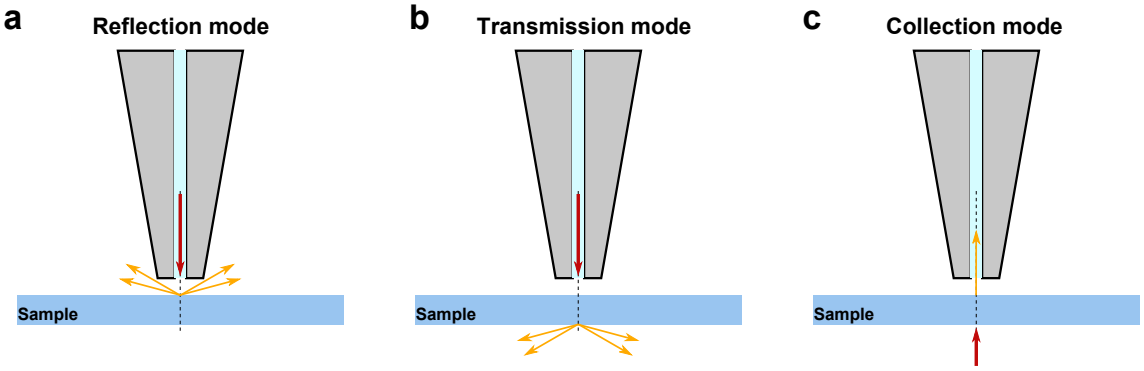

Figure 3.11: Schematic representation of NSOM operating regimes: **(a)** reflection mode, **(b)** transmission mode, **(c)** collection mode.

Plasmonic waveguides fabricated as part of this project were imaged using a Nanonics Multiview 2000 NSOM system. A 1064 nm laser was used to excite surface plasmons and an Au-covered NSOM probe (in collection mode) with an aperture diameter of 500 nm and resonance frequency of 32.4 kHZ was used to map the propagating plasmons. The system also provides the capacity to simultaneously collect AFM images of the scanned samples by collecting data from the distance regulation mechanism.

3.3.4 Scanning photocurrent microscopy

Scanning photocurrent microscopy is an experimental technique that has the ability to extract spatially resolved information about semiconductor properties [141, 142]. A highly focused laser beam is used to locally excite the semiconductor in a non-equilibrium state and the spatial position of the beam is correlated with the photocurrent collected at the terminals. The direction of the photocurrent, its amplitude and transient response (if a pulsed optical excitation is used) provide rich information such as the type of semiconductor barrier or the mean free path of the charge carriers. In addition to these, the photocurrent map provides an information about

the performance of different parts of a device that may be hard to extract from the normal device operation.

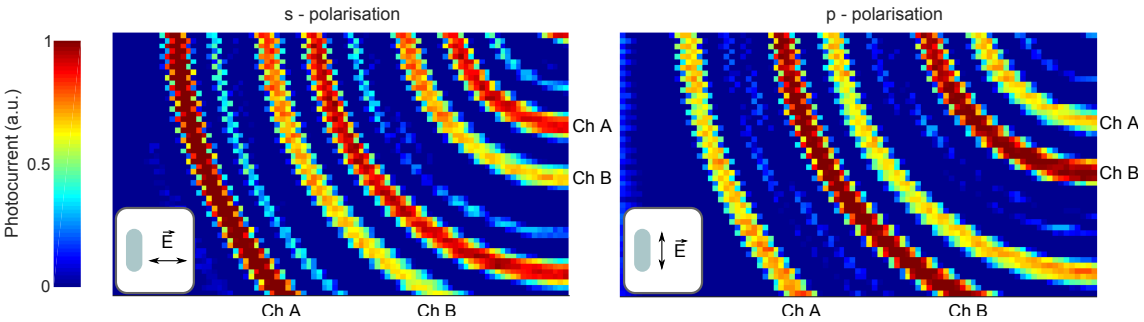

Figure 3.12: Normalised photocurrent maps of the differential photodetector (see Section 8.1.4 for details).

In this project a scanning photocurrent microscope was used to analyse the properties of fabricated Schottky photodetectors. For SPCM measurements a Thorlabs S1FC635 fiber-coupled diode laser and Nikon CFI Plan Fluor x50 long working distance microscope objective were used to obtain a spot size of 1 µm. The spatial resolution in both the x and y directions was of the order of 200 nm. A Keithley 487 source meter was used for precision biasing and a Stanford Research Systems SR570 Current Preamplifier was used to amplify and filter the signal from the photodetectors. The amplified photocurrent was recorded as a function of the x and y coordinates of the beam. The signal from the amplifiers was sampled by a National Instruments USB-6343 DAQ. A LabView program was developed to control the position of the sample, biasing and build the photocurrent maps. The program supports up to 2 separate channels and provides serpentine and raster scanning regimes.

3.4 Conclusion

In this chapter the techniques required for design, fabrication and characterisation of logic gates with plasmonic interconnects were discussed. A typical fabrication process represents a sequence of fabrication and characterisation steps and the number of steps in each sequence depends on a particular device and usually involves 8-12 stages. A modified process used to fabricate each device will be briefly described in each section.

The excitation and guiding of surface plasmons is the first task that must be

accomplished in order to build plasmonic integrated circuits. In the next chapter a design for an input port for such circuits will be discussed.

4. Design of input port for plasmonic integrated circuits

4.1 Introduction

Utilisation of surface plasmons as signal carriers in integrated circuits requires optimisation of their excitation mechanism as well as the development of ways to build comprehensive networks to guide the signal on chip. Due to the wave nature of SPPs, conventional metallic wires used in microelectronics cannot support their propagation. Analogous to photonic optical circuitry surface plasmons can be transmitted using waveguides. The advantage of SPPs arises from their capacity to circumvent the conventional diffraction limit as well as their use of metal interfaces which makes plasmonic waveguides compatible with conventional microelectronic technology. In recent decades comprehensive research into plasmonic waveguides with different configurations [16, 111, 112], shapes [87, 19] and materials [143, 144, 145] has been undertaken. It was also shown that plasmonic waveguides can be used to create sophisticated networks [29] providing an ability to fan-out the logic gates. A need remains, however, for improved designs to compensate for the high level of loss in plasmonic waveguides.

Another challenging task is the excitation of surface plasmons in a circuit. Ideally this would be undertaken by microlasers connected to the output of logic gates. These lasers, in turn, need to be coupled to the plasmonic waveguides forming a complete electro-optic circuit and here is the point where utilisation of silicon is impractical. The primary disadvantage of silicon in photonic applications arises

Part of the work presented in this chapter has been published in Evgeniy Panchenko, Timothy D James, and Ann Roberts. "Modified stripe waveguide design for plasmonic input port structures." *Journal of Nanophotonics*, 10(1):016019–016019, 2016

from its indirect bandgap [85]. This bandgap structure makes radiative electron-hole recombination improbable and, hence, the lasing process very inefficient.

A common solution to this issue involves utilisation of either only direct bandgap materials such as GaAs [146] or using a combination of direct and indirect bandgap semiconductors [147]. Both these methods have drawbacks associated with a relatively high cost and incompatibility with silicon technology due to the mismatch in crystal structures. Even though a large effort has been made in recent years to integrate microlasers onto silicon chips, this technology still needs substantial improvement to become usable in commercial ICs.

An alternative method involves surface plasmon excitation from the far-field using external lasers. As outlined in Chapter 2 due to the mismatch in the wave vectors between SPPs and freely propagating light, SPPs cannot be excited by direct irradiation of a metal surface with light. In this chapter a flexible design for a plasmonic input port which can be embedded in VLSI circuits is presented. A comprehensive study of grating coupling into plasmonic waveguides and mode analysis of the waveguides themselves has been performed to optimise surface plasmon excitation. Furthermore, two different strategies for increasing the SPP propagation length of the fundamental mode have been proposed and analysed. The design was then experimentally implemented and studied using NSOM. This port structure is suitable for far-field excitation of surface plasmon modes on a waveguide and does not require unwieldy laboratory equipment such as near-field microscope or prisms.

4.2 Design and simulations

An ideal input port should be compatible with far-field surface plasmon excitation with no additional equipment, be VLSI compatible, and have compact dimensions. The use of normally incident illumination is also preferable as the port will be easier to access in multilayer integrated circuits (a proper multilayer design is required to open 'windows' for plasmon excitation ports).

The whole structure can be divided into three main components: an excitation grating section, a tapered section and the waveguide. The waveguide was initially chosen to have a width w of 5 µm and thickness t of 60 nm. Such parameters permit improving far-field coupling and the decoupling of top and bottom surface

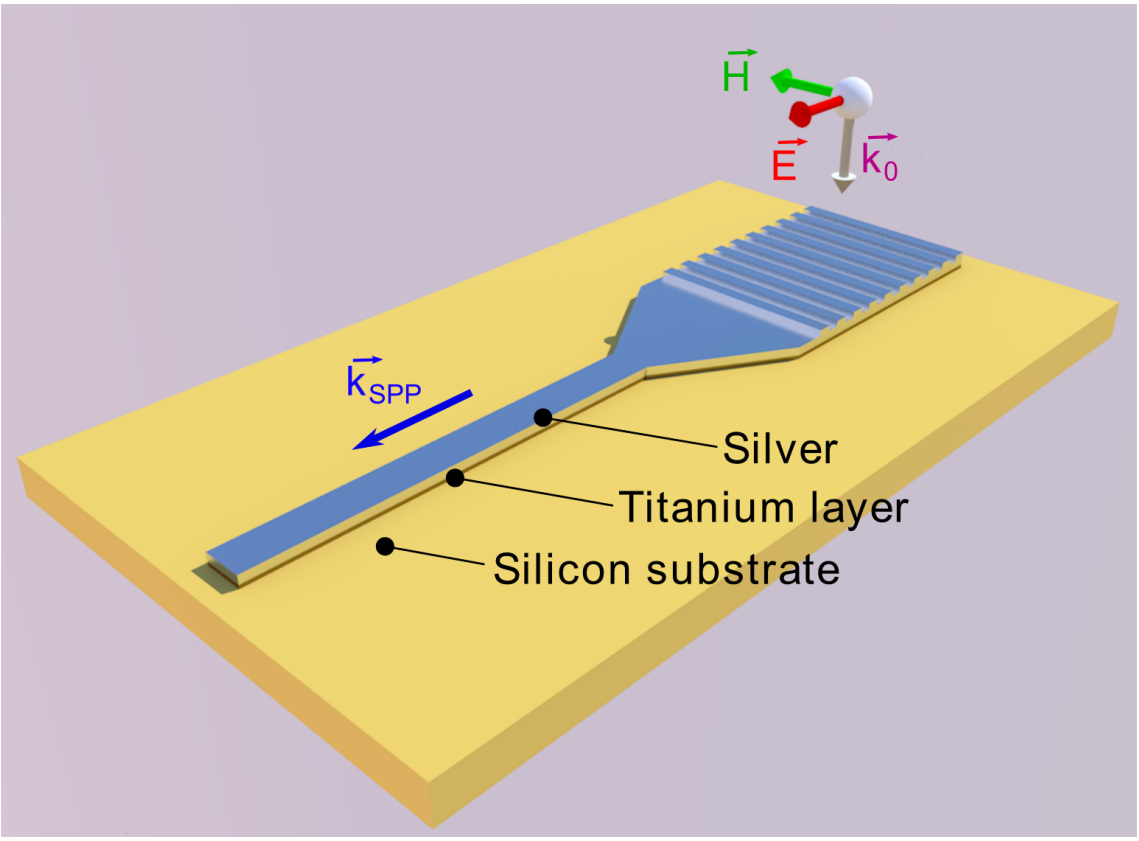

Figure 4.1: Schematic representation of plasmonic input port coupled with a stripe waveguide. Incident p-polarized light with momentum k_0 excites an SPP (with momentum k_{SPP}) which is focused into waveguide.

plasmons in a stripe waveguide, reducing attenuation. As can be seen from Figure 4.1, the port is implemented on a silicon substrate. Different materials such as silver, gold or aluminum can be used as a material for the waveguide depending on the operating wavelength. Since a wavelength of $\lambda_0 = 632.8$ nm (He-Ne laser) was chosen as the design wavelength for SPP excitation the utilisation of aluminum is impractical as it exhibits much higher loss. Silver or gold, therefore, can be used as the waveguide materials (silver provides lower losses while gold requires no passivation layer). In most cases a thin layer of titanium needs to be included to improve the typically poor adhesion of noble metals and prevent diffusion into silicon [148, 149]. Additionally, the port may includes a passivation layer of silica to prevent oxidation and degradation of silver and also to improve field confinement.

In the proposed structure, SPPs are excited using grating coupling [150], and a maximum coupling efficiency of 50% was demonstrated [151] numerically. The optimal grating structure dimensions are dependent on the materials used, the excitation wavelength, and the angle of illumination. Since the excitation section of

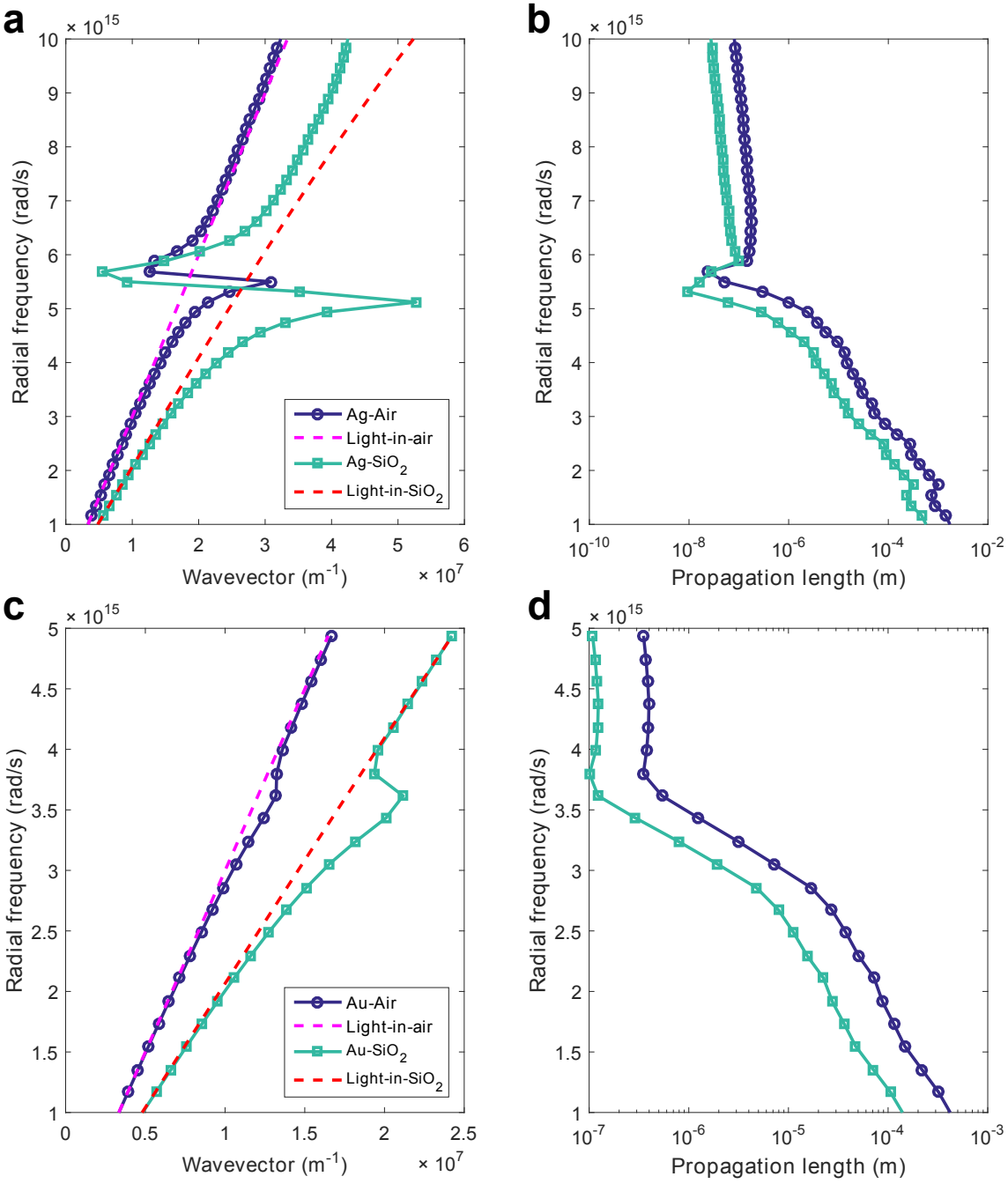

Figure 4.2: Dispersion curves for silver **(a)** and gold **(c)** slabs with different cladding dielectrics and associated with them SPP propagation lengths **(b)**,**(d)**. Magenta and red dashed lines represent light-in-air and light-in-silica wave vectors respectively.

the port was chosen to have dimensions much wider than the excitation wavelength and the metal thickness of 60 nm is sufficient to decouple SPPs propagating along the upper and lower surfaces of the film, the wave vector of the surface plasmon can be calculated as a simple 2-dimensional metal-dielectric interface [26].

The dispersion curve of Figure 4.2a is used to calculate the SPP propagation constant β which is essential for designing the port. The real part of this constant is needed to calculate the grating period while the imaginary part can be used to estimate the SPP propagation length. The optical properties of bulk noble metals from [89] were used in calculating the curves. Figure 4.2 shows calculated dispersion curves for silver (see Fig.4.2a) and gold (see Fig.4.2c) films with different dielectric claddings. The SPP propagation length for an infinitely wide interface can be calculated using the expression:

$$L = \frac{1}{2}(Im(\beta))^{-1} \tag{4.1}$$

Finite element method (FEM) analysis, implemented in COMSOL Multiphysics 4.3a with the RF module, was used to simulate the far-field excitation of SPPs (3D model) as well as to find the modes supported by the waveguide (2D model). The optical properties of materials used in the model were again taken from measurements of bulk material [89]. A plane wave with electric field directed perpendicular to the grating lines was used to excite SPPs. A waveguide length of 20 μm was used to minimize the influence of reflections from its end since the waveguide length is much larger than the SPP propagation length. A mesh with a maximum element size of 10 nm was used in the areas where a high simulation accuracy is desired (excitation grating, waveguide surface, MSM fingers). A perfectly matched layer (PML) was used together with scattering boundary conditions to decrease reflections from the model boundaries. Utilisation of FEM allowed to locally increase a mesh density of coupling grating and waveguide surface without avoiding a significant increase in computational time. The total simulation time was of the order of 4 hours and required 103 Gb of RAM (direct solver was used).

As can be seen from Figures 4.2b,d surface plasmons travelling along silver films have a longer propagation length than SPPs at a gold-dielectric interface due to the lower loss. Utilisation of silver, however, requires the use of a protective cladding to prevent film oxidation. This, in turn, red-shifts the resonance (see Fig.4.2a) and increases the loss at a given wavelength. At the same time gold can be used without a protective cladding due to its inertness. In practice, therefore, the propagation lengths of surface plasmons at the Ag-SiO_2 and Au-Air interfaces are similar.

The real part of the propagation constant at the given wavelength was used to

determine the period of the coupling grating. As mentioned previously, the structure is designed to work with normally incident illumination so the SPP momentum is determined only by the grating period a:

$$k_{SPP} = \frac{2\pi}{a}. \tag{4.2}$$

The SPP wavevector in the case of a Ag-SiO_2 interface at $\lambda = 632.8$ nm wavelength is equal to $k_{SPP} = 15.47$ µm^{-1} giving a grating period of $a = 380$ nm. Two different grating designs may be used to excite surface plasmons. The first design assumes the deposition of a shallow grating on top of the metal film (see Fig.4.3a). Analysis of a parametric sweep over the grating depth showed that the maximum coupling efficiency from the far-field into surface plasmons is achieved with a grating depth of 20 nm. This can be explained by the fact that (Eq.4.2) is valid only in the case of shallow gratings [26]. With an increase in the grating depth beyond this figure, the excitation of vertical modes [26, 152] leads to a decrease in the coupling efficiency.

The second design involves creating complete gaps in the metal film, thus, forming a grating structure (see Fig.4.3b). In comparison with the shallow grating this design exhibits a lower coupling efficiency. Nevertheless, despite these drawbacks this design is preferable as it is more robust to fabrication imperfections since the coupling efficiency of the shallow grating design is very sensitive to the thickness of these grating. It also requires only one fabrication step which, in turn, results in a much lower manufacturing cost.

The propagation constant extracted from the dispersion curve is strictly applicable only for an infinitely wide waveguide and grating. The assumption is still valid, however, for the excitation gratings used in the port design as they are much wider than a wavelength ($w_{grating} > \lambda$). Therefore, although this propagation constant can be used to design a coupling grating, it significantly varies from the actual value when surface plasmons experience significant lateral confinement. Waveguide narrowing particularly affects the imaginary part of the propagation constant, increasing the attenuation. Figure 4.4 shows the normalised magnitude of the electric field on the top of two plasmonic ports with different waveguide widths. As can be seen from the simulation, in the case of the 5 µm wide waveguide (see Fig.4.4a) the surface plasmon propagates a much longer distance compared to that with a width of 300 nm (see Fig.4.4b).

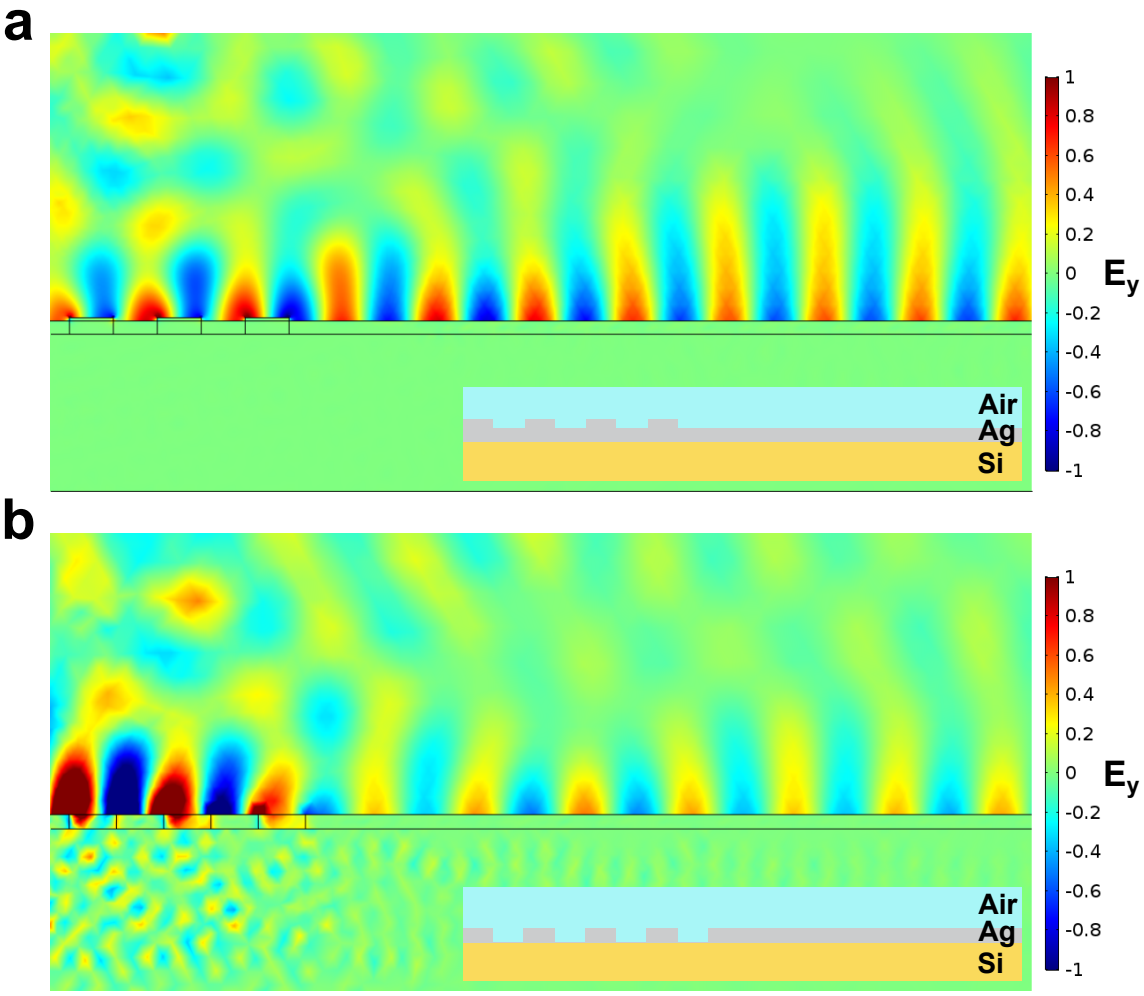

Figure 4.3: Normalised electric field distribution on the top of the waveguide in case of shallow **(a)** and through **(b)** grating designs. The insets depict the schematic representation of the structures.

Despite the relatively low attenuation of wide waveguides (for example those with widths grater than 5 µm) they are too large for VLSI plasmonic circuits. To be suitable for this application, the waveguide needs to be narrowed to less than 3 µm [153], leaving the excitation region unchanged. To design a comprehensive waveguide network, therefore, the propagation constant needs to be calculated more accurately. To identify the propagating plasmon modes supported by a narrow waveguide with a rectangular cross section, a numerical study was undertaken. Such a study cannot be performed analytically [16] so a computational approach was used to find supported modes. The fundamental symmetric mode ss_b^0 of the structure should have the smallest imaginary part of the propagation constant and, hence, the lowest attenuation. This mode was found to have a propagation constant of $\beta = 15.48 - 0.432i$ µm^{-1} and a propagation length of approximately 1.16 µm along the waveguide. The electric field distribution of the fundamental mode is shown

on Figure 4.5. The distribution shows that in the rectangular stripe waveguide the energy is mostly concentrated near the edges. This leads to strong attenuation and, thus, a relatively short propagation length.

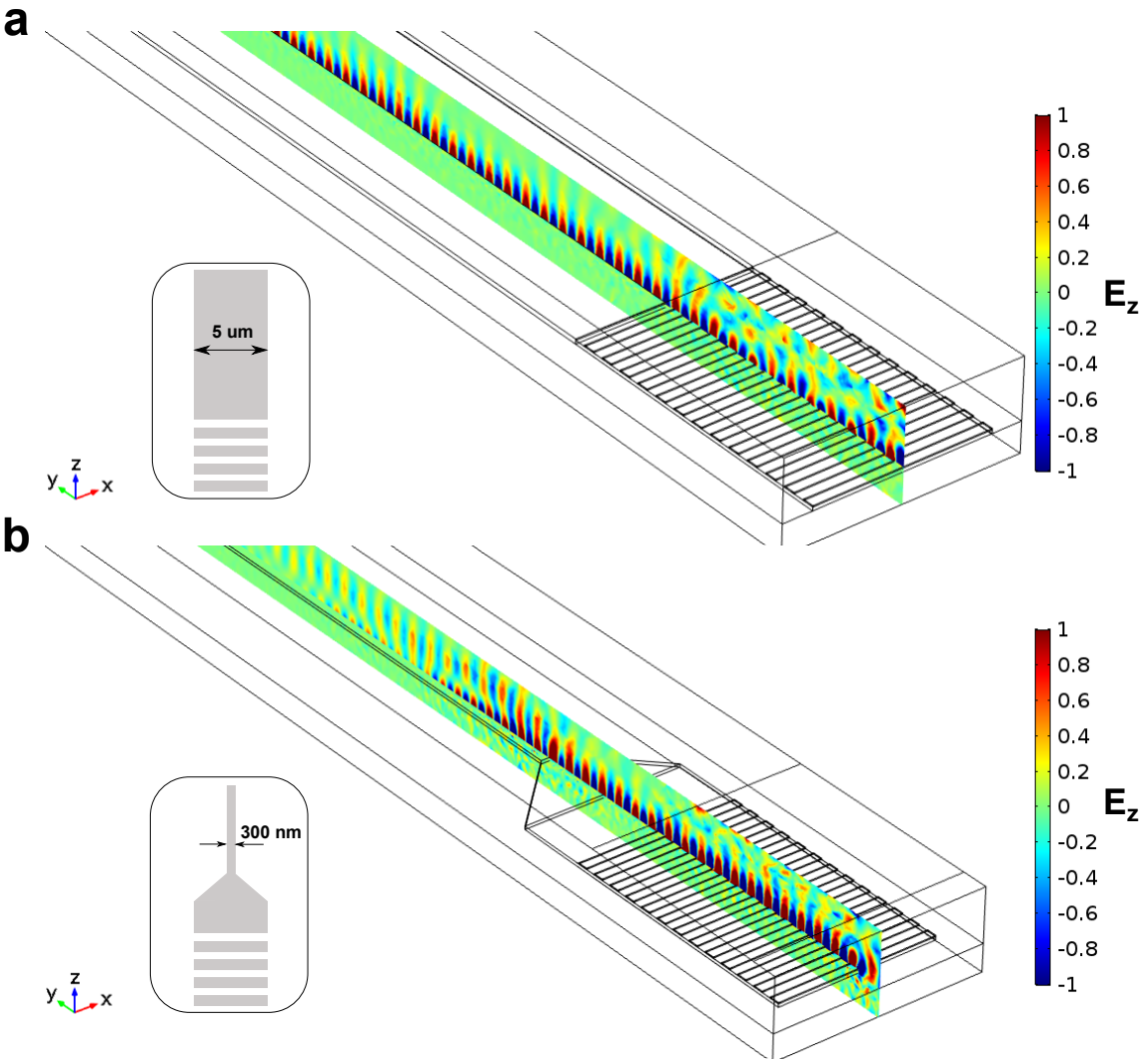

Figure 4.4: Normalised electric field distribution on two plasmonic ports with 5 µm **(a)** and 300 nm **(b)** wide waveguides. Narrow waveguide exhibits a larger attenuation of surface plasmons.

4.3 Waveguide improvement techniques

Weak attenuation of the propagating signal is a highly desirable property of a waveguide. Several techniques can be used to increase the propagation length of surface plasmons. Since the attenuation arises from fundamental limitations such as metal properties or field confinement, these techniques require some compromises. An

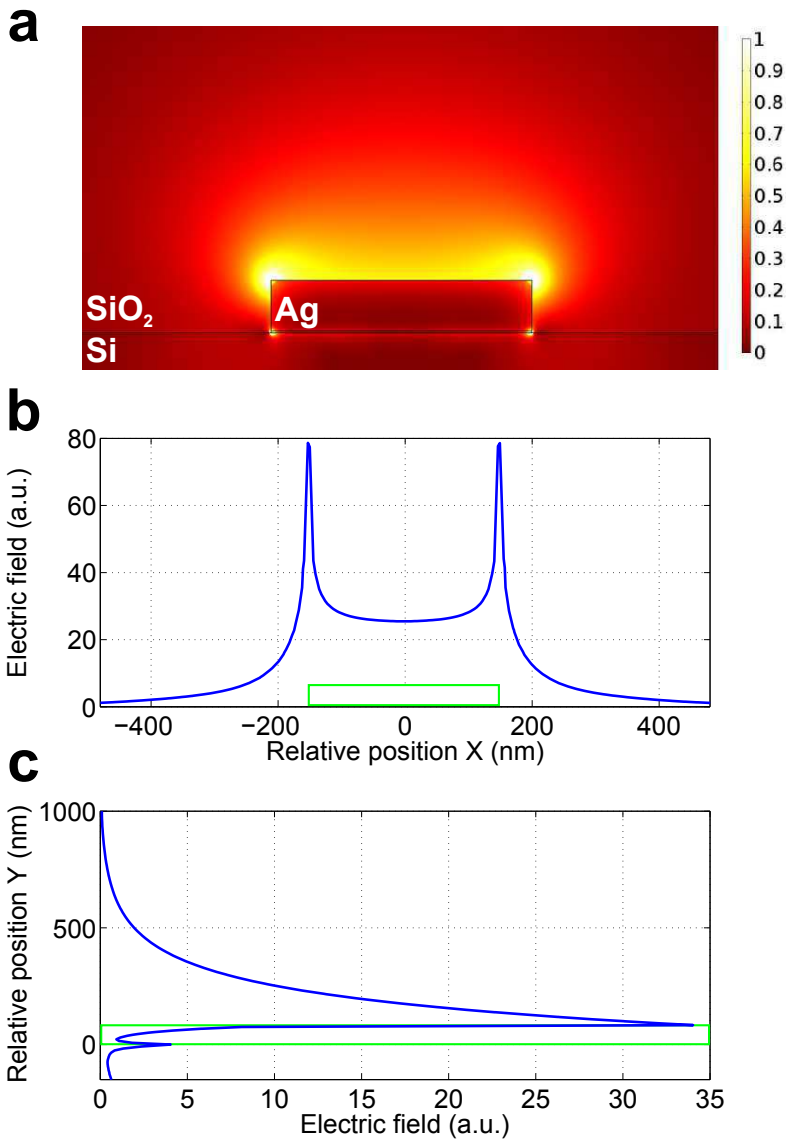

Figure 4.5: Normalized electric field profile **(a)** and distribution along x **(b)** and y **(c)** coordinates of rectangular shape waveguide. Green curve represents the waveguide outline.

increase in the propagation length will almost certainly affect other useful characteristics. Therefore, each method has its own pros and cons and the choice will depend on the particular application.

4.3.1 Reduction of the mode confinement

It is possible to increase the propagation length by changing the geometry of the waveguide to decrease the field confinement. The strategy used in this case is the

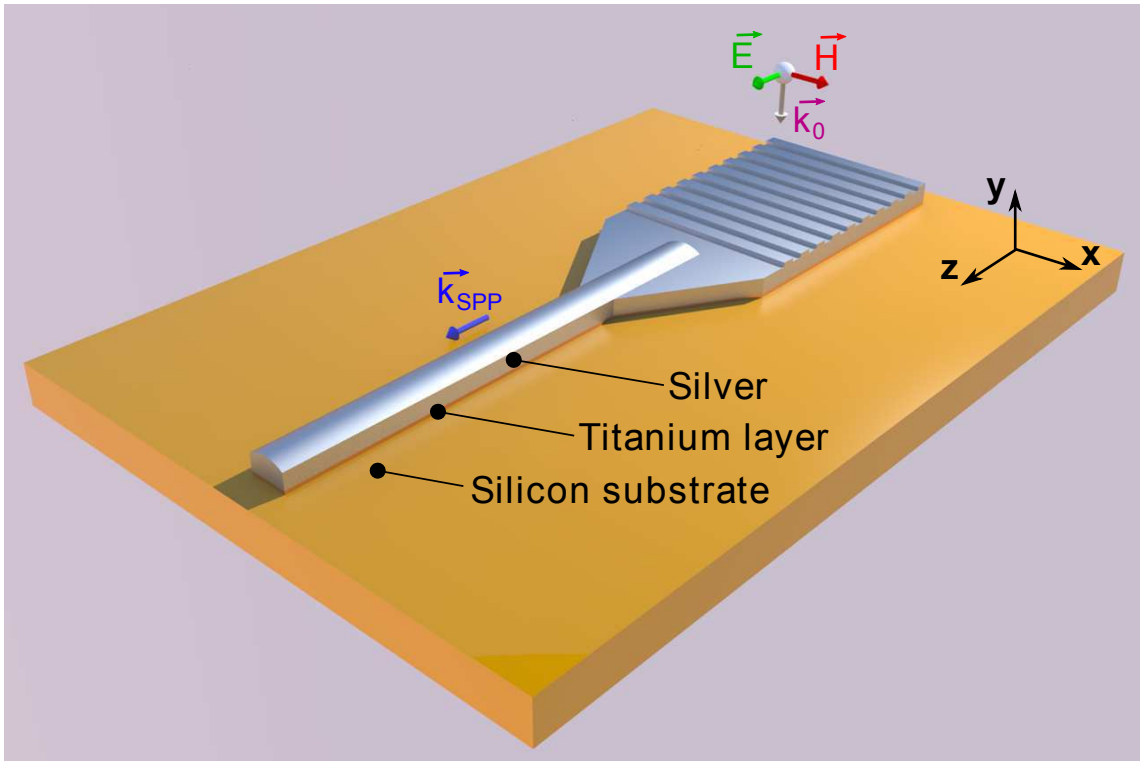

Figure 4.6: Schematic representation of plasmonic input port with hybrid-shape waveguide. Incident p-polarized light with momentum k_0 excites an SPP (with momentum k_{SPP}) which is focused into waveguide.

elimination of sharp edges. In the extreme case the waveguide should not contain any corners. This could be achieved by creating a semicircular profile (see Fig.4.7) at the top surface of the waveguide. The electric field profile of such a waveguide is shown in Figure 4.8a.

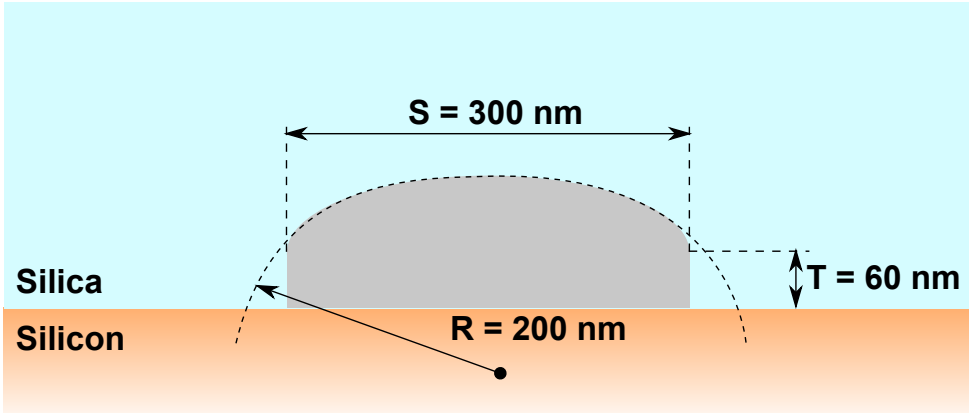

Figure 4.7: The crossection of a modified stripe waveguide. The top surface is curved with the radius of 200 nm to decrease attenuation.

Introducing a circular profile leads to a more uniform distribution of the field

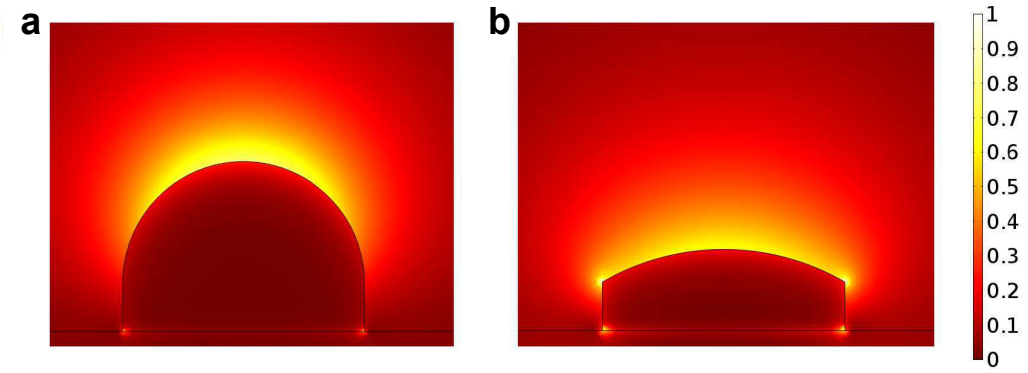

Figure 4.8: The normalised electric field profile of the modified stripe waveguide with circle radius of 150 nm **(a)** and 300 nm **(b)** respectively.

along the top surface of the waveguide. Furthermore, such a shape leads to an increase in the waveguide thickness without increasing the width, lowering the attenuation even further. The propagation constant in this case is $\beta = 15.96 - 0.101i$ μm^{-1} and the propagation distance is 4.98 µm, respectively, which is 4.3 times greater than for the of rectangular profile waveguide.

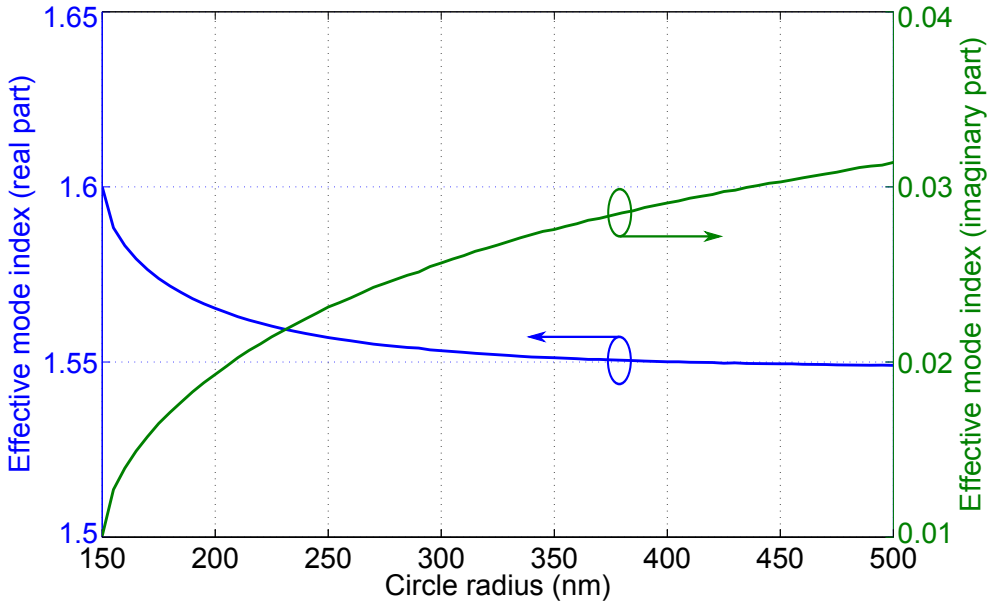

Figure 4.9: The evolution of the real (blue) and imaginary (green) parts of the effective mode index. The waveguide mode index approaches that of a rectangular waveguide as the radius of curvature is increased ($n_{rec} = 1.55 - 0.041i$).

To understand the change in the fundamental mode as the curvature changes, an analysis of the waveguide design for different radii of surface curvature was performed. As an example, Figure 4.8b represents the field distribution in the case of a curvature of 300 nm. The propagation constant of the waveguide with such a cross

section is $\beta = 15.49 - 0.256i$ μm^{-1} with the propagation length increased by a factor of 2.54 over that of the rectangular profile waveguide.

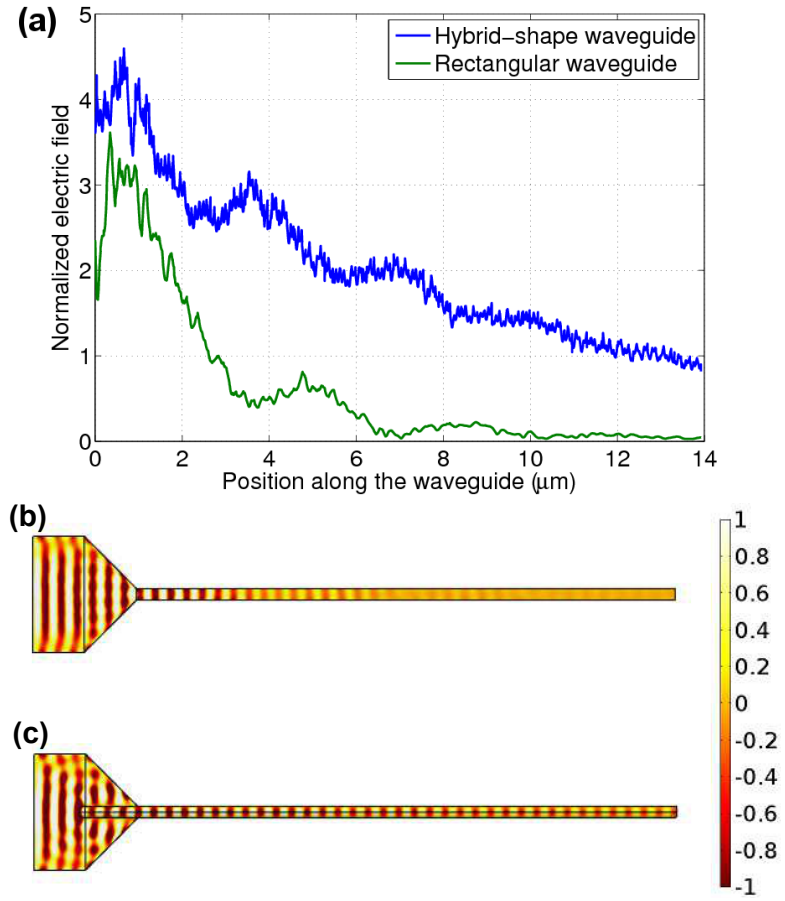

Figure 4.10: The normalized electric field distribution **(a)** on the top surfaces of the rectangular (green) and modified stripe (blue) waveguides. Graphs **(b)** and **(c)** show the distribution of a z-component of electric field on the rectangular and modified stripe waveguides respectively.

The evolution of the real (blue) and imaginary (green) parts of the effective mode index with radius of curvature is shown in Figure 4.9. As can be seen, as the radius of curvature increases, the propagation constant of the mode approaches that of the rectangular waveguide. Increasing the metal thickness of a waveguide will decrease the leakage into the substrate and, therefore, the imaginary part of an effective mode index. However, the improvement in propagation length observed in the hybrid-shaped waveguide over a stripe waveguide cannot be explained by considering only the mode leakage into the substrate resulting from the increased thickness caused by the waveguides circular profile. In our simulations we observed up to a 14% decrease in the imaginary part of the effective index for a given thickness for the hybrid-shape waveguide compared to the stripe waveguide, which results in

a similar increase in the SPP propagation length.

The normalized electric field distribution (2 nm above the surface) along the initial and the fully curved waveguides is shown in Figure 4.10a. The z-components of the field are presented in Figure 4.10b and Figure 4.10c. The plots show a marked improvement in the SPP propagation length in the case of the modified stripe waveguide in comparison with the rectangular waveguide cross-section.

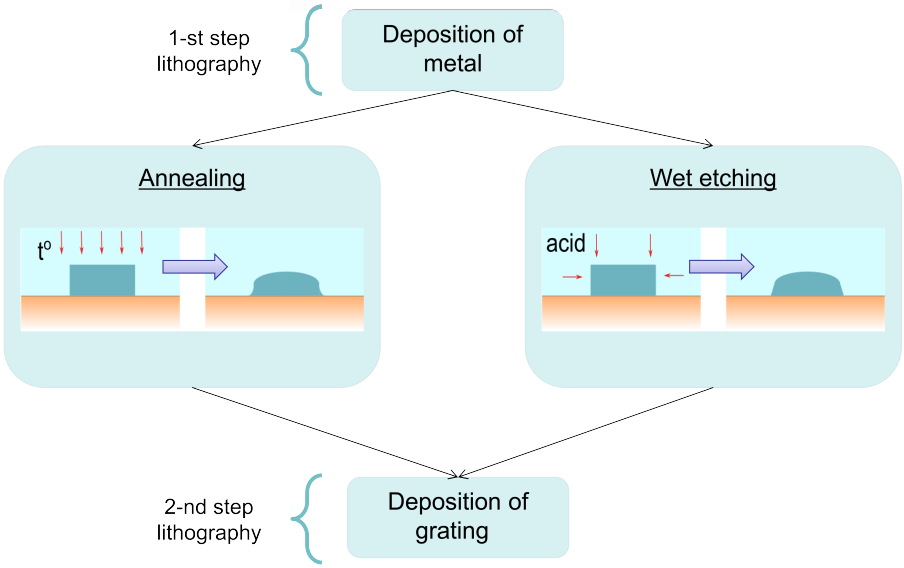

Figure 4.11: Possible fabrication techniques of hybrid-shape waveguide.

Possible ways to fabricate such a waveguide (see Fig.4.11) shape involve either annealing [154] or wet etching [155]. In a first step the base of a port can be deposited onto the silicon substrate. Then one of the proposed methods is performed, smoothing the corners of the rectangular waveguide. Both methods are compatible with CMOS technology but require specialised tools and process calibration.

4.3.2 Waveguide expansion

Given the challenges of implementing the methods described above, as previously mentioned another possible method to increase the surface plasmon propagation length involves increasing of the waveguide width. As previously discussed, the imaginary part of the propagation constant rapidly increases as the surface plasmon starts to experience lateral confinement. Therefore, the simple expansion of the waveguide can improve the SPP propagation distance. Although the waveguide expansion is in contradiction with miniaturisation principle, this method is still

suitable for low density interconnects where large waveguides are acceptable.

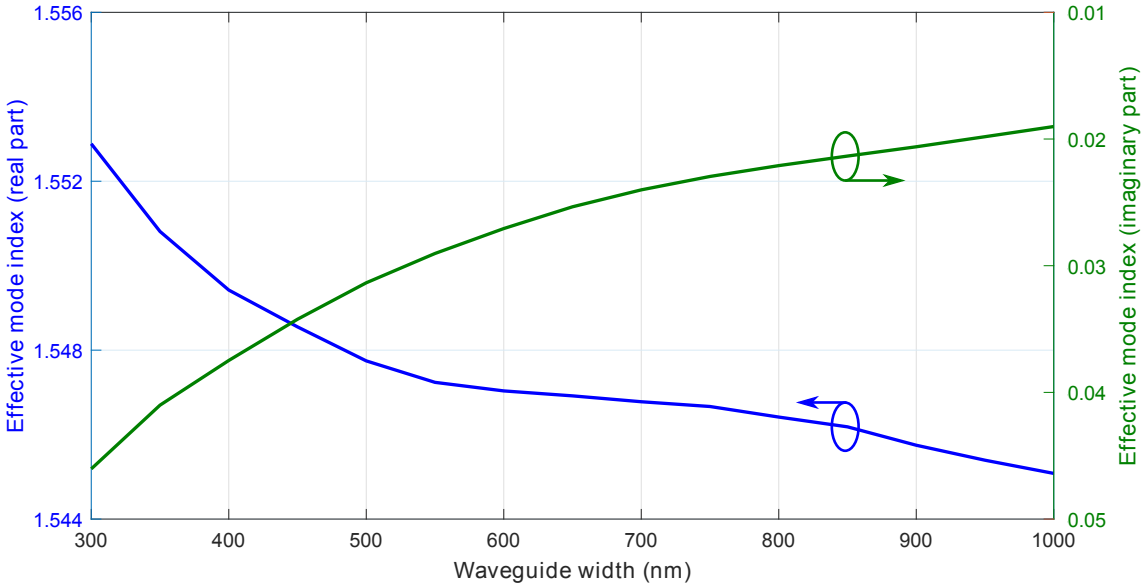

Figure 4.12: The evolution of the real (blue) and imaginary (green) parts of the effective mode index as a function of the waveguide width. The expansion of the waveguide allows to reduce the loss by the factor of 2.5.

Figure 4.12 shows the evolution of the real and imaginary parts of the fundamental mode as a function of the waveguide width. As can be seen, by increasing the width from 300 nm to 1 µm the imaginary part of the propagation constant can be reduced by a factor of 2.5. Although the improvement is less compared to the previous technique, the simplicity of the method makes it more appealing for low cost fabrication.

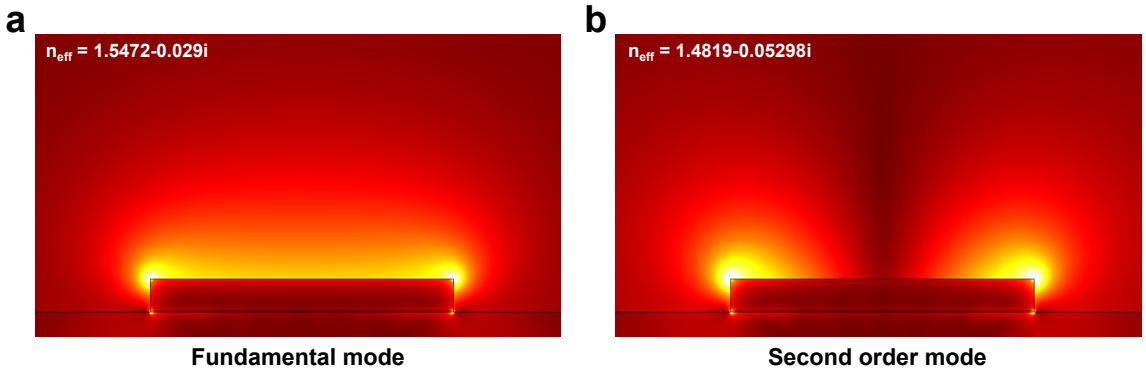

Figure 4.13: Fundamental **(a)** and second order **(b)** modes supported by 550 nm wide waveguide. The higher order mode has much greater imaginary part of the effective mode index n_{eff} and, therefore, experience higher attenuation.

In addition to increased dimensions, this method is also associated with another drawback. As the width increases, the waveguide starts to support higher order

modes so the guided power is divided between them. These modes are intrinsically lossier than the fundamental mode and, thus, their presence is undesirable. The normalised electric field distribution of two lowest order modes supported by a waveguide with a width of 550 nm is shown in Figure 4.13. As can be seen the symmetric second order mode (see Fig.4.13b) has a larger imaginary component of the effective mode index, indicating a higher loss.

Despite all the issues associated with this method, it is still a preferable approach for the plasmonic input port design due to its fabrication simplicity and relatively low cost. Therefore, the final port design was chosen to have an expanded 2.5 µm wide waveguide. The metal film thickness was also increased to 85 nm to further decrease the losses.

4.4 Application of microwave theory to plasmonic waveguides

The capacity to separate and join waveguides is necessary to trace the interconnects between the logic gates in an integrated circuit. In electric circuits operating at low frequencies the linkage can be performed simply by connecting receivers directly to the output of the signal source (fan-out). This method is valid as long as the dimensions of the transmission line are much smaller than the signal wavelength. In digital integrated circuits the low frequency approximation may still be valid for short interconnects as the signal wavelength rarely exceeds 5 cm.

The substitution of electrical with plasmonic interconnects assumes a substantial increase in the transmission signal frequency. With the increase in frequency the wave nature of a signal cannot be neglected and must be taken into account. The waveguides must be properly coupled with an appropriate junction to minimize wave reflections which can increase losses and, therefore, negatively affect circuit operation. Therefore, a simple fan-out approach used for low frequency circuits becomes inappropriate.

To couple waveguides it is necessary to match their characteristic impedances. Impedance matching techniques [156] are well-known and commonly used in microwave engineering. Since plasmonic waveguides are, in substance, very similar to their microwave counterparts (the differences are in operating frequencies and

dimensions) it should be possible to apply methods used in microwave engineering [113]. Thus, to couple MIM and IMI waveguides the characteristic impedance must be determined.

4.4.1 Characteristic impedance definition and matching techniques

Plasmonic waveguides can be represented as high frequency transmission lines so impedance matching techniques can be applicable for coupling different waveguides. The method can be used to maximize the power transfer to the load or minimize wave reflections from it. The waveguides to be coupled can be represented as a source and a load respectively. Depending on the particular task the source and load impedances can be matched by enforcing the conditions:

$$Z_S = \begin{cases} Z_L, & \text{for minimizing reflections} \\ Z_L^*, & \text{for maximizing power transfer,} \end{cases} \tag{4.3}$$

where Z_S and Z_L are the characteristic impedances of the source and load (for example two wavegiudes) respectively and Z_L^* is the complex conjugate of the load impedance. In transmission line theory [114] the dependence of the input impedance at a specified distance from the load, l, can be found using the following expression:

$$Z_{in}(l) = Z_0 \frac{Z_L + Z_0 \tanh(\gamma l)}{Z_0 + Z_L \tanh(\gamma l)}, \tag{4.4}$$

where Z_0 and Z_L are impedances of the transmission line and the load respectively, $\gamma = \alpha + i\beta$ is the propagation constant (α is an attenuation coefficient and β is a wavenumber). This is the general equation for lossy transmission lines.

The characteristic impedance of the transmission line is usually defined as the ratio of the voltage to current amplitudes and, in general, can be calculated using a following expression [157]:

$$Z_0 = \frac{\sqrt{R + j\omega L}}{\sqrt{G + j\omega C}}, \tag{4.5}$$

where ω is the angular frequency, L and C are the transmission line inductance and capacitance per unit length, R is the resistance of the line and G is the conductance of the insulating dielectric per unit length. R and G represent losses of the transmission line. For a lossless transmission line (or in the case where losses are negligibly small) the expression can be further simplified:

$$Z_0 = \frac{V}{I} = \sqrt{\frac{L}{C}}. \tag{4.6}$$

The current and voltage associated with a transmission line are well-defined only for TEM modes. In this case the voltage and current are uniquely defined and, therefore, the characteristic impedance, as given in equation (Eq.4.6) is constant at any point on the line. Plasmonic waveguides, however, cannot support TEM modes and the spatial distribution of electric and magnetic fields in plasmonic modes is not uniform. This is particularly true for stripe waveguides as supported modes are hybrid (a combination of TE and TM modes). Thus, the characteristic impedance becomes a spatially dependent parameter. Nevertheless, it is possible to apply this theory if the longitudinal component of the electric field is much smaller than the transverse component. Therefore, the propagating mode can be considered as quasi-TEM.

In the case of MIM plasmonic waveguides the characteristic impedance can be calculated using the voltage-current notation. Assuming the metallic components of the waveguide are carrying counter-propagating currents and neglecting the electric field at the corners [115] the voltage and current can be calculated using the following equations:

$$\begin{cases} V = \int_l \vec{E} \cdot d\vec{l} & \text{(4.7a)} \\ I = \oint_c \vec{H} \cdot d\vec{c}, & \text{(4.7b)} \end{cases}$$

where l is an integration path across the gap between the metallic parts and c is a closed contour around a current carrying component (see Fig.4.14).

This method has been previously shown [113] to provide a good agreement with

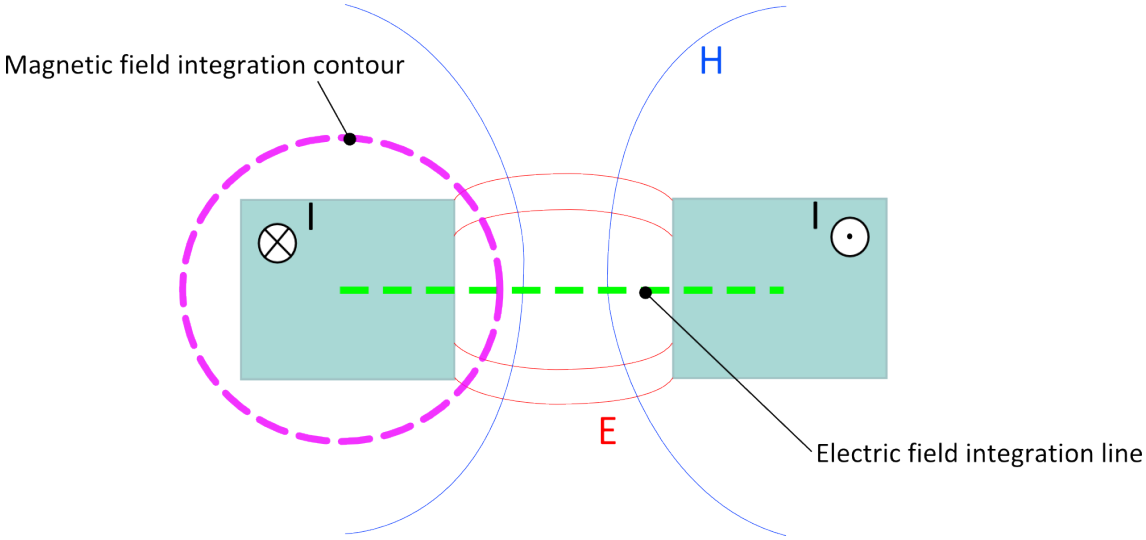

Figure 4.14: Schematic representation of a MIM plasmonic waveguide with field lines between the metallic parts. Electric (green) and magnetic (magenta) integration paths are used for V and I determination respectively.

analytical calculations of the characteristic impedance for MIM waveguides. The electromagnetic wave in these waveguides is mostly confined in the gap region. The resulting mode is assumed to be quasi-TEM allowing the application of the transmission line theory.

Even though the method described above showed good results with MIM structures, it is inappropriate for IMI waveguides. Since this waveguide type has only one metallic part the voltage and current integration paths are not uniquely defined. Figure 4.15 shows the typical distributions of electric and magnetic field lines. As can be seen these fields are not confined.

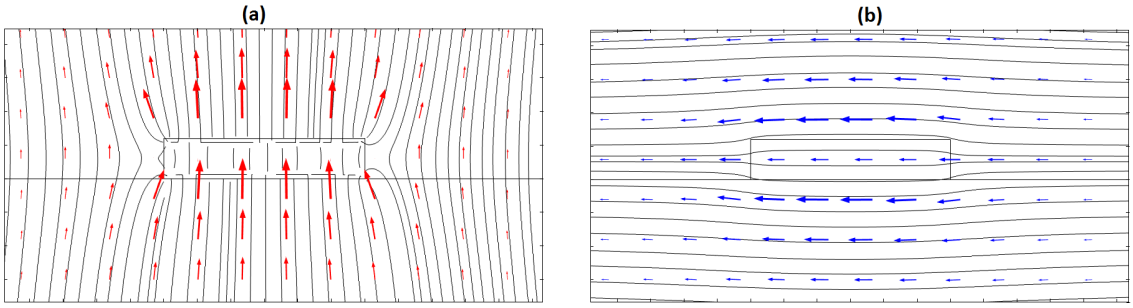

Figure 4.15: The distribution of electric **(a)** and magnetic **(b)** field lines around symmetric stripe waveguide.

The voltage-current definition of the characteristic impedance can also be defined in terms of power-current or power-voltage [157]:

$$Z_0 = \frac{P}{2I^2} = \frac{V^2}{2P}, \tag{4.8}$$

where P is the power transmitted along the stripe waveguide which, in turn, can be calculated using a following expression:

$$P = \frac{1}{2}\oint_S \vec{E} \times \vec{H}^* \cdot d\vec{a}, \tag{4.9}$$

where S is an effective area (through which the most power is guided) of the waveguide.

The power-current definition is preferable for plasmonic waveguides since the impedance can be easily calculated from the component of the Poynting vector P_z in the longitudinal direction and the longitudinal component of the current density J_z:

$$Z_0 = \frac{P}{2I^2} = \frac{\frac{1}{2}\iint P_z dxdy}{\left(\iint J_z dxdy\right)^2}, \tag{4.10}$$

As the electric field decays exponentially away from the waveguide, the integration area for the Poynting vector and current density can be truncated to $[0\ \frac{max(P_z)}{e^2}]$ and $[0\ \frac{max(J_z)}{e}]$ respectively (areas where power and current densities decrease in e^2 and e times respectively). Figure 4.16 shows the integration area for the Poynting vector determined using this expression.

A parametric sweep over the width was performed to calculate the change in the effective characteristic impedance of the waveguide. The Poynting vector and current density of the fundamental mode were integrated using the method described above. Figure 4.17 shows the variation in the real and imaginary parts of the effective characteristic impedance.

As can be seen, at a wavelength of 632 nm the characteristic impedance of the stripe waveguide has a large imaginary component (4.27%-18.8% of real part). This, in turn, implies substantial losses associated with surface plasmon propaga-

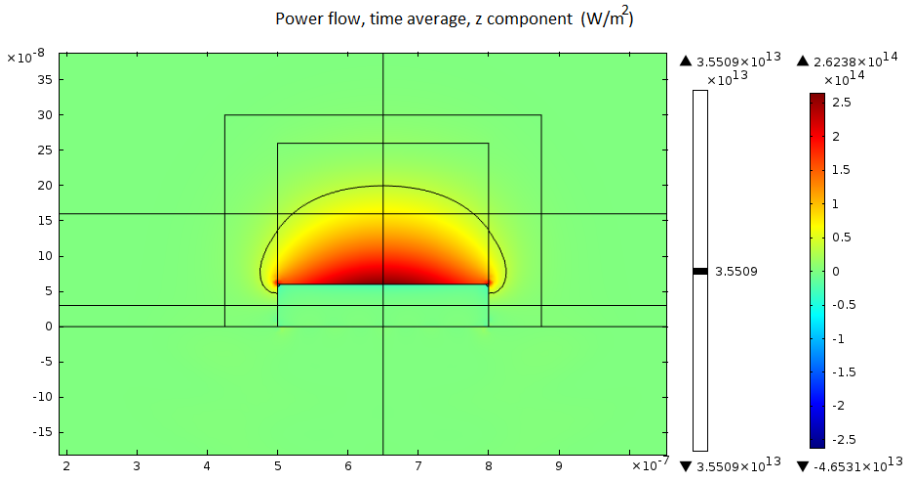

Figure 4.16: Poynting vector distribution along the cross section of the stripe waveguide. Curved black line shows the integration area where $P_z > max(P_z)/e^2$.

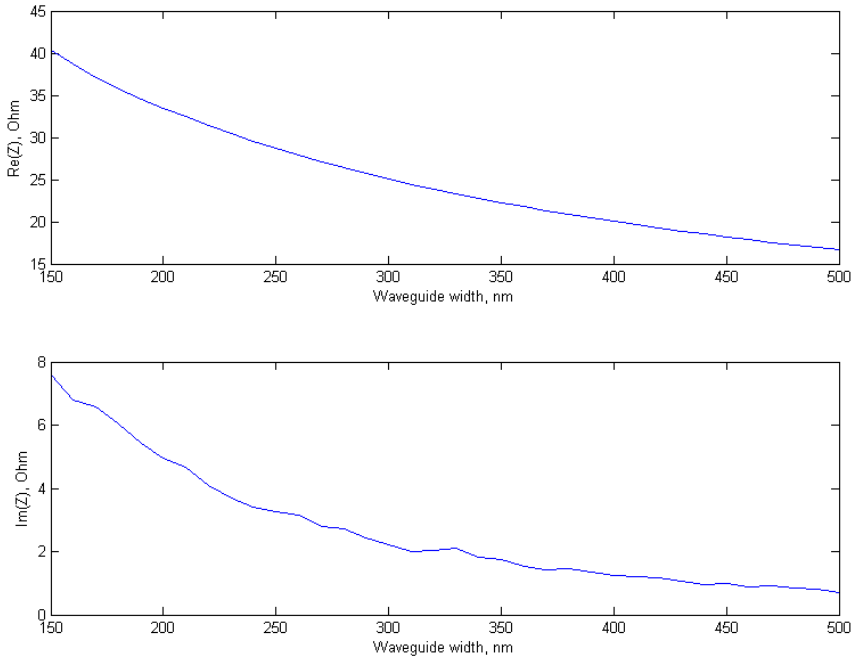

Figure 4.17: The dependence of the dielectric loaded waveguide characteristic impedance from the width.

tion along the waveguide. Therefore, the assumption of lossless or even low-loss transmission line is inappropriate. Therefore, the general equation (Eq.4.5) needs to be solved to calculate the line impedance. Since the problem becomes analytically intractable FEM simulations must be used in order to estimate the value of the particular transmission line characteristic impedance. In the near-infrared, however, this strategy provides a useful design alternative to computationally prohibitive full-field approaches [115, 116, 113].

4.5 Fabrication

Plasmonic input ports with waveguide widths of 0.5, 1.5, 2.5 and 5 µm were fabricated and measured as a proof of concept. It was decided to use a through grating design (see Fig.4.3b) to excite surface plasmons. The approach discussed in Section 4.2 was utilised to find a suitable grating period for Au and Al films. The waveguides were fabricated on [100] n-type (phosphorus doped) silicon wafer with a bulk resistivity of 1-10 Ω·cm. The wafer was covered with a 280 nm thick layer of PMMA A4 950k resist and exposed to create structures using a 100 kV EBPG5000+ electron beam lithography (EBL) system. The pattern was developed in 1:3 MIBK:IPA solution for 1 minute followed by 30 s rinsing in IPA and deionised water. The native oxide layer under the waveguides was stripped using 4% hydrofluoric (HF) acid. The wafer was then cleaved in two parts separating the structures for Au and Al evaporation. The samples were sequentially loaded into IntlVac NanoChrome II e-beam evaporator. The adhesion titanium layer with a thickness of 2 nm was deposited at 0.2 Å/s followed by 85 nm of gold deposited at 0.6 Å/s evaporation rates. The 85 nm thick aluminium film was evaporated at 0.6 Å/s rate without an adhesion layer. After evaporation a lift-off step in hot acetone was performed.

4.6 Experimental results

SEM images of the aluminium and gold waveguides are shown on Figure 4.18. As can be seen, the aluminium film (see Fig.4.18a) is very grainy and non-uniform. It was assumed that such a poor film quality is caused by a non-optimal evaporation rate [158]. Several additional samples were fabricated using different evaporation rates from 0.2 to 1.5 Å/s. Although the film quality was slightly dependent on the rate, the results were similar to the first sample. The surface plasmons propagating along such film will experience additional attenuation as the corrugations on the film may induce scattering [26]. The spots around the waveguides are result of local native oxide etching due to the HF acid penetration through the PMMA layer.

In the case of the gold film, it was found that the evaporation rate of 0.6 Å/s provides a smooth, small-grain film (see Fig.4.18b). The experiments showed a good repeatability of the results. Surface plasmons propagating along this film would be expected to have a propagation constant closer to theoretically calculated values.

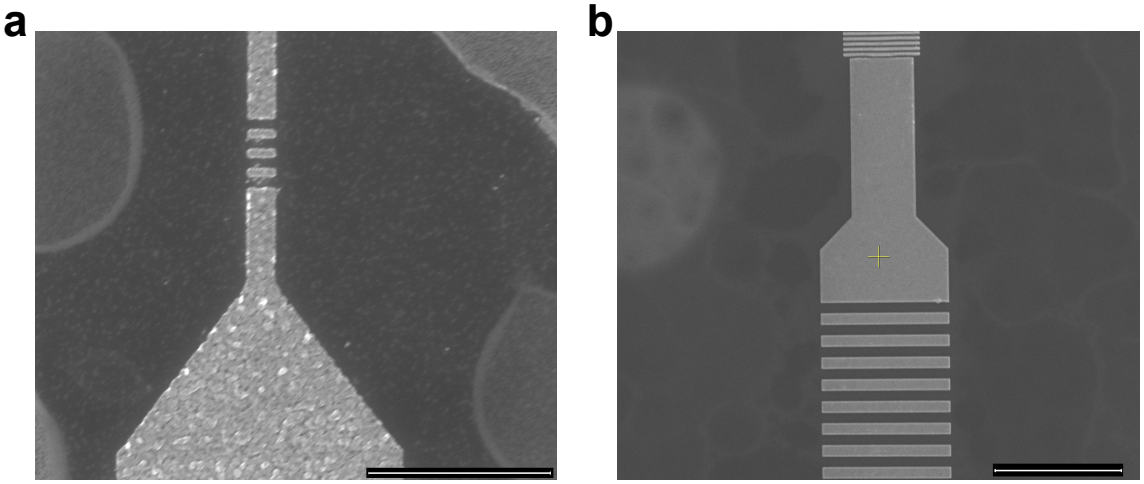

Figure 4.18: SEM images of 500 nm wide aluminium **(a)** and 2.5 µm wide gold **(b)** waveguides respectively. The scale bar for image **(a)** is 3 µm and 5 µm for **(b)**.

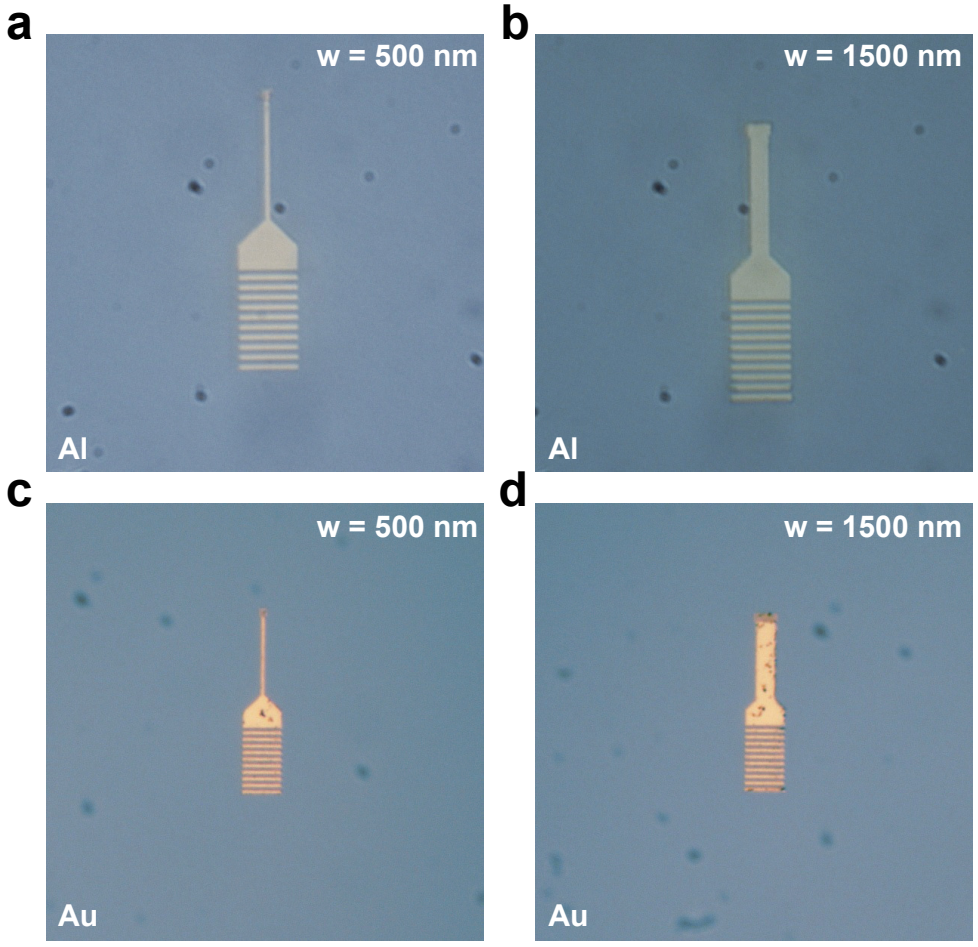

Figure 4.19: Optical images of 0.5 and 1.5 µm waveguides made of aluminium **(a,b)** and gold **(c,d)**.

Therefore, gold films were chosen for plasmonic input ports fabrication.

The fabricated plasmonic ports (see Fig.4.19) were then analysed using a Nanonics Multiview 2000 NSOM system. Due to the limitation of the available tool, a 1064 nm laser was used to excite surface plasmons. To accomodate the change in wavelength the excitation grating was redesigned to have a period of 1040 nm and 50% duty cycle while the excitation grating design, the rest of the port structure remained unchanged. An NSOM probe (in collection mode) with an aperture diameter of 500 nm was used to map the propagating plasmons.

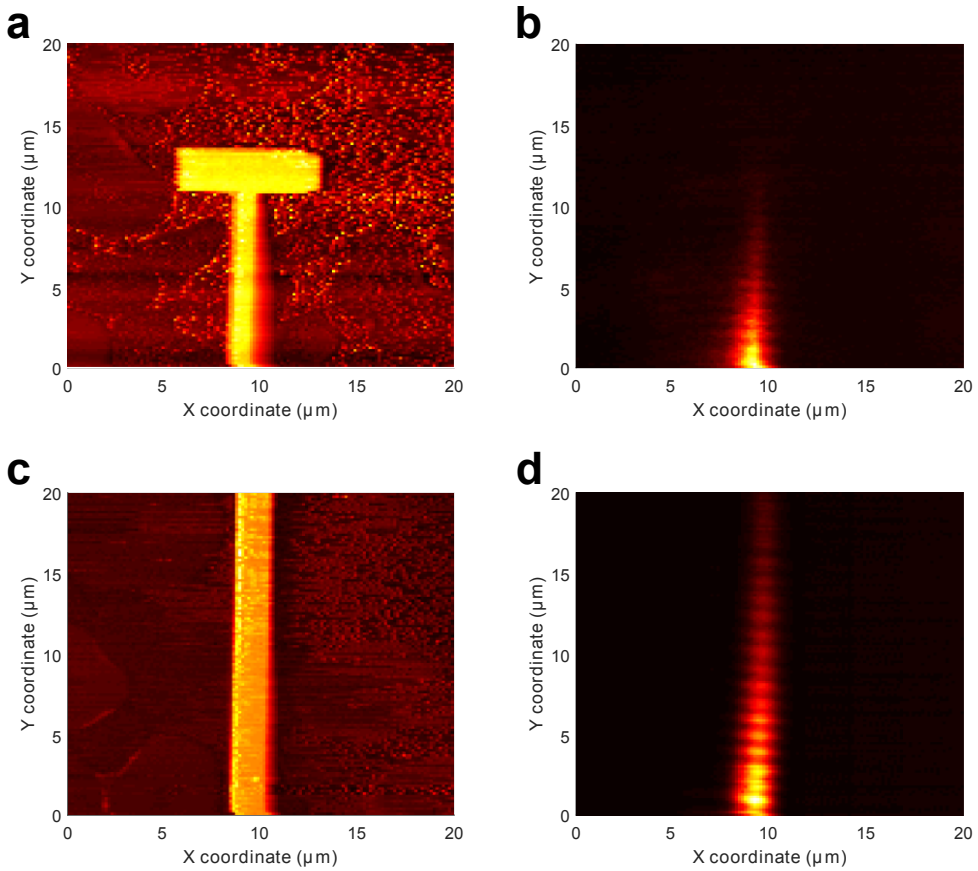

Figure 4.20: The AFM scans **(a,c)** and surface plasmon maps **(b,d)** of the 0.5 and 1.5 µm wide gold waveguides respectively.

Figure 4.20 shows AFM scans of 0.5 and 1.5 µm wide waveguides and their associated surface plasmon maps. NSOM maps (see Fig.4.20b,d) confirm the excitation of SPPs and their propagation along the waveguide. As can be seen, in the case of the 500 nm wide waveguide (see Fig.4.20a) the surface plasmons decay faster and have a shorter propagation length compared to the 1 µm wide waveguide (see Fig.4.20c). This is in a good agreement with theoretical predictions as discussed in Section 4.2 (see Fig.4.12).

Aluminium waveguides were also been studied using NSOM. As can be seen from

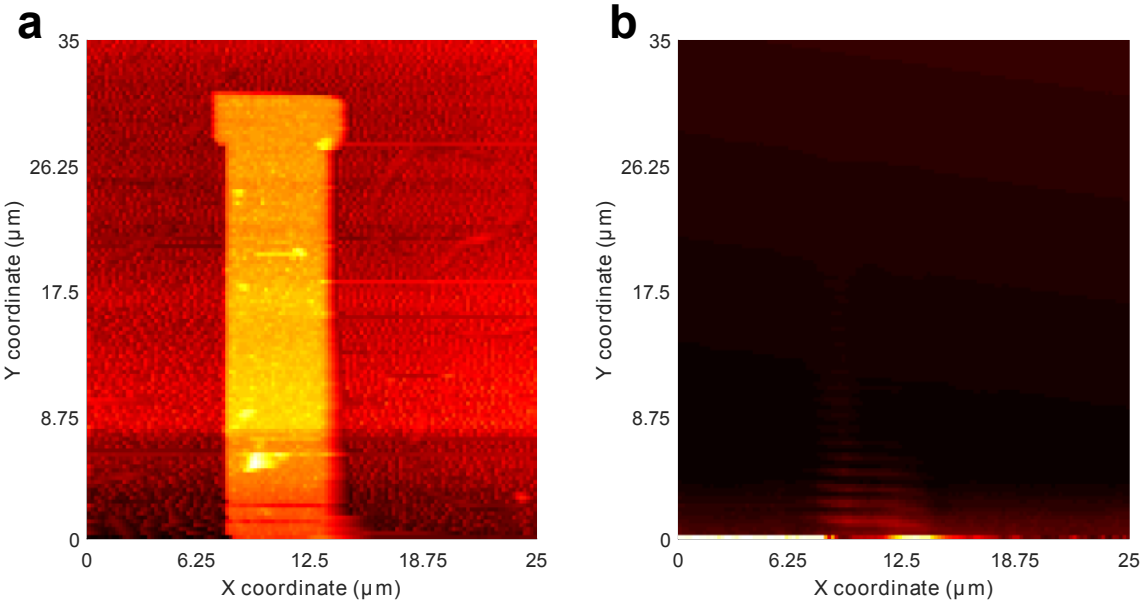

Figure 4.21: The AFM scan **(a)** and surface plasmon map **(b)** of the 5 µm wide aluminium waveguide.

Figure 4.21b, the excited surface plasmon decays much more quickly than the gold waveguide. It should also be noted that surface plasmons in Al waveguides were studied only for the 5 µm wide waveguide where the attenuation is the lowest. The poor film quality and high losses associated with aluminium make its utilisation for SPP waveguides impractical, at least in the visible and near-IR regions of the spectrum. Although gold is not currently compatible with CMOS technology, several techniques such as utilisation of a barrier metal such as Ti or W [159, 160] can be used to incorporate such plasmonic ports the integrated circuits.

4.7 Conclusion

In summary, the proposed design for a stripe waveguide coupled with a plasmonic input port provides a key component for compact plasmonic integrated circuits. The mode analysis undertaken and studies into changing the waveguide shape indicate the possibility of improving the propagation length of SPPs by a factor of up to 4.3 in comparison with a waveguide with a rectangular cross section. A plasmonic port was fabricated in Au and Al and experimentally analysed using NSOM technique, confirming its functionality in the case of Au. The proposed structure is potentially CMOS compatible and very flexible, and could be adjusted to particular needs following the design sequence described in this chapter.

Moving the operating wavelength into the NIR part of the spectrum can sufficiently improve the propagation length. This opportunity was also considered but due to the lack of NIR optics (objectives, waveplates, filters) and electrical equipment (lock-in amplifiers) for characterisation it was decided to focus on visible response. Nevertheless, the results obtained within this project proved the concept can be extended to NIR.

This design is used further in this work as a base structure in conjunction with semiconductor detectors and absorption modulators. In the next chapter a planar surface plasmon detection technique will be discussed and experimentally demonstrated.

5. Planar surface plasmon detection

5.1 Introduction

In order to utilize surface plasmons as a signal carrier it is essential to provide a reliable detection mechanism. Numerous SPP detection techniques using nanowires [161] or metal-insulator-metal waveguides [18] have been recently reported. Although these approaches showed a good capacity for detecting surface plasmons, their practical application is limited by complexity of design and fabrication. For smooth integration of plasmonic interconnects with detectors a planar geometry and reproducible characteristics are essential. Furthermore, for modern electronic applications, minimising the device footprint is critical. In this section a nanoscale alternative, based on utilising a metal-semiconductor-metal photodiode coupled to a plasmonic waveguide suitable for in-plane SPP detection is proposed. A device such as this could form one of the building blocks for high-speed optoelectronic integrated circuits.

5.2 Surface plasmon detection

One of the possible approaches for surface plasmon detection is based on outcoupling back to the far-field. Far-field outcoupling opens up an opportunity to use conventional photodiodes to detect surface plasmons instead of bulky and more expensive scientific instruments such as NSOM or utilising quantum dots.

5.2.1 Electron-hole pair generation

If the energy of the surface plasmon is larger than the bandgap of the semiconductor ($h\nu > E_{bg}$) it will be absorbed in it, generating a electron-hole pair. This pair can be separated by an electric field, creating a photocurrent. This photocurrent is proportional to the power absorbed in the semiconductor.

The optical power absorbed in the silicon per unit volume at a particular frequency can be calculated using the energy flux - divergence of the Poynting vector ($\tilde{S}$):

$$P(\vec{r},\omega)_{absorp} = -\Re\{\nabla \cdot \tilde{S}\}. \tag{5.1}$$

According to the Poynting theorem [162] the continuity of the energy flow can be found using the following equation:

$$\nabla \cdot \tilde{S} = \frac{1}{2} \cdot \left[j\epsilon\omega\tilde{E} \cdot \tilde{E}^* - j\mu\omega\tilde{H} \cdot \tilde{H}^* - \tilde{E} \cdot \tilde{J}^* \right], \tag{5.2}$$

where $\tilde{E} \cdot \tilde{J}^*$ represents either a power dissipation due to ohmic losses or power generation by the energy source inside the volume, $\mu\omega\tilde{H} \cdot \tilde{H}^*$ is an energy stored in the magnetic field and $\epsilon\omega\tilde{E} \cdot \tilde{E}^*$ is an energy stored in the electric field respectively.

Since there are no power generators in silicon and for simplicity the ohmic and magnetic losses are neglected compared to the electric losses, the equation (Eq.5.2) can be further simplified:

$$P(\vec{r},\omega)_{absorp} = -\frac{1}{2}\omega\Im\{\epsilon(\vec{r},\omega)\} \left|\tilde{E}(\vec{r},\omega)\right|^2. \tag{5.3}$$

As can be seen, in this case the power absorbed in the silicon is proportional to the imaginary part of the dielectric permittivity. Assuming all the photons absorbed will generate an electron-hole pair (since other effects are neglected) the spatial distribution of the generation rate can be found using following expression:

$$\Gamma(\vec{r},\omega) = \frac{P(\vec{r},\omega)_{absorp}}{\hbar\omega} = -\frac{\pi}{h}\Im\{\epsilon(\vec{r},\omega)\}\left|\tilde{E}(\vec{r},\omega)\right|^2, \tag{5.4}$$

where $\hbar\omega$ is energy of photon which is equal or larger than the bandgap energy of the semiconductor. The total photocurrent based on electron-hole pairs generation can be calculated by performing a volume integration over the active region of the photodetector:

$$I(\omega) = \int q\Gamma(\vec{r},\omega)dV = q\int \Gamma(\vec{r},\omega)dV, \tag{5.5}$$

where q is an electron charge.

For the case when the photocurrent is generated by direct absorption in a semiconductor (electron-hole pair generation) almost any type of the photodiode can be used to detect surface plasmons. For example the p-n junction based photodetectors can exhibit a high responsivity, while photodetectors based on the Schottky barrier can provide a higher operation speed.

5.2.2 Hot-electron generation

Conventional PN or PIN junction based photodiodes are incapable of detecting photons with energies below the bandgap of the semiconductor. Nevertheless, the low-energy photons can still be detected by means of Schottky photodiodes. This type of photodiode is based on a metal-semiconductor barrier which is usually lower than the bandgap of the semiconductor [85]. The power absorbed in the metal can deliver sufficient kinetic energy to the electrons to overcome the potential (Schottky) barrier. Therefore, if the photon has an energy lower than the semiconductor bandgap but larger than the Schottky barrier ($\Phi_B < h\nu < E_{bg}$) it can generate a hot-electron which can be swept by the electric field through the depletion region and detected as a photocurrent. This process can be enhanced by multiple reflections from the boundaries [163] in a thin metal film.

Since a Schottky photodiode detection mechanism is based on internal photoemission the internal quantum efficiency (η_i) is dependant on the probability of a hot-electron overcoming a metal-semiconductor barrier. Therefore, the internal quantum

efficiency can be found using following expression [163]:

$$\eta_i = \frac{1}{h\nu} \int_{\Phi_B}^{h\nu} P(E) dE, \tag{5.6}$$

where h is a Plank's constant, ν is a wave frequency, Φ_B is a Schottky barrier height and $P(E)$ is a probability of an internal photoemission of an electron with a certain energy E.

The internal photoemission probability is dependent on many parameters such as the structure shape, the metal used and its quality. Therefore, the analytical calculation of the integral in (Eq.5.6) becomes complicated and may be inaccurate. Thus, a FEM simulation can be performed to calculate it numerically.

As mentioned before, the photocurrent generated by a Schottky photodetector is proportional to the internal quantum efficiency and can be found using the following equation:

$$I = q\eta_i, \tag{5.7}$$

where q is the electron charge.

The responsivity of the photodetector describes the ratio between the optical power at a specified wavelength and the generated photocurrent:

$$R = \frac{I}{P} = \frac{q\eta_i}{h\nu}. \tag{5.8}$$

5.3 Metal-semiconductor-metal photodetectors

Metal-semiconductor-metal (MSM) photodiodes are commonly used in ultrafast optoelectronic devices. It has been shown that Si-based MSM photodiodes can operate up to a frequency of 140 GHz [164], demonstrating that very high-speed operation can be achievable. It was recently showed [39] that by utilizing the properties of plasmonic structures it is possible to design photodetectors that are sensitive to the

polarization state of an incident optical beam.

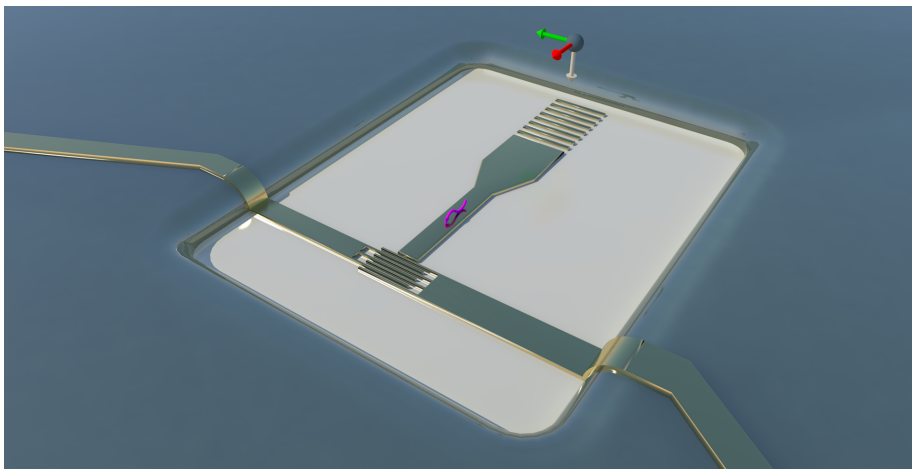

Figure 5.1: Schematic representation of a waveguide-coupled MSM photodetector with excitation grating.

An MSM photodetector consists of two interdigitated metal electrodes (see Fig.5.2b) deposited on a low-doped semiconductor. Each of these electrodes forms a Schottky barrier with the substrate. A typical band diagram of an MSM photodetector under reverse bias is shown on Figure 5.2a. Since the substrate is common, the MSM photodetector represents two Schottky diodes connected back-to-back (see Fig.5.2c).

Similarly to PIN or PN photodiodes, Schottky photodetectors can work in either photovoltaic (without biasing) or photoconductive (under reverse bias) regimes [165]. Usually photodetectors are designed to operate in photoconductive mode as it exhibits a faster operating speed and higher responsivity. If low-noise operation is required then photovoltaic mode is preferable. Since MSM photodetectors are unidirectional they will always operate under reverse bias independent of which electrode is at the higher potential. The diode operating in the photoconductive regime can detect photocurrent generated by both hot-electrons and electron-hole pairs.

The device is implemented on a silicon substrate with a bulk resistivity of 1-10 Ω·cm. It was decided to use 85 nm thick gold as the waveguide material deposited on a 2 nm thick titanium adhesion layer. Surface plasmons are excited on a plasmonic input port design described in Chapter 4. The grating was designed for a normally incident 635 nm plane wave and, therefore, has a period of 600 nm. The operating wavelength was chosen to be in visible spectrum (but in red part to decrease the losses) as the electron-hole pair generation is much more efficient process than hot-electron injection and, therefore, is easier to detect. Furthermore, the excitation of surface plasmons can be confirmed by scattering from the MSM grating which

can be detected using a conventional CMOS camera. The depth of the grating is identical to the thickness of the metal film and is equal to 85 nm. This thickness was chosen to ensure the top and bottom modes were decoupled and to minimize leakage of surface plasmons into the substrate [16]. The excitation section is then tapered into a 2.5 µm wide asymmetric stripe waveguide which, in addition to a fundamental mode, can support several higher order modes at this wavelength. The width chosen is a compromise balancing loss and size. The waveguide is used to deliver surface plasmons to the active zone of the MSM photodiode. The expansion of the waveguide leads to a reduction in the attenuation constant and an increase in the SPP propagation length.

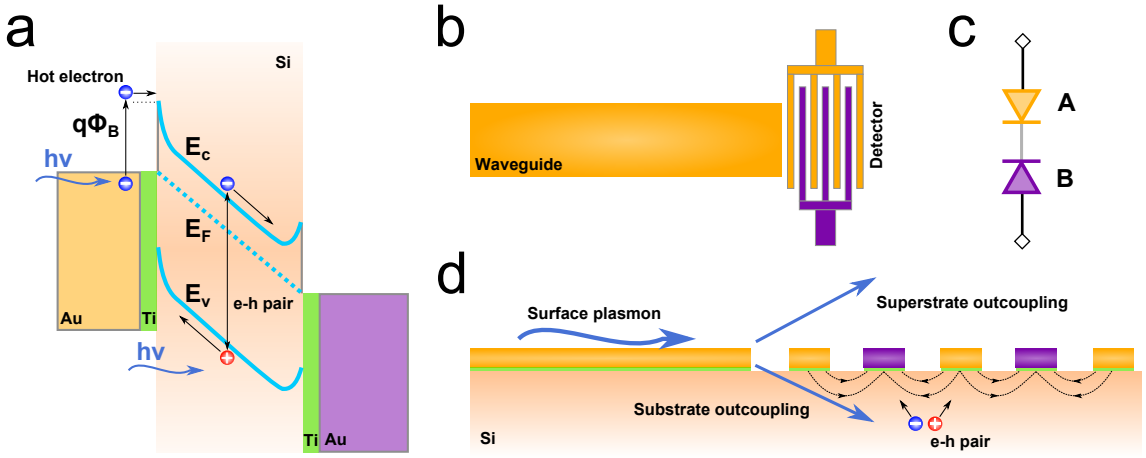

Figure 5.2: A band diagram of biased MSM photodetector **(a)** describing two possible mechanisms of photocurrent generation. $q\Phi_B$ is a height of the Schottky barrier, E_v, E_c and E_F are valence, conduction and Fermi energy levels respectively. Schematic representation of MSM photodetector coupled with waveguide **(b)** and equivalent electric circuit of the detector **(c)**. The surface plasmon outcoupling mechanism on MSM photodetector **(d)**.

Several phenomena are simultaneously contributing to the photocurrent generated by this device. The fingers of the detector can couple surface plasmons back into the far-field (see Fig.5.2d) allowing photons to penetrate into the substrate. If the photon energy is above the band gap of a semiconductor ($h\nu > E_{bg}$) it will be absorbed resulting in electron-hole pair generation. The energy of generated electrons in this case is by definition (since the metal-semiconductor barrier is smaller than the bandgap of the semiconductor [85]) larger than the energy of the Schottky barrier and, therefore, can overcome it. Furthermore, surface plasmons can nonradiatively decay in the metal fingers [152] and be absorbed in them. This in turn, will lead to hot-electron generation and injection through the Schottky barrier into the substrate. Therefore, such a device enables the detection of surface plasmons

with energies, both above and below the band gap of a semiconductor.

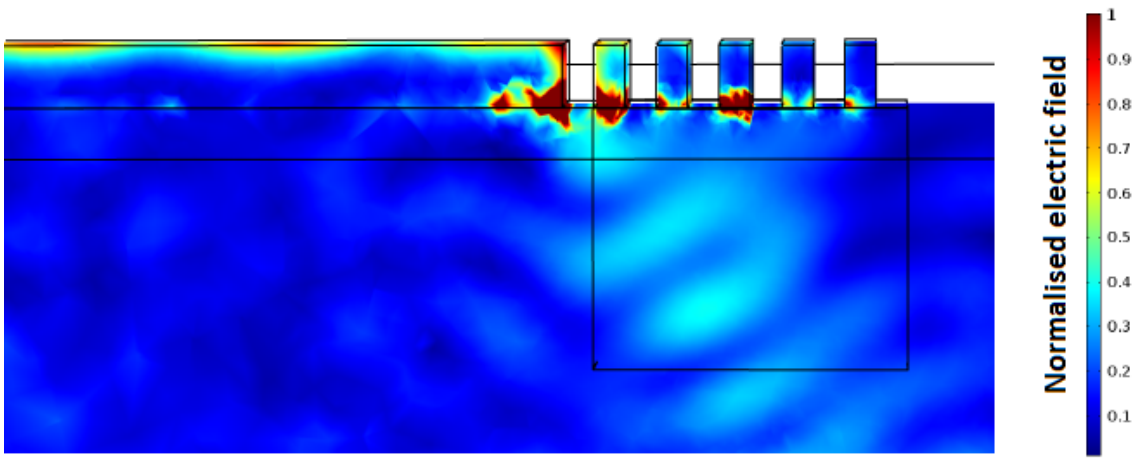

Figure 5.3: Normalised electric field map of the photodetector active region (under grating).

Applying a bias to the electrodes of the detector leads to the formation of an electric field gradient (see Fig.5.2d) in the active zone under the fingers. Every charge carrier generated or injected into the semiconductor substrate will be swept by this electric field to the top electrode resulting in a photocurrent flowing through the device. Since the device operating wavelength is in visible spectrum (these photons have energy above the Si bandgap), the influence of hot electron injection is neglected.

Finite element method (FEM) analysis, implemented in COMSOL Multiphysics 5.1 with RF module, was used to simulate the excitation of surface plasmons as well as their propagation along the waveguide and decay in MSM photodetector active area. Scattering boundary conditions terminate the model at all boundaries. An excitation port above the grating was used to launch a polarised electromagnetic wave. A mesh with a maximum element size of 10 nm was used in the areas where a high simulation accuracy is desired (excitation grating, waveguide surface, MSM fingers). The optical properties of Au used in the model were taken from experimental data for bulk material [89].

The parameters describing the MSM photodetector electrodes such their period and duty cycle will affect the outcoupling of surface plasmons. Therefore, to optimize the sensitivity of the device an FEM simulation was performed to determine the relationship between the irradiance delivered to the photodetector's active region (see Fig.5.3), the separation between the fingers and their duty cycle. The outcoupling of surface plasmons into the substrate involves two effects: a momen-

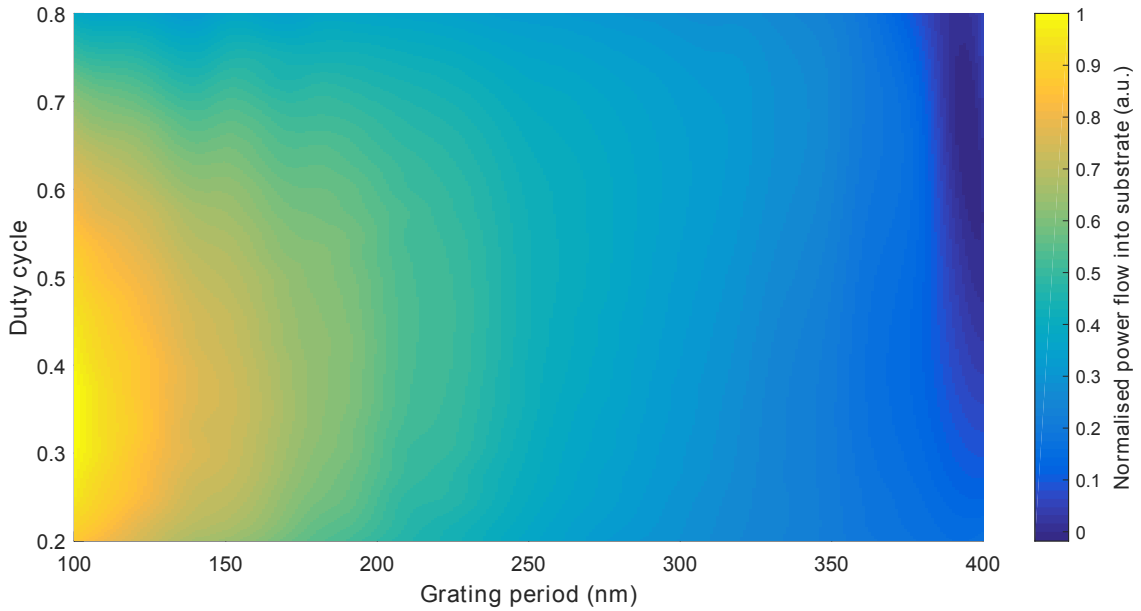

Figure 5.4: Simulated power flow into the substrate as a function of grating period and duty cycle. A higher power flow indicates a more efficient surface plasmon outcoupling into the substrate.

tum transfer provided by the MSM grating and the localised plasmon resonance of each finger which enhances the radiation. Increasing the period while keeping the duty cycle fixed (see Fig.5.4), increases the separation of the fingers, weakening the near-field coupling of each finger to its neighbours which, in turn, decreases the power flow into the substrate. The same tendency can be observed in the case of large duty cycles. This can be explained by the narrowing of the slits through which the surface plasmons outcouple into the substrate. As the thickness of waveguides was 85 nm it was difficult to obtain the gap between MSM photodetector fingers less than 80 nm. Considering these results together with fabrication limitations a grating with a duty cycle of 0.6 and with a period of 200 nm (see Fig.5.5) was chosen. The photodetector consists of 13 fingers (see Fig.5.5b) giving an active area of 12.5 μm^2 (5 x 2.5 µm).

5.4 Fabrication

Photodetectors and waveguides were fabricated on [100] n-type (phosphorus doped) silicon wafer with bulk resistivity of 1-10 Ω·cm. The wafer was covered with a 280 nm thick layer of PMMA A4 950k resist and exposed to create structures using a 100 kV EBPG5000+ electron beam lithography (EBL) system. The pattern was

developed in 1:3 MIBK:IPA solution for 1 minute followed by 30 s rinsing in IPA and deionised water. The native oxide layer that might form during these steps was removed using 2% hydrofluoric (HF) acid and immediately loaded into an IntlVac NanoChrome II e-beam evaporator. The titanium adhesion layer with a thickness of 2 nm was deposited at 0.2 Å/s followed by 85 nm of gold deposited at 0.6 Å/s evaporation rates. After evaporation a lift-off step in hot acetone was performed. A wet dicing saw (Disco DAD321) was used to separate the photodetectors for packaging. The samples were glued into LCC20 ceramic packages and bonded using Kulicke & Soffa 4522D Ball bonder.

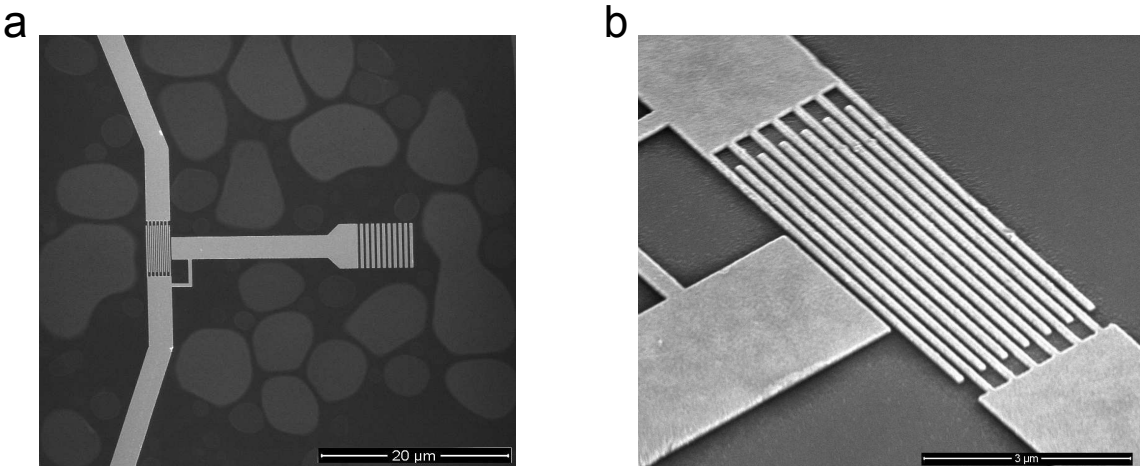

Figure 5.5: Scanning electron microscope images of the entire structure **(a)** and close-up of the MSM photodetector grating **(b)**.

5.5 Experimental results

The dark I-V characteristic of the photodetecor is shown in Figure 5.6a. As previously mentioned, the detector consists of two identical Schottky diodes connected back-to-back and, therefore shows similar behavior under both positive and negative bias. The curve saturates around 0.1 V which means that the Schottky barrier height is lower than usually reported for Ti-Si contacts [166, 167]. This can be explained by imperfections introduced during the fabrication process since there are a number of factors that can affect the height of the barrier such as contamination of the Si surface, quality of the metal film and the inevitable formation of an ultra-thin layer of native oxide prior to the metal evaporation. For simplicity the contact pads (250 μm^2 each) were deposited onto the silicon in the same fabrication step with the detector fingers. As a consequence, the detector exhibits a relatively large dark

current due to the large metal-semiconductor contact area.

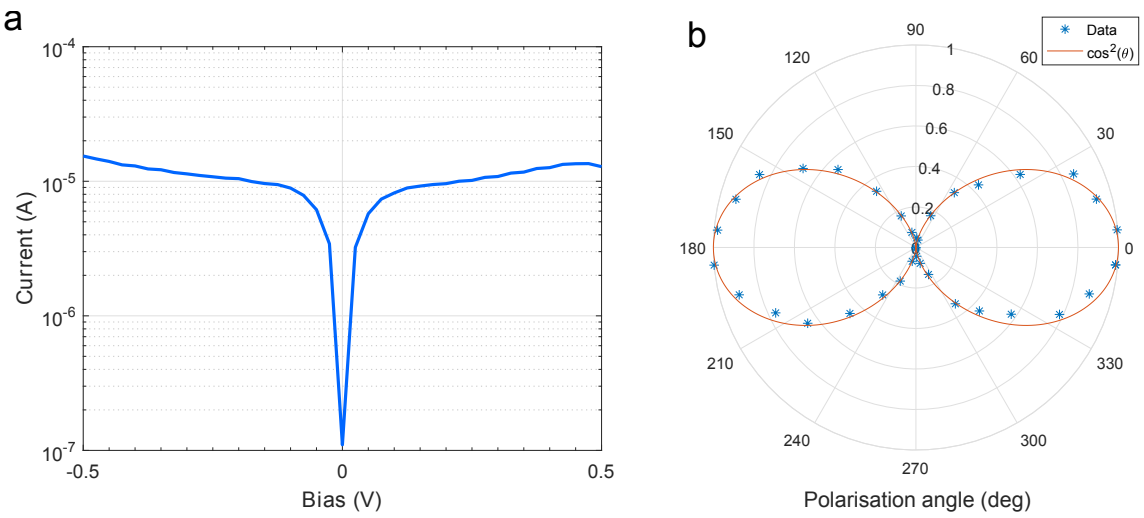

Figure 5.6: Measured I-V curve of the MSM photodetector **(a)**. Dependence of the normalized scattering intensity from MSM fingers from polarization of the excitation beam **(b)**.

The device was characterized optically using a 635 nm Thorlabs S1FC635 Benchtop Fiber-Coupled Laser Source. A combination of polariser with half-wave plate was used to produce and control the linear polarization of the beam. The half-wave plate AHWP05M-600 was mounted in a Thorlabs PRM1Z8 rotation stage. Utilisation of a Nikon CFI Plan Fluor x50 long working distance objective permitted the illumination of the coupling grating area. A polarization insensitive 50:50 beam splitter (Thorlabs BS013) was used to align the beam. A Stanford Research Systems SR570 current preamplifier was used to bias and amplify the photocurrent generated by the detector. The amplification coefficient and biasing voltage were fixed during all measurements and set to be 10 nA/V and 0.15 V respectively. The signal from the amplifier was then sampled by a National Instruments USB-6343 DAQ. The fingers of the photodetector act as a decoupling grating enabling the observation of surface plasmons by scattering. The laser beam was focused on the coupling grating and a half-wave plate was used to control beam polarization. The reflected image was captured using a DCC1645C CMOS camera. As can be seen from Figure 5.7b,c the scattering from the detector exists only when the electric field of the incident beam is perpendicular to the lines of the coupling grating (TM polarization), which confirms the excitation and guiding of the surface plasmon. The normalized scattering intensity as a function of polarization is shown on Figure 5.6b. The intensity follows Malus' law which is in agreement with theoretical prediction.

A scanning photocurrent microscopy (SPCM) technique was used to confirm

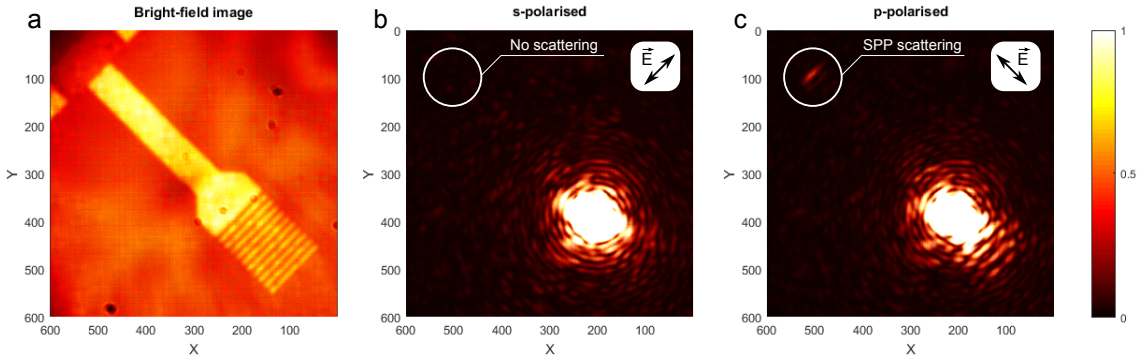

Figure 5.7: Bright-field image of a waveguide-coupled MSM photodetector **(a)**. Scattering from the fingers (circled) of 2.5 µm wide waveguide-coupled MSM photodetector for s (TE) **(b)** and p (TM) **(c)** polarization of the excitation beam respectively.

the functionality of the device. For SPCM measurements the same laser was used together with a Nikon CFI Plan Fluor x100 long working distance objective to obtain a highly focused spot (approximately 600-700 nm in diameter) and to scan the device footprint. The piezo-stage step resolution in both x and y directions was of approximately 100 nm. The MSM photodetector was biased at 0.15 V and the generated photocurrent was collected and correlated with the position of the beam. The scanning was performed for both TE and TM polarised light and the photocurrent maps were then normalized and subtracted one from another (I(TM)-I(TE), see Fig.5.8). As can be seen, the photocurrent is maximal when either the active zone of photodetector (due to the direct photon detection) or the excitation grating are illuminated. In the case of the in-coupling grating illumination, the generated photocurrent is higher for TM-polarised light due to surface plasmon excitation and subsequent detection by the MSM photodetector (see Fig.5.8). This confirms that the increase in the photocurrent near to the excitation grating is caused by the outcoupling of the surface plasmons into the photodetector active region.

Since the insulator-metal-insulator (IMI) waveguide structure [16] utilized in this device exhibits a strong attenuation constant due to its vertical asymmetry (the superstrate has a much smaller dielectric constant than the substrate), the intensity of the surface plasmons decay strongly as they propagate along the waveguide. To investigate the decay of surface plasmons four identical waveguide-coupled photodetectors with different lengths were fabricated and characterized using a similar setup that was used to obtain the scattering images (see Fig.5.7c,d). The laser beam was focused onto the coupling grating to excite surface plasmons on the waveguide. The

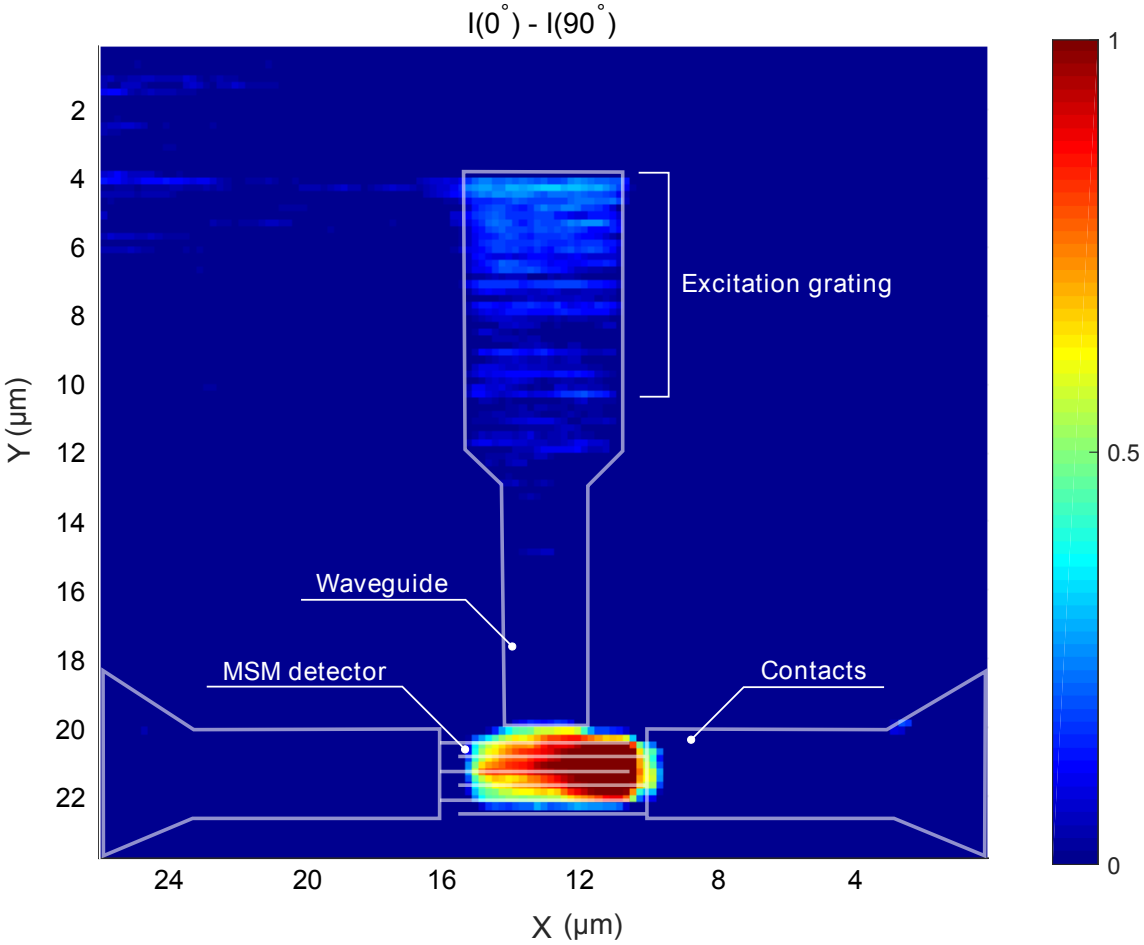

Figure 5.8: Difference of scanning photocurrent maps of a waveguide-coupled MSM photodetector obtained under TM (0°) and TE (90°) polarised 635 nm laser beam.

photocurrent from the detector was recorded during the rotation of the half-wave plate. For normalisation purposes the dark current of each detector was subtracted from the output signals. Figures 5.9a-d show the relation between the registered photocurrent and the polarisation state of the incident beam for 21.75, 16.75, 11.75 and 6.75 µm long waveguides respectively. As can be seen, the amplitude of the signal decreases with increasing length which is in a good agreement with expectations. The lower responsivity of the photodetector coupled to the 11.75 µm long waveguide could be due to imperfections introduced during the fabrication stage.

The root mean square value of each signal as a function of the waveguide length is shown in Figure 5.9e together with the calculated decay of the fundamental mode. Both curves show similar behaviour and reflect the decrease in RMS photocurrent as the waveguide length increases. As mentioned before, the waveguide utilized in this device can support higher order modes at a wavelength of 635 nm. Although, they have higher attenuation constants their impact on the power guided to the

detector can explain the difference in decay rates of the RMS photocurrent and the fundamental mode.

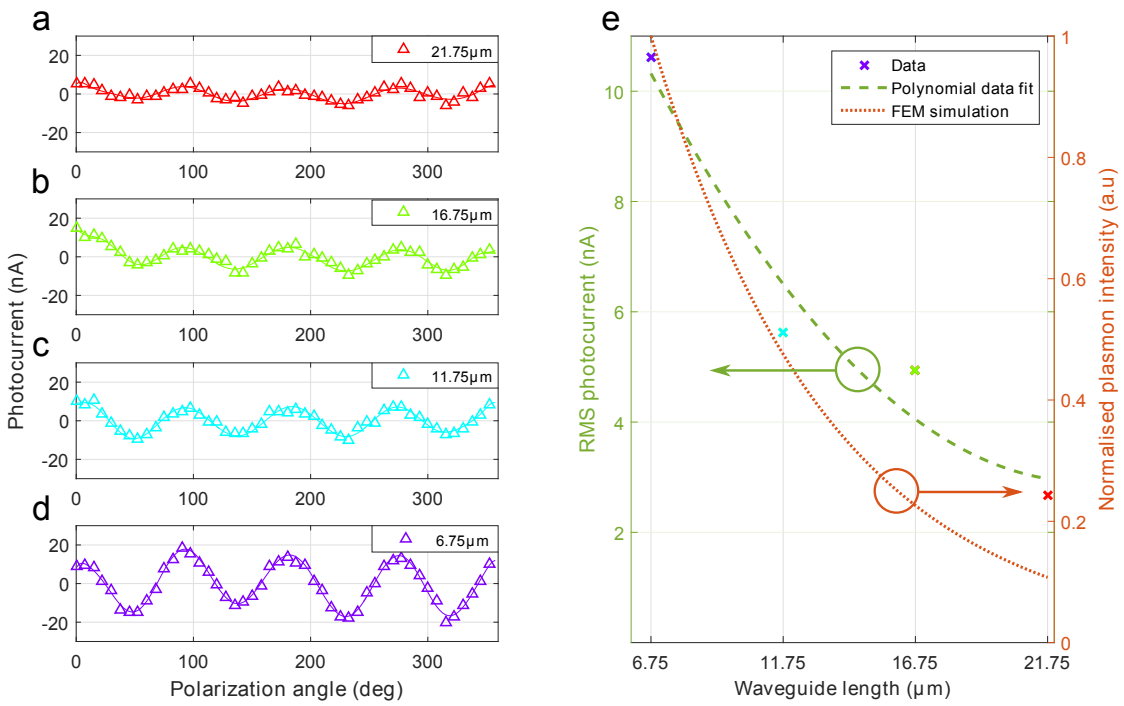

Figure 5.9: Photocurrect as a function of polarisation angle **(a-d)** for different waveguide lengths. Root mean square values of signals at each waveguide length (crosses) and normalised plasmon intensity (dotted line) are shown on **(e)**.

5.6 Conclusion

In this chapter a novel planar surface plasmon detection technique which could form a component of future high-speed integrated optoelectronic circuits has been proposed and experimentally demonstrated. Even though the device presented in this work was designed to operate in the part of visible spectrum, the architecture is flexible and permits adjusting the parameters such as operating wavelength (couping grating period), waveguide shape and materials. It is also possible to tailor the waveguide network by utilizing junctions which will allow to distributing the signal to multiple detectors.

In the next chapter the design of a plasmonic absorption modulator will be presented and steps towards its implementation will be experimentally demonstrated.

6. Progress towards a surface plasmon modulator

A fully functional plasmonic transistor requires a mechanism to control the propagation of surface plasmons. A major goal of active plasmonics, therefore, is to create a device capable of modulating an input signal. As mentioned before, surface plasmon polaritons have a remarkable feature - they are very sensitive to the properties of the surrounding media. Hence, the high degree of field confinement opens up the significant possibility of designing highly efficient modulators and perform modulation even on nanoscale dimensions. In this chapter a comprehensive theoretical and numerical study of waveguide-based surface plasmon modulator will be demonstrated. Furthermore, fabrication techniques of ITO and SiO_2 films as well as the characterisation of their properties will be presented. This study lays the fundations for future development of plasmonic modulators.

6.1 Design and theory of operation

Modulation of surface plasmons can be achieved by changing one or both of the real and imaginary components of the local permittivity of a plasmonic waveguide structure. Metal-insulator-metal waveguides can further enhance the electric field confinement and, in turn, enhance the interaction between SPPs and surrounding media. It was recently shown [20, 22] that this waveguide configuration enables a reasonably high modulation depth on the micrometer scale.

A change of the real part of the permittivity can shift the plasmonic resonance to shorter or longer wavelengths. In structures such as a Fabry-Perot interferometer, even a small change in the resonance wavelength can lead to a significant phase shift

in one of the arms and, in turn, lead to destructive beam interference at the output. Moreover, if the real part of the permittivity at a certain wavelength becomes negative, the behaviour of a medium changes from dielectric to metallic. This opens up the possibility of changing the characteristic impedance of the waveguide which enables a larger modulation depth.

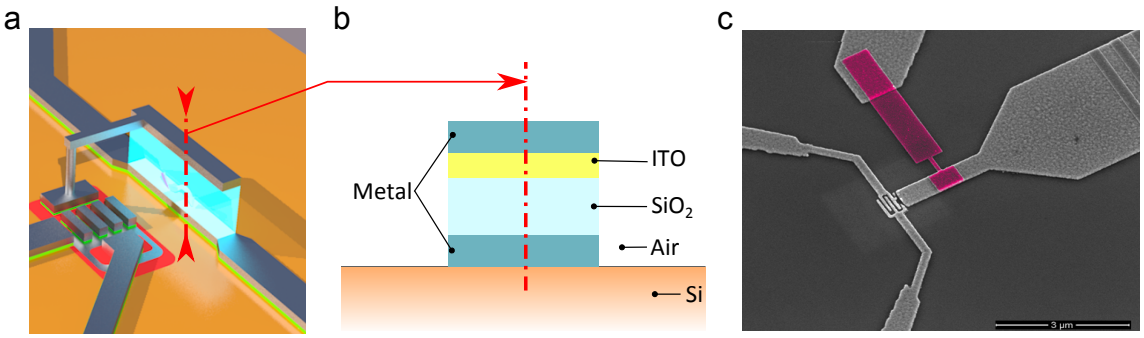

Figure 6.1: Schematic representation of a waveguide-embedded plasmonic ITO modulator **(a)**, its cross-section **(b)** and SEM image **(c)** of an implementation attempt (modulator section is artificially coloured in purple).

The losses in a dielectric are represented by the imaginary part of the permittivity. Therefore, the modification of this part will lead to a corresponding change of the absorption of electromagnetic waves, propagating in this medium. This type of modulator can be broadband [168] and operate at high speeds [169]. Absorption modulators are usually more effective than phase modulators in terms of power consumption and require a lower voltage to achieve a desired modulation depth compared to electro-optic modulators. This is essential for high-density integrated circuits and, hence, this approach was chosen to modulate the propagation of surface plasmons.

6.1.1 Metal-oxide-semiconductor capacitor structure

Unlike some other ITO devices designed to modulate the propagation of hybrid modes [90], the plasmonic modulator presented here is designed to modulate the propagation of a fully plasmonic mode and has a cross-section typical for metal-oxide-semiconductor (MOS) capacitors (see Fig.6.1). Furthermore, the design presented here can be easily integrated into waveguide-coupled MSM photodetector structure (see Chapter 5) completing a functionality of desired optoelectronic logic gate. Theoretical [170] and experimental [90, 171] studies of such structures showed a modulation depth up to -20 dB for a 20 µm long device [90] at telecommunication

frequencies. The modulator is based on a MIM waveguide configuration and consists of two metal slabs sandwiching dielectric and semiconductor layers. The choice of the semiconductor material depends on the operating wavelength. Silicon can be used for wavelengths longer than 1100 nm as it becomes transparent. It cannot, however, be used for shorter wavelengths (for example in the visible spectrum) since the associated propagation losses are too high. It was decided, therefore, to investigate indium-tin-oxide as an active medium to modulate propagation of surface plasmons.

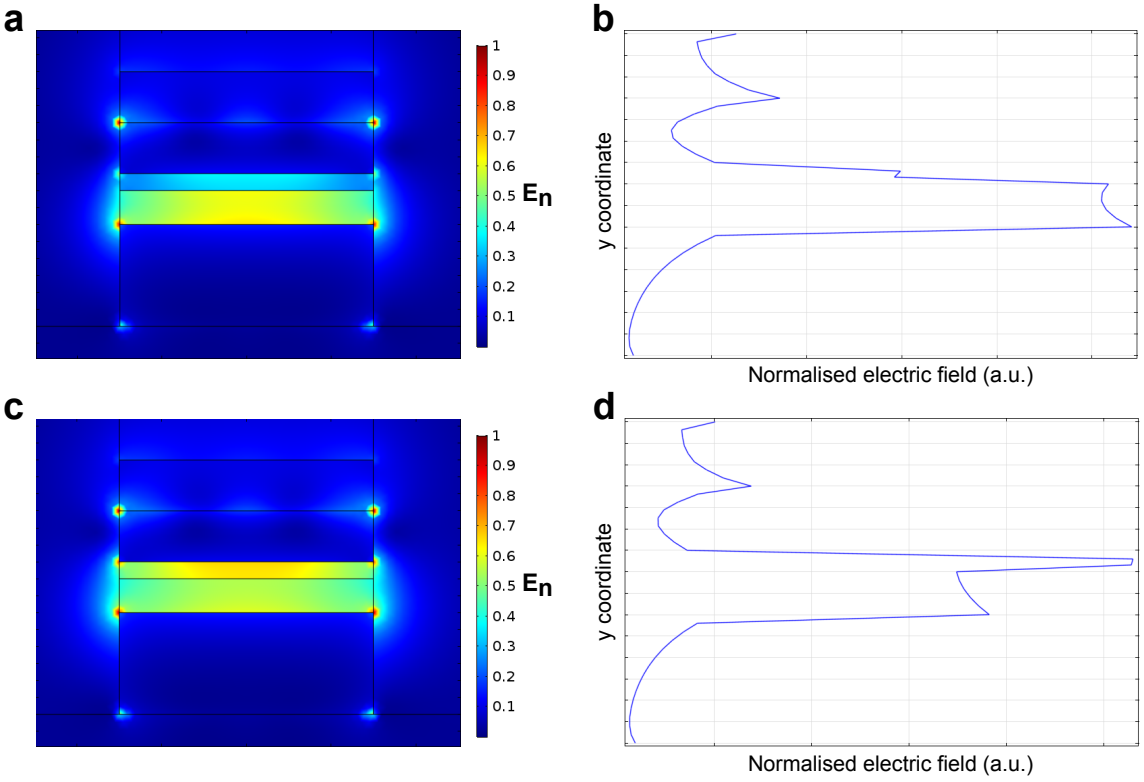

Figure 6.2: Normalised electric field map of the fundamental mode supported by the modulator in "OFF" **(a)** and "ON" **(c)** states respectively. Graphs **(b)**,**(d)** show the electric field distribution across the vertical cut-line through the middle of the waveguide.

The modulation principle is based on the modification of ITO layer properties. According to the Drude-Sommerfeld model [26], the permittivity of a material depends on the concentration of charge carriers (see Eq.6.1). Therefore, the application of an external potential to the metallic terminals leads to the formation of an electron accumulation layer at the ITO-SiO_2 interface. This causes a local change in refractive index in the ITO layer. Moreover, the growing carrier concentration leads to an increase in the imaginary component and a simultaneous decrease in the real component of the ITO dielectric permittivity.

In the 'OFF' state (see Fig.6.2a), due to the higher permittivity of ITO, the electric field is stronger inside the silica layer (see Fig.6.2b). In this state the SPPs can pass through the modulator without experiencing high attenuation as losses in the silica layer are negligibly small. On the other hand, in the 'ON' state, when a potential is applied to the metal contacts, the electric field is stronger inside the ITO layer. Since the imaginary part of the dielectric constant in ITO is much larger than in silica, the surface plasmons experience a stronger attenuation. The nanoscale dimensions of the structure open up the potential to achieve a deep modulation with a relatively low applied voltage of the order of several volts.

6.2 Waveguide-embedded plasmon modulator

As stated before, the relation between dielectric permittivity and charge carrier concentration can be found using a Drude-Sommerfeld model (see Section 2.1.3). Substituting (Eq.2.18) into (Eq.2.20) and assuming that the static permittivity and electron collision frequency remain constant (since the collision frequency has a negligible dependence on wavelength and carrier concentration [170]) the general relation between dielectric permittivity, surface plasmon frequency and carrier concentration can be written:

$$\epsilon_{ITO}(\omega) = \epsilon_{\infty} - \frac{n_e e^2}{m^* \epsilon_0} \frac{1}{(\omega^2 + i\omega\gamma)}, \tag{6.1}$$

where n_e is the electron density, m^* is the effective electron mass, e is the electron charge, ϵ_0 is the dielectric permittivity of vacuum, ω and γ are radial and collision frequencies respectively.

Equation 6.1 was used to evaluate the real (see Fig.6.3a,b) and imaginary (see Fig.6.3c,d) parts of the refractive index and dielectric permittivity as a function of wavelength for different carrier concentrations. The constants related to the ITO were chosen to be $\epsilon_{\infty} = 3.9$, $m^* = 0.35m_0$, $\gamma = 1.8\text{x}10^{14}$ rad/s [90].

As can be seen, the increase in the electron concentration (since ITO is a n-type semiconductor [172]) induces changes in the ITO layer behaviour from dielectric ($\Re(\epsilon) > 1$, $\Im(\epsilon)$ is small) to metallic ($\Re(\epsilon) < 1$, $\Im(\epsilon)$ is large) at a certain wavelength. For example a change in the carrier concentration from 10^{21}cm^{-3} to $5\text{x}10^{21}\text{cm}^{-3}$ at

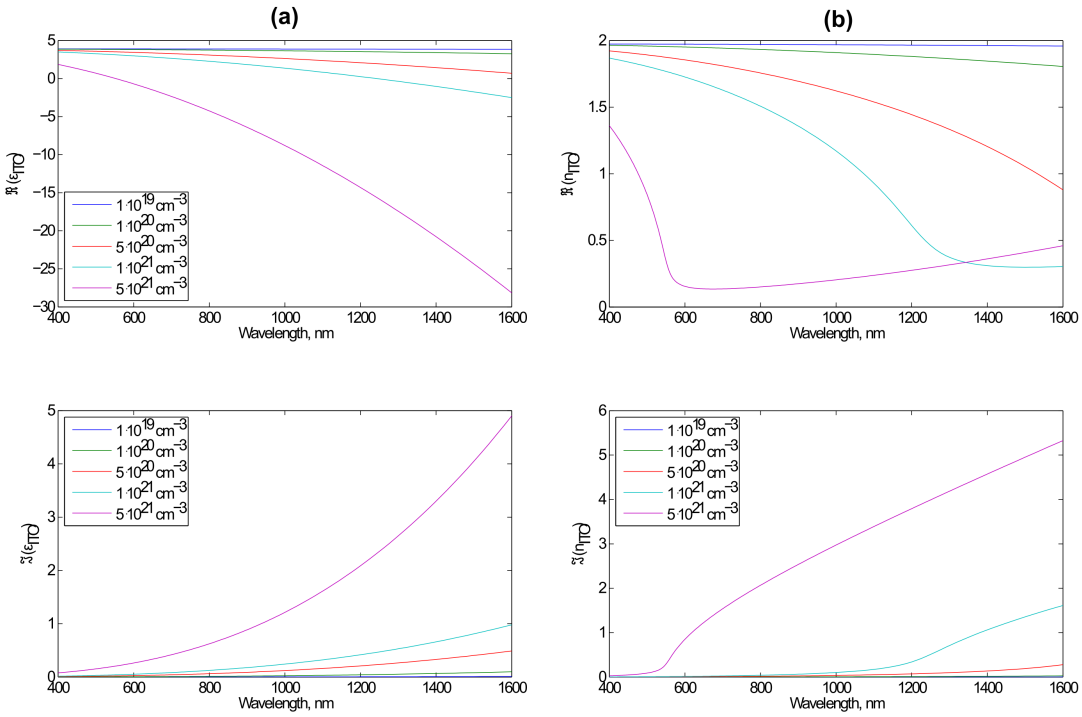

Figure 6.3: The dependence between the wavelength and the real **(a,b)** and imaginary **(c,d)** parts of the ITO permittivity and refractive index respectively. The colours represent different carrier concentrations.

a wavelength of 630nm increases the losses in the ITO layer by a factor of 60.

The relationship between the carrier concentration and the applied voltage can be extracted from Thomas-Fermi screening theory [173] (a special case of Lindhard theory). It provides a theoretical approach to calculating the kinetic energy of an electron gas in defined electrical potential $\phi(r)$ as a function of the electron density. This theory gives a satisfactory approximation without solving the Schrodinger wave equation.

According to this theory (a one-dimensional case is considered), the Fermi momentum for a system of electrons can be found using the following expression:

$$k_F(x) = \sqrt[3]{3\pi^2 n(x)}, \tag{6.2}$$

where $n(x)$ is the electron concentration. Therefore, the carrier concentration can be found re-arranging this to yield:

$$n(x) = \frac{k_F^3(x)}{3\pi^2}, \tag{6.3}$$

Also, the chemical potential of the system (Fermi level) can be described as:

$$\mu(x) = \frac{\hbar^2}{2m_{DOS}} k_F^2(x), \tag{6.4}$$

where $\hbar$ is Planck constant and m_{DOS} is an electron density-of-states effective mass [174].

Eliminating k_F from (Eq.6.3) and (Eq.6.4) and solving the equation for the variable n gives:

$$n(\mu) = \frac{1}{3\pi^2} \left(\frac{2m_{DOS}}{\hbar^2} \mu \right)^{\frac{3}{2}}. \tag{6.5}$$

The formula (Eq.6.5) shows that the concentration of charge carriers is proportional to power 3/2 of the chemical potential of the system. Considering the one-dimensional case for simplicity, the equilibrium chemical potential of the system with an applied voltage $\phi(x)$ can be found from following formula:

$$\mu(x) = \mu_0 + e\phi(x), \tag{6.6}$$

where μ_0 is the chemical potential or Fermi level, e is the electron charge and $\phi(x)$ is a function of potential at some point in the ITO layer. Substituting (Eq.6.3) and (Eq.6.4) into (Eq.6.6) gives:

$$n(x) = \frac{(2m_{DOS})^{\frac{3}{2}}}{3\pi^2\hbar^3} \left(\mu_0 + e\phi(x)\right)^{\frac{3}{2}}. \tag{6.7}$$

Equation (Eq.6.7) gives the distribution of electrons inside the ITO layer at position x. The Fermi level μ_0 can be calculated using the value of the initial carrier concentration in the ITO. The only unknown variable in this case is the distribution of the electric potential.

Poisson's equation can be used to find the potential distribution inside the modulator layers:

$$\frac{d^2}{dx^2}\phi(x) = -\frac{4\pi}{\epsilon}\rho_{ind}(x), \tag{6.8}$$

where ρ_{ind} is the induced charge density at a coordinate x and ϵ is the relative permittivity of a material (in this formula the CGS Gaussian units are used). In the ITO layer the induced charge is proportional to the difference between the electron density at x with an applied voltage and without it:

$$\rho_{ind}(x) = q\Delta n(x) = -e\left[n(\mu_0 + e\phi(x)) - n(\mu_0)\right]. \tag{6.9}$$

In the SiO_2 layer the induced charge density is equal to zero since there are no free charge carriers in this material. Substituting (Eq.6.9) into (Eq.6.8) and using the fact that $\mu_0 = \frac{\hbar^2}{2m_{DOS}}(3\pi^2 n_0)^{\frac{3}{2}}$, where n_0 is the initial electron density in ITO gives:

$$\frac{d^2}{dx^2}\phi(x) = \frac{4\pi e}{\epsilon}n_0\left[\left(1 + \frac{e\phi(x)}{\mu_0}\right)^{\frac{3}{2}} - 1\right]. \tag{6.10}$$

The expression (Eq.6.10) is a second order differential equation which describes the distribution of the electric potential inside the ITO layer. Solving this equation together with (Eq.6.7) gives the spatial distribution of the electron concentration.

To obtain the optical characteristics of the ITO layer in the absence and presence of the applied voltage, a system of two differential equations must be solved. Figure 6.4 shows a schematic representation of the modulator and the initial parameters for the 3-point boundary problem.

This system can be described by two differential equations, one for each region (ITO for $x \in [10\text{nm}; 0]$ and silica for $x \in (0; -20\text{nm}]$):

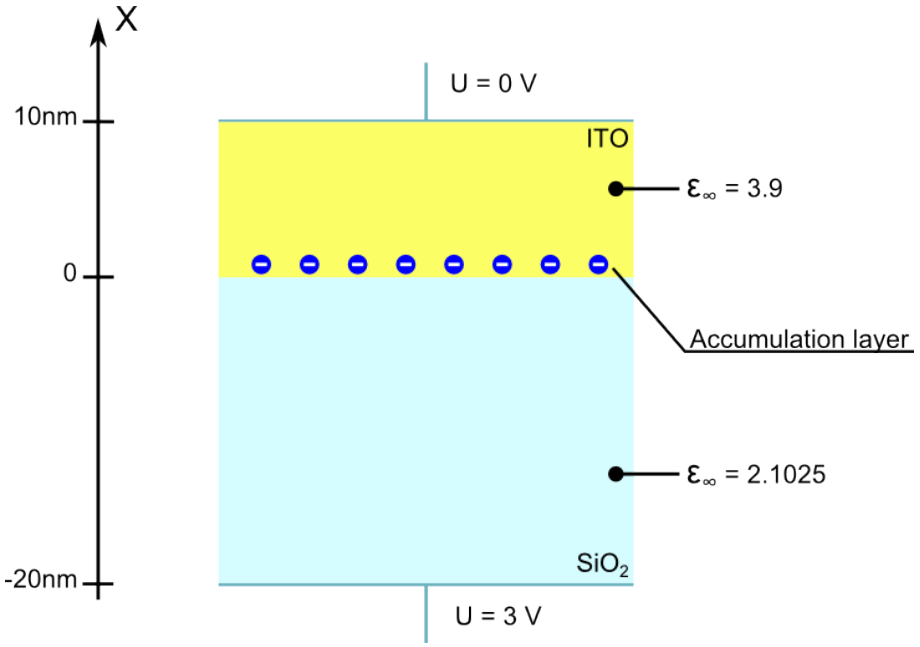

Figure 6.4: The schematic representation and initial parameters for the ITO plasmonic modulator model. One-dimensional case is considered.

$$\begin{cases} \frac{d^2}{dx^2}\phi(x) = \frac{4\pi e}{\epsilon_\infty^{ITO}} n_0 \left[\left(1 + \frac{e\phi(x)}{\mu_0}\right)^{\frac{3}{2}} - 1 \right] & , x \in [10\text{nm}; 0] \\ \frac{d^2}{dx^2}\phi(x) = 0 & , x \in (0; -20\text{nm}] \end{cases} \tag{6.11}$$

Also the continuity conditions for the potential and the electric displacement field must be satisfied at the interface between the ITO and silica ($x = 0$):

$$\begin{cases} \phi(-0) = \phi(+0) \\ \epsilon_\infty^{SiO_2} \left.\frac{d\phi(x)}{dx}\right|_{x\to(-0)} = \epsilon_\infty^{ITO} \left.\frac{d\phi(x)}{dx}\right|_{x\to(+0)} \end{cases} \tag{6.12}$$

The potential function $\phi(x)$ can be obtained by solving the set of equations (Eq.6.11) with the initial parameters $\phi(10\text{nm}) = 0$, $\phi(-20\text{nm}) = 3\text{V}$ together with the conditions (Eq.6.12) at the point $x = 0$. Figure 6.5 represents the potential distribution in the system.

Finally, the spatial distribution of the carrier concentration inside the ITO layer ($x \in [10\text{nm}; 0]$) can be found by using the expression (Eq.6.7) together with the potential distribution function $\phi(x)$ (the calculation performed for the initial carrier

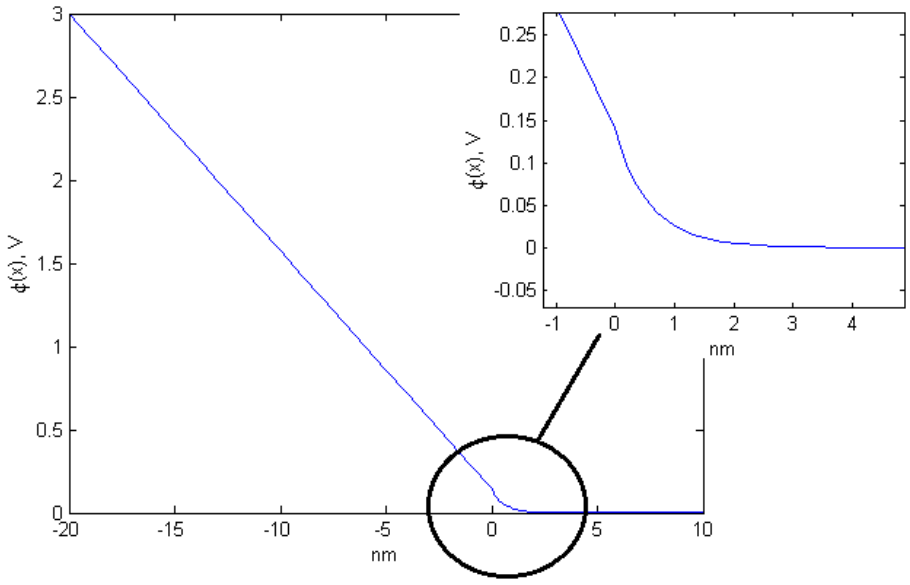

Figure 6.5: The potential distribution across the active area of the ITO modulator.

concentration of $n_0 = 10^{19}\text{cm}^{-3}$):

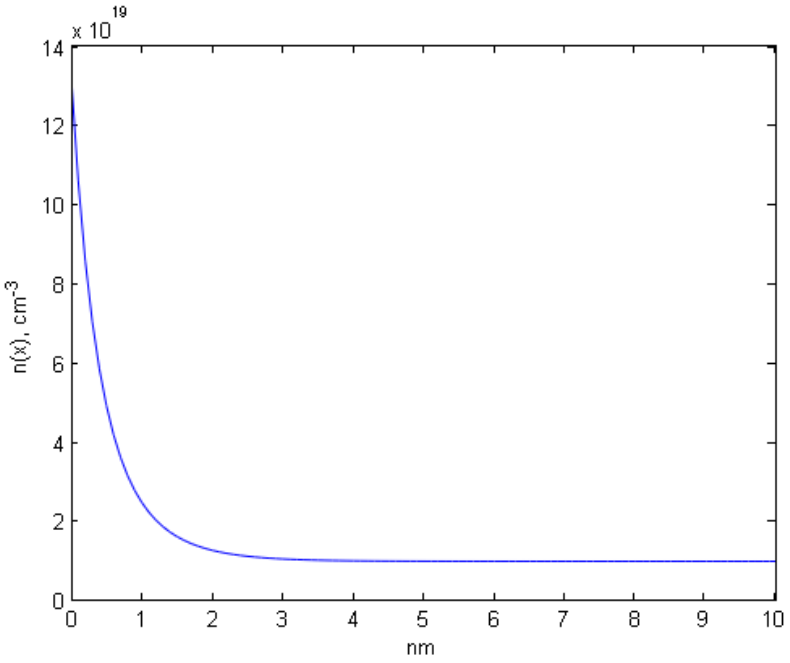

Figure 6.6: A charge carrier concentration profile of the ITO layer in the plasmonic modulator.

Figure 6.6 shows that with the voltage applied an accumulation layer is formed at the SiO_2-ITO interface. This, in turn, leads to a 14 fold increase in the carrier concentration. Therefore, by applying a potential of 3 V to the modulator it is possible to change the ITO permittivity from $\epsilon_{OFF} = 3.89 - 0.0006147i$ to

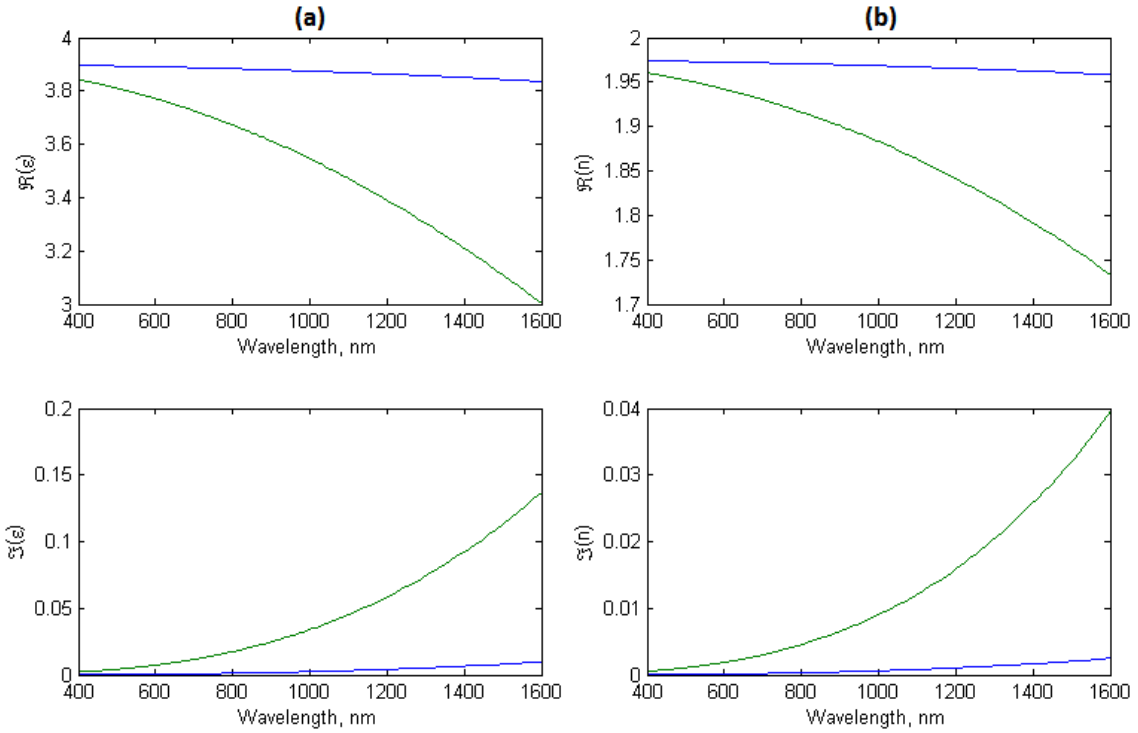

Figure 6.7: The real and imaginary parts of the dielectric permittivity **(a)** and refractive index **(b)** of the ITO layer in "ON" (green) and "OFF" (blue) states respectively.

$\epsilon_{ON} = 3.757 - 0.0086i$ at a wavelength of 632 nm. A mode analysis was performed using the calculated permittivity values to investigate surface plasmon absorption in the modulator in the 'ON' and 'OFF' states. The simulation showed that at a wavelength of 632 nm there is insufficient change in the imaginary part in the refractive index to give a useful modulation depth. For longer wavelengths the change in the permittivity is much higher (see Fig.6.7). and the modulation depth is much larger. Moreover, it was previously reported [90, 171] that the change in the carrier concentration in the accumulation layer is much stronger than the Thomas-Fermi screening theory predicts. This can be explained by a strong dependence of the ITO properties on the fabrication technology used (film deposition, annealing procedures). Therefore, the initial properties of the ITO film (fabricated using a particular technique) need to be determined to increase the simulation accuracy.

6.3 ITO film fabrication and characterisation

ITO films are usually fabricated by using either e-beam evaporation [175] or sputtering [176] techniques. The methods are similar and permits fabrication of films with a thickness ranging from tens of nanometers up to several microns. E-beam evaporation usually requires post-deposition annealing [177] to improve the film quality. Two samples were fabricated using these techniques and then characterised to determine the ITO film properties.

A p-type (boron doped) [100] silicon wafer with a bulk resistivity of 1-10 Ω·cm was used as a substrate for the samples. The wafer was placed into a HiTech Furnace and a 150 nm SiO_2 layer was grown using dry thermal oxidation. It was then cleaved into two pieces. One of the samples was placed into an IntlVac Nanochrome AC/DC sputtering tool and 125 nm of ITO were evaporated in an Ar environment. The composition of the ITO sputtering target was In_2O_3: 90% wt. SnO_2: 10% wt.

The second sample was loaded into the IntlVac NanoChrome II E-beam evaporator and an ITO film with a thickness of 12.5 nm was deposited at 0.8 Å/s. The sample was then annealed on a hot plate (in air) at 320° C for 15 min to anneal the film. During this step a substantial colour change was observed (from black to transparent).

6.3.1 Hall-effect measurements

The samples were measured using the van der Pauw method [178] to determine the bulk resistance, carrier density and mobility of the ITO films obtained by e-beam evaporation and sputtering. Firstly, both samples were cut into 3x3 mm pieces (see Fig.6.8) using a Disco DAD321 wet dicing saw. An aluminium foil was used to mask the ITO film everywhere except at the corners or the samples. The samples with the mask were then transferred to the e-beam evaporator and 60 nm of Cr were deposited at 0.5 Å/s rate. Finally, the samples were glued into ceramic LCC20 packages and bonded using a Kulicke & Soffa 4523 wedge bonder.

The determination of the ITO film parameters is based on the Hall effect. When the electric current is flowing through the sample between the opposing Cr contacts (see Fig.6.9) an applied magnetic field B deflects the electron flow to one of the other

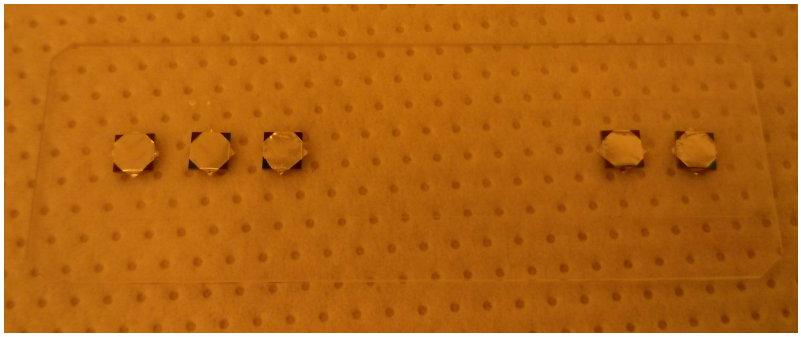

Figure 6.8: Photo of the ITO samples with Al foil as a shadow mask before the Cr contacts deposition.

electrodes the electrons experiencing the Lorentz force. An excessive concentration of the electrons near one of the electrodes results in a potential difference between it and other electrode. This potential difference is called a Hall voltage V_H.

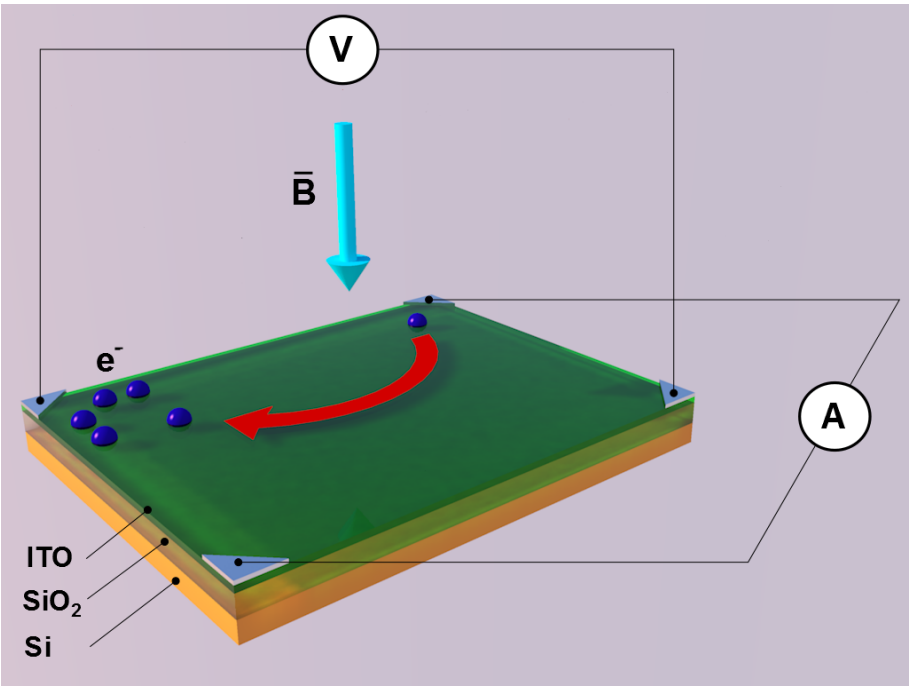

Figure 6.9: Schematic representation of a setup for the Hall Effect measurement of the ITO film.

The Hall voltage V_H is dependent on the current I flowing through the sample, the applied magnetic field B and the electrical properties of the semiconductor. Therefore, the desired parameters can be extracted from the following expression [179, 180]:

$$V_H = \frac{IB}{t} \cdot \frac{p\mu_h^2 - n\mu_e^2}{e(p\mu_h + n\mu_e)^2}, \tag{6.13}$$

where t is a film thickness, e is the electron charge, n and p are the electron and hole concentrations and μ_e and μ_h are the electron and hole mobilities respectively.

The Hall resistance R_{xy} is defined as:

$$R_{xy} = \frac{V_H}{I}. \tag{6.14}$$

A Janis ST-300S flow cryostat was used to control the sample temperature during the temperature-dependent analysis of the films. The temperature can be controlled from room temperature down to 77 K (liquid nitrogen was used to cool down the sample). Two room-temperature operated electro-magnets Kepco BOP72-28 were used to create a range of DC magnetic fields from -0.5 T to +0.5 T. The resistivity and Hall voltages of the films were extracted using a 4-terminal van der Pauw geometry. A Keithley 6220 current source, a Keithley 2000 voltage meter and a Keithley 6487 current-meter were used to set the reference current flowing through the sample and measure the voltage and current extracted from the remaining contacts respectively. A Keithley 7001 matrix switch module in combination with a Keithley 7065 Hall Effect expansion card were used together to cycle through the different current-voltage configurations in order to efficiently extract the longitudinal and the Hall voltages.

A sweep of the DC magnetic field from -0.5 T to 0.5 T was performed to analyse the samples with sputtered and evaporated ITO films. The measurements were repeated at room temperature and at 77 K in order to investigate the dependence of the film properties on the temperature. As can be seen from Figure 6.10 the Hall resistance of both samples shows a linear dependence on the applied magnetic field which means that the quantum Hall effect was not observed in these films. Table 6.1 shows the main properties of both ITO films.

The slope of the curves (see Fig.6.10) confirms that ITO is an n-type semiconductor. Both films displayed high carrier concentrations (see Tab.6.1) which results in a metal-like conductivity (degenerate semiconductor). The samples were also cooled down to 77 K and the measurements showed similar results which means that the

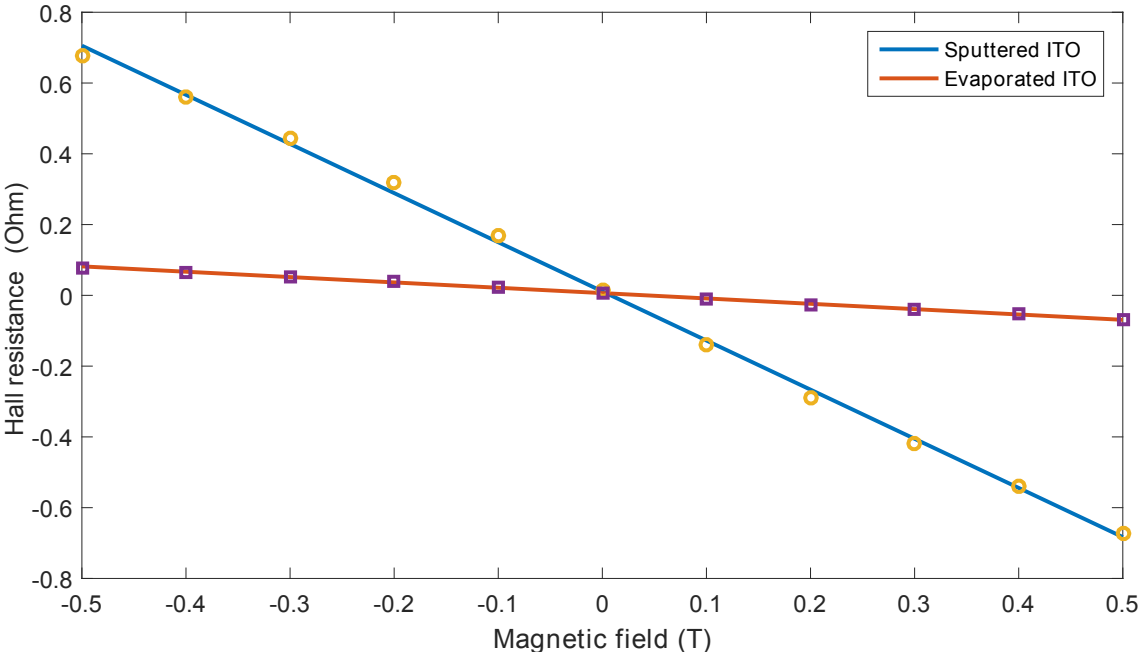

Figure 6.10: Hall resistance as a function of the applied magnetic field. Both samples showed a linear dependence from the magnetic field, although the sputtered ITO film has larger resistance compare to the e-beam evaporated.

Table 6.1: ITO film properties.

Film type	**Sheet resistance,** $\rho[m\Omega \cdot cm]$	**Carrier concentration,** $n_e[1/cm^3]$	**Carrier mobility,** $\mu_e[cm^2/(V \cdot s)]$
Sputtered	3.6	$3.31 \cdot 10^{20}$	5.1
Evaporated	0.815	$3.6 \cdot 10^{20}$	21.3

carrier concentrations in these films are independent of temperature. As can be seen from Table 6.1 the evaporated ITO film has a slightly larger carrier density and a much higher electron mobility which, in turn, results in a smaller bulk resistance of 0.815 $m\Omega \cdot cm$ (similar results were observed in [175]). The higher carrier concentration and mobility should enable a fast surface plasmon modulation even at short wavelengths (see Fig.6.3). Therefore, e-beam evaporation is the preferred method for ITO film deposition.

6.3.2 CV measurements

Capacitance-Voltage (C-V) measurements were performed to evaluate the insulating properties of the e-beam evaporated layer of SiO_2. The MOS capacitor structures

(see Fig.6.11) were fabricated on degenerately doped (bulk resistivity of 0.001-0.005 Ω·cm) n-type silicon. The substrate was cleaned using 65°C acetone, IPA and deionised water. The sample was then placed into an IntlVac NanoChrome II e-beam evaporator. The 5 nm thick adhesion layer of Cr was followed by 150 nm of Ag, 20 nm of SiO_2 and 10 nm of ITO deposited at 0.5, 0.8, 0.3 and 0.5 Å/s respectively. The sample was then annealed on a hot plate (in air) at 320° C for 15 min to anneal the film. A shadow mask with an array of holes with 0.5 mm diameter was placed on the sample. It was then returned into the evaporator and 60 nm of Ag was deposited at a rate of 0.8 Å/s. The sample was cleaved and glued into a LCC20 ceramic package. An In-Ga eutectic alloy was used to create an ohmic contact with the substrate (and, in turn, with the back plate of the MOS capacitors).

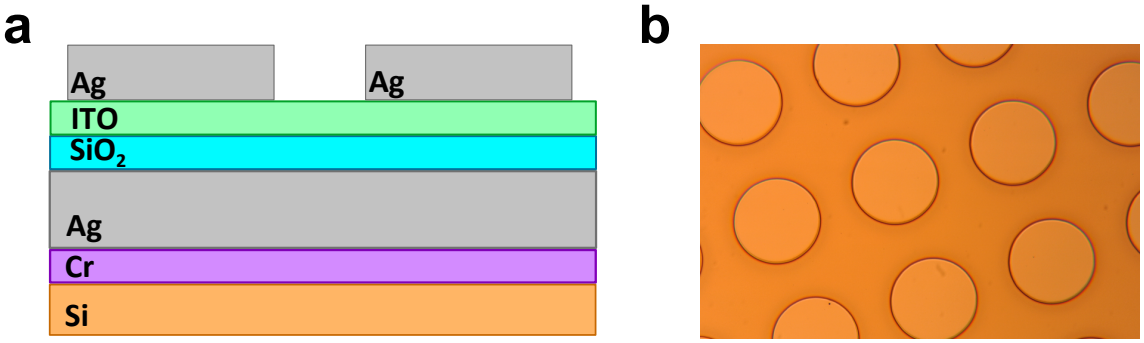

Figure 6.11: A schematic representation of the MOS capacitor structures **(a)** used for SiO_2 insulation properties determination and a photo **(b)** of the fabricated sample under 2.5x magnification.

A needle probe was successively brought in contact with the top electrodes of the MOS capacitors and a DC voltage offset sweep was performed to build a C-V dependence curve. As can be seen from Figure 6.12 the average capacitance of the structures is 1450 pF. The breakdown (characterised by a steep drop of the capacitance and rise of a leakage current) of the e-beam evaporated SiO_2 occurs around +0.25 V and -0.4 V respectively. The breakdown voltage remained relatively stable across the measured MOS capacitor structures.

Such a low breakdown voltage can be explained by the poor quality of the e-beam evaporated multicomponent oxide films [181]. The decomposition of the material during the evaporation leads to the formation of multiple holes. For thin films this results in a large decrease in the breakdown voltage. Note that for 10 nm of thermally grown oxide the breakdown was observed at 12 V [182] which is two orders of magnitude larger than the measured 0.25 V for the evaporated SiO_2 film.

The low breakdown voltage makes achieving the carrier density required for SPP

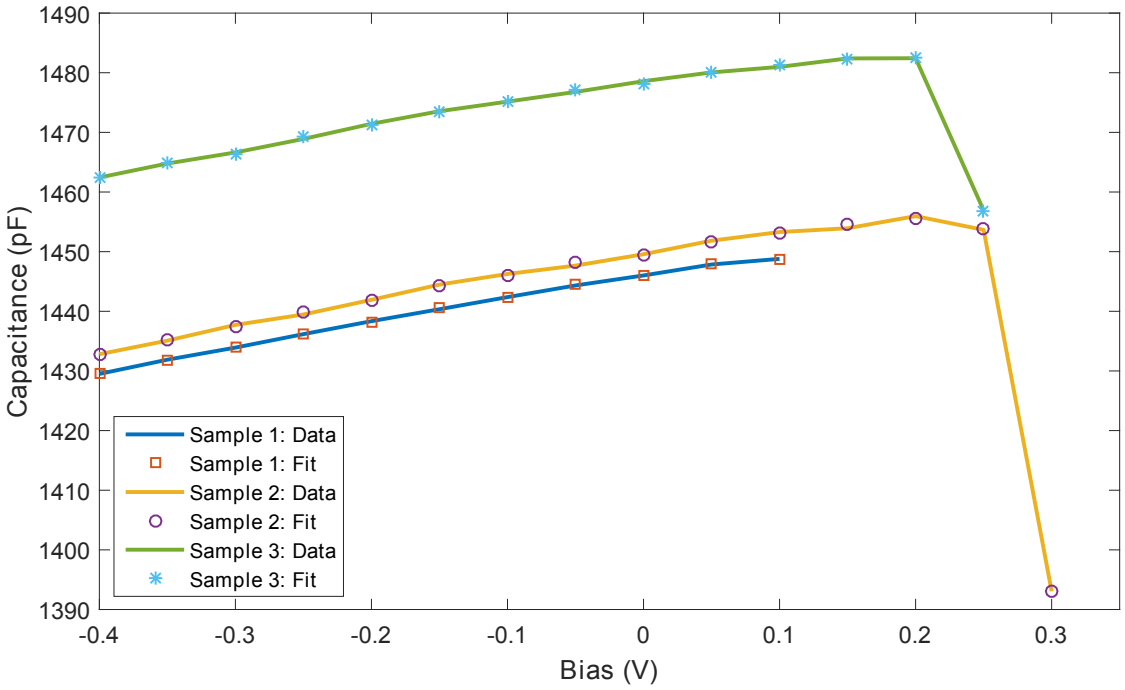

Figure 6.12: CV characteristics of 3 measured MOS capacitors. The breakdown occurs at -0.4 V and +0.25 V and remains stable among the samples.

modulation difficult. The quality of sputtered SiO_2 films was analysed previously by McCallum et al.[183]. Although the insulating properties of these films were slightly better (breakdown occurred around 1.3V), they were still insufficient to achieve a desired modulation depth. Therefore, another fabrication method for producing the insulating oxide is required. This may involve an atomic layer deposition (ALD) technique [184] or the utilisation of spin-on glasses such as HSQ [185].

6.4 Summary

In this chapter a comprehensive theoretical study of materials that could be used for a plasmonic absorption modulator on ITO has been presented. The modulator design is potentially capable of modulating the propagation of a fully plasmonic mode and can be easily embedded into the plasmonic stripe waveguide studied in the Chapter 4. The detailed principle of operation and analytical calculations required for the modulator design have been presented.

Furthermore, two fabrication techniques for producing ITO films were proposed and experimentally demonstrated. The properties of the films obtained by the e-

beam evaporation and sputtering techniques have been determined using the Hall-effect. The experiment showed that the ITO film deposited by evaporation has a higher electron mobility and carrier density and is, therefore, preferred for use in a modulator.

The insulating properties of the e-beam evaporated SiO_2 film have also been evaluated by performing C-V measurements. It was shown that this deposition technique results in a poor film quality which, in turn, leads to the large decrease of the breakdown voltage. The poor insulating properties of the silica layer will not permit achieving a sufficient plasmon modulation depth as a higher voltage is required to form a sufficient accumulation layer according to the calculations performed earlier in this chapter. The e-beam evaporation method is, therefore, inappropriate for the modulator fabrication and other methods such as ALD or the utilisation of spin-on glasses must be used.

7. Plasmonic interconnects summary

In Chapter 4 the task of developing a plasmonic input port capable of coupling far-field radiation to the surface plasmons was investigated using a grating coupler and stripe waveguide. The input port was designed to operate at the specific wavelength of 635 nm. Different designs were analysed using FEM simulation to obtain an optimal device structure. Several waveguide improvement techniques were proposed to decrease the losses associated with surface plasmon propagation. Mode analysis was undertaken and changes in the waveguide shape show the possibility of improving the propagation length of SPPs by a factor of up to 4.3 using a hybrid-shape waveguide in comparison with widely used rectangular cross section waveguides. Nevertheless, due to fabrication complexity in subsequent work it was decided to improve the propagation length by widening the stripe waveguide, rather than modifying the shape of the waveguide cross-section. This came at the cost of larger dimensions compared to the hybrid-shape waveguide cross-section design. A plasmonic input port was fabricated and experimentally analysed using NSOM, confirming its functionality and performance. The proposed structure is potentially CMOS compatible: the fabrication methods used to produce the samples were fully CMOS compatible, although gold is not a CMOS compatible material. Nevertheless, a spacer metals such as tungsten or titanium can be used to prevent gold migration into silicon. The same technique is used in modern microelectronics to isolate copper metallisation from the semiconductor. The structure is also very flexible, and could be adjusted to particular needs by using the design sequence described in this thesis. In summary, the proposed design of stripe waveguide coupled with a plasmonic input port presents an opportunity for compact plasmonic integrated circuits.

The plasmonic input port was then coupled with an MSM photodetector (see

Chapter 5) to enable in-plane detection of surface plasmons - an important feature required for successful integration into modern semiconductor technology. A numerical study of the MSM photodetector finger configuration was undertaken to find optimal parameters maximising the surface plasmon outcoupling into the photodetector active region. Considering the power flow optimisation and technological limitations the period and duty cycle were chosen to be 200 nm and 0.6 respectively and the total active area of the photodetector was 12.5 μm^2. The ability of the MSM photodetector grating to couple surface plasmons into the far-field was optically characterised using a CCD camera. The scattering detected from the grating confirmed the assumptions about grating performance. The photodetector was then characterised electrically by measuring the generated photocurrent. It was found that, as expected, the amplitude of the photocurrent depends on the polarisation of excitation wave and length of the waveguide. The proposed architecture is flexible and permits modifying the design for different operating wavelengths, waveguide configurations and materials.

In Chapter 6 a comprehensive theoretical study of an absorption-based SPP modulator on indium-tin-oxide was presented. The proposed device is capable of modulating the propagation of a fully plasmonic mode in a waveguide and could be embedded into the plasmonic input port. The detailed principle of operation and analytical calculations required for the modulator design were presented. Furthermore, two fabrication techniques for the required ITO films were proposed and experimentally demonstrated. The properties of the films obtained with e-beam evaporation or sputtering were determined using the Hall-effect. Both films displayed high carrier concentrations of $3.6\text{x}10^{20}$ cm^{-3} and $3.31\text{x}10^{20}$ cm^{-3} respectively which results in a metal-like conductivity. It was observed that the evaporated ITO film has a higher electron mobility (21.3 $cm^2/(V{\cdot}s)$ compared with 5.1 $cm^2/(V{\cdot}s)$ in the case of the sputtered film) which, in turn, results in a smaller bulk resistance of 0.815 $m\Omega{\cdot}cm$. The higher carrier concentration and mobility potentially enables fast surface plasmon modulation even at short wavelengths. Therefore, e-beam evaporation is the preferred method for ITO film deposition for plasmonic applications. The insulating properties of e-beam evaporated SiO_2 film were evaluated by performing C-V measurements. It was shown that this deposition technique results in a poor film quality which, in turn, leads to a large decrease in breakdown voltage. A breakdown of the e-beam evaporated SiO_2 occurs at applied potential lower than -0.4 V and higher than +0.25 V. The breakdown voltage remained relatively stable among the measured samples. The poor insulating properties of the silica layer are incompatible with a high modulation depth as higher voltages are required to

form a sufficient accumulation layer according to calculations performed here. It is, therefore, essential to use other deposition methods to obtain insulating films with sufficient breakdown voltage.

Future work on a hybrid optoelectronic logic gate with plasmonic interconnects will be discussed in Chapter 10.

8. Plasmon-enhanced photodetectors

The ability of localised surface plasmons to modify properties of semiconductor devices facilitates an opportunity of designing photodetectors with remarkable characteristics. Recently, novel plasmonic nanoantennas have been used in conjunction with Schottky and PIN photodetectors [57, 84, 186, 187]. The integration of plasmonic metasurfaces into conventional detectors opens significant potential to enhance their sensitivity [186], wavelength or polarisation selectivity [57] and to broaden their operating range via hot electron injection [84]. Polarisation and wavelength selectivity enabled by plasmonic metasurfaces are of particular interest as they permit designing nanoscale alternatives to conventional bulky optical systems. In this chapter two novel plasmonic-enhanced photodetectors will be described and discussed. The first photodetector is capable of detecting a polarisation state of the incident beam while the second integrates colour selectivity.

8.1 Plasmonic metasurface-enabled differential photodetector

8.1.1 Introduction

In this section two integrated photodetectors suitable for differential signalling and beam polarisation determination will be demonstrated. These detectors are based

Part of the work presented in this chapter has been published in Evgeniy Panchenko, Jasper J Cadusch, Timothy D James, and Ann Roberts. "Plasmonic metasurface-enabled differential photodetectors for broadband optical polarization characterization." *ACS Photonics*, 3(10):1833–1839, 2016

on planar metal-semiconductor-metal (MSM) photodiodes incorporating tailored arrays of plasmonic nanoantennas in the active region of each photodetector and are capable of discriminating between optical signals with different polarisations. Therefore, the detector generates a null response for only unpolarised light. The utilisation of aluminium provides broadband performance across much of the visible spectrum as well as significantly decreases the cost of the device. Each photodetector incorporating nanoantennas has a sensitivity tailored to different polarisation states. The devices are fully compatible with standard CMOS fabrication techniques as no noble metals such as Ag or Au were used. The approach presented here could be extended to the extraction of more comprehensive polarisation information from an optical field in the form of Stokes parameters as well as exotic polarisation states (for example azimuthal or radial polarisation) or different properties such as wavelength or phase. As a consequence, the design presented here demonstrates the potential for a new generation of compact, low-cost detectors which could be used in future optical systems.

8.1.2 Design and theory of operation

Utilization of plasmonic nanoantennas - the analogue of conventional antennas for optical frequencies - permits the creation of metasurfaces sensitive to particular polarisation states of light. The electromagnetic properties of such surfaces can be tailored by varying the geometry and constituent materials [26]. Most metasurfaces that consist of nanoantennas with a broken symmetry are intrinsically sensitive to the state of linear polarisation of an electromagnetic wave. The simplest and the most widely used antenna shape is the rod which behaves as an electric dipole. Such a geometry has two lower order plasmonic resonances (with dipole moments directed along the short and long axis) that depend on its longitudinal and transverse dimensions. Figures 8.1a,b show the distribution of the change density on the nanoantenna surface for transverse and longitudinal electric field orientation of the incident wave. In the cases of orthogonal states of circularly polarised light, nanorods do not exhibit a distinguishable difference in response due to the fully symmetrical geometry. To detect these polarisation states the symmetry of nanoantenna must be broken. Chiral nanoantennas [188, 57, 28] are utilised in order to distinguish between left and right circularly polarised light. An example of such structure is shown in Figure 8.1c,d.

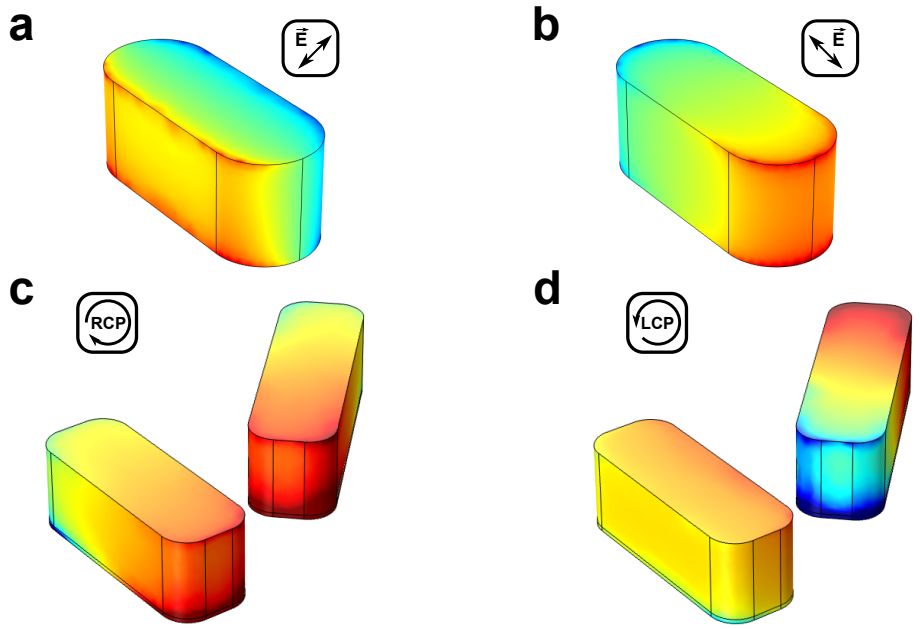

Figure 8.1: FEM calculated normalized distribution of charge density on the nanoantenna surface. Figures **(a)** and **(b)** show the cases when the electric field of the incident wave is perpendicular and parallel to the long axis of the nanorod respectively. Figures **(c)** and **(d)** show distribution of surface charge density on chiral nanoantennas illuminated with right and left circularly polarised light respectively.

The resonance condition increases the absorption in nanoantenna. This can, in turn, lead to a rise in hot-electron generation in the metal and, if the nanoantenna is connected to an electrical circuit, the generated photocurrent [84]. It also increases the reflection from the metasurface - the phenomenon used in plasmonic filters. The wavelength at which the resonance occurs is approximately proportional to the length of nanoantnna. As can be seen from Figure 8.2a for an Al nanoantenna design used in the linear-polarisation sensitive photodetector, stronger absorption is observed for a p-polarised incident field where the electric field is along the longest axis of the antenna at 780-800 nm wavelength. The weaker resonance (see Fig.8.1b) occurs for orthogonal polarisation of the incident beam around 550-600 nm. Note that both resonance curves have multiple local maxima. This can be explained by the presence of higher order modes of the structure due to the relatively large height of the nanoantenna, diffraction effects due to the high refractive index substrate as well as the large asymmetry between the dielectric permittivities of the substrate and superstrate [189]. Aluminium also has an inter-band transition around 780 nm which also affects the behaviour of the antennas.

Metasurface sensitivity is not limited to linearly polarised light. Creating a com-

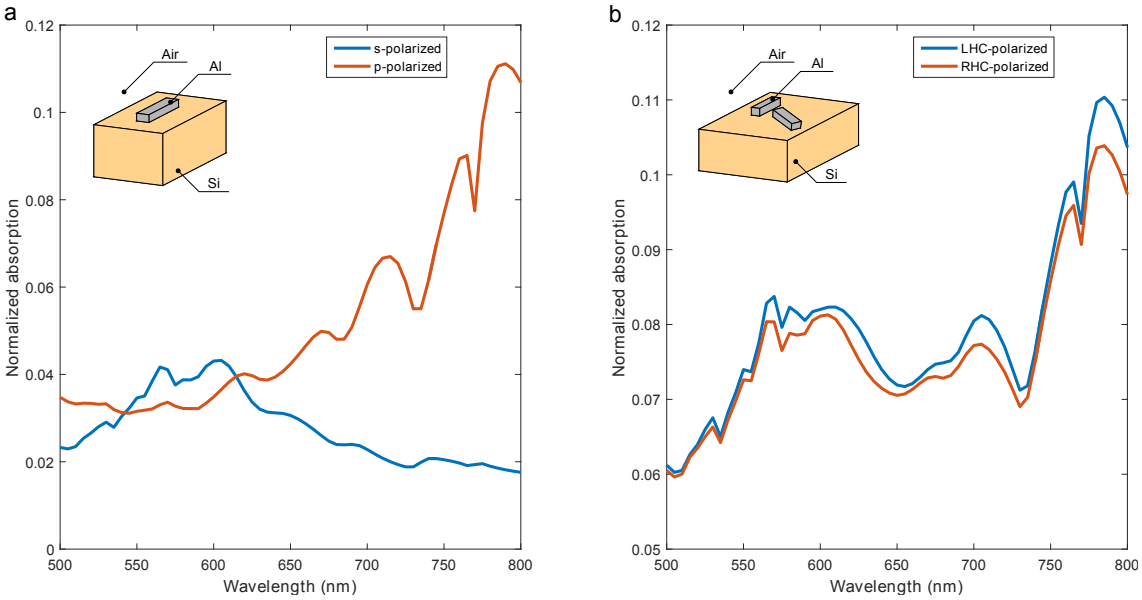

Figure 8.2: FEM calculated normalized absorption spectra for normally incident orthogonal polarisations for linear **(a)** and chiral **(b)** Al nanoantennas. The spectra consist of several distinct resonances.

posite antenna consisting of two appropriately located and oriented nanorods can create an antenna sensitive to other polarisation states such as left and right circular polarisation [188]. Figure 8.2b shows the absorption a metasurface composed of chiral nanoantennas in the case of both left and right circularly polarised light illumination. As can be seen, the difference between the two different polarisation states is much smaller than for the rod antennas and linear polarisation. This can be explained by the intrinsically weaker resonance in the planar nanoantenna metasurface used compared with 3D chiral structures [188]. The aforementioned surrounding conditions and antenna design further weaken the resonance. Nevertheless, Figure 8.1b shows a noticeable difference in absorption (and, therefore, reflection) in the nanoantenna for orthogonal polarisation states which is sufficient for device functionality. When a metasurface with these properties is placed in front of an active region of photodetector it behaves as a polarisation sensitive filter making this detector sensitive to one of the polarisation states.

As previously discussed, to permit a differential response two separate channels in each photodetector are required. These channels should have a different response to each orthogonal polarisation of the incident light. It was decided to demonstrate two photodetectors capable of distinguishing polarisation states of either linearly or circularly polarised light (see Fig.8.3). Each photodetector consists of three planar Al contacts twisted in a spiral (see Fig.1.13) to spatially match the circular beam

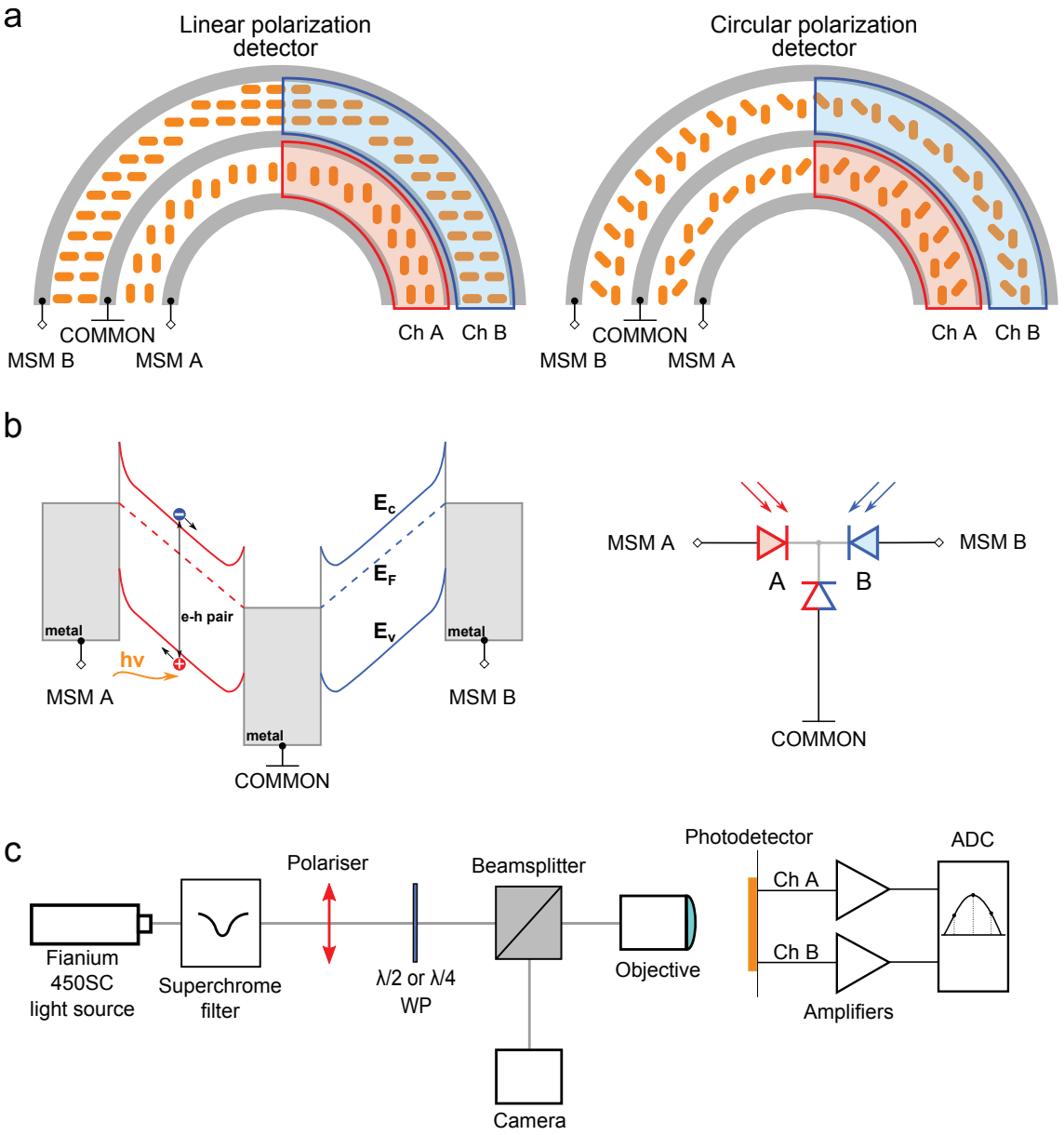

Figure 8.3: Schematic representation showing both channels of photodetectors integrated with nanorods to sense either linear (left) or circular (right) polarisation states **(a)**. Active areas of channels (A and B) are formed between common and signal contacts. A band diagram under bias and a circuit diagram of each photodetector are shown on **(b)**. E_v, E_c and E_F are valence, conduction and Fermi energy levels respectively. Experimental setup used to obtain wavelength-dependent differential photocurrent measurements **(c)**.

profile used. Furthermore, the overall circular shape of the detector opens up the possibility of differentiating cylindrical vector beams [190] and other orthogonal beams. The width of the contacts and the spacing between them were chosen to be 1.25 µm and 1.5 µm respectively. The diameter of the photodetector is 50 µm.

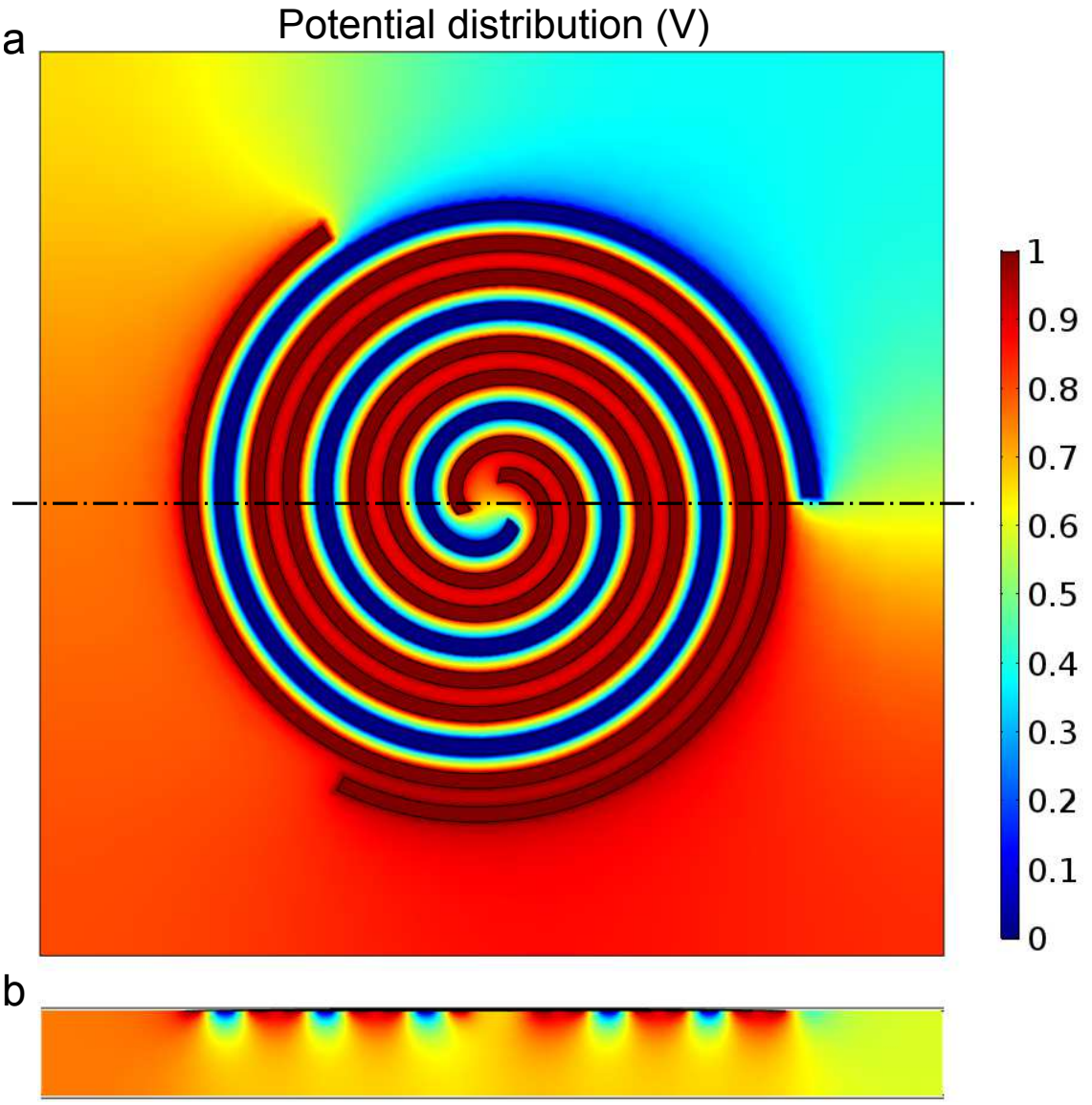

Figure 8.4: FEM calculated potential distribution on the surface **(a)** and inside **(b)** the silicon substrate of the differential photodetector under 1 V bias. Since there is no potential gradient between the signal leads (red) carriers generated within this region will not contribute to the output signal.

Each contact forms a Schottky barrier with the Si substrate. Taking the middle contact as common, the whole structure represents two metal-semiconductor-metal (MSM) [191] photodetectors connected back-to-back (see Fig.8.3b). A schematic showing the double MSM photodetector band diagram under bias is shown on Fig.8.3b. The biasing of the photodiode's contacts leads to the presence of an electric field gradient in the semiconductor substrate. Every electron-hole pair generated by absorption in Si (in the case where $h\nu > E_g$) will be swept by this electric field to the electrodes, thus creating a photocurrent. Figure 8.4 shows a potential

distribution on the surface (a) and inside (b) the silicon substrate under biased spiral photodetector. A dark blue region in Figure 8.4a represents an area under a common contact and is located between two others. As can be seen the gradient of electric field appears only between the common and signal contacts. At the same time the potential between two signal contacts (two dark red regions in Fig.8.4a) remains constant. Therefore, the charge carriers generated within this region will not contribute to the resulting photocurrent of each channel of the photodetector.

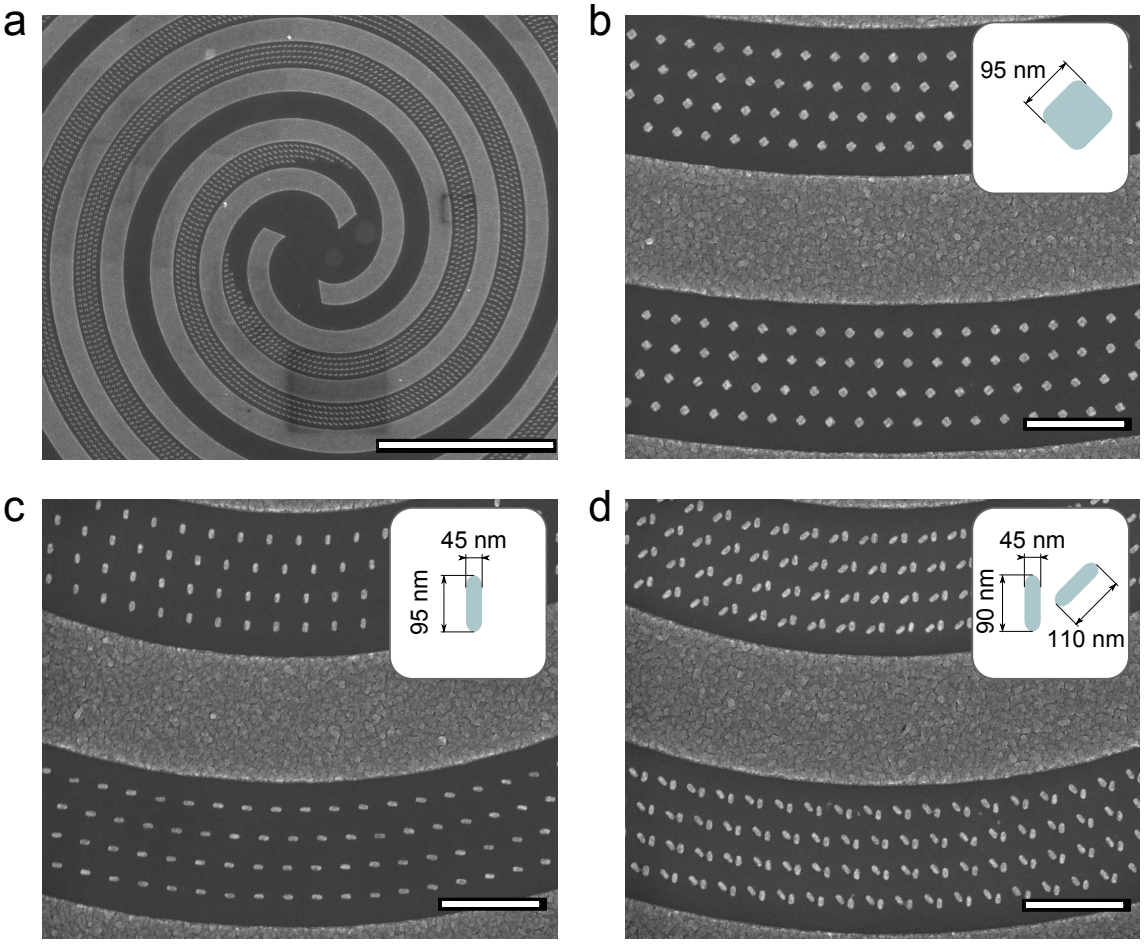

Figure 8.5: Scanning electron microscope image of the spiral photodetector **(a)**. Nanoantennas are absent between two signal contacts. The active regions with square **(b)**, rectangular **(c)** and chiral **(d)** nanoantennas respectively. The scale bar for image **(a)** is 10 µm and 1 µm for images **(b)**,**(c)**,**(d)**.

The photocurrent in each photodetector is determined by direct absorption of photons in their active regions. The number of photons transmitted into the Si and, hence, absorbed, is sensitive to the presence of nanoantennas on the surface and depends on their geometry. If the orientation of the antennas between each pair of contacts is different, there will be an imbalance between the photocurrents generated between each pair producing a polarisation-dependent differential signal. The

responsivity $R_q(\lambda)$ of each photodetector [85], therefore, is affected by the spectral response [84] of the metasurface:

$$R_q(\lambda) = \eta_0 \frac{L}{L+W}(1 - e^{-\alpha(\lambda)d})S_q(\lambda), \tag{8.1}$$

where λ is the wavelength and q describes the polarisation state of the incident field, $\alpha(\lambda)$ is an absorption coefficient of Si, d is the thickness of the MSM absorbing region, η_0 is a internal quantum efficiency, $S_q(\lambda)$ is the spectral response of the metasurface to the polarisation state q and L and W are the finger spacing and width respectively.

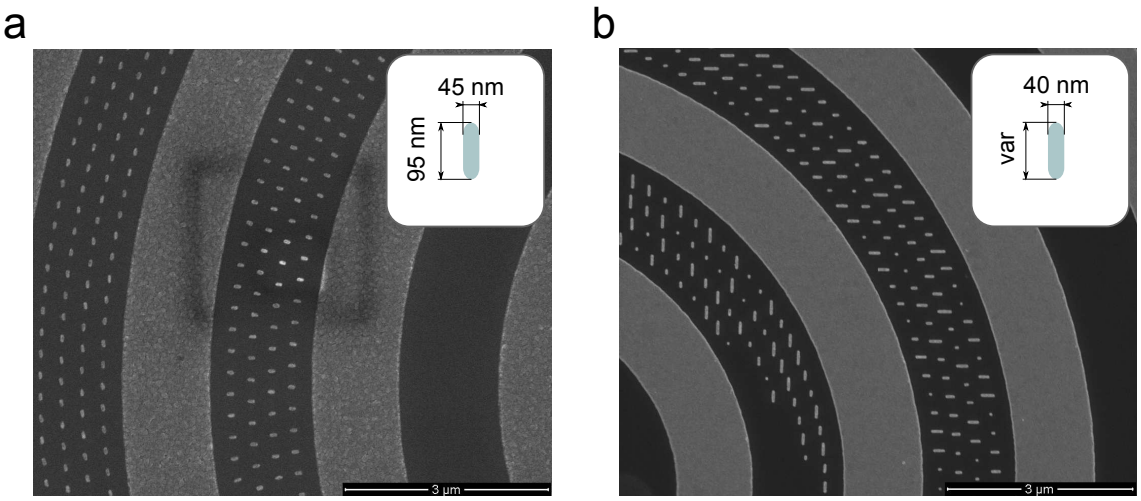

Figure 8.6: The detector shown in **(a)** is equipped with linear nanoantennas arranged to detect the polarization state of cyclindrical vectros beams (radial and azimuthal basis states). The design implemented in **(b)** consists of orthogonal linear gold nanoantenna of various lengths. It is designed to extend the operating wavelength range of the linear polarization detector from the visible into the near infrared region.

To tailor the sensitivity of each channel, nanoantennas were placed inside the photodetector's active regions (see Fig.8.5a). Each nanoantenna array responds to a different polarisation state. Two different sets of nanoantennas are used in the design presented. This produces a photodetector sensitive to orthogonal states of either linearly (see Fig.8.5c) or circularly polarised light (see Fig.8.5d). The wavelength of the photodetectors can be broadened even further by utilisation of nanoantennas with different lengths (see Fig.8.6b). A control photodetector with square nanoantennas (see Fig.8.5b) has also been designed. Since square nanoantennas have no preferential polarisation sensitivity this photodetector will generate a null response

for every possible polarisation state. In addition to that a photodetector suitable for detection of the polarization state of cyclindrical[192] vectros beams (see Fig.8.6a) has also been fabricated. This was not measured due to the malfunctioning of one of the channels.

The polarisation sensitive metasurfaces consist of arrays of Al nanoantennas. Single rectangular rods with a length of 95 nm and width of 45 nm were used to distinguish different states of linear polarisation. The second detector incorporates a superposition of two 45 nm wide rods with lengths of 90 nm and 110 nm respectively to create a single layer chiral structure which responds differently to left and right circular polarisation. These two rods were oriented at 45° to each other to maximise their chiral response [188]. As mentioned before, to reinforce the role played by the nanoantenna geometry a polarisation insensitive control detector consisting of arrays of square nanoantennas of side 95 nm has also been investigated. The spacing between these antennas was chosen to be 300 nm in both directions preventing near-field coupling. Nanoantennas and contacts were deposited in the same fabrication step and all have a thickness of 85 nm.

8.1.3 Fabrication

Photodetectors were fabricated on low doped [100] n-type silicon wafer with bulk resistance of $\rho = 1 - 10\ \Omega\cdot$cm. Aluminium was used as a material for MSM contacts and pads as well as nanoantennas. This choice of materials allows full compatibility with CMOS technology together with a low fabrication cost. The wafer was spincoated with 240 nm PMMA 950k resist and then exposed to create structures using a 100 kV EBPG5000+ electron beam lithography system. The pattern was developed in 1:3 MIBK:IPA solution for 1 minute. The native oxide layer on the silicon substrate was stripped using 4% hydrofluoric (HF) acid and the substrate was immediately loaded into IntlVac NanoChrome II e-beam evaporator. The aluminium layer with a thickness of 85 nm was deposited at 0.7 Å/s. After evaporation a lift-off step in pure acetone was performed. During the lift-off process the solution was heated to 60 °C. A wet dicing saw (Disco DAD321) was used to separate the photodetectors. The dies were glued into a ceramic LCC20 package and bonded using Kulicke & Soffa 4522D Wedge bonder with aluminium wire.

8.1.4 Experimental results

The optical characterisation setup is shown in Figure 8.3c. A Fianium SC450 supercontinuum white light source coupled with a Fianium SuperChrome VIS tunable filter was used to illuminate the devices at different wavelengths. Half (HWP) and quarter (QWP) wave plates were used to control the linear and circular polarisation states of the incident light to determine the detector's responsivity (HWP AHWP05M-600 and QWP AQWP05M-600 were fixed in a Thorlabs PRM1Z8 rotation stage). A wavelength sweep from 500 nm to 800 nm with 25 nm step and 10 nm bandwidth was performed to characterise the photodetectors. The photodetector was illuminated through a microscope objective with NA 0.4 to produce a spot. Utilisation of a Nikon CFI Plan Fluor x20 long working distance objective permitted uniform illumination of the entire photodetector area. A polarization insensitive 50:50 beam splitter (Thorlabs BS013) was used to align the beam. After alignment it was withdrawn from the system. A pair of transimpedance amplifiers were designed and fabricated to work with the differential photodetector (see Appendix A). The amplification coefficient was fixed on both channels and set to 10^6. A Keithley 487 source meter was used for precision biasing. The amplified photocurrent was recorded as a function of the rotation angle of the waveplates (the signal from the amplifiers was sampled by a National Instruments USB-6343 DAQ). A mean power of 2.5 µW (see Characterisation section for more information) and bias voltage of 3 V were maintained at each measurement during the experiment. For SPCM measurements a Thorlabs S1FC635 fiber-coupled diode laser and Nikon CFI Plan Fluor x50 long working distance were used to obtain a spot size of 1 µm. The piezo-stage step resolution in both x and y directions was of 200 nm.

An I-V characteristic of one arm of the differential photodetector with square nanoantennas is shown in Figure 8.7a. As discussed in the previous section, since this detector consists of two back-to-back Schottky diodes, the characteristic has no forward bias region. A slight asymmetry of the curve for positive and negative bias can be explained by possible contamination of the surface during fabrication or defects introduced when bonding the sample into a chip carrier. The photocurrent generated by the photodetector as a function of the incident laser power at 625 nm wavelength and 3 V bias is shown in Figure 8.7b. Each channel of the photodetector was found to have a total responsivity of approximately 0.08 A/W.

To illustrate the principle of operation and demonstrate device performance pho-

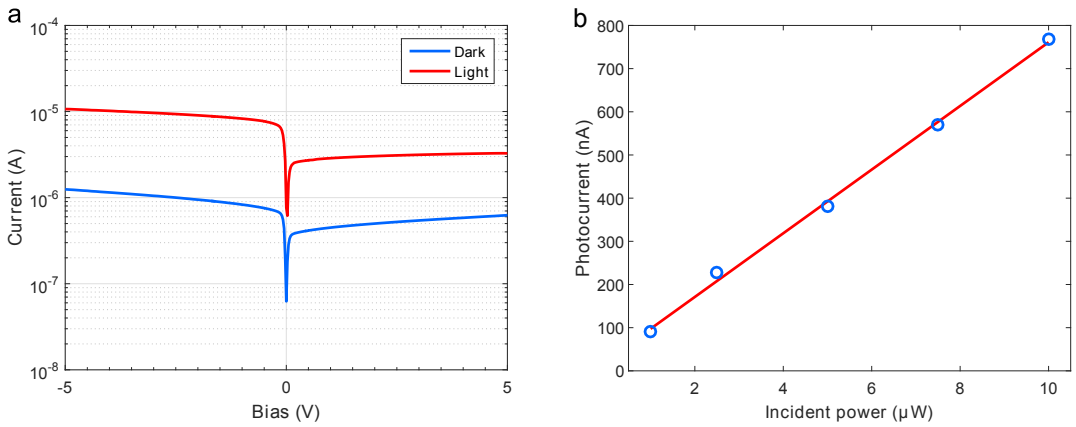

Figure 8.7: An IV characteristic showing the differential photodetector's channel in darkness and under illumination **(a)**. Generated photocurrent as a function of an incident power **(b)**.

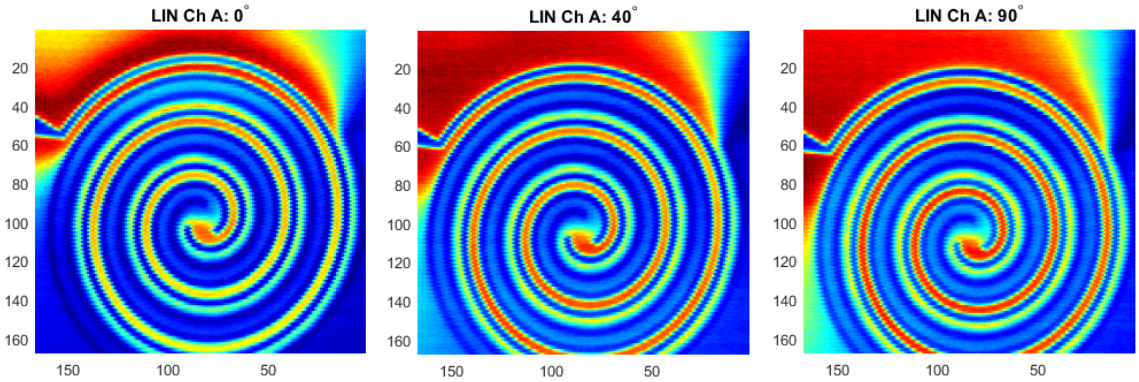

Figure 8.8: Normalised photocurrent maps of a single channel of linear-polarisation sensitive photodetector for different polarisation angles of the incident beam. The photocurrent generated by this channel increases with progression of the polarisation angle.

tocurrent maps of a differential photodetector with nanorod antennas (sensitive to linearly polarised light) were obtained using scanning photocurrent microscopy (SPCM) [142]. The spatial position of a highly focused, polarised beam was correlated with the photocurrent generated by each channel of the photodetector. These currents were then normalised and plotted together on the same scale. Figure 8.8 shows the photocurrent maps collected for channel A of the photodetector at different polarisation angles of the incident light. As can be seen, the photocurrent generated by this channel increases with increasing of the angle. Note that the spiral contacts of the detector form a diffraction grating and, therefore, have their own resonances. Even though the effects of this resonance is removed during normal operation (since it is present in both channels) it contributes to the resulting photocurrent and makes it harder to see the difference for single channel.

Figure 8.9 shows a photocurrent map of a section of the detector in normal operation mode when both channels are biased. As can be seen, the photocurrent generation in each channel is different for each linear orthogonal polarisation state. If the polarisation of the incident light is parallel to the long axis of the nanorods (p polarisation for Ch A) then there is a maximum in reflection from them resulting in lower photocurrent generation. This is in contrast to the hot electron generation regime when the photocurrent increases as a result of the higher absorption in nanoantennas [84]. Although this effect is also present in this device, it is negligible due to the much lower efficiency compared with direct photon absorption in Si. The photocurrent generated outside the photodetector active area is much lower since for MSM photodetectors the maximum in the electric field gradient appears between the contacts. The light blue lines represent the increase of the photocurrent when the area near the metal contacts is illuminated with a focussed beam. Such behavior can be explained by electron-hole pair generation within the depletion region of each Schottky photodiode which has a width of less than 300 nm for the materials used [193].

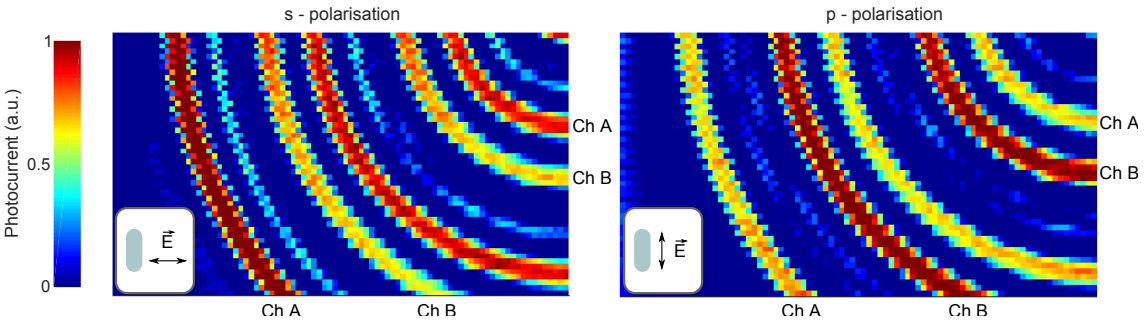

Figure 8.9: Normalised photocurrent maps of a photodetector with rectangular nanoantennas obtained with orthogonal polarisation states of the light. The nanoantennas of channel A (Ch A) and B (Ch B) are oriented along x and y axis of the graph respectively. The maximum photocurrent appears when the incident electric field is perpendicular to the long axis of the nanoantenna.

The normalised photocurrent at a wavelength of 625 nm produced by each photodetector integrated with either rectangular or chiral sets of nanoantennas is shown in Figure 8.10a,b,c as a function of HWP or QWP rotation angle respectively. Due to fabrication imperfections, each channel of the photodetector has a small variation in dark current. This results in a different offset of the output signal. For normalization purposes the dark current of each channel was subtracted from the output signals. A full rotation of a HWP takes 8 min during which the laser source exhibited significant intensity fluctuations (random changes in the output signal Fig.8.10a). The photocurrent from the detectors can also vary due to heating of the sample dur-

ing measurements (a constant slope of the signal Fig.8.10b). These fluctuations are reflected in the raw signals (see Fig.8.10a,b,c) from both photodetectors. Although the average value of the signals from each photodetector individually varies, the differential photocurrent (see Fig.8.10d,e,f) has a relatively constant mean. Since the variation of power affects both photodetectors and remains in-phase, a simple subtraction of photocurrents eliminates the influence of this type of noise. An optical system utilizing differential spiral photodetectors, therefore, is relatively insensitive to fluctuations in signal intensity compared with conventional devices. This significantly increases a signal-to-noise ratio [194] and, therefore, opens up the possibility of higher communication speeds.

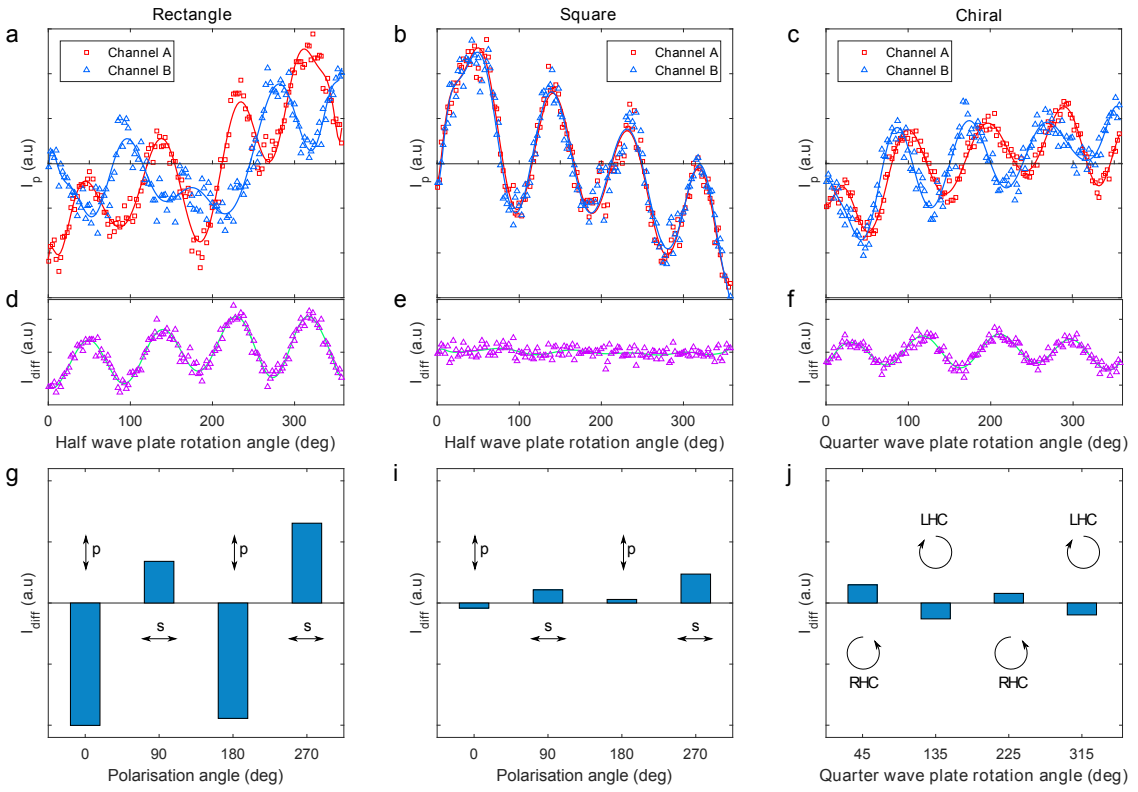

Figure 8.10: Normalised photocurrent affected by a signal power fluctuation from both channels of photodetectors with rectangular **(a)**, square **(b)** and chiral **(c)** sets of nanoantennas. As can be seen, differential photocurrent of each photodetector **(d)**,**(e)**,**(f)** is not affected by this type of noise. Figure **(g)**,**(i)** and **(j)** show the amplitude of the differential signal at each orthogonal state of polarisation. The rotation of HWP and QWP are relative to the fast axis of the polariser.

A nanorod antenna has a polarisation response of a simple electric dipole oriented parallel to the long-axis of the rod. The maximum in its induced dipole moment appears when the electric field of the incident beam is directed parallel to the long axis of the rod (s and p polarised light, see Fig.8.10g). As can be seen from Figure

8.10d in the case of the array of rectangular nanoantennas the differential photocurrent follows Malus' law. At the same time, the difference between the two channels in the case of square nanoantennas (see Fig.8.10e,i) remains zero for all polarisation states. Such behavior can be explained by the absence of a polarisation dependence in symmetric plasmonic nanoantennas.

In the case of the chiral metasurface (see Fig.8.11f), the differential response is a result of two phenomena. The superposition of two rectangular nanoantennas oriented at 45° to each other has a net dipole moment which is rotated 22.5° counter- or clockwise (depending on the structure) relative to the longitudinal dimension of each rod. The rotation of a QWP changes the polarisation of the beam from linear through elliptical to circular. In this case the effective linear component of the elliptical polarisation state varies from -22.5° to 22.5°. The maximum difference of the photocurrent occurs when the effective linear polarisation angle matches the net dipole moment of the chiral structure. At the same time the differential photocurrent changes for left and right circularly polarised light (see Fig.8.10j). As expected, the chiral response is weaker compared that of the linear detector since the circular dichroism for the 2D structures used is around 10-15% [188].

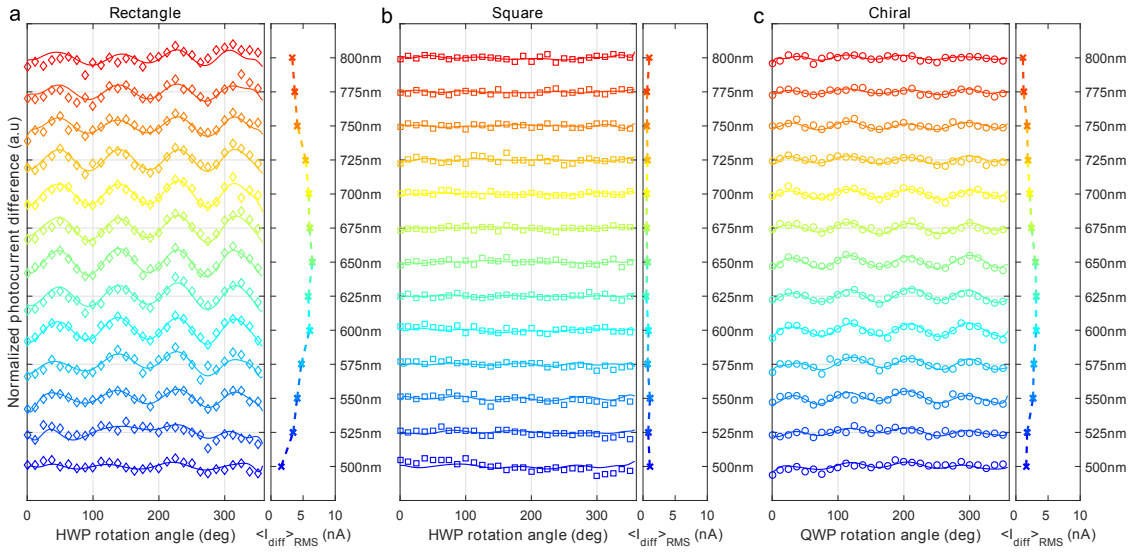

Figure 8.11: Differential signals at different wavelengths for photodetectors with rectangular **(a)**, square **(b)** and chiral **(c)** nanoantennas (the solid lines are polynomial fits of experimental data to guide the eye). The side graphs show root mean square values of photocurrent and reflect a differential responsivity at each wavelength.

The differential responses of photodetectors with rectangular, square and chiral nanoantennas for a range of wavelengths 500 nm - 800 nm is shown in Fig.8.11a,b,c.

Although the extinction ration is relatively large (especially for circularly polarised light), it can be distinguished since this photodetector utilises differential detection technique. For example the extinction ratio of linear polarisation plasmonic filter at 700 nm is equal to 0.32. It is, therefore, one of the advantages of proposed design. The insets in Fig.8.11 show root mean square values of photocurrent and reflect a differential responsivity at each wavelength. The use of Al as a material for the antennas produces a relatively broad plasmonic resonance [195] compared with other metals such as silver and gold. Although in most applications this is an unwanted characteristic, in the case of polarisation differential signaling it significantly reduces the sensitivity of the photodetector to signal wavelength drift and permits the use of the same design for each channel in wavelength division multiplexing systems. Operating at frequencies outside of the plasmonic resonance (below 575 nm) leads to a proportional decrease in metasurface polarisation sensitivity. This fact explains the lower amplitude of the differential signal for short wavelengths. The decrease in amplitude at wavelengths above 750 nm can be explained by the decrease in absorption coefficient in Si at these frequencies (see Eq.8.1).

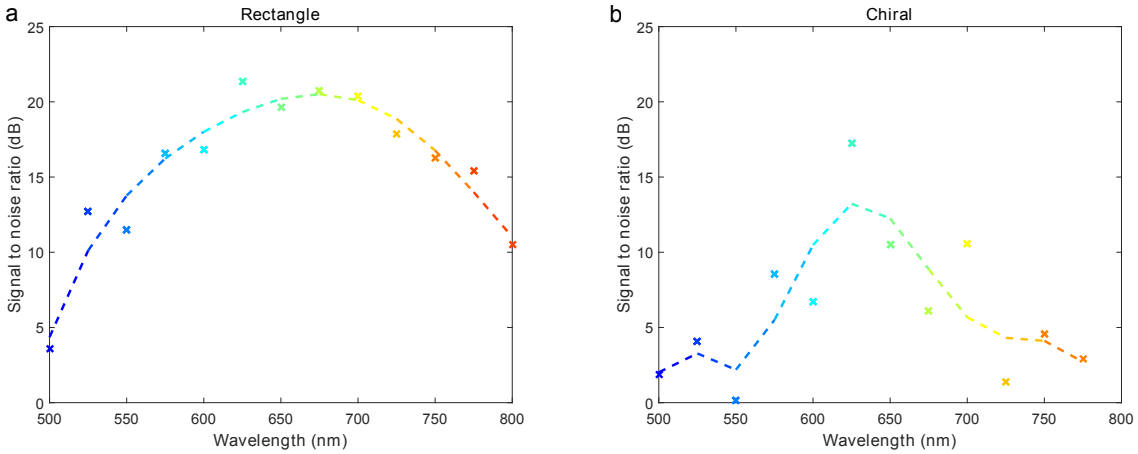

Figure 8.12: Measured signal to noise ratios for the linear **(a)** and circular **(b)** photodetectors. The line is a polynomial fit to guide the eye. The measured SNR is a function of both the antenna reflectivity and the Si MSM photodetector responsivity.

To calculate a spectral signal to noise ratio $SNR(\lambda)$ the signal generated by the photodetector with square nanoantennas was used as a reference:

$$SNR(\lambda) = 10\log_{10}\left(\frac{\sigma_{signal}(\lambda)}{\sigma_{ref}(\lambda)}\right)^2, \tag{8.2}$$

where λ is the wavelength, $\sigma_{signal}(\lambda)$ is the RMS average of the differential photocurrent from the photodetector with either rectangular or chiral nanoantennas and $\sigma_{ref}(\lambda)$ is the RMS average of the differential photocurrent produced by the photodetector with square nanoantennas as a reference (since this detector is insensitive to the polarization of the incident beam).

8.1.5 Summary

In this section a compact, fully CMOS compatible plasmonic, metasurface-enabled photodetector, suitable for differential determination of orthogonal polarisation states of light, has been demonstrated. The performance of two antenna designs suitable for the detection of different states of either linear or circularly polarised light has been experimentally demonstrated. Based on spiral design presented here, the differential photodetector can potentially be applied, along with a suitable antenna design, to determining other polarisation states of light, such as spatially modulated radially and azimuthally polarised optical beams. The differential nature of the photodetector ensures that in-phase noise associated with changes in incident intensity, thermal or operating frequency fluctuations are strongly suppressed in the measured photocurrent difference. Substituting Si with a lower band gap semiconductor would open up the potential of producing a device that could operate at near-IR wavelengths. This photodetector design, therefore, could play a role in future telecommunication systems permitting increased operation speeds and even higher channel multiplexing densities due to improved signal-to-noise ratios. Furthermore, the concept presented here also lends itself to the development of devices for the full determination of the Stokes parameters of an incident field and, taking advantage of recent developments in the design of metasurfaces for sensing wavelength [196] and phase [197], the concept could be extended to extraction of other information from optical fields.

8.2 Plasmonic camera pixel

8.2.1 Introduction

In this section a novel integrated camera pixel design utilising plasmonic effects will be presented. The pixels are based on the MSM photodetectors presented earlier in this chapter. Additionally, a pixel based on a conventional Schottky detector will be demonstrated. The detectors incorporate plasmonic filters implemented in the same fabrication step which will reduce fabrication costs. Each pixel design is capable of detection in the visible as well as in near-IR parts of the spectra depending on the nanoantenna geometry used. Finally, a polarisation sensitive pixel design is also demonstrated to indicate the flexibility of the approach.

8.2.2 Design and theory of operation

As mentioned before a simple digital camera colour pixel consists of a photosensitive detector with no preferential spectral sensitivity and a colour filter. The inclusion of the filter means that the intensity of the light at each photodetector includes information about the colour. The signal from each detector is then amplified, digitised and processed by the camera electronics. Simple methods interpolate the colour value of the pixels of the same colour in the neighbourhood [198]. The final picture, therefore, is a result of an algorithm which recovers a colour image from raw data. The program algorithm in particular and the camera characteristics in general depend on the type of filter. The colour filter type used most commonly in digital cameras is a mosaic Bayer filter [199].

In colour theory two main approaches are used to create a full palette by mixing base colours (see Fig.8.13a). The first technique is known as additive mixing [200]. Each of the primary colours can be represented by a bandpass filter applied to different parts of the visible spectrum (see Fig.8.13b). This model is similar to the way the human eye detects different colours. A simple Bayer filter based on an RGB model consists of multiply repeated 2x2 patterns (RGGB, see Fig.8.13c) composed of red, blue and two green cells. Additional green cells are used to reproduce the increased human eye sensitivity in this spectral range.

Another approach uses secondary colours [201, 200] as a base - cyan, yellow and

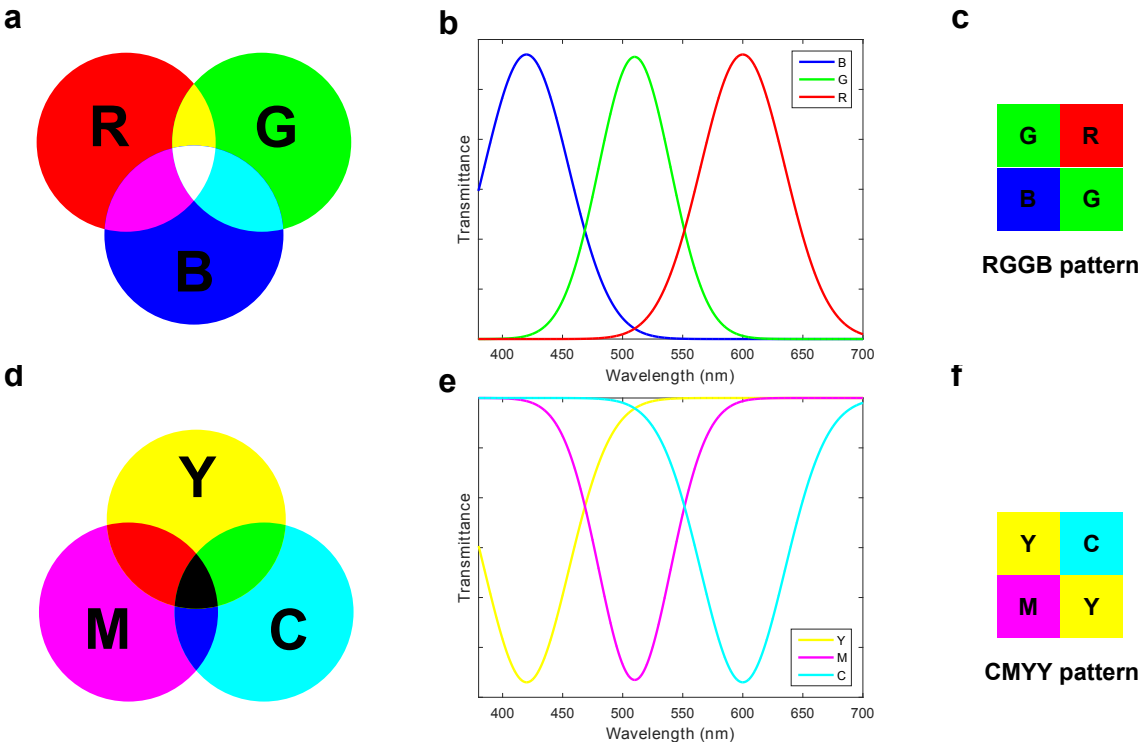

Figure 8.13: Two main colour schemes used to create a full gamut: RGB **(a)** and CMY **(d)**. Each main colour in the model is represented via bandpass **(b)** or rejection **(e)** filters. The colour filter used in digital camera consists of either RGGB **(c)** or CMYY **(f)** patterns depending on which colour model is used.

magenta (see Fig.8.13d). This method implies that colours are created by subtracting (absorbing) parts of the spectrum of light present in white light. Therefore, the resulting colour is called 'subtractive'. Each of the secondary colours can be represented by a rejection filter (see Fig.8.13e). Similar to the Bayer filter, the pattern used in digital cameras based on the CMY colour model consists of cyan, magenta and two yellow colour cells (see Fig.8.13f).

Digital cameras based on the CMY colour scheme provides better characteristics in terms of sensitivity. This is a consequence of the utilisation of bandpass filters in RGB-based pixels. Each of the red, green or blue filters blocks 2/3 of the incident light intensity. Only 1/3 of the intensity, therefore, reaches the photodetector. In contrast the CMY colour filters block only 1/3 of the incident light leading to a higher overall sensitivity of the sensor. RGB filters, however, provide better colour reproduction [202]. This is essential for high definition and scientific cameras and, therefore, RGB filters are a preferable approach to designing of a plasmonic pixel.

It was recently shown [37] that plasmonic nanoantenna structures based on the

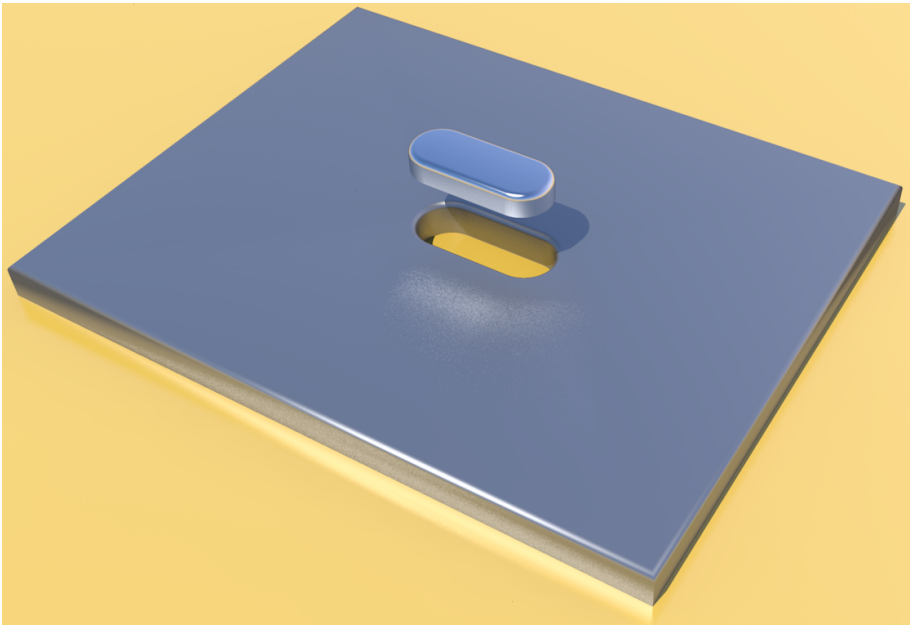

Figure 8.14: Schematic representation of a simple perfect absorber structure.

principals of a perfect absorber [203] can be used to create CMY colour filters. The technique allowed the fabrication of plasmonic pixels which are capable of producing a wide colour gamut [196]. These filters were designed to operate in reflection mode and showed moderate insensitivity to the viewing angle as well as a strong polarisation response. A similar approach is used here to create colour filters for plasmonic camera pixels.

Figure 8.14 shows a schematic representation of a simple perfect absorber structure. It consists of a nanohole in a metal film with a nanoantenna 'floating' above the surface. The principle underlying plasmonic perfect absorbers is based on the coupling between the nanoantenna and Fabry-Perot resonances of the supporting dielectric. Due to the fast electric field decay with vertical distance the effect is observed only when the distance between nanoantenna and an underlying film is less than a wavelength (permitting near-field coupling) [37]. The overlap between the resonances increases the quality of the plasmonic response significantly. In the plasmonic pixels presented here, silicon pillars are used to support the nanoantennas above the metal surface (see Fig.8.15). Silicon is very absorbing in visible spectrum and since it has a very large refractive index at these wavelengths, the distance between the nanoantenna and back mirror is larger than a wavelength at the operating frequency (in silicon). The coupling between them is, therefore, weak and the responsivity of a colour filter is primarily defined by the nanoantenna resonance.

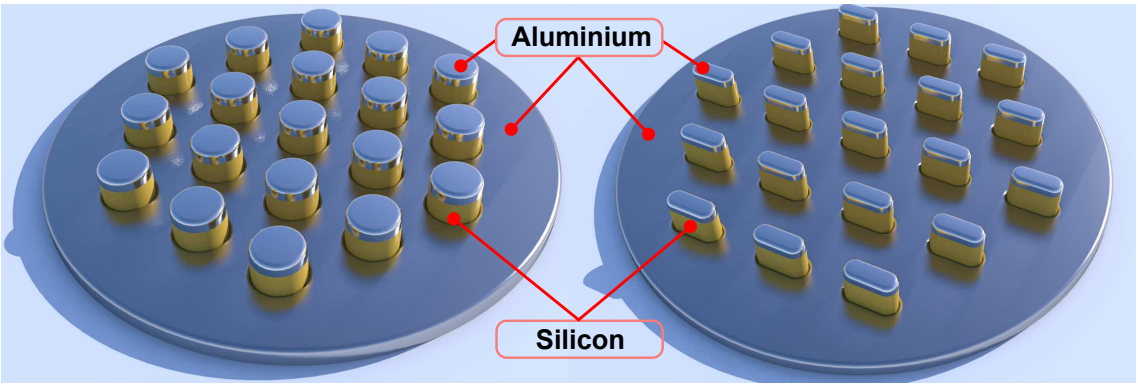

Figure 8.15: Schematic representation of two sets of plasmonic filters used in plasmonic camera pixel design. A filter composed of circular **(left)** and rectangular **(right)** nanoantena sets will show null or high polarisation responsivity respectively.

FEM simulations were performed to determine suitable parameters for the nanoantennas for each of the colour filters. The thickness of the metal and the height of supporting silicon pillar were chosen to be fixed at 50 and 230 nm respectively. In the case of the nanorod design the rod width was held constant at 35 nm during the sumilation. The antennas were arranged in a hexagonal lattice with side length of 200 nm. Parametric sweeps from 400 - 1500 nm wavelength and over nanorod lengths from 50 - 250 nm (or diameter in case of circular nanoantennas) were performed. Figure 8.16a shows the calculated, normalised absorption spectrum of a plasmonic colour filter as the nanoantenna length changes. Several phenomena such as LSP resonances, effects associated with periodic array diffraction and mode coupling between the nanoantenna and metal film all contribute to the spectra giving a vast parameter field for optimisation. Using the simulation results suggests three nanoantennas with lengths of 180, 100 and 60 nm to create plasmonic filters for red (see Fig.8.16d), green (see Fig.8.16c) and blue (see Fig.8.16b) parts of the spectrum respectively. Note that simulation of highly asymmetric structures such as plasmonic nanoantenna on a silicon substrate surrounded by air is very complicated and computational resource demanding [189]. It is, therefore, possible to perform only a coarse estimation of nanoantenna dimensions and detailed quantitative predictions were not possible.

Utilisation of Schottky photodetectors extends the sensitivity of the plasmonic pixels outside the visible spectra. A similar approach can be used to create an infrared plasmonic pixel. In this case the filtered photon flux is absorbed in the metallic back mirror resulting in hot-electron generation which can overcome the Schottky barrier and contribute to photocurrent. Since this process has a signifi-

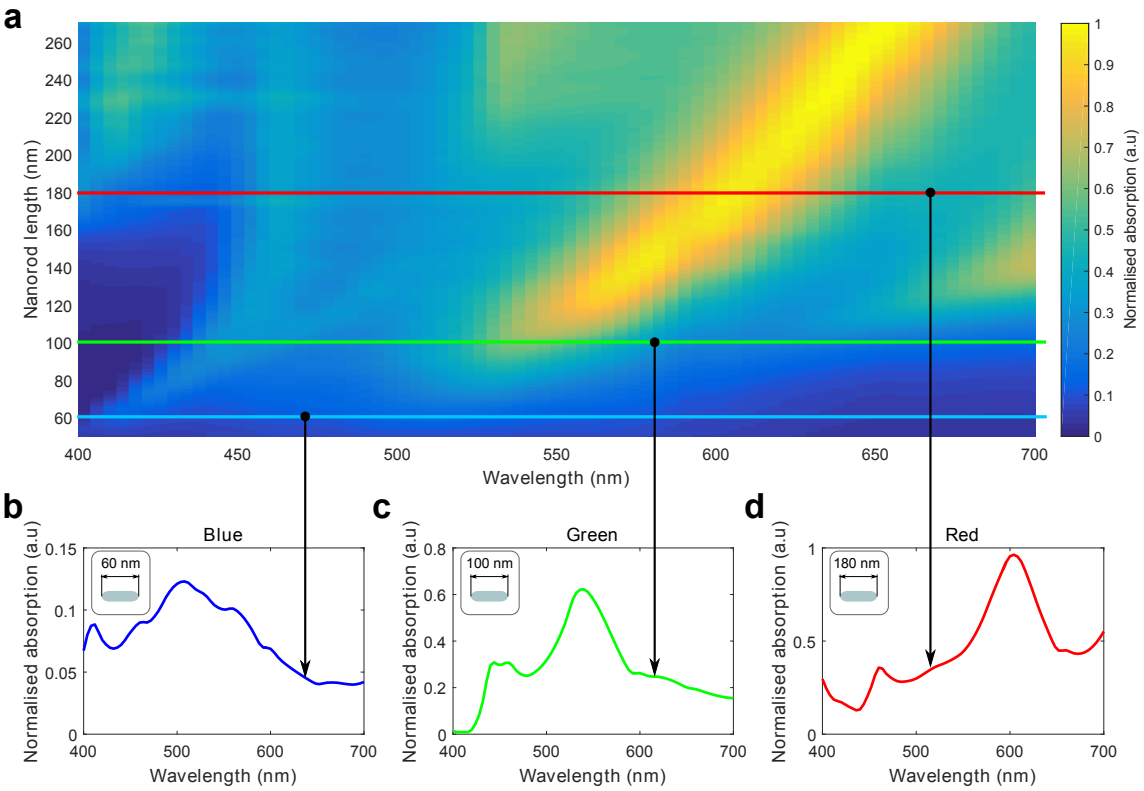

Figure 8.16: **(a)** Plot of the simulated normalised absorption of plasmonic nanoantenna for different lengths. **(b)**, **(c)** and **(d)** are absorption spectra in visible region for nanoantenna with 60, 100 and 180 nm respectively. These nanoantenna are used to create blue, green and red filters.

cantly lower efficiency a larger metal area is desirable. Note that in the infrared detection regime an appropriate nanoantenna design must also be accompanied by a 1100 nm longpass filter to suppress electron-hole pair generation associated with the visible part of the spectrum.

Figure 8.17a shows the simulated absorption in metallic back mirror of the plasmonic pixel for near-infrared wavelengths (1100 - 1700 nm). As mentioned before the absorption in this mirror is proportional to the rate of hot-electron generation and, thus, to the photocurrent detected by the channels. Similarly to visible spectra filters, this plasmonic metasurface can screen the active region of the photodetector at certain wavelengths. Figures 8.17b,c,d show the spectra of absorption in the back mirrors of the plasmonic filters with maxima at 1130, 1350 and 1530 nm respectively. Note that detectors based on hot-electron generation have intrinsically lower responsivity than photodetectors based on electron-hole pair generation. For example, as can be seen from Figure 8.17 only approximately 5% of the incident power is absorbed in the metal. Even less power will contribute in hot-electron generation

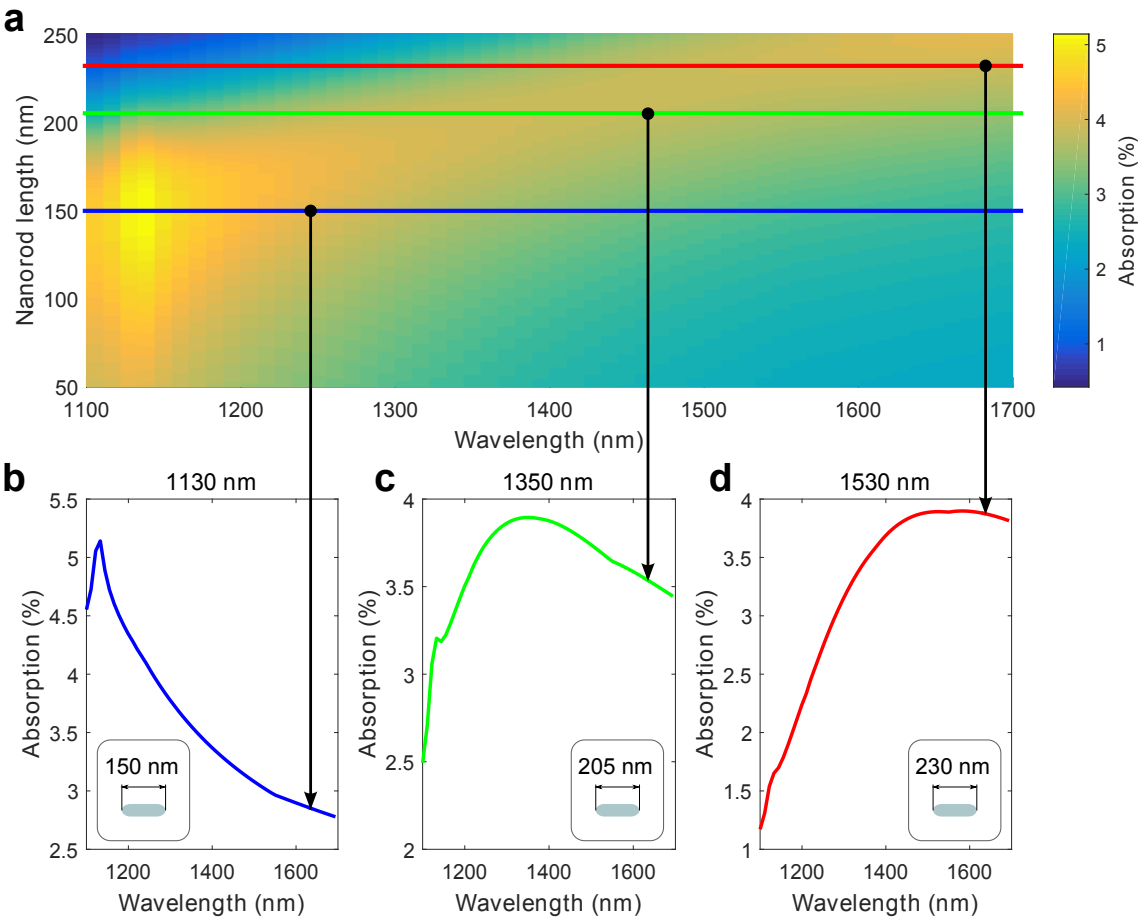

Figure 8.17: **(a)** Plot of the simulated absorption in back mirror of the plasmonic pixel for different lengths of the nanorod. **(b)**, **(c)** and **(d)** are absorption spectra in infrared region for nanoantenna with 150, 205 and 230 nm respectively. These nanoantenna are used to create 1130, 1350 and 1530 nm bandpass filters.

based on the internal quantum efficiency [85] of the device. Such detectors, therefore, require higher signal amplification and are more sensitive to noise. Due to the lack of the equipment required for these measurements there were no measurements made on hot-electron based photodetectors.

The pixels demonstrated here were chosen to have a circular shape. For easier fabrication the diameter of the pixel was chosen to be 175 µm, but the pixel could have smaller dimensions, down to several periods of nanoantennas (for example of the order of 2 µm), if required. Each plasmonic camera pixel consists of three detectors with filters responsible for the red, green and blue parts of the spectrum respectively. Nanoantenna filters are embedded into the photodiode structure and fabricated in the same step. It is important to note that filters work in the transmission regime and, therefore, the channels will detect cyan, yellow or magenta parts of the spectrum (red, green and blue parts are subtracted). Figure 8.18a shows

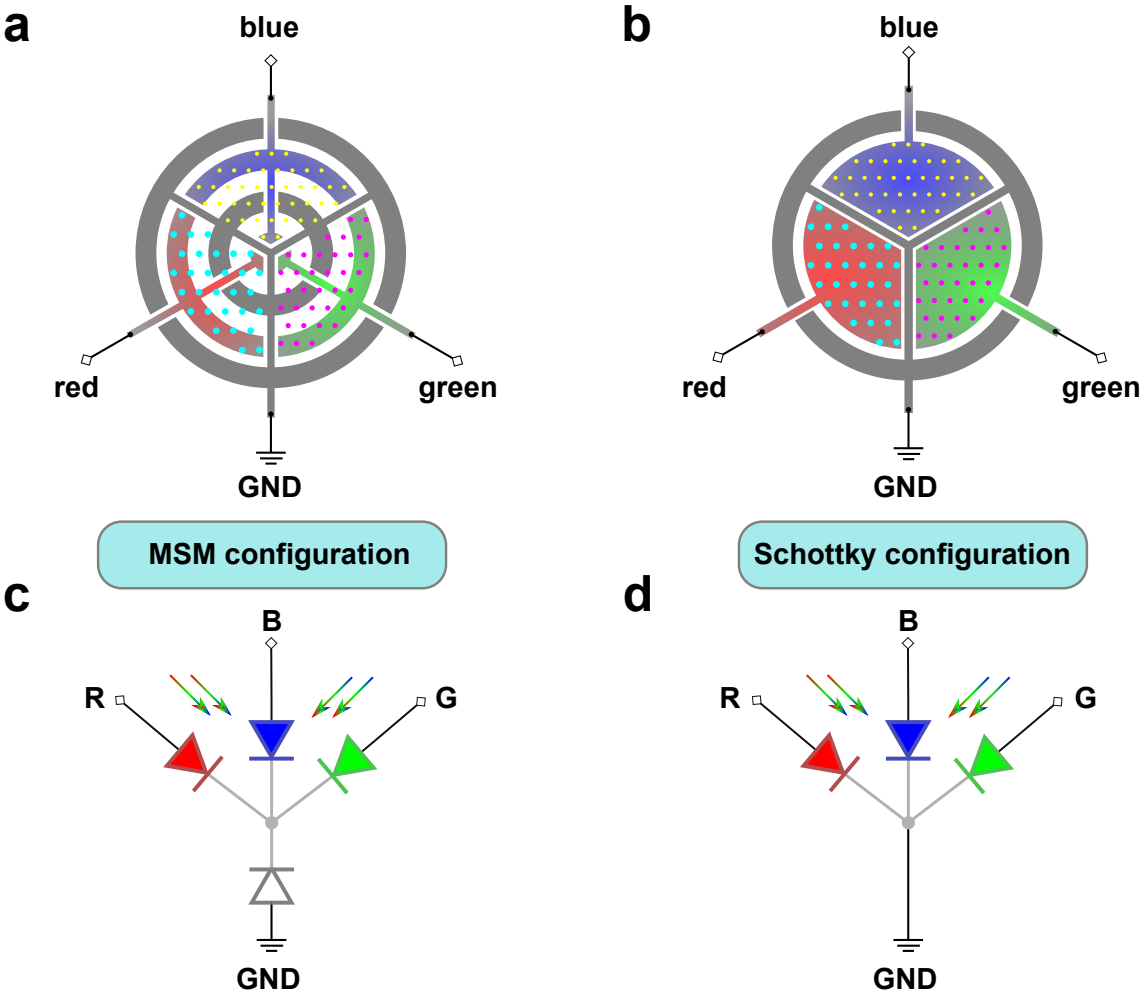

Figure 8.18: Schematic diagrams of plasmonic camera pixels based on MSM **(a)** and Schottky **(b)** photodetectors. The equivalent electric circuit of the each pixel is represented by 4 **(c)** or 3 **(d)** doides with common cathodes.

the plasmonic colour pixel design based on an MSM photodetector. The pixel is divided in to 3 sections each of those incorporating different plasmonic metasurfaces with a hexagonal lattice. Since 3 distinct channels are used, the equivalent electric circuit is represented by 4 diodes with connected cathodes (see Fig.8.18c). When the corresponding wavelength is reflected by the filter, the transmitted light will be absorbed in the active region of the detector resulting in photocurrent generation corresponding to the CMY colour model.

A similar configuration utilising Schottky photodiodes is shown in Figure 8.18b. The design implies that the framing electrode (grey) forms an ohmic contact with the silicon substrate. It is also possible to use an ohmic contact on the back side of the silicon wafer. Therefore, the electric circuit (see Fig.8.18d) will consist of 3 Schottky diodes with a common cathode. Photons that pass through the filter will

penetrate the semitransparent metal layer and generate electronhole pairs in the silicon. Furthermore, this configuration is capable of the detection of photons with energies below the bandgap of the silicon.

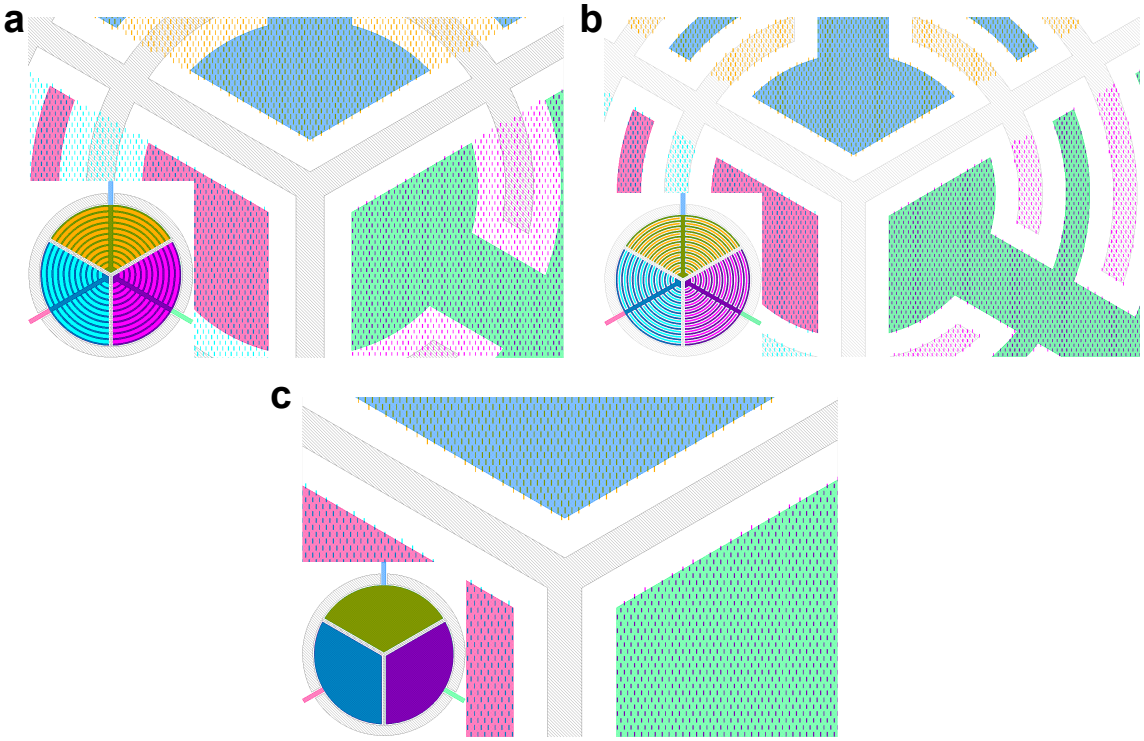

Figure 8.19: Plasmonic camera pixel designs utilising MSM **(a)**,**(b)** and Schottky **(c)** configurations respectively. The insets on each figure show the entire pixel design.

Figure 8.19 shows three different pixel designs with rectangular nanoantenna sets (the same designs were used to produce pixels with nanodiscs). The MSM photodetector design can have two configurations. The first, where nanoantennas are present everywhere in the active zone of the photodetector, is displayed in Figure 8.19a. This configuration is important for visible spectrum operation mode as it filters light in the areas between the MSM fingers. The absence of metal in these regions will suppress the resonance since Si has a lower reflectivity than Al causing a decrease in filter quality. The second photodetector still utilises the MSM configuration but the nanoantennas are absent from the spacing between the fingers. This design is preferable when the photodetector operates in the near-IR spectrum, as the energy of the photon is lower than the bandgap of the semiconductor only hot-electrons excited in the metal will contribute to the photocurrent. There is no necessity, therefore, to screen the entire active region of the detector. In both MSM configurations the width of and the spacing between the fingers were chosen to be 1.5 µm. The final design considered is shown in Figure 8.19c and utilises the Schottky

configuration. This plasmonic pixel can work in both visible and near-IR spectrum modes. The fabrication of this photodetector is, however, slightly more complicated as additional steps are required to create an ohmic contact with the substrate.

8.2.3 Fabrication

The fabrication of the photodetectors required multiple lithography steps (see Fig.8.20). Pixels were fabricated on low doped [100] n-type silicon wafer with bulk resistance of $\rho = 1 - 10\ \Omega\cdot$cm. A sequential ultrasonic cleaning in acetone, IPA and deionised water was performed to remove any contamination that might be present on the wafer. It was then spincoated with 280 nm PMMA A4 950k resist and baked at 180°C for 5 min.

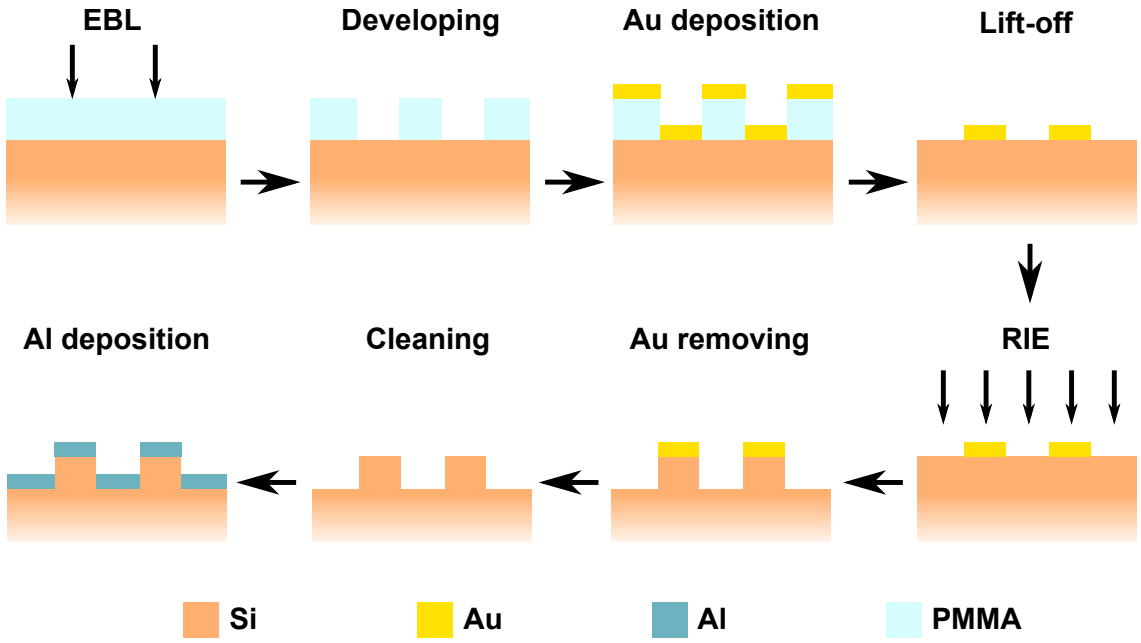

Figure 8.20: Plasmonic colour pixel fabrication steps.

In the first lithography step the alignment markers and nanoantennas were exposed using a 100 kV EBPG5000+ electron beam lithography system. The pattern was developed in 1:3 MIBK:IPA solution for 1 minute. The adhesion titanium layer with a thickness of 2 nm was deposited at 0.2 Å/s followed by 80 nm of gold deposited at 0.6 Å/s evaporation rates. After evaporation a lift-off step in hot acetone followed by rinsing in IPA was performed.

The sample was then spincoated with a 600 nm thick high resolution ZEP520A resist and baked at 180°C for 3 min. Apart from having better resolution compared

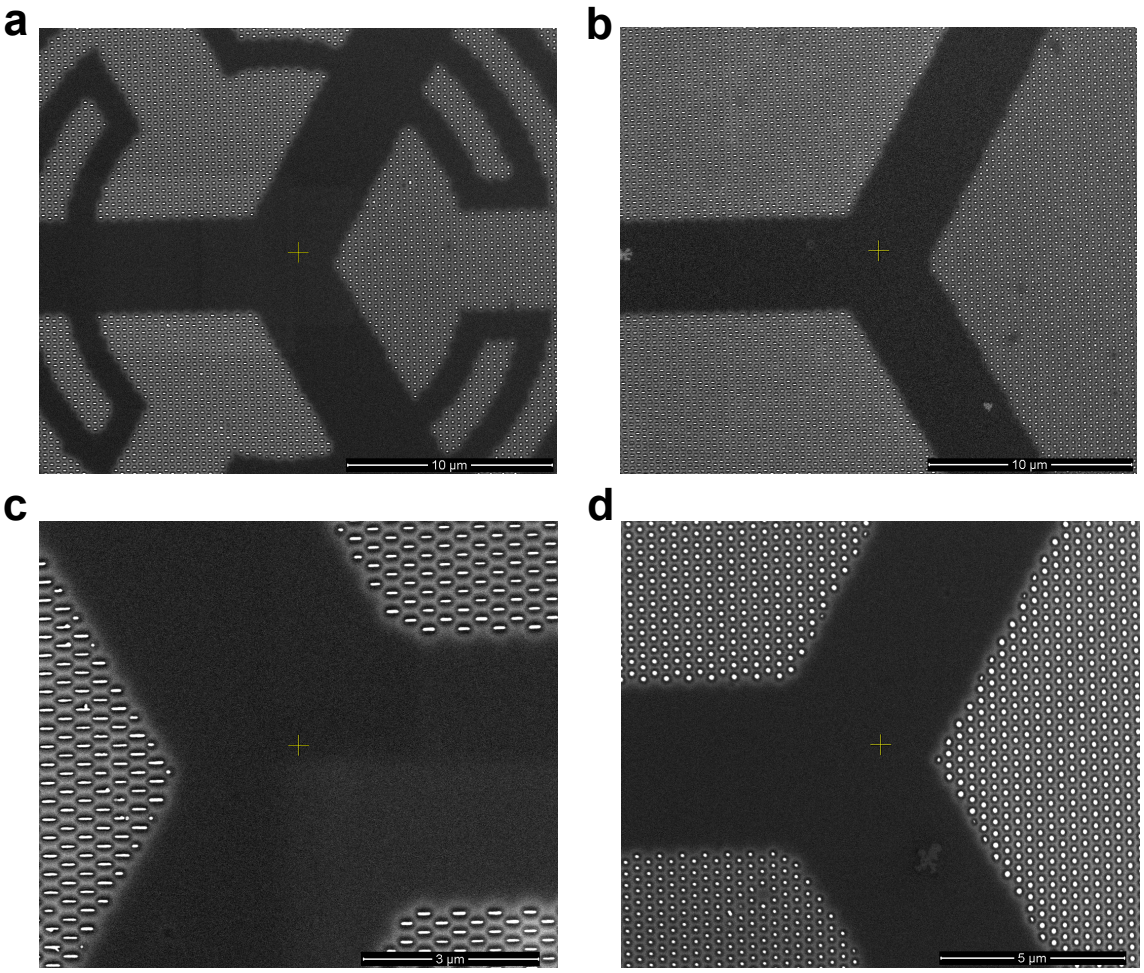

Figure 8.21: SEM images of nanoantenna metasurfaces after RIE step. **(a)** and **(b)** show the plasmonic filters for MSM and Schottky photodetector designs respectively. The filters consist of either nanorods **(c)** or nanodiscs **(d)**.

to PMMA, this resist is more robust to reactive ion etching which is essential for further fabrication steps. The second lithography step involved the definition of pixel contacts and pads. Gold markers obtained during the previous step were used for alignment. A dose of 230 µC/cm^2 was used to expose the resist. A development step in n-amyl acetate for 2 min followed by 30 s rinsing in IPA was then performed.

The developed sample was transferred into an Oxford Instruments PLASMALAB 100 ICP380 reactive ion etching tool. A combination of Ar and Cl_2 gases with flow speeds of 5 and 30 sccm respectively was used to etch Si. The etching was performed at a pressure of 5 mTorr for 30 s. The sample was then immersed into GE-8148 gold etchant (potassium iodide and iodine (KI:I2) solution) for 30 s to remove any gold residue that remain after the etching. The native oxide layer which may have formed on the silicon substrate was stripped using 1% hydrofluoric (HF) acid and the

sample was immediately loaded into an IntlVac NanoChrome II e-beam evaporator. The aluminium layer with a thickness of 50 nm was deposited at 0.7 Å/s. After evaporation, a lift-off step in dimethylacetamide (ZDMAC) was performed.

Finally, the sample was coated with 100 nm PMMA A2 layer to protect the structures during the next step. A wet dicing saw (Disco DAD321) was used to separate the photodetectors. The dies were glued into a ceramic LCC20 package and bonded using a Kulicke & Soffa 4522D Wedge bonder with aluminium wire.

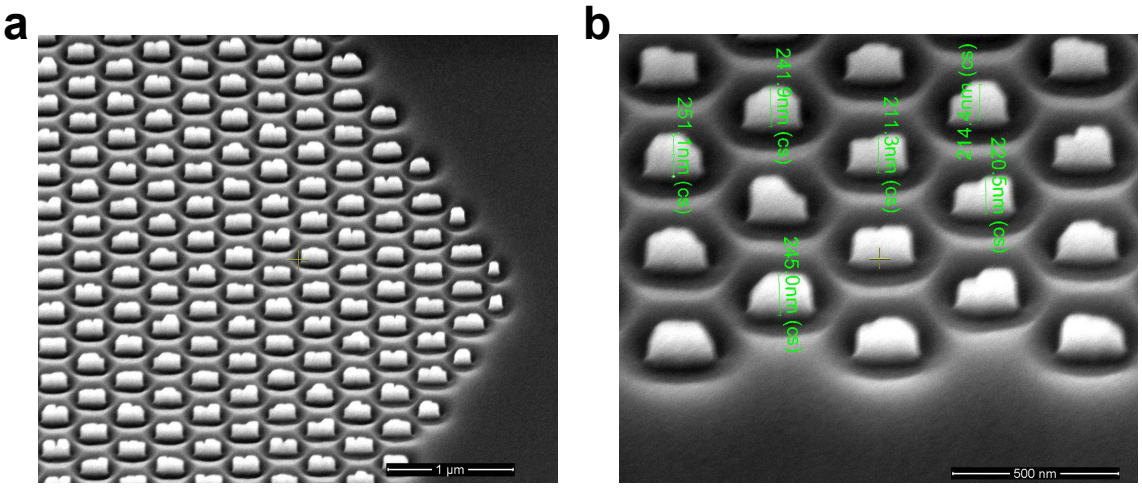

Figure 8.22: SEM image **(a)** of plasmonic nanorod metasurface obtained at 30° angle. Figure **(b)** shows the measured height of supporting nanopillars.

Figure 8.21 shows two test sections after the first lithography step (nanoantennas only). The SEMs were obtained straight after reactive ion etching. Figure 8.21a and Figure 8.21b show the plasmonic filters for the MSM and Schottky photodetector designs respectively. As can be seen in the case of the MSM configuration the nanoantennas are absent in the regions between the fingers. The magnified views of the middle sections of both designs are shown on Figure 8.21c and Figure 8.21d respectively. Each of three pixel filters consists of sets of nanoantennas with different lengths (in the case of nanorods) or diameters (in the case of nanodiscs).

To investigate the geometry of the pillars supporting the nanoantennas, the sample was tilted at 30°. Figure 8.22a shows one of the plasmonic colour filters. As can be seen the pillars have rough top surfaces. This is due to the presence of metal residue which can be removed in further fabrication steps. The magnified view of the nanopillars (see Fig.8.22b) shows a honeycomb lattice in the substrate around the pillars. This is due to the 'trenching phenomenon' [204, 205], appearing during reactive ion etching. One possible explanation of this effect is that ions scatter

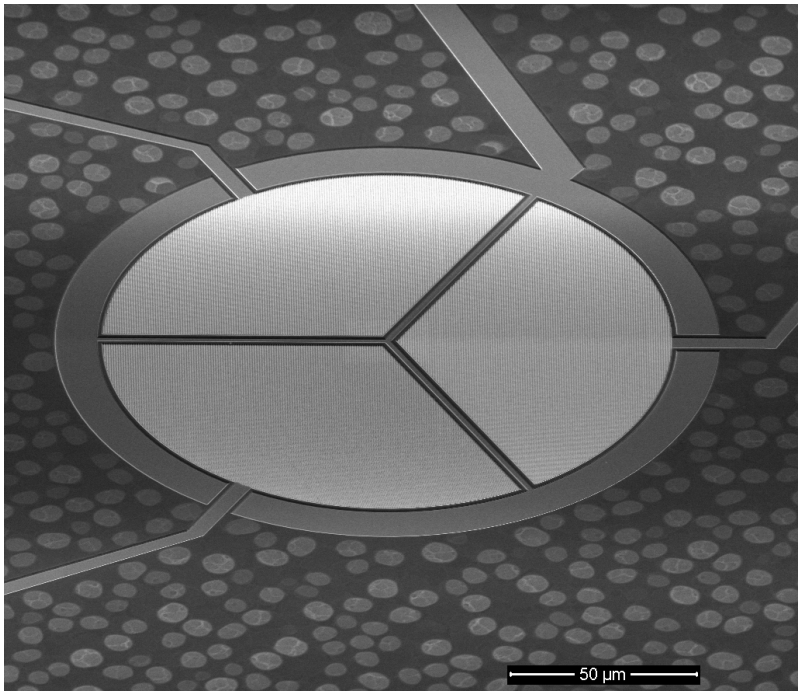

Figure 8.23: SEM image of the entire plasmonic colour pixel structure utilising Schottky configuration.

from the sloped sidewall surfaces [206] which can be suppressed by further etching parameter optimisation. From the Figure 8.22b the average height of the nanopillars obtained is found to be around 230 nm consistent with the design parameters. Other parameters such as the width and length of nanoantennas were found to be approximately 10-15% larger than expected due to overexposure during the EBL step (it was later found that the EBL tool was malfunctioning, resulting in a higher than expected dose delivered to the exposed regions). This will result in a red-shift of the resonant wavelengths.

The entire plasmonic colour pixel utilising the Schottky configuration is shown in Figure 8.23. The image was taken at an angle of 30°. An In-Ga liquid alloy was applied to the back side of the die to obtain an ohmic contact with silicon. The metallisation around the pixel channels, therefore, acted as a guard ring to suppress noise and electrical pixel cross-talk. As mentioned before the white spots around the structure are due to HF acid diffusion through the PMMA layer during the native oxide stripping step. HF can easily penetrate through the pinholes in PMMA mask. Although performing additional HF etching after metal deposition can clean the silicon surface, it is unnecessary since these white spots do not affect device performance.

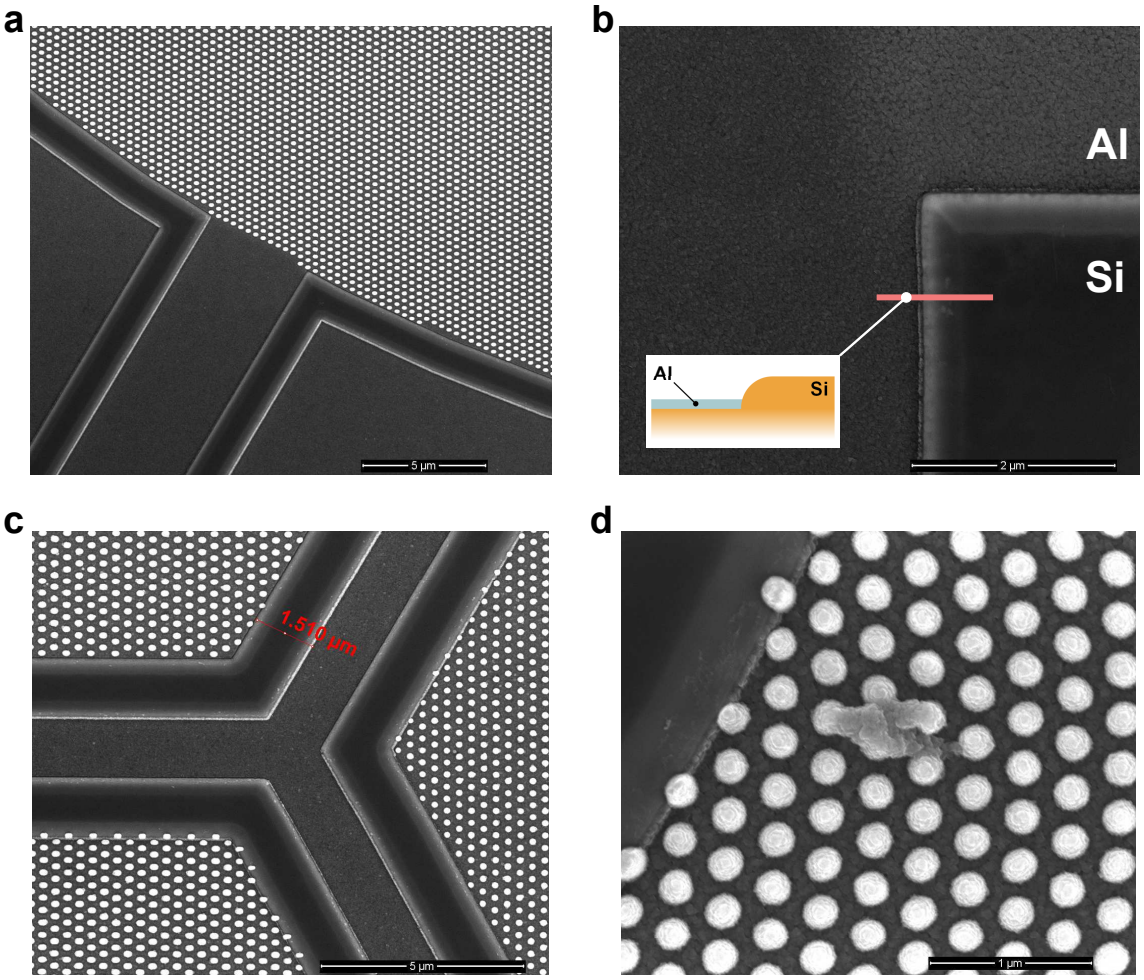

Figure 8.24: SEM images of different regions of the plasmonic colour pixel: **(a)** contact with one of the photodetectors, **(b)** metallisation around the pixel (the inset shows a schematic representation of the etching profile), **(c)** centre of the pixel and **(d)** plasmonic colour filter.

Close-up views of different areas of the plasmonic pixel are shown in Figure 8.24. As can be seen from Figure 8.24a,c the active zone of each of three photodetectors and the perimeter of the entire pixel are shielded by additional metallisation. In the MSM configuration the common contact provides the same functionality. Due to the anisotropic etch rate for different crystal planes of the silicon the etched profile has a trapezoidal shape (see Fig.8.24c). Figure 8.24d shows a magnified image of one of the colour filters. As can be seen the metal present on the top side of the pillars as well as on the silicon underneath creating the desired structure of a plasmonic colour pixel.

8.2.4 Experimental results

It was shown in Figure 8.15 and Figure 8.24 that plasmonic filters consisting of circular nanoantennas were also fabricated in the same technological step. These metasurfaces are polarisation insensitive. Nevertheless, polarisers are widely used in modern professional cameras to improve the image quality. It was, therefore, decided to focus on polarisation sensitive metasurfaces as they can be of larger interest for industry and also provided an integrated control for testing performance.

The fabricated samples were inspected under a microscope using white light illumination. Figure 8.25 shows a test sample with two different photodetector designs illuminated with s- and p-polarised light[1]. All images were captured using a Nikon 1 J1 camera. For this sample nanorods were used as the basis for the colour filters. Aluminium was deposited everywhere and, therefore, the surrounding area is highly reflective and appears white.

Each pixel is divided inon 3 sections, each representing a separate photodetector responsible for reflection of either the red, green or blue part of the spectrum. Note that, as said before, the plasmonic filters work in the transmission regime. The part of the spectrum which passes through the filter is registered by the photodetector. These filters, therefore, are expected to sense cyan, magenta and yellow colours respectively. Colour differences can be seen when the incident light is parallel to the long axis of nanoantennas (see Fig.8.25 left column). As expected, the reflected colours are red-shifted with respect to those the simulation predicts (for example yellow colour instead of green) due to the overexposure of the nanoantennas. The nanoantenna exposure dose could be optimised to eliminate this issue but the devices presented here demonstrate proof-of-principle.

Figures 8.27a,b show reflection spectra normalised to the reflection from 50 nm thick Al for each plasmonic pixel channel utilising the MSM and Schottky configurations. As can be seen the reflection spectra are in reasonable agreement with simulation (see Fig.8.26). These reflection spectra result in the underlying photodetector registering subtractive colours with depths around 510, 550 and 635 nm in the case of the Schottky configuration respectively. The divergence from the FEM simulation can be explained by fabrication imperfections such as differences in nanoantenna sizes or metal thickness and the well-known change of modelling

[1]The incident light is s- or p-polarised when the electric field is perpendicular or parallel to the longest axis of the nanorod respectively.

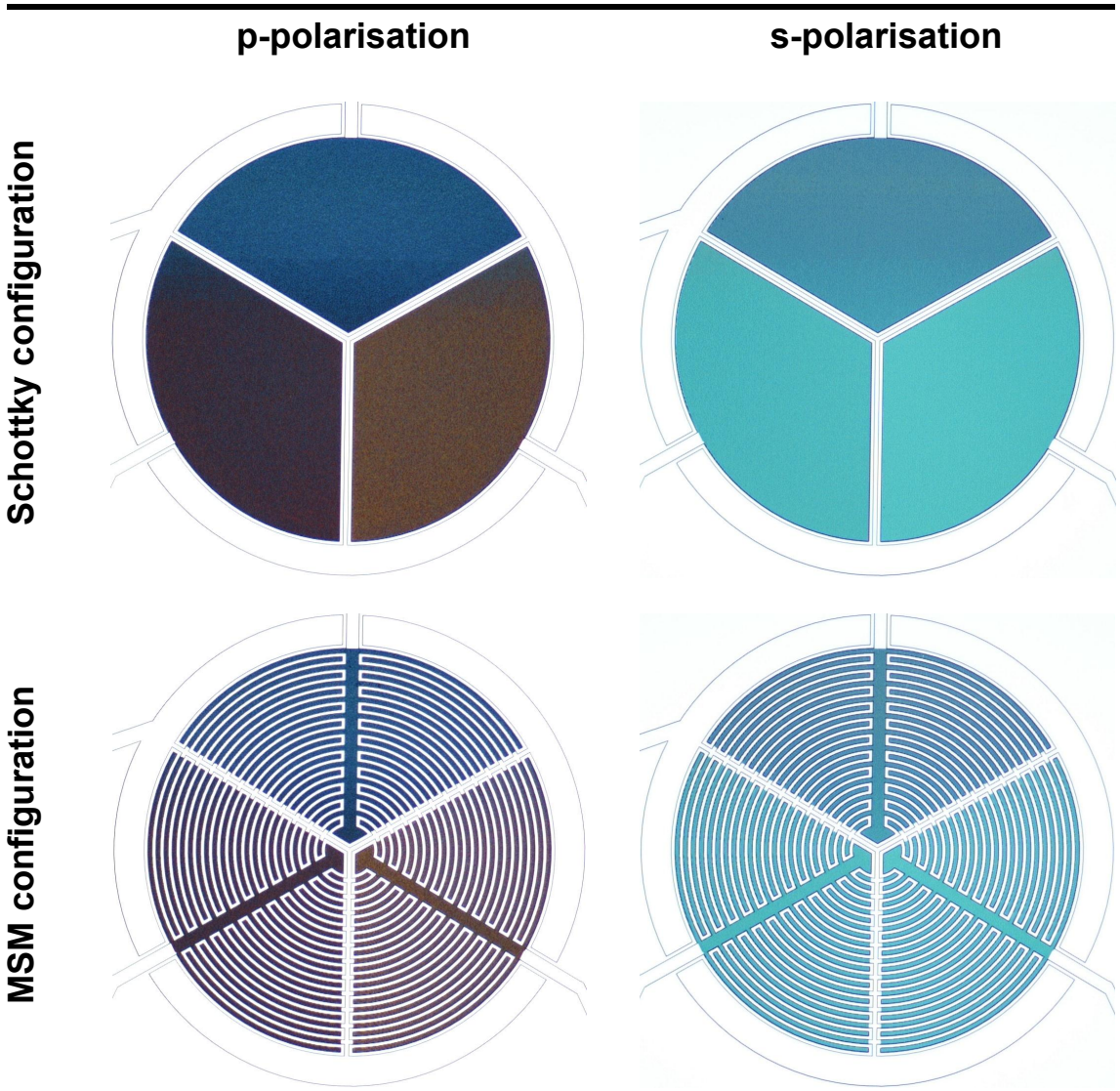

Figure 8.25: Image of plasmonic camera pixels taken under illumination with s- and p-polarised light. Top and bottom rows show pixels utilising Schottky and MSM designs respectively. Both configurations show strong polarisation response.

high index materials [189]. Although the reproduced gamut is relatively small (see Fig.8.27c,d), it could be subsequently enhanced by adjusting a sensitivity of each pixel channel.

Both pixel designs exhibit a strong polarisation response. When the electric field of the incident field is perpendicular to the long side of the nanorods all colour channels reflect the same colours (see Fig.8.25 right column). A slight difference in colour between the three sectors can be explained by an unintended variation of nanoantenna width (due to the aforementioned EBL tool malfunction) and, in turn, higher absorption. The intrinsic polarisation sensitivity can be beneficial not only for scientific applications but also for professional photography where polarisers are

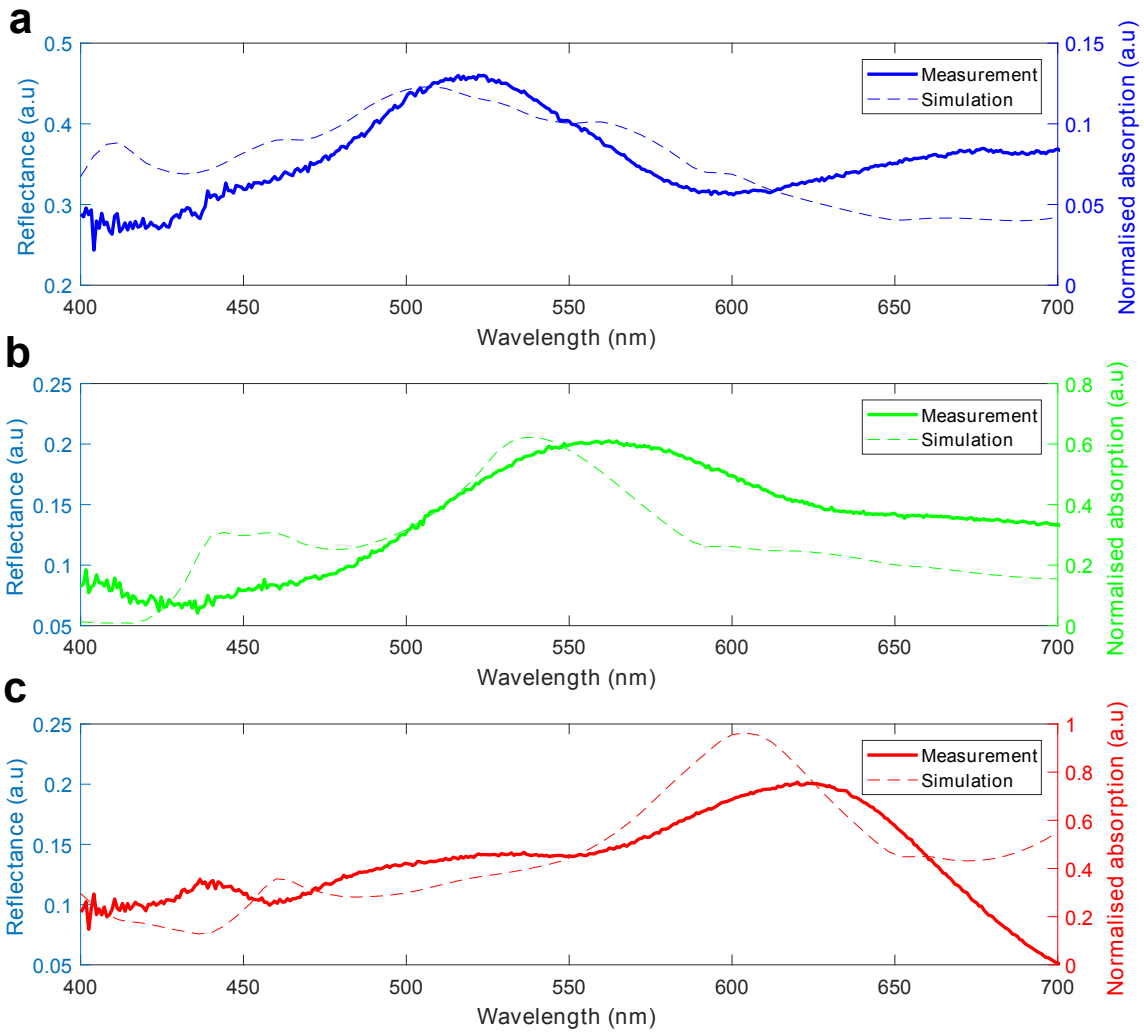

Figure 8.26: Normalised simulated absorption in nanoantenna and measured reflection spectra from blue **(a)**, green **(b)** and red **(c)** channels of plasmonic colour pixel.

used in order to improve image quality or create specific effects.

An image of a functional plasmonic camera pixel in the MSM configuration is shown in Figure 8.28. Here the aluminium was deposited only on the specific regions forming photodetectors, electrical connections with them and contact pads (not shown on the image). The grey region around the structure is bare silicon.

IV characteristics of plasmonic pixels utilising the MSM and Schottky configurations were obtained using a Keithley 487 source/meter are shown in Figures 8.29a,b. The shape of each curve is typical for the photodetector types used [191, 207] and is symmetric for the MSM and asymmetric for the Schottky detector under positive and negative biasing. In the case of the Schottky configuration, an ohmic contact

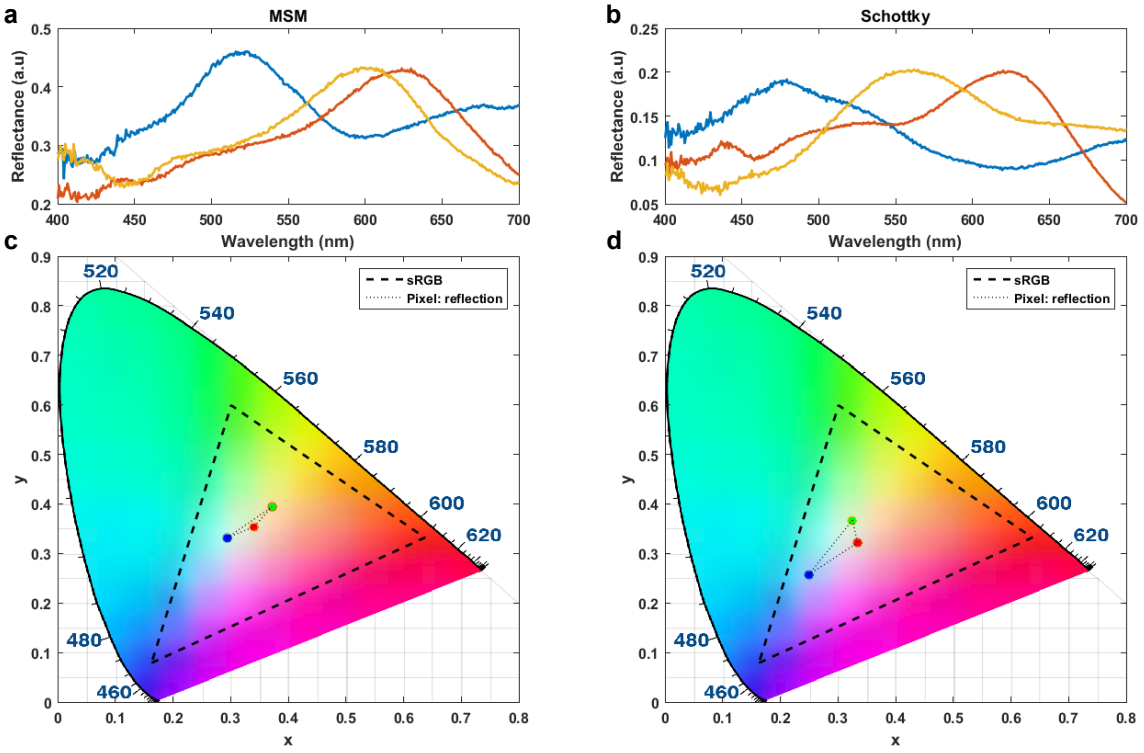

Figure 8.27: Normalised reflection spectra from plasmonic pixel colour filters utilising the MSM **(a)** and Schottky **(b)** configurations respectively. Figures **(c)** and **(d)** show the reflection gamut of these pixels.

with a silicon substrate was created using In-Ga liquid metal alloy. This contact acts as a common cathode (see Fig.8.18d) for all 3 channels of the pixel. Unlike the MSM photodetectors, Schottky diodes have different behaviour under forward and reverse bias. Under forward biasing (positive voltage applied) the metal-semiconductor junction is open and the current rises quickly. At the same time the current under reverse biasing (negative voltage applied) is much lower and saturates at a certain value before breakdown. Schottky photodetectors are usually utilised under reverse bias as in this case they have better responsivity [85].

Each channel exhibits virtually almost identical IV characteristics and are indistinguishable when plotted. This is in agreement with expectations since the photodetectors have the same area and were fabricated in the same step. The sensitivity of each channel can be adjusted by using different amplification coefficients for the signal amplifiers. The IV curves also reveal a negative aspect of the pixel. As can be seen from Figure 8.29 each pixel exhibits a relatively large dark current (the characteristics were obtained without illumination). This could be the result of a very large metal-semiconductor contact area. Note that for simplicity the pads for bonding were deposited onto the silicon substrate without insulation. Furthermore,

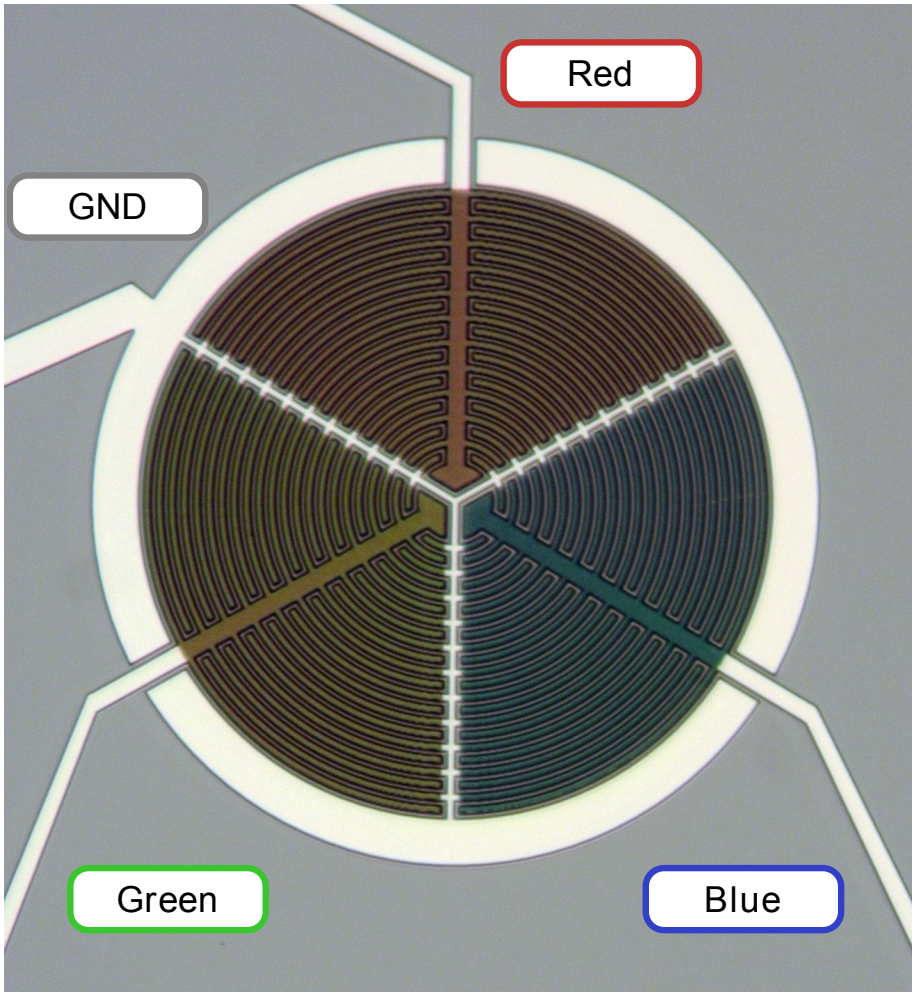

Figure 8.28: Image of a functional plasmonic colour pixel utilising MSM configuration. The labels show the assignations of each aluminium contact.

leakage could be caused by high electric fields at the edges of the metal contacts [208].

The plasmonic pixel utilising Schottky photodiodes suffers from a similar problem as the MSM detector. The large metal-semiconductor area and sharp metal edges markedly increase the leakage current. This also lowers the forward voltage of the photodetector [209]. As can be seen from Figure 8.29 each photodetector has almost zero forward voltage and a relatively large reverse current. The dark current, therefore, could be reduced by lifting the pads above the substrate by introducing a thick silica layer or p-wells underneath and including guard rings around the metal edges.

Channel selectivity is one of the main characteristics of the camera pixel. To demonstrate this, IV curves of each channel were recorded as the pixel was illumi-

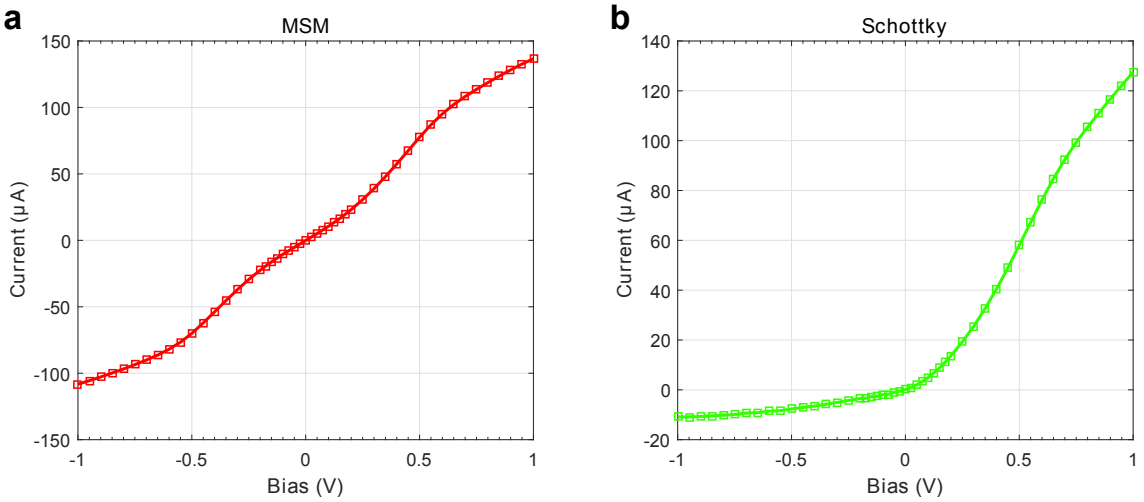

Figure 8.29: IV characteristics of each colour channel of the plasmonic pixel utilising MSM **(a)** and Schottky **(b)** configurations respectively (with no illumination).

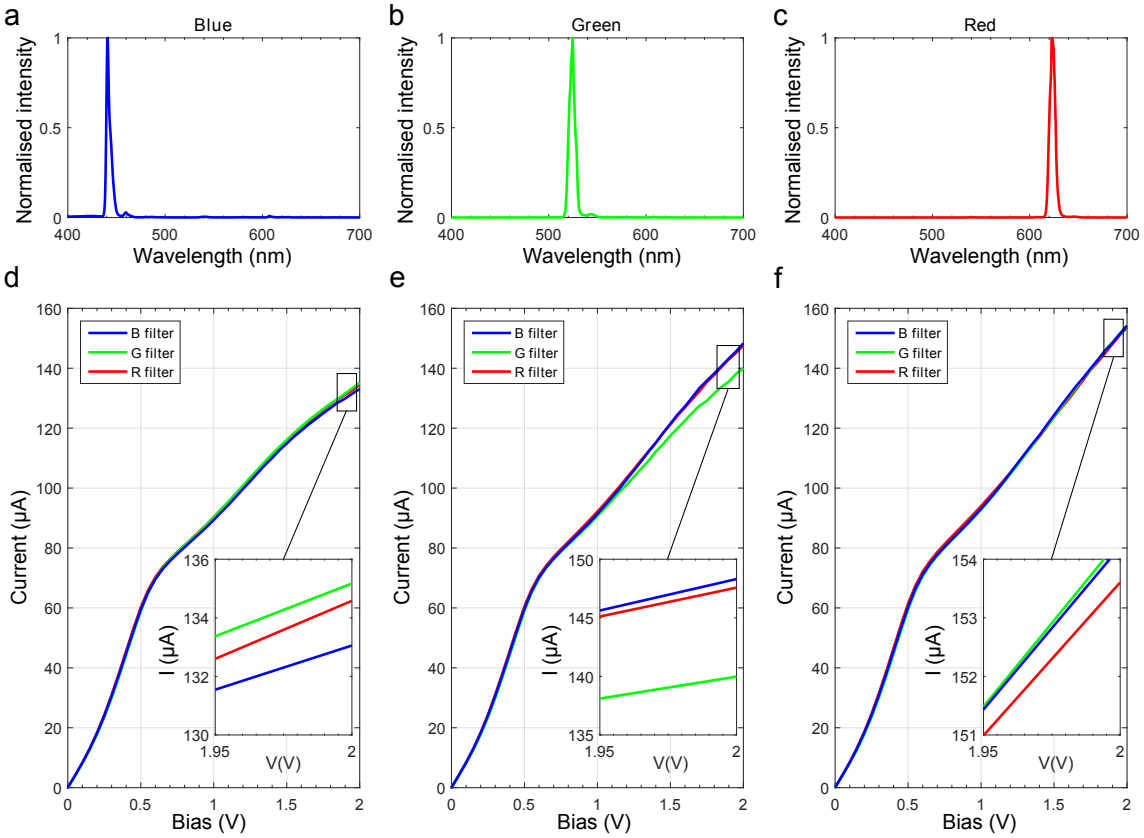

Figure 8.30: IV characteristics of each colour channel of the plasmonic camera pixel utilising the MSM configuration under illumination. Figures **(a)**,**(b)** and **(c)** show the illumination spectra. The IV curves obtained under these spectra are shown in **(d)**,**(e)** and **(f)** respectively. As can be seen the lower photocurrent is generated by detector with a filter designated for particular part of the spectrum.

nated with light with different spectral content. The beams were focused using a Nikon CFI Plan Fluor 10x long working distance objective to produce a spot which uniformly covered almost the entire area of the pixel. Since a beam covers the whole pixel area, the power delivered to the top surface of each channel is constant for each illumination spectra. Figures 8.30a,b,c show the spectral characteristics of the beams with peak intensities at 450, 532 and 632 nm and full width at half maximum (FWHM) of 10 nm. Each beam is, therefore, blue, green and red in colour respectively. Since the incident power and the bandwidths are kept constant, the sensitivity of each channel should depend only on the absorption in the silicon substrate and the spectral characteristics of the plasmonic filters. As all 3 channels were fabricated on the same substrate and have identical dark currents, the responsivities of the channels are equal. Thus, one channel should produce a lower photocurrent for each source than the other two channels.

Figures 8.30d,e,f show the IV characteristics of the pixel channels collected under blue, green and red illuminations respectively. As expected, a lower photocurrent in each case is generated by the channel with the appropriate plasmonic filter. At the same time the filters of the other 2 channels are less reflective at these wavelength which results in a higher detected photocurrent. Note that the difference between the IV curves is relative. As can be seen from Figure 8.30d and Figure 8.30f more photocurrent is generated at longer wavelengths. This is due to the non-linear photoresponsivity of silicon [85] for different wavelengths. The effect is usually compensated by adjusting the amplification coefficient of each colour channel or during post-processing of the signal. As can be seen from Figures 8.30d,e,f since the extinction ratio of plasmonic filters relatively large due to aforementioned fabrication issues, all three channels respond to different wavelengths. Nevertheless, the difference in response of each channel is distinguishable. Therefore, it is possible to compensate the lack of extinction ratio by calibration of channel amplifiers. It can be further improved by using higher biasing voltages but this will require improving the Schottky barrier quality (introducing a very thin oxide layer between semiconductor and metal [210]). Additionally, the selectivity of a plasmonic metasurface greatly depends on the size of the nanoantennas. Due to the aforementioned EBL issues, the e-beam focus varied in an unpredictable way during the exposure process. Therefore, the nanoantennas had different sizes and, therefore, different resonances. Since the total response of the fabricated metasurface consisted of several different slightly shifted resonances, it appeared to be very broad. The selectivity can be, thus, improved by further optimisation of EBL exposure process.

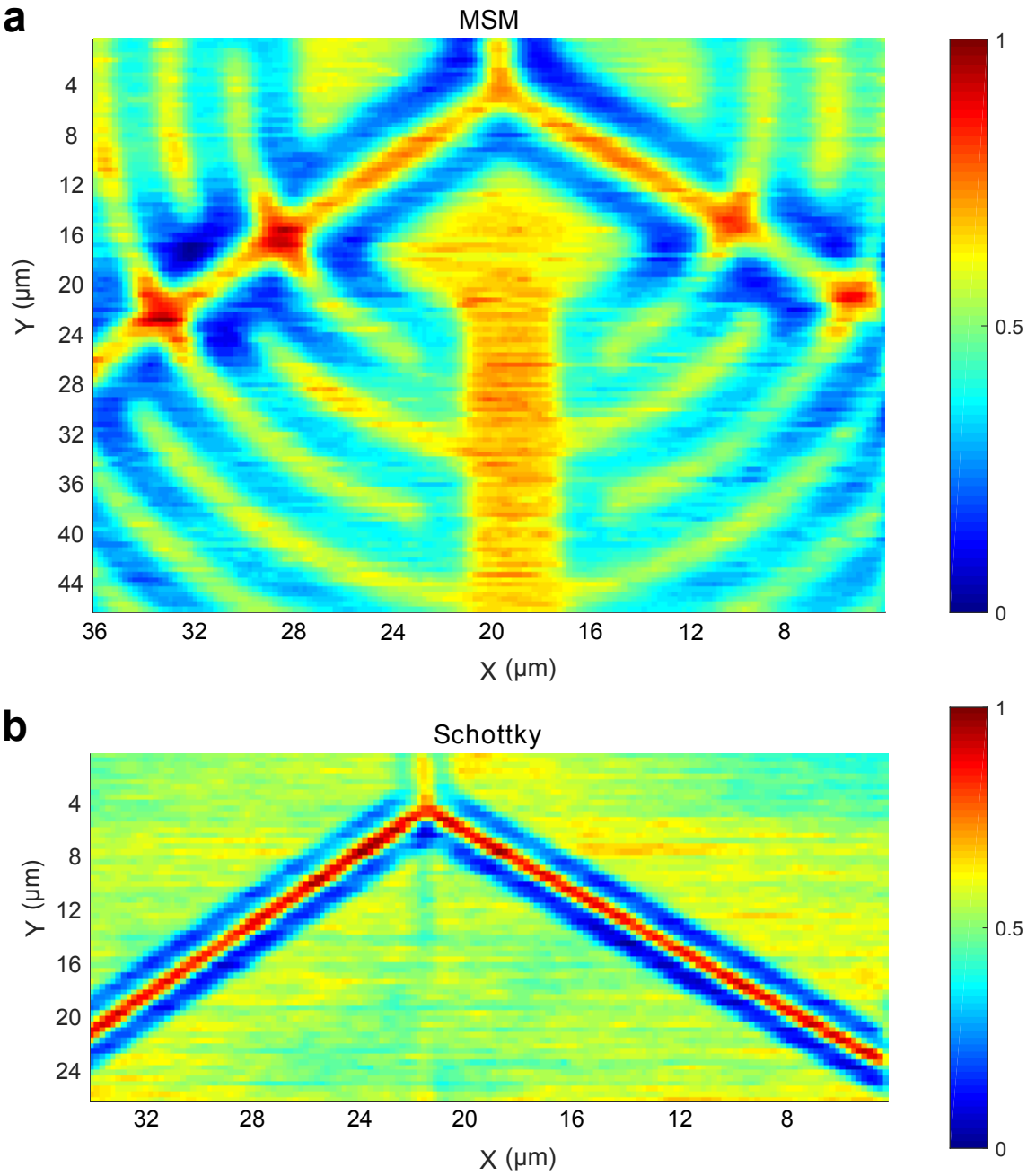

Figure 8.31: Scanning photocurrent microscopy maps of central area of plasmonic pixels with the MSM **(a)** and Schottky **(b)** configurations respectively.

SPCM scans of the plasmonic pixels utilising the MSM (see Fig.8.31a) and Schottky (see Fig.8.31b) configurations were obtained to observe the pixel structure and further confirm its functionality. A Thorlabs S1FC635 fibre-coupled diode laser with 635 nm wavelength was focused using a Nikon CFI Plan Fluor x50 long working distance objective to obtain a spot size of approximately 1 µm. Since the range of the piezo stage is 80x80 µm, less than the entire diameter of the structure (175 µm), the scan was performed over the centre of the pixel since this region contains all essen-

tial parts: three colour channels and separating metallisation. The smaller region size permitted an increase in resolution and identifying smaller features. The photocurrent from all channels was plotted as a function of the x and y position of the stage. As can be seen from Figure 8.31 the obtained photocurrent maps represent the design of the MSM and Schottky configurations of pixels.

The common electrode which splits the channels is also acting as a screen. The electron-hole pairs generated in one pixel channel will not be able to reach the neighbouring channels as there is no electric field gradient between them. Therefore, the design provides an intrinsic suppression of interchannel cross-talk. As can be seen from Figure 8.31b the scans across the colour filters are relatively uniform even at regions close to the edges of the channels. The photocurrent in the MSM device exhibits a different behaviour (see Fig.8.31a). Since the active regions consist of interdigitated fingers, the SPCM scans have multiple maxima and minima depending on which zone is illuminated. Although the maps obtained are non-uniform, the identical layouts and areas of the photodetectors ensure that the same conditions will present at each channel. Therefore, the overall photocurrent is determined only by the characteristics of the filters. This could be extended to multichannel SPCM with the additional amplifiers that is the subject of ongoing work.

8.2.5 Summary

In this section fully CMOS compatible camera pixels with embedded plasmonic filters have been demonstrated. Each pixel consists of three independent channels each incorporating nanoantenna arrays forming a perfect absorber structure. The utilisation of plasmonic metasurfaces as colour filters instead of conventional pigments permits planarisation of the pixel design and avoids cross-talk. It also allows scaling down the overall dimensions of the pixel. Both MSM and Schottky photodetector configurations demonstrated an ability to distinguish between different spectral bands. Furthermore, the photodetectors with rectangular nanoantennas exhibited an intrinsic polarisation sensitivity. Although the pixels shown were designed for the visible part of the electromagnetic spectrum it is potentially possible to extend the sensitivity range into the UV and near-IR regions, creating a 'hyperspectral' pixel configurations with more than three channels. Additionally, since E-beam writing and ion milling are both suitable only for prototyping, a deep-UV lithography with phase-masks which is widely utilised in modern semiconductor fabrication will be

more suitable for mass production. The plasmonic pixel, therefore, can be used as a planar nanoscale alternative to conventional colour pixels in future high-resolution or scientific cameras or in the emerging field of single-pixel imaging [211].

9. Plasmonic-enhanced photodetectors summary

In Chapter 8 a compact, fully CMOS compatible plasmonic metasurface-enabled photodetector suitable for differential determination of orthogonal polarisation states of light was demonstrated. The photodetector has a diameter of 100 µm and a total responsivity of 80 mA/W. The performance of two antenna designs suitable for the detection of states of either linear or circularly polarised light was experimentally demonstrated. Utilisation of Al as a material for contacts and nanoantenna enabled not only a full CMOS compatibility but also a broadband plasmonic response of the metasurfaces. It was experimentally demonstrated that the linear polarisation photodetector shows a stable non-zero differential response from wavelengths of 550 - 800 nm. In the case of the circular polarisation detector a non-zero differential response was observed from 550 - 700 nm. Utilizing the spiral design presented, the differential photodetector can potentially be applied, along with a suitable antenna design, to determining other polarisation states of light, such as spatially modulated radially and azimuthally polarised optical beams. The differential nature of the photodetector ensures that in-phase noise associated with changes in incident intensity, thermal or operating frequency fluctuations are strongly suppressed in the measured differential photocurrent. Chapter 8 also demonstrates fully CMOS compatible camera pixels with embedded plasmonic filters. Each pixel consists of 3 independent channels each incorporating nanoantenna arrays. The utilisation of plasmonic metasurfaces as colour filters instead of conventional pigments permits planarisation of the pixel design and avoids cross-talk. It can potentially significantly reduce the overall dimensions of the pixel as the plasmonic nanoantennas have subwavelength dimensions. The limitation to the smallest colour channel size is the size of the nanoantenna. It is, therefore, theoretically possible to fabricate 100-200 nm pixel. Although the pixels shown were designed for use with visible light it is potentially possible to extend the sensitivity range into the UV and near-IR

regions, creating a 'hyperspectral' pixel configurations. Both MSM and Schottky photodetector configurations demonstrated an ability to distinguish between different wavelength bandwidths and, as an additional feature, photodetectors with integrated rectangular nanoantennas exhibited an intrinsic polarisation sensitivity.

10. Thesis summary and future work

The goal of this thesis was to pursue two main aims based on utilising of surface plasmon phenomena. The first aim was to progress a technology that would circumvent the limitations prohibiting a further increase in the speed of digital circuit operation such as the signal propagation delay in metallic interconnects. The second goal was to develop a concept to improve existing or enable novel extensions to conventional photodetectors such as introducing polarisation-sensitivity and new colour camera pixels. This chapter discusses the outcomes of this research and possible extensions of planar surface plasmon detection techniques, plasmon modulators and optical filters. Further, conceptual designs of a 'NAND' logic gate with plasmonic interconnects and plasmonic metasurface based photodetectors are proposed, which could exploit the technologies demonstrated in this thesis.

10.1 Thesis outcomes

In summary, to achieve the above-mentioned goals of creating logic gates with plasmonic interconnects and developing novel plasmonics-enabled photodetectors and camera pixels, the following specific outcomes were achieved in this research:

- Development of a novel plasmonic input port design that provides coupling of far-field radiation into guided surface plasmon. [19]
- Demonstration of a new planar metal-semiconductor-metal photodetector design capable of detecting the surface plasmons in-plane. [212]

- Development of a fabrication method that is capable of producing waveguide-coupled metal-semiconductor-metal photodetectors in the same fabrication step.
- Characterisation of indium-tin-oxide and evaporated silica films properties, necessary for understanding the film breakdown mechanism and future plasmonic modulator fabrication. [177]
- Demonstration of a novel plasmon-enabled differential photodetector design which permits noise-robust discrimination of incident beam polarisation states. [39]
- Development of a planar pixel design with integrated plasmonic colour filters. Devices were fabricated and their performance demonstrated. [213]

10.2 Future work

Potential future work arising from this thesis has been separated into two sections. The first section is related to the logic gate with plasmonic interconnects and describes the current issues and a further expansion of experimental work presented in Chapters 4, 5 and 6. The second section is dedicated to plasmonic enhanced photodetectors described in Chapter 8. It discusses the possible application of the results obtained in this thesis to the fabrication of unique optical devices for telecommunications and scientific measurements.

10.2.1 Logic gates with plasmonic interconnects

The essential components required for plasmonic logic gates such as coupling, guiding and detection have been experimentally demonstrated within this thesis. The only part that still requires experimental investigation is the plasmonic modulator. Since the e-beam evaporated SiO_2 films studied in this thesis showed an unsatisfactory low breakdown voltage. This can be explained by the poor film quality of the e-beam evaporated multicomponent oxides [181]. The low breakdown voltage limits of the maximum potential that can be applied to the modulator, thus, making achieving a carrier density sufficient for SPP modulation impossible. Although an attempt to fabricate a waveguide-embedded modulator was performed as a part of

the project (see Fig.1.8b), the low breakdown voltage of the SiO_2 layer precluded any measurable surface plasmon modulation.

It is, therefore, essential to use another fabrication method for producing the insulating oxide. One possible technique is atomic layer deposition (ALD) [184]. It was reported [214] that SiO_2 films obtained using this method have an electrical breakdown field of approximately 10 MV/cm. Using a relatively low deposition temperature of 280°C ensures that no previously deposited metallic structure will be damaged during the film growing process. Another possible solution could be using spun-on dielectrics such as hydrogen silsesquioxane (HSQ) [185]. Although HSQ films have lower breakdown electrical fields (5 MV/cm [215]) compared to the ALD method their use is simpler and requires no specialised equipment. Since the deposition of HSQ can be performed on a spin-coater followed by the baking on a hot plate of less than 300°C. As is the same case with ALD, the low baking temperatures will cause no damage to the predeposited structures.

The device presented in this work was designed to operate at a wavelength of 635 nm. Although this wavelength is easier to detect ($h\nu > E_g$), it is also associated with high losses in plasmonic waveguides. Shifting the operating wavelength into the near-IR spectra can sufficiently decrease the losses. The architecture presented in this thesis is flexible and permits adjusting various parameters such as the operating wavelength, the waveguide shape and materials used. Therefore, a change in operating wavelength could be performed by a redesign of the device using the sequence presented in this thesis.

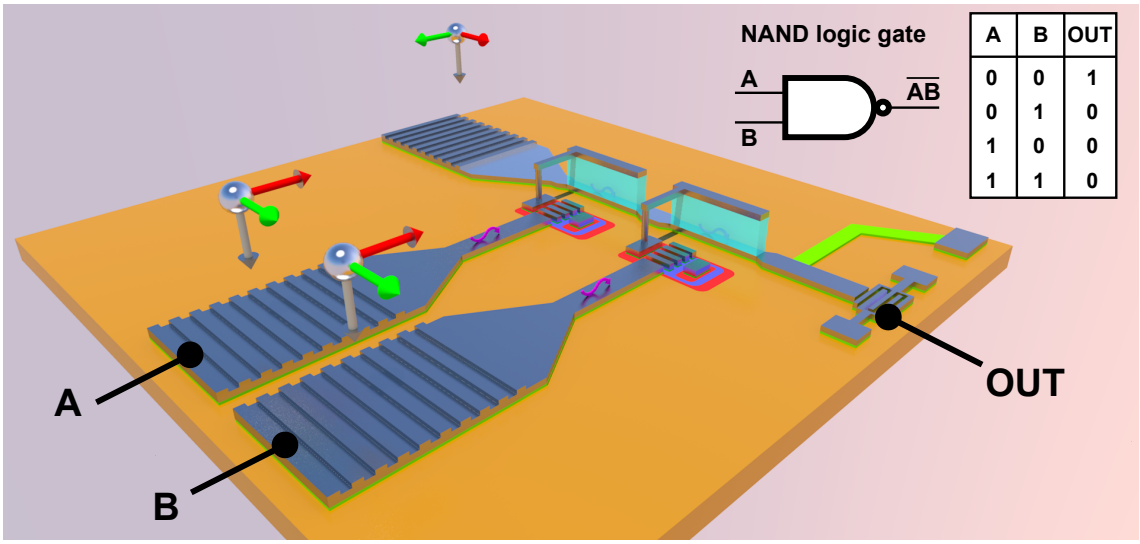

A	B	OUT
0	0	1
0	1	0
1	0	0
1	1	0

Figure 10.1: Concept design of a 'NAND' logic gate with plasmonic interconnects.

The plasmonic logic gate presented in this thesis implements a 'NOT' logic function. It could easily be modified to perform a 'NAND' logic function by adding another input and modulator along the output waveguide (see Fig.10.1). The implementation of a 'NAND' logic gate would enable functional completeness [35] so any boolean function could be implemented using their combination. Such a design, therefore, could be used to create fully functional electro-plasmonic digital integrated circuits.

10.2.2 Plasmonic-enhanced photodetectors

The concept of the differential photodetector presented here also lends itself to the development of devices for the full determination of the Stokes parameters of an incident field (see Fig.10.2) and, taking advantage of recent developments in the design of metasurfaces for sensing wavelength [196] and phase [197], the concept could be extended to extraction of other information from optical fields.

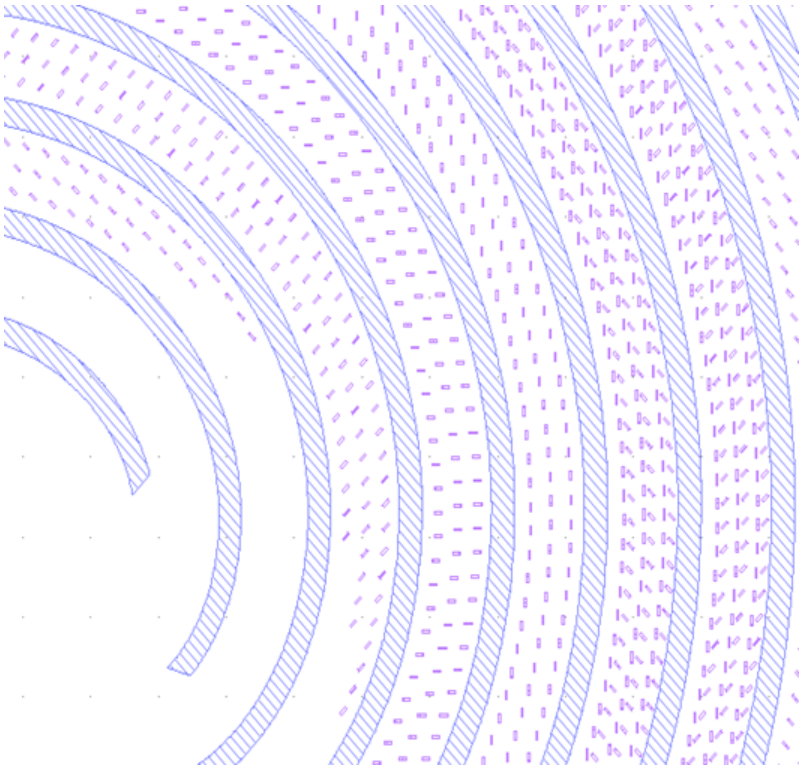

Figure 10.2: Schematic representation of differential photodetector capable of full determination of the Stokes parameters of an incident field.

Furthermore, the substitution of Si with a lower band gap semiconductor would open up the potential of producing a device that could operate at near-IR wave-

lengths. This photodetector design, therefore, could play a role in future telecommunication systems permitting increased operation speeds and even higher channel multiplexing densities due to improved signal-to-noise ratios. Similarly to the differential photodetectors, the plasmonic pixels shown can be improved to extend the sensitivity range into UV and near-IR regions. The plasmonic pixels, therefore, can be used as a planar nanoscale alternative to conventional colour or even hyperspectral pixels in future high-resolution or scientific cameras.

10.3 Summary

Finally, this thesis has demonstrated how surface plasmon phenomena can be used to overcome current limitations in optical and semiconductor technologies and enable new features in conventional photodetectors. Significant achievements include the development of the design for a plasmonic input port and demonstrating experimentally a surface plasmon planar detection mechanism. In addition, a comprehensive analytical and numerical study of a plasmonic modulator has been presented. The integration of plasmonic metasurfaces to enable polarisation and colour sensitivity in Schottky diode based photodetectors was also demonstrated. Furthermore, a novel photodetector design utilising a differential detection approach which significantly improves signal-to-noise ratio was also demonstrated. The work presented in this thesis will enable the next generation of optoelectronic integrated circuits, polarisation-based telecommunication systems and compact high-resolution camera pixels and sensors.

Bibliography

[1] Tsann-Bim Chiou, Mircea Dusa, Alek C Chen, and David Pietromonaco. Lithographic challenges and their solutions for critical layers in sub-14nm node logic devices. In *SPIE Advanced Lithography*, pages 86830R–86830R. International Society for Optics and Photonics, 2013.

[2] Walid Hafez, William Snodgrass, and Milton Feng. 12.5 nm base pseudomorphic heterojunction bipolar transistors achieving ft=710ghz and fmax=340ghz. *Applied Physics Letters*, 87(25):252109, 2005.

[3] Edward-Yi Chang, Chien-I Kuo, Heng-Tung Hsu, Che-Yang Chiang, and Yasuyuki Miyamoto. Inas thin-channel high-electron-mobility transistors with very high current-gain cutoff frequency for emerging submillimeter-wave applications. *Applied Physics Express*, 6(3):034001, 2013.

[4] A Critique of Pure Speed. http://5gnews.org/critique-pure-speed/, 2014. [Online; accessed 03-11-2016].

[5] A_K Sinha, JA Cooper, and HJ Levinstein. Speed limitations due to interconnect time constants in vlsi integrated circuits. *IEEE Electron Device Letters*, 3(4):90–92, 1982.

[6] Dietmar Korn. *Silicon-Organic Hybrid Platform for Photonic Integrated Circuits*, volume 15. KIT Scientific Publishing, 2015.

[7] Mark T Bohr et al. Interconnect scaling-the real limiter to high performance ulsi. In *International Electron Devices Meeting*, pages 241–244. INSTITUTE OF ELECTRICAL & ELECTRONIC ENGINEERS, INC (IEEE), 1995.

[8] Ruichen Liu, Chien-Shing Pai, and Emilio Martinez. Interconnect technology trend for microelectronics. *Solid-State Electronics*, 43(6):1003–1009, 1999.

[9] CH Diaz, KL Young, JH Hsu, JCH Lin, CS Hou, CT Lin, JJ Liaw, CC Wu, CW Su, CH Wang, et al. A 0.18/spl mu/m cmos logic technology with dual gate oxide and low-k interconnect for high-performance and low-power applications. In *VLSI Technology, 1999. Digest of Technical Papers. 1999 Symposium on*, pages 11–12. IEEE, 1999.

[10] Mehmet Fatih Yanik, Shanhui Fan, Marin Soljačić, and John D Joannopoulos. All-optical transistor action with bistable switching in a photonic crystal cross-waveguide geometry. *Optics Letters*, 28(24):2506–2508, 2003.

[11] Sajeev John and Marian Florescu. Photonic bandgap materials: towards an all-optical micro-transistor. *Journal of Optics A: Pure and Applied Optics*, 3(6):S103, 2001.

[12] Yuanliang Zhang, Yao Zhang, and Baojun Li. Optical switches and logic gates based on self-collimated beams in two-dimensional photonic crystals. *Optics Express*, 15(15):9287–9292, 2007.

[13] Jibo Bai, Junqin Wang, Junzhen Jiang, Xiyao Chen, Hui Li, Yishen Qiu, and Zexuan Qiang. Photonic 'not' and 'nor' gates based on a single compact photonic crystal ring resonator. *Applied optics*, 48(36):6923–6927, 2009.

[14] Johann Riemensberger, Klaus Hartinger, Tobias Herr, Victor Brasch, Ronald Holzwarth, and Tobias J Kippenberg. Dispersion engineering of thick high-q silicon nitride ring-resonators via atomic layer deposition. *Optics Express*, 20(25):27661–27669, 2012.

[15] F Müller, A Birner, U Gösele, V Lehmann, S Ottow, and nH Föll. Structuring of macroporous silicon for applications as photonic crystals. *Journal of Porous Materials*, 7(1-3):201–204, 2000.

[16] Pierre Berini. Plasmon-polariton waves guided by thin lossy metal films of finite width: Bound modes of symmetric structures. *Physical Review B*, 61(15):10484, 2000.

[17] Yoichi Kurokawa and Hideki T Miyazaki. Metal-insulator-metal plasmon nanocavities: Analysis of optical properties. *Physical Review B*, 75(3):035411, 2007.

[18] Pieter Neutens, Pol Van Dorpe, Iwijn De Vlaminck, Liesbet Lagae, and Gustaaf Borghs. Electrical detection of confined gap plasmons in metal–insulator–metal waveguides. *Nature Photonics*, 3(5):283–286, 2009.

[19] Evgeniy Panchenko, Timothy D James, and Ann Roberts. Modified stripe waveguide design for plasmonic input port structures. *Journal of Nanophotonics*, 10(1):016019–016019, 2016.

[20] Wenshan Cai, Justin S White, and Mark L Brongersma. Compact, high-speed and power-efficient electrooptic plasmonic modulators. *Nano Letters*, 9(12):4403–4411, 2009.

[21] Jennifer A Dionne, Kenneth Diest, Luke A Sweatlock, and Harry A Atwater. Plasmostor: a metal- oxide- si field effect plasmonic modulator. *Nano Letters*, 9(2):897–902, 2009.

[22] Hua Lu, Xueming Liu, Leiran Wang, Yongkang Gong, and Dong Mao. Ultrafast all-optical switching in nanoplasmonic waveguide with kerr nonlinear resonator. *Optics Express*, 19(4):2910–2915, 2011.

[23] Carsten Marquart, Sergey Bozhevolnyi, and Kristjan Leosson. Near-field imaging of surface plasmon-polariton guiding in band gap structures at telecom wavelengths. *Optics Express*, 13(9):3303–3309, 2005.

[24] Max Born and Emil Wolf. *Principles of optics: electromagnetic theory of propagation, interference and diffraction of light*. Cambridge university press, 1999.

[25] Ling Liao, Dean Samara-Rubio, Michael Morse, Ansheng Liu, Dexter Hodge, Doron Rubin, Ulrich D Keil, and Thorkild Franck. High speed silicon mach-zehnder modulator. *Optics Express*, 13(8):3129–3135, 2005.

[26] Stefan Alexander Maier. *Plasmonics: Fundamentals and Applications*. Springer, 2007.

[27] Jasper J Cadusch, Timothy D James, and Ann Roberts. Experimental demonstration of a wave plate utilizing localized plasmonic resonances in nanoapertures. *Optics Express*, 21(23):28450–28455, 2013.

[28] Jasper J Cadusch, Timothy D James, Amir Djalalian-Assl, Timothy J Davis, and Ann Roberts. A chiral plasmonic metasurface circular polarization filter. *Photonics Technology Letters, IEEE*, 26(23):2357–2360, 2014.

[29] Hong Wei, Zhipeng Li, Xiaorui Tian, Zhuoxian Wang, Fengzi Cong, Ning Liu, Shunping Zhang, Peter Nordlander, Naomi J Halas, and Hongxing Xu. Quantum dot-based local field imaging reveals plasmon-based interferometric logic in silver nanowire networks. *Nano Letters*, 11(2):471–475, 2010.

[30] Stuart K Earl, Timothy D James, Timothy J Davis, Jeffrey C McCallum, Robert E Marvel, Richard F Haglund, and Ann Roberts. Tunable optical antennas enabled by the phase transition in vanadium dioxide. *Optics Express*, 21(22):27503–27508, 2013.

[31] Stuart K Earl, Timothy D James, Robert E Marvel, Daniel E Gomez, Timothy J Davis, Jason G Valentine, Jeffrey C McCallum, Richard F Haglund, and Ann Roberts. Vanadium dioxide thickness effects on tunable optical antennas. In *SPIE Micro+ Nano Materials, Devices, and Applications*, pages 89232S–89232S. International Society for Optics and Photonics, 2013.

[32] Maziar P Nezhad, Kevin Tetz, and Yeshaiahu Fainman. Gain assisted propagation of surface plasmon polaritons on planar metallic waveguides. *Optics Express*, 12(17):4072–4079, 2004.

[33] Noel M Morris. Operational amplifier circuits. In *Mastering Electronic and Electrical Calculations*, pages 305–317. Springer, 1996.

[34] Graham T Reed, G Mashanovich, FY Gardes, and DJ Thomson. Silicon optical modulators. *Nature Photonics*, 4(8):518–526, 2010.

[35] Heinrich Wansing. *The logic of information structures*. 1993.

[36] Nanfang Yu and Federico Capasso. Flat optics with designer metasurfaces. *Nature materials*, 13(2):139–150, 2014.

[37] Timothy D James, Paul Mulvaney, and Ann Roberts. The plasmonic pixel: large area, wide gamut color reproduction using aluminum nanostructures. *Nano Letters*, 2016.

[38] Nanfang Yu, Francesco Aieta, Patrice Genevet, Mikhail A Kats, Zeno Gaburro, and Federico Capasso. A broadband, background-free quarter-wave plate based on plasmonic metasurfaces. *Nano Letters*, 12(12):6328–6333, 2012.

[39] Evgeniy Panchenko, Jasper J Cadusch, Timothy D James, and Ann Roberts. Plasmonic metasurface-enabled differential photodetectors for broadband optical polarization characterization. *ACS Photonics*, 3(10):1833–1839, 2016.

[40] Guixin Li, Ming Kang, Shumei Chen, Shuang Zhang, Edwin Yue-Bun Pun, Kok Wai Cheah, and Jensen Li. Spin-enabled plasmonic metasurfaces for manipulating orbital angular momentum of light. *Nano Letters*, 13(9):4148–4151, 2013.

[41] Jiao Lin, Patrice Genevet, Mikhail A Kats, Nicholas Antoniou, and Federico Capasso. Nanostructured holograms for broadband manipulation of vector beams. *Nano Letters*, 13(9):4269–4274, 2013.

[42] B Zhu, TF Taunay, M Fishteyn, X Liu, S Chandrasekhar, MF Yan, JM Fini, EM Monberg, and FV Dimarcello. 112-tb/s space-division multiplexed dwdm transmission with 14-b/s/hz aggregate spectral efficiency over a 76.8-km seven-core fiber. *Optics Express*, 19(17):16665–16671, 2011.

[43] Joseph C Chon, Benjamin B Jian, and Jerry R Bautista. High-capacity and high-speed dwdm and nwdm optical devices for telecom and datacom applications. In *Symposium on Integrated Optics*, pages 36–45. International Society for Optics and Photonics, 2001.

[44] Nenad Bozinovic, Yang Yue, Yongxiong Ren, Moshe Tur, Poul Kristensen, Hao Huang, Alan E Willner, and Siddharth Ramachandran. Terabit-scale orbital angular momentum mode division multiplexing in fibers. *Science*, 340(6140):1545–1548, 2013.

[45] Bahram Javidi and Takanori Nomura. Polarization encoding for optical security systems. *Optical Engineering*, 39(9):2439–2443, 2000.

[46] Johannes F De Boer, Thomas E Milner, Martin JC van Gemert, and J Stuart Nelson. Two-dimensional birefringence imaging in biological tissue by polarization-sensitive optical coherence tomography. *Optics Letters*, 22(12):934–936, 1997.

[47] Norma J Greenfield. Using circular dichroism spectra to estimate protein secondary structure. *Nature Protocols*, 1(6):2876–2890, 2006.

[48] Daniel E Browne and Terry Rudolph. Resource-efficient linear optical quantum computation. *Physical Review Letters*, 95(1):010501, 2005.

[49] Maki Koike-Tani, Tomomi Tani, Shalin B Mehta, Amitabh Verma, and Rudolf Oldenbourg. Polarized light microscopy in reproductive and developmental biology. *Molecular Reproduction and Development*, 82(7-8):548–562, 2015.

[50] Avtar S Matharu, Shehzad Jeeva, and PS Ramanujam. Liquid crystals for holographic optical data storage. *Chemical Society Reviews*, 36(12):1868–1880, 2007.

[51] Peter Zijlstra, James WM Chon, and Min Gu. Five-dimensional optical recording mediated by surface plasmons in gold nanorods. *Nature*, 459(7245):410–413, 2009.

[52] Yan Han and Guifang Li. Coherent optical communication using polarization multiple-input-multiple-output. *Optics Express*, 13(19):7527–7534, 2005.

[53] Werayut Srituravanich, Liang Pan, Yuan Wang, Cheng Sun, David B Bogy, and Xiang Zhang. Flying plasmonic lens in the near field for high-speed nanolithography. *Nature Nanotechnology*, 3(12):733–737, 2008.

[54] Ling Lin, Xiao M Goh, Liam P McGuinness, and Ann Roberts. Plasmonic lenses formed by two-dimensional nanometric cross-shaped aperture arrays for fresnel-region focusing. *Nano Letters*, 10(5):1936–1940, 2010.

[55] Aurelien Drezet, Cyriaque Genet, and Thomas W Ebbesen. Miniature plasmonic wave plates. *Physical Review Letters*, 101(4):043902, 2008.

[56] Sozo Yokogawa, Stanley P Burgos, and Harry A Atwater. Plasmonic color filters for cmos image sensor applications. *Nano Letters*, 12(8):4349–4354, 2012.

[57] Wei Li, Zachary J Coppens, Lucas V Besteiro, Wenyi Wang, Alexander O Govorov, and Jason Valentine. Circularly polarized light detection with hot electrons in chiral plasmonic metamaterials. *Nature Communications*, 6, 2015.

[58] Keang-Po Ho. *Phase-modulated optical communication systems*. Springer Science & Business Media, 2005.

[59] Anoma D McCoy, Peter Horak, Benn C Thomsen, Morten Ibsen, and David J Richardson. Noise suppression of incoherent light using a gain-saturated soa: Implications for spectrum-sliced wdm systems. *Journal of Lightwave Technology*, 23(8):2399, 2005.

[60] Mingshan Zhao, Geert Morthier, and Roel Baets. Analysis and optimization of intensity noise reduction in spectrum-sliced wdm systems using a saturated semiconductor optical amplifier. *Photonics Technology Letters, IEEE*, 14(3):390–392, 2002.

[61] Xiang Zhou, Jianjun Yu, Dayou Qian, Ting Wang, Guodong Zhang, and Peter Magill. 8x114 gb/s, 25-ghz-spaced, polmux-rz-8psk transmission over 640 km of ssmf employing digital coherent detection and edfa-only amplification. In

National Fiber Optic Engineers Conference, page PDP1. Optical Society of America, 2008.

[62] Peter J Winzer, Martin Pfennigbauer, and René-Jean Essiambre. Coherent crosstalk in ultradense wdm systems. *Journal of Lightwave Technology*, 23(4):1734, 2005.

[63] B Cai, LA Johansson, CFC Silva, S Bennett, and Alwyn J Seeds. Crosstalk, noise, and stability analysis of dwdm channels generated by injection locking techniques. *Lightwave Technology, Journal of*, 21(12):3029–3036, 2003.

[64] DJ Shin, DK Jung, Jung Keun Lee, JH Lee, YH Choi, YC Bang, HS Shin, JK Lee, ST Hwang, and YJ Oh. 155 mbit/s transmission using ase-injected fabry-perot laser diode in wdm-pon over 70 c temperature range. *Electronics Letters*, 39(18):1331–1332, 2003.

[65] Ashok Narasimhan, Manish Kasotiya, and Ramalingam Sridhar. A low-swing differential signalling scheme for on-chip global interconnects. In *VLSI Design, 2005. 18th International Conference on*, pages 634–639. IEEE, 2005.

[66] Don Anderson and Dave Dzatko. *Universal serial bus system architecture*. Addison-Wesley Longman Publishing Co., Inc., 2001.

[67] Stevan Eidson, Brett Gaines, and Paul Wolf. 30.2: Hdmi: High-definition multimedia interface. In *SID Symposium Digest of Technical Papers*, volume 34, pages 1024–1027. Wiley Online Library, 2003.

[68] Abhay Joshi, Xinde Wang, Dan Mohr, Don Becker, and Christoph Wree. Balanced photoreceivers for analog and digital fiber optic communications. In *Defense and Security*, pages 39–50. International Society for Optics and Photonics, 2005.

[69] Xiang Liu, S Chandrasekhar, and Andreas Leven. Digital self-coherent detection. *Optics Express*, 16(2):792–803, 2008.

[70] David Prakel. *The visual dictionary of photography*. Ava Publishing, 2009.

[71] Francis M Reininger. Imaging spectrometer/camera having convex grating, August 8 2000. US Patent 6,100,974.

[72] J Itatani, F Quéré, Gennady L Yudin, M Yu Ivanov, Ferenc Krausz, and Paul B Corkum. Attosecond streak camera. *Physical Review Letters*, 88(17):173903, 2002.

[73] Rainer Lenzen, Reiner Hofmann, Peter Bizenberger, and Andreas Tusche. Conica: the high-resolution near-infrared camera for the eso vlt. In *Astronomical Telescopes & Instrumentation*, pages 606–614. International Society for Optics and Photonics, 1998.

[74] George R Carruthers and Thornton Page. Apollo 16 far-ultraviolet camera/spectrograph: Earth observations. *Science*, 177(4051):788–791, 1972.

[75] Digital camera sensor colour filters. http://www.jthonline.com/WordPress/archives/7268, 2015. [Online; accessed 08-08-2016].

[76] Ting Chen, Peter B Catrysse, Abbas El Gamal, and Brian A Wandell. How small should pixel size be? In *Electronic Imaging*, pages 451–459. International Society for Optics and Photonics, 2000.

[77] Joyce Farrell, Feng Xiao, and Sam Kavusi. Resolution and light sensitivity tradeoff with pixel size. In *Electronic Imaging 2006*, pages 60690N–60690N. International Society for Optics and Photonics, 2006.

[78] iPhone 6S And iPhone 6S Plus: Best And Worst Camera Features. http://www.forbes.com/sites/paulmonckton/2015/09/12/iphone-6s-and-iphone-6s-plus-camera-features/#889ed427805c, 2015. [Online; accessed 15-01-2017].

[79] Tzu-Hsuan Hsu, Yean-Kuen Fang, CY Lin, SF Chen, CS Lin, Dun-Nian Yaung, Shou-Gwo Wuu, HC Chien, CH Tseng, JS Lin, et al. Light guide for pixel crosstalk improvement in deep submicron cmos image sensor. *IEEE Electron Device Letters*, 25(1):22–24, 2004.

[80] Diffraction Limited Photography: Pixel Size, Aperture and Airy Disks. http://www.cambridgeincolour.com/tutorials/diffraction-photography.htm, 2016. [Online; accessed 15-01-2017].

[81] Douglas J Guerrero, William DiMenna, Tony D Flaim, Ramil Mercado, and Sam Sun. Dyed red, green, and blue photoresist for manufacture of high-resolution color filter arrays for image sensors. In *Electronic Imaging 2003*, pages 298–306. International Society for Optics and Photonics, 2003.

[82] Daniela Baierl, Lucio Pancheri, Morten Schmidt, David Stoppa, Gian-Franco Dalla Betta, Giuseppe Scarpa, and Paolo Lugli. A hybrid cmos-imager with a solution-processable polymer as photoactive layer. *Nature Communications*, 3:1175, 2012.

[83] Ranjith Rajasekharan, Eugeniu Balaur, Alexander Minovich, Sean Collins, Timothy D James, Amir Djalalian-Assl, Kumaravelu Ganesan, Snjezana Tomljenovic-Hanic, Sasikaran Kandasamy, Efstratios Skafidas, et al. Filling schemes at submicron scale: Development of submicron sized plasmonic colour filters. *Scientific Reports*, 4:6435, 2014.

[84] Mark W Knight, Heidar Sobhani, Peter Nordlander, and Naomi J Halas. Photodetection with active optical antennas. *Science*, 332(6030):702–704, 2011.

[85] Horst Zimmermann. *Integrated silicon optoelectronics*. Springer, 2010.

[86] Lukas Novotny and Bert Hecht. *Principles of Nano-optics*. Cambridge university press, 2012.

[87] Shinji Hayashi and Takayuki Okamoto. Plasmonics: visit the past to know the future. *Journal of Physics D: Applied Physics*, 45(43):433001, 2012.

[88] Max Born and Emil Wolf. *Principles of Optics*. Cambridge University Press, 1997.

[89] Peter B Johnson and R-W_ Christy. Optical constants of the noble metals. *Physical Review B*, 6(12):4370, 1972.

[90] Volker J Sorger, Norberto D Lanzillotti-Kimura, Ren-Min Ma, and Xiang Zhang. Ultra-compact silicon nanophotonic modulator with broadband response. *Nanophotonics*, 1(1):17–22, 2012.

[91] Ernst Jan R Vesseur, René de Waele, Martin Kuttge, and Albert Polman. Direct observation of plasmonic modes in au nanowires using high-resolution cathodoluminescence spectroscopy. *Nano Letters*, 7(9):2843–2846, 2007.

[92] Toon Coenen, Ernst Jan R Vesseur, Albert Polman, and A Femius Koenderink. Directional emission from plasmonic yagi–uda antennas probed by angle-resolved cathodoluminescence spectroscopy. *Nano Letters*, 11(9):3779–3784, 2011.

[93] A Hatta, Y Suzuki, and W Suëtaka. Infrared absorption enhancement of monolayer species on thin evaporated ag films by use of a kretschmann configuration: Evidence for two types of enhanced surface electric fields. *Applied Physics A*, 35(3):135–140, 1984.

[94] JT Van Wijngaarden, E Verhagen, A Polman, CE Ross, HJ Lezec, and HA Atwater. Direct imaging of propagation and damping of near-resonance surface

plasmon polaritons using cathodoluminescence spectroscopy. *Applied Physics Letters*, 88(22):221111, 2006.

[95] Shuwen Zeng, Ken-Tye Yong, Indrajit Roy, Xuan-Quyen Dinh, Xia Yu, and Feng Luan. A review on functionalized gold nanoparticles for biosensing applications. *Plasmonics*, 6(3):491–506, 2011.

[96] Marek Piliarik, Hana Vaisocherová, and Jiří Homola. Surface plasmon resonance biosensing. *Biosensors and Biodetection*, pages 65–88, 2009.

[97] J Bodesheim and A Otto. On the quantitative measurement of the roughness spectrum of silver films. *Surface Science*, 45(2):441–456, 1974.

[98] B Hecht, H Bielefeldt, L Novotny, Y Inouye, and DW Pohl. Local excitation, scattering, and interference of surface plasmons. *Physical Review Letters*, 77(9):1889, 1996.

[99] NA Janunts, KS Baghdasaryan, Kh V Nerkararyan, and B Hecht. Excitation and superfocusing of surface plasmon polaritons on a silver-coated optical fiber tip. *Optics Communications*, 253(1):118–124, 2005.

[100] R Dallapiccola, C Dubois, A Gopinath, Francesco Stellacci, and L Dal Negro. Near-field excitation and near-field detection of propagating surface plasmon polaritons on au waveguide structures. *Applied Physics Letters*, 94(24):243118, 2009.

[101] Jean-Claude Weeber, Alain Dereux, Christian Girard, Joachim R Krenn, and Jean-Pierre Goudonnet. Plasmon polaritons of metallic nanowires for controlling submicron propagation of light. *Physical Review B*, 60(12):9061, 1999.

[102] Bogdan Dragnea, Jodi M Szarko, Stefan Kowarik, Thomas Weimann, Jochen Feldmann, and Stephen R Leone. Near-field surface plasmon excitation on structured gold films. *Nano Letters*, 3(1):3–7, 2003.

[103] Harald Ditlbacher, Andreas Hohenau, Dieter Wagner, Uwe Kreibig, Michael Rogers, Ferdinand Hofer, Franz R Aussenegg, and Joachim R Krenn. Silver nanowires as surface plasmon resonators. *Physical Review Letters*, 95(25):257403, 2005.

[104] Tobias Holmgaard and Sergey I Bozhevolnyi. Theoretical analysis of dielectric-loaded surface plasmon-polariton waveguides. *Physical Review B*, 75(24):245405, 2007.

[105] Volker J Sorger, Rupert F Oulton, Jie Yao, Guy Bartal, and Xiang Zhang. Plasmonic fabry-pérot nanocavity. *Nano Letters*, 9(10):3489–3493, 2009.

[106] Abram L Falk, Frank HL Koppens, L Yu Chun, Kibum Kang, Nathalie de Leon Snapp, Alexey V Akimov, Moon-Ho Jo, Mikhail D Lukin, and Hongkun Park. Near-field electrical detection of optical plasmons and single-plasmon sources. *Nature Physics*, 5(7):475–479, 2009.

[107] Bing Wang. Plasmon bragg reflectors and nanocavities on flat metallic surfaces. *Applied Physics Letters*, 87(1):013107–013107, 2005.

[108] PA Belov, SA Tretyakov, and AJ Viitanen. Nonreciprocal microwave band-gap structures. *Physical Review E*, 66(1):016608, 2002.

[109] Florencio García Santamaría. *Photonic crystals based on silica microspheres cristales fotónicos basados en microesferas de sílice*. PhD thesis, Universidad Autonoma de Madrid, 2003.

[110] Ken Kuriki, Ofer Shapira, Shandon Hart, Gilles Benoit, Yuka Kuriki, Jean Viens, Mehmet Bayindir, John Joannopoulos, and Yoel Fink. Hollow multilayer photonic bandgap fibers for nir applications. *Optics Express*, 12(8):1510–1517, 2004.

[111] Thomas Søndergaard and Sergey I Bozhevolnyi. Surface plasmon polariton guiding in photonic bandgap structures. In *Surface Plasmon Nanophotonics*, pages 73–86. Springer, 2007.

[112] Sergey I Bozhevolnyi. Plasmonic nano-guides and circuits. In *Plasmonics and Metamaterials*, page MWD3. Optical Society of America, 2008.

[113] Amir Hosseini, Hamid Nejati, and Yehia Massoud. Design of a maximally flat optical low pass filter using plasmonic nanostrip waveguides. *Optics Express*, 15(23):15280–15286, 2007.

[114] Jer-Shing Huang, Thorsten Feichtner, Paolo Biagioni, and Bert Hecht. Impedance matching and emission properties of nanoantennas in an optical nanocircuit. *Nano Letters*, 9(5):1897–1902, 2009.

[115] Dongying Li and Er-Ping Li. Impedance calculation and equivalent circuits for metal–insulator–metal plasmonic waveguide geometries. *Optics Letters*, 38(17):3384–3386, 2013.

[116] Amir Hosseini, Hamid Nejati, and Yehia Massoud. An analytical model for characteristic impedance in nanostrip plasmonic waveguides. In *Circuits and Systems, 2008. ISCAS 2008. IEEE International Symposium on*, pages 2346–2349. IEEE, 2008.

[117] Hong Wei, Zhuoxian Wang, Xiaorui Tian, Mikael Käll, and Hongxing Xu. Cascaded logic gates in nanophotonic plasmon networks. *Nature Communications*, 2:387, 2011.

[118] Yoshiaki Hisakado, Hirotsugu Kikuchi, Toshihiko Nagamura, and Tisato Kajiyama. Large electro-optic kerr effect in polymer-stabilized liquid-crystalline blue phases. *Advanced Materials*, 17(1):96–98, 2005.

[119] William T Lotshaw, Dale McMorrow, Constantinos Kalpouzos, and Geraldine A Kenney-Wallace. Femtosecond dynamics of the optical kerr effect in liquid nitrobenzene and chlorobenzene. *Chemical Physics Letters*, 136(3):323–328, 1987.

[120] Luke A Sweatlock and Kenneth Diest. Vanadium dioxide based plasmonic modulators. *Optics Express*, 20(8):8700–8709, 2012.

[121] TD James, S Earl, J Valentine, TJ Davis, J McCallum, RF Haglund, and A Roberts. Vanadium dioxide based tunable plasmonic antennas. In *Optoelectronic and Microelectronic Materials & Devices (COMMAD), 2012 Conference on*, pages 113–114. IEEE, 2012.

[122] Brett A Kruger, Arash Joushaghani, and Joyce KS Poon. Design of electrically driven hybrid vanadium dioxide (vo2) plasmonic switches. *Optics Express*, 20(21):23598–23609, 2012.

[123] Josef Stoer and Roland Bulirsch. *Introduction to numerical analysis*, volume 12. Springer Science & Business Media, 2013.

[124] Krishnan Thyagarajan, Simon Rivier, Andrea Lovera, and Olivier JF Martin. Enhanced second-harmonic generation from double resonant plasmonic antennae. *Optics Express*, 20(12):12860–12865, 2012.

[125] Luke A Sweatlock. *Plasmonics: Numerical methods and device applications*. PhD thesis, Citeseer, 2008.

[126] Krishnan Thyagarajan, Jeremy Butet, and Olivier JF Martin. Augmenting second harmonic generation using fano resonances in plasmonic systems. *Nano Letters*, 13(4):1847–1851, 2013.

[127] Michele Celebrano, Xiaofei Wu, Milena Baselli, Swen Großmann, Paolo Biagioni, Andrea Locatelli, Costantino De Angelis, Giulio Cerullo, Roberto Osellame, Bert Hecht, et al. Mode matching in multiresonant plasmonic nanoantennas for enhanced second harmonic generation. *Nature Nanotechnology*, 10(5):412–417, 2015.

[128] Gilbert Strang and George J Fix. *An analysis of the finite element method*, volume 212. Prentice-hall Englewood Cliffs, NJ, 1973.

[129] Lumerical: Knowledge base. https://kb.lumerical.com/en/particle_scattering_nanowire_discussion_results.html, 2017. [Online; accessed 15-06-2017].

[130] Mark A McCord and Michael J Rooks. Spie handbook of microlithography, micromachining and microfabrication. In *SPIE, Bellingham*, 2000.

[131] Cen Shawn Wu, ChiiDong Chen, and Yoshiyuki Makiuchi. *High-energy electron beam lithography for nanoscale fabrication*. INTECH Open Access Publisher, 2010.

[132] Microelectronics: Fabrication of micro/nano structures on silicon surface. http://www.dileepnanotech.com/articles/Lithography.html, 2011. [Online; accessed 08-08-2016].

[133] Alec N Broers. Resolution limits of pmma resist for exposure with 50 kv electrons. *Journal of The Electrochemical Society*, 128(1):166–170, 1981.

[134] ZEP520A: Technical Report. https://www.zeonchemicals.com/pdfs/ZEP520A.pdf, 2010. [Online; accessed 04-10-2016].

[135] Electron Beam Source for Electron Beam Deposition. http://www.jeol.co.jp/en/science/eb.html, 2016. [Online; accessed 04-10-2016].

[136] MVU TM RIT - vacuum RIE machine. http://www.made-in-zelenograd.com/products/mvu-tm-rit/, 2016. [Online; accessed 14-11-2016].

[137] Hitachi Launches Worlds Highest Resolution FE-SEM. http://www.nanotech-now.com/news.cgi?story_id=42612, 2011. [Online; accessed 15-11-2016].

[138] Michael A Paesler and Patrick J Moyer. *Near-field optics: theory, instrumentation, and applications*. Wiley-Interscience, 1996.

[139] Olympus Microscopy Resource Center. http://www.olympusmicro.com/primer/techniques/nearfield/nearfieldintro.html, 2015. [Online; accessed 03-11-2016].

[140] Sergey I Bozhevolnyi, Valentyn S Volkov, Eloise Devaux, and Thomas W Ebbesen. Channel plasmon-polariton guiding by subwavelength metal grooves. *Physical Review Letters*, 95(4):046802, 2005.

[141] Jonathan E Allen, Daniel E Perea, Eric R Hemesath, and Lincoln J Lauhon. Nonuniform nanowire doping profiles revealed by quantitative scanning photocurrent microscopy. *Advanced Materials*, 21(30):3067–3072, 2009.

[142] Jonathan E Allen, Eric R Hemesath, and Lincoln J Lauhon. Scanning photocurrent microscopy analysis of si nanowire field-effect transistors fabricated by surface etching of the channel. *Nano Letters*, 9(5):1903–1908, 2009.

[143] Kevin F MacDonald, Zsolt L Sámson, Mark I Stockman, and Nikolay I Zheludev. Ultrafast active plasmonics. *Nature Photonics*, 3(1):55–58, 2009.

[144] Alexey V Krasavin and Anatoly V Zayats. Silicon-based plasmonic waveguides. *Optics Express*, 18(11):11791–11799, 2010.

[145] Rupert F Oulton, Volker J Sorger, DA Genov, DFP Pile, and X Zhang. A hybrid plasmonic waveguide for subwavelength confinement and long-range propagation. *Nature Photonics*, 2(8):496–500, 2008.

[146] Christoph Walther, Giacomo Scalari, Maria Ines Amanti, Mattias Beck, and Jérôme Faist. Microcavity laser oscillating in a circuit-based resonator. *Science*, 327(5972):1495–1497, 2010.

[147] Ting Wang, Huiyun Liu, Andrew Lee, Francesca Pozzi, and Alwyn Seeds. 1.3-μm inas/gaas quantum-dot lasers monolithically grown on si substrates. *Optics Express*, 19(12):11381–11386, 2011.

[148] TS Chao. Introduction to semiconductor manufacturing technology. 2001.

[149] Panos C Andricacos. Copper on-chip interconnections. *The Electrochemical Society Interface*, 8(1):6, 1999.

[150] Ivan S Maksymov and Yu S Kivshar. Broadband light coupling to dielectric slot waveguides with tapered plasmonic nanoantennas. *Optics Letters*, 38(22):4853–4856, 2013.

[151] Jesse Lu, Csaba Petre, Eli Yablonovitch, and Josh Conway. Numerical optimization of a grating coupler for the efficient excitation of surface plasmons at an ag-sio 2 interface. *JOSA B*, 24(9):2268–2272, 2007.

[152] Ali Sobhani, Mark W Knight, Yumin Wang, Bob Zheng, Nicholas S King, Lisa V Brown, Zheyu Fang, Peter Nordlander, and Naomi J Halas. Narrowband photodetection in the near-infrared with a plasmon-induced hot electron device. *Nature Communications*, 4:1643, 2013.

[153] Robert H Havemann and James A Hutchby. High-performance interconnects: An integration overview. *Proceedings of the IEEE*, 89(5):586–601, 2001.

[154] Weize Xiong, Gabriel Gebara, Joyti Zaman, Michael Gostkowski, Billy Nguyen, Greg Smith, David Lewis, C Rinn Cleavelin, Rick Wise, Shaofeng Yu, et al. Improvement of finfet electrical characteristics by hydrogen annealing. *Electron Device Letters, IEEE*, 25(8):541–543, 2004.

[155] R Böhme, J Zajadacz, K Zimmer, and B Rauschenbach. Topography and roughness evolution of microstructured surfaces at laser-induced backside wet etching. *Applied Physics A*, 80(2):433–438, 2005.

[156] David M Pozar. *Microwave engineering*. John Wiley & Sons, 2009.

[157] David H Schrader. *Microstrip circuit analysis*. Prentice Hall PTR, 1995.

[158] Kevin M McPeak, Sriharsha V Jayanti, Stephan JP Kress, Stefan Meyer, Stelio Iotti, Aurelio Rossinelli, and David J Norris. Plasmonic films can easily be better: rules and recipes. *ACS Photonics*, 2(3):326–333, 2015.

[159] Kamalesh K Srivastava, Jonathan H Griffith, Mary C Cullinan-Scholl, William H Brearley, and Peter C Wade. Integrated method for etching of blm titanium-tungsten alloys for cmos devices with copper metallization, September 25 2001. US Patent 6,293,457.

[160] Chit Hwei Ng and Chaw Sing Ho. Method to fabricate dual-metal cmos transistors for sub-0.1 μm ulsi integration, June 25 2002. US Patent 6,410,376.

[161] Dmitri K Gramotnev and Sergey I Bozhevolnyi. Plasmonics beyond the diffraction limit. *Nature Photonics*, 4(2):83–91, 2010.

[162] David Jeffrey Griffiths and Reed College. *Introduction to electrodynamics*, volume 3. prentice Hall Upper Saddle River, NJ, 1999.

[163] Christine Scales and Pierre Berini. Thin-film schottky barrier photodetector models. *IEEE Journal of Quantum Electronics*, 46(5):633–643, 2010.

[164] MY Liu, E Chen, and SY Chou. 140-ghz metal-semiconductor-metal photodetectors on silicon-on-insulator substrate with a scaled active layer. *Applied Physics Letters*, 65(7):887–888, 1994.

[165] M Hack, M Shur, and CC Tsai. Amorphous silicon photoconductive diode. *Applied Physics Letters*, 54(2):96–98, 1989.

[166] MO Aboelfotoh and KN Tu. Schottky-barrier heights of ti and tisi 2 on n-type and p-type si (100). *Physical Review B*, 34(4):2311, 1986.

[167] Marc A Taubenblatt and CR Helms. Silicide and schottky barrier formation in the ti-si and the ti-siox-si systems. *Journal of Applied Physics*, 53(9):6308–6315, 1982.

[168] John Marsh. Electro-absorption modulator with broad optical bandwidth, March 14 2003. US Patent App. 10/507,670.

[169] Ning-Ning Feng, Dazeng Feng, Shirong Liao, Xin Wang, Po Dong, Hong Liang, Cheng-Chih Kung, Wei Qian, Joan Fong, Roshanak Shafiiha, et al. 30ghz ge electro-absorption modulator integrated with 3μm silicon-on-insulator waveguide. *Optics Express*, 19(8):7062–7067, 2011.

[170] Yu A Akimov and HS Chu. Plasmon–plasmon interaction: controlling light at nanoscale. *Nanotechnology*, 23(44):444004, 2012.

[171] Eyal Feigenbaum, Kenneth Diest, and Harry A Atwater. Unity-order index change in transparent conducting oxides at visible frequencies. *Nano Letters*, 10(6):2111–2116, 2010.

[172] H Kim, CM Gilmore, A Pique, JS Horwitz, H Mattoussi, H Murata, ZH Kafafi, and DB Chrisey. Electrical, optical, and structural properties of indium–tin–oxide thin films for organic light-emitting devices. *Journal of Applied Physics*, 86(11):6451–6461, 1999.

[173] EH Hwang and S Das Sarma. Dielectric function, screening, and plasmons in two-dimensional graphene. *Physical Review B*, 75(20):205418, 2007.

[174] DL Young, TJ Coutts, VI Kaydanov, AS Gilmore, and WP Mulligan. Direct measurement of density-of-states effective mass and scattering parameter

in transparent conducting oxides using second-order transport phenomena. *Journal of Vacuum Science & Technology A*, 18(6):2978–2985, 2000.

[175] Kyoung-Kook Kim, Hyunsoo Kim, Sung-Nam Lee, and Soohaeng Cho. Structural, optical, and electrical properties of e-beam and sputter-deposited ito films for led applications. *Electronic Materials Letters*, 7(2):145–149, 2011.

[176] Ocal Tuna, Yusuf Selamet, Gulnur Aygun, and Lutfi Ozyuzer. High quality ito thin films grown by dc and rf sputtering without oxygen. *Journal of Physics D: Applied Physics*, 43(5):055402, 2010.

[177] LH Willems van Beveren, Evgeniy Panchenko, Nik Anachi, Lachlan Hyde, Dan Smith, TD James, Ann Roberts, and JC McCallum. Indium tin oxide film characterization using the classical hall effect. In *2014 Conference on Optoelectronic and Microelectronic Materials & Devices*, pages 144–145. IEEE, 2014.

[178] Patrick M Hemenger. Measurement of high resistivity semiconductors using the van der pauw method. *Review of Scientific Instruments*, 44(6):698–700, 1973.

[179] Neil W Ashcroft and N David Mermin. *Introduction to Solid State Physics*. Saunders, Philadelphia, 1976.

[180] Safa Kasap. Hall effect in semiconductors. *Electronic Booklet*, 2001.

[181] KC Park and EJ Weitzman. E-beam evaporated glass and mgo layers for gas panel fabrication. *IBM Journal of Research and Development*, 22(6):607–612, 1978.

[182] J Nulman, JP Krusius, and A Gat. Rapid thermal processing of thin gate dielectrics. oxidation of silicon. *IEEE Electron Device Letters*, 6(5):205–207, 1985.

[183] Private communications, 2015. [McCallum Jeffrey et al.].

[184] Mikko Ritala, Kaupo Kukli, Antti Rahtu, Petri I Räisänen, Markku Leskelä, Timo Sajavaara, and Juhani Keinonen. Atomic layer deposition of oxide thin films with metal alkoxides as oxygen sources. *Science*, 288(5464):319–321, 2000.

[185] Chang-Chung Yang and Wen-Chang Chen. The structures and properties of hydrogen silsesquioxane (hsq) films produced by thermal curing. *Journal of Materials Chemistry*, 12(4):1138–1141, 2002.

[186] Liang Tang, Sukru Ekin Kocabas, Salman Latif, Ali K Okyay, Dany-Sebastien Ly-Gagnon, Krishna C Saraswat, and David AB Miller. Nanometre-scale germanium photodetector enhanced by a near-infrared dipole antenna. *Nature Photonics*, 2(4):226–229, 2008.

[187] Inga A Fischer, Jyh-Lih Wu, Ralf Vogelgesang, and Jörg Schulze. Towards electrical detection of plasmons in all-silicon pin-diodes. *Physica Status Solidi (b)*, 249(4):773–777, 2012.

[188] Fatima Eftekhari and TJ Davis. Strong chiral optical response from planar arrays of subwavelength metallic structures supporting surface plasmon resonances. *Physical Review B*, 86(7):075428, 2012.

[189] SK Earl, DE Gómez, TD James, TJ Davis, and A Roberts. Material effects on v-nanoantenna performance. *Nanoscale*, 7(9):4179–4186, 2015.

[190] Qiwen Zhan. Cylindrical vector beams: from mathematical concepts to applications. *Advances in Optics and Photonics*, 1(1):1–57, 2009.

[191] Paul R Berger. Msm photodiodes. *Potentials, IEEE*, 15(2):25–29, 1996.

[192] Haoran Ren, Xiangping Li, Qiming Zhang, and Min Gu. On-chip noninterference angular momentum multiplexing of broadband light. *Science*, page aaf1112, 2016.

[193] BL Sharma. *Metal-semiconductor Schottky barrier junctions and their applications*. Springer Science & Business Media, 2013.

[194] Bernard Sklar. *Digital communications*, volume 2. Prentice Hall NJ, 2001.

[195] Mark W Knight, Nicholas S King, Lifei Liu, Henry O Everitt, Peter Nordlander, and Naomi J Halas. Aluminum for plasmonics. *ACS Nano*, 8(1):834–840, 2013.

[196] Shawn J Tan, Lei Zhang, Di Zhu, Xiao Ming Goh, Ying Min Wang, Karthik Kumar, Cheng-Wei Qiu, and Joel KW Yang. Plasmonic color palettes for photorealistic printing with aluminum nanostructures. *Nano Letters*, 14(7):4023–4029, 2014.

[197] Timothy J Davis, Daniel E Gómez, and Fatima Eftekhari. All-optical modulation and switching by a metamaterial of plasmonic circuits. *Optics Letters*, 39(16):4938–4941, 2014.

[198] Ian T Young, Jan J Gerbrands, and Lucas J Van Vliet. *Fundamentals of image processing*. Delft University of Technology Delft, 1998.

[199] Takao Toi and Mutsumi Ohita. A subband coding technique for image compression in single ccd cameras with bayer color filter arrays. *IEEE Transactions on Consumer Electronics*, 45(1):176–180, 1999.

[200] Jim Adams, Ken Parulski, and Kevin Spaulding. Color processing in digital cameras. *IEEE Micro*, 18(6):20–30, 1998.

[201] Patrick SP Wang. *Pattern recognition, machine intelligence and biometrics*. Springer, 2011.

[202] Marko Tkalcic, Jurij F Tasic, et al. Colour spaces: perceptual, historical and applicational background. In *Eurocon*, 2003.

[203] Na Liu, Martin Mesch, Thomas Weiss, Mario Hentschel, and Harald Giessen. Infrared perfect absorber and its application as plasmonic sensor. *Nano Letters*, 10(7):2342–2348, 2010.

[204] KL Lee, D Boyd, J Brancaccio, J Bucchignano, J Cai, K Chan, H Hanafi, P Kozlowski, R Miller, R Roy, et al. New polysilicon disposable sidewall process for sub-50 nm cmos. In *Solid-State Device Research Conference, 2001. Proceeding of the 31st European*, pages 159–162. IEEE, 2001.

[205] Liudi Jiang, NOV Plank, MA Blauw, R Cheung, and E van der Drift. Dry etching of sic in inductively coupled cl2/ar plasma. *Journal of Physics D: Applied Physics*, 37(13):1809, 2004.

[206] Gyeong S Hwang and Konstantinos P Giapis. Aspect ratio independent etching of dielectrics. *Applied Physics Letters*, 71(4):458–460, 1997.

[207] Yanbin An, Ashkan Behnam, Eric Pop, and Ant Ural. Metal-semiconductor-metal photodetectors based on graphene/p-type silicon schottky junctions. *Applied Physics Letters*, 102(1):013110, 2013.

[208] Katsunori Ueno, Tatsue Urushidani, Kouichi Hashimoto, and Yasukazu Seki. The guard-ring termination for the high-voltage sic schottky barrier diodes. *IEEE Electron Device Letters*, 16(7):331–332, 1995.

[209] SK Cheung and NW Cheung. Extraction of schottky diode parameters from forward current-voltage characteristics. *Applied Physics Letters*, 49(2):85–87, 1986.

[210] Ji Yu, Chong-Xin Shan, Qian Qiao, Xiu-Hua Xie, Shuang-Peng Wang, Zhen-Zhong Zhang, and De-Zhen Shen. Enhanced responsivity of photodetectors realized via impact ionization. *Sensors*, 12(2):1280–1287, 2012.

[211] Jaewook Shin, Bryan T Bosworth, and Mark A Foster. Single-pixel imaging using compressed sensing and wavelength-dependent scattering. *Optics Letters*, 41(5):886–889, 2016.

[212] Evgeniy Panchenko, Jasper J Cadusch, Timothy D James, Daniel Gomez, and Ann Roberts. Planar surface plasmon detection technique for high speed interconnects in integrated circuits. *In preparation.*

[213] Evgeniy Panchenko, Jasper J Cadusch, Timothy D James, Daniel Gomez, and Ann Roberts. Plasmonic metasurface-enabled hyperspectral camera pixel. *In preparation.*

[214] Seok-Jun Won, Sungin Suh, Myung Soo Huh, and Hyeong Joon Kim. High-quality low-temperature silicon oxide by plasma-enhanced atomic layer deposition using a metal–organic silicon precursor and oxygen radical. *IEEE Electron Device Letters*, 31(8):857–859, 2010.

[215] Ta-Shan Chang, Ting-Chang Chang, Po-Tsun Liu, Tien-Shan Chang, Chun-Hao Tu, Feng-Sheng Yeh, et al. Improvement of hydrogenated amorphous-silicon tft performances with low-k siloxane-based hydrogen silsesquioxane (hsq) passivation layer. *IEEE Electron Device Letters*, 27(11):902–904, 2006.

[216] Amir Djalalian-Assl, Jasper J Cadusch, Zhi Qin Teo, Timothy J Davis, and Ann Roberts. Surface plasmon wave plates. *Applied Physics Letters*, 106(4):041104, 2015.

[217] Ali Akbari, R Niall Tait, and Pierre Berini. Surface plasmon waveguide schottky detector. *Optics Express*, 18(8):8505–8514, 2010.

[218] Michael Kanellos. Intel scientists find wall for moores law. *ZDNet News, December*, 1, 2003.

[219] Mark T Bohr and Youssef A El-Mansy. Technology for advanced high-performance microprocessors. *Electron Devices, IEEE Transactions on*, 45(3):620–625, 1998.

[220] B Lamprecht, JR Krenn, G Schider, H Ditlbacher, M Salerno, N Felidj, A Leitner, FR Aussenegg, and JC Weeber. Surface plasmon propagation in microscale metal stripes. *Applied Physics Letters*, 79(1):51–53, 2001.

[221] Eloise Devaux, Thomas W Ebbesen, Jean-Claude Weeber, and Alain Dereux. Launching and decoupling surface plasmons via micro-gratings. *Applied Physics Letters*, 83(24):4936–4938, 2003.

[222] Andrei Andryieuski and Andrei V Lavrinenko. Nanocouplers for infrared and visible light. *Advances in OptoElectronics*, 2012, 2012.

[223] John H Lau. *Flip chip technologies*. McGraw-Hill Professional, 1996.

[224] R Willett, JP Eisenstein, HL Störmer, DC Tsui, AC Gossard, and JH English. Observation of an even-denominator quantum number in the fractional quantum hall effect. *Physical Review Letters*, 59(15):1776, 1987.

[225] Ekaterina V Astrova. Processing of macroporous silicon. In *Handbook of Porous Silicon*, pages 715–729. Springer, 2014.

[226] Frank Forstmann and Rolf R Gerhardts. Metal optics near the plasma frequency. 1986.

[227] Jasmin Smajic, Christian Hafner, Ludmila Raguin, Kakhaber Tavzarashvili, and Matthew Mishrikey. Comparison of numerical methods for the analysis of plasmonic structures. *Journal of Computational and Theoretical Nanoscience*, 6(3):763–774, 2009.

Appendix A

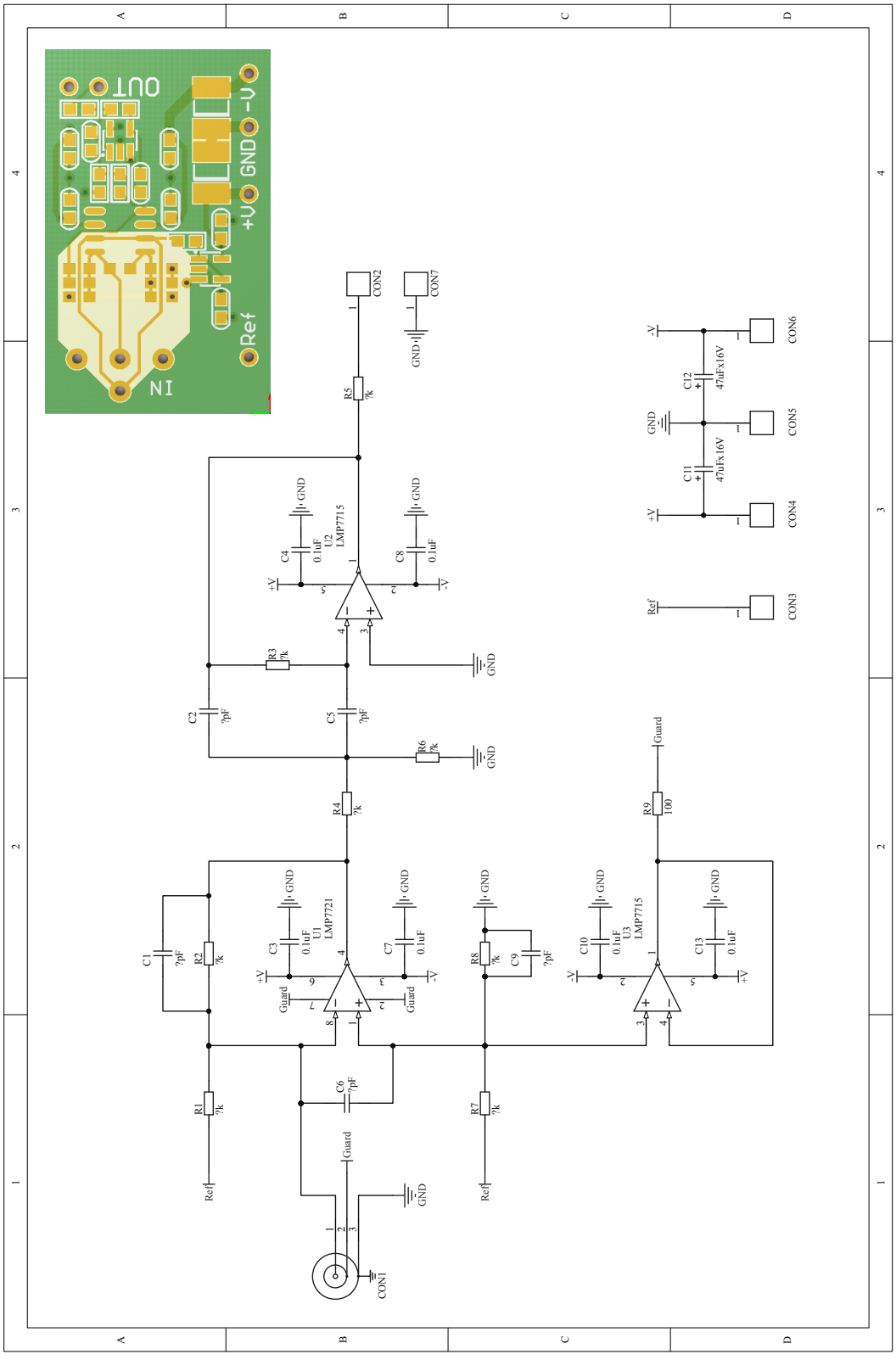

Figure A1: Electronic schematic of transimpedance amplifier specially designed for differential photodetector. The inset demonstrates the printed circuit board of the amplifier.

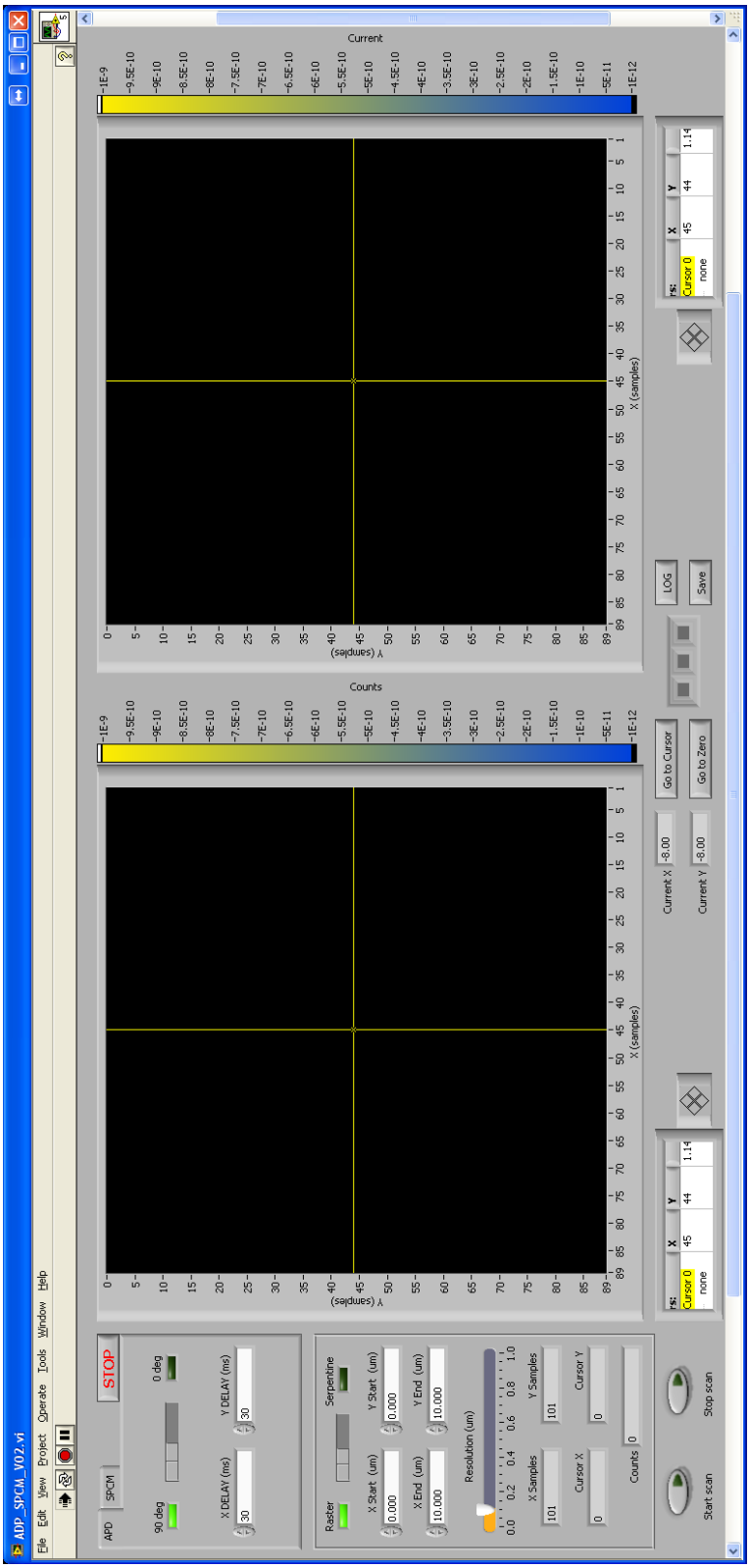

Figure A2: Interface of the LabView program developed for the SPCM setup.